Studies of Four-Top-Quark Production in Proton-Proton Collisions at the LHC With The Same-Sign Dilepton and Multilepton Final States

by

Meng-Ju Tsai

A dissertation submitted in partial fulfillment
of the requirements for the degree of
Doctor of Philosophy
(Physics)
in the University of Michigan
2024

Doctoral Committee:

Professor Jianming Qian, Chair
Professor Thomas Schwarz
Professor James Wells
Associate Professor Qiong Yang
Professor Bing Zhou

Meng-Ju Tsai
metsai@umich.edu
ORCID ID: 0000-0002-4728-9150

ACKNOWLEDGEMENTS

First and foremost, I would like to express my deepest gratitude to my thesis advisor, Professor Jianming Qian, for his unwavering support and guidance through my entire doctoral program in Michigan. Jianming has always given me the best advice, suggestions, and ideas. His vision, passion, and tremendous knowledge have profoundly influenced me. I am incredibly fortunate to have Jianming as my advisor.

I sincerely thank Zhi Zheng, the former Ph.D. student working with Jianming and current postdoc at SLAC. Zhi is my closest collaborator and almost my second advisor in my entire Ph.D., providing significant support in physics and technical knowledge for the analyses I worked on. I also thank Zhi and Zhi's husband, Shang Zhang, for their support during the pandemic and ample discussions on different topics.

I am immensely grateful to the Michigan ATLAS group. I thank Professors Bing Zhou, Dante Amidei, Junjie Zhu, and Thomas Schwarz for their insightful discussions of my research projects and the frontier physics results. This advances my knowledge of physics and experience. I thank Tiesheng Dai and Zhen Yan (Boston University) for training and supervising me on the sMDT commissioning project and the muon MDT operation. I also thank Matthew Klein for the great ideas and help on any random technical problems I encountered. I want to thank Jem Guhit and Nicholas Kyriacou for their friendship and help in the daily support at CERN. I would also like to thank the former and present colleagues in the Michigan ATLAS group: Andy Chen, Aaron White, Hui-Chi Lin, Ismet Siral, Kevin Nelson, Rongkun Wang, Wenhao Xu, Yanlin Liu, Zhichen

Wang, Zhe Yang, Zhongyukun Xu, Zirui Wang, and many others for their friendship and help. Finally, I thank Wendy Dronen and Shawn Mckee for technical support in the computing environment at Michigan to keep me productive in the analyses.

I am incredibly fortunate to work with many outstanding physicists in the ATLAS collaboration. I am highly grateful to Aurelio Juste Rozas, Elizaveta Shabalina, Nedaa Alexandra Asbah, and Tamara Vazquez Schroeder for their insightful suggestions and support on $t\bar{t}t\bar{t}$ analyses and the $t\bar{t}W$ analysis (one of my side work, not covered in this dissertation). I want to thank the strong leadership of Frederic Deliot, Yang Qin, and Zhi for achieving the first observation of $t\bar{t}t\bar{t}$. I am incredibly thankful for Frederic's daily progress check, which helps me keep my productivity. I also thank Haichen Wang, Elizaveta, Nedaa, Frederic, Yang, and Zhi for the insightful discussions on every detail of the analyses and the support for the development of the new method for background modeling. I also want to thank Shuo Han, Tsai-Chen Lee, Rachel Lindley, Ryan Roberts, Xiang Chen, and many others for the fruitful and pleasant collaborations in the SM $t\bar{t}t\bar{t}$ team. I also thank Daniela Paredes, Nicola Orlando, and Shuhui Huang for the great collaborations in the BSM $t\bar{t}t\bar{t}$ team. I want to thank Zirui Wang, Sebastien Roy-Garand, and other colleagues for the pleasant collaborations in the 2HDM+a combination analysis. I also want to thank Nihal Brahimi, Brendon Bullard, Rohin Narayan, Marcel Niemeyer, Chenliang Wang, and many others for their support and collaborations in the $t\bar{t}W$ analysis. I also want to thank Binbin Dong, Philipp Gadow, Krisztian Peters, and Frederic for the fruitful collaborations in the ongoing multitop analyses. I also would like to thank all my friends inside and outside the collaboration, Jay Chan, Ya-Feng Lo, and Yuan-Tang Chou.

Finally, I would like to thank my parents, Chin-An Tsai and Kuei-Hui Lee, and my girlfriend, Candice Lee, for their love and support in my pursuit of academic achievement. This thesis is dedicated to them.

TABLE OF CONTENTS

LIST OF FIGURES

Figure

LIST OF TABLES

Table

LIST OF ABBREVIATIONS

$b\bar{b}H$ associated production with a pair of bottom quarks

B blue

χ^2 chi-square

ΔR angular distance

η pseudorapidity

E_T transverse energy

E_T^{miss} missing transverse momentum

$\vec{E}_T^{miss}$ missing transverse momentum vector

G green

$\hat{H}$ Higgs oblique parameter

I weak isospin

λ_I nuclear interaction length

L instantaneous luminosity

μ signal strength

μ_F factorization scale

μ_R renormalization scale

$PbPb$ lead-lead

p_T transverse momentum

pp proton-proton

$p\bar{p}$ proton-anitproton

pPb proton-lead

Q electric charge

R red

R_M Moliere radius

σ standard deviations

t_μ test statistic

tW single-top

tH associated production with a single top quark

$t\bar{t}H$ associated production with a pair of top quarks

$t\bar{t}t$ three-top-quark

$t\bar{t}t\bar{t}$ four-top-quark

VH associated production with a vector boson

y rapidity

1LOS one lepton or two leptons with opposite electric charge

2HDM Two-Higgs-Doublet Model

AUC area under the ROC curve

ALICE A Large Ion Collider Experiment

ATLAS A Toroidal LHC Apparatus

BDT Boosted Decision Trees

BSM beyond the Standard Model

CL confidence level

CP charge-parity

CR control region

CMS Compact Muon Solenoid

CSC Cathode Strip Chambers

CTP Central Trigger Processor

CERN European Organization for Nuclear Research

DM dark matter

EW electroweak

EM electromagnetic

EFT Effective Field Theory

EWSB electroweak symmetry breaking

ECIDS Electron Charge ID Selector

FE Front-End

FS flavor scheme

FSR final-state radiation

FCNC Flavor Changing Neutral Currents

FCal liquid-argon forward calorimeter

ggF gluon fusion

GNN Graph Neural Network

GPMC General-purpose Monte Carlo

HF heavy-flavor

HL High-Luminosity

HEC liquid-argon hadronic end-cap calorimeter

HLT High-Level Trigger

ID inner detector

ISR initial-state radiation

IP interaction point

IBL Insertable B-Layer

JES jet energy scale

JER jet energy resolution

JVT jet vertex tagger

L1 Level-1

LS 'Long Shutdowns'

LF light-flavor

LH likelihood

LO leading order

LAr liquid-argon

LHC Large Hadron Collider

LHCb Large Hadron Collider beauty

L1Calo L1 calorimeter

L1Muon L1 muon

L1Topo L1 topological

MC Monte Carlo

ME matrix element

ML multilepton

MS muon spectrometer

MDT Monitored Drift Tubes

MLP multilayer perceptron

MVA multivariate analysis

MSSM Minimal Supersymmetric Standard Model

NF normalization factor

NLO next-to-leading order

NNLO next-to-next-to-leading order

NNLL next-to-next-to-leading-logarithm

NN neural network

NP nuisance parameter

OS opposite-sign

PS parton shower

PDF parton distribution function

POI parameter of interest

pBDT mass-parameterized Boosted Decision Trees

PCBT pseudo-continuous b-tagging

PFlow particle flow

PLImproved Prompt Lepton Improved

PV primary vertex

QED Quantum Electrodynamics

QCD Quantum Chromodynamics

QFT Quantum Field Theory

QmisID Charge mis-assigned electrons

RPC Resistive Plate Chambers

RMS Root Mean Square

ROC Receiver Operating Characteristic

ROS ReadOut System

RNN Recurrent Neural Network

ROIs Regions of Interest

RODs ReadOut Drivers

SS same-sign

SM Standard Model

SR signal region

SF scale factor

SCT Semiconductor Tracker

SSML same-sign dilepton and multilepton

SUSY supersymmetry

stat-only statistical-only

T tesla

TRT Transition Radiation Tracker

TGC Thin Gap Chambers

TDAQ Trigger and Data Acquisition

UE underlying events

UFO Universal FeynRules Output

WP working point

WIMPs Weakly Interacting Massive Particles

VR validation region

VBF vector boson fusion

VEV Vacuum Expectation Value

XGBoost Extreme Gradient Boosting

ABSTRACT

This dissertation presents the measurements and searches of four-top-quark ($t\bar{t}t\bar{t}$) production with same-sign dilepton and multilepton final states in proton-proton collision data collected using the ATLAS detector at the LHC. Four-top-quark production, a rare process in the Standard Model (SM) with a cross section around 12 fb at a center-of-mass energy of 13 TeV, is one of the heaviest final states produced at the LHC, and it is naturally sensitive to beyond SM (BSM) physics. An early analysis by the ATLAS experiment (referred to as the $t\bar{t}t\bar{t}$ evidence analysis) resulted in an evidence for SM $t\bar{t}t\bar{t}$ production with a significance of 4.3 standard deviations with respect to the background-only hypothesis, but the measured $t\bar{t}t\bar{t}$ cross section is twice the SM prediction. This dissertation focuses on three major topics on the $t\bar{t}t\bar{t}$ production: the observation of the SM $t\bar{t}t\bar{t}$ production, a search of BSM $t\bar{t}t\bar{t}$ production ($t\bar{t}H/A \to t\bar{t}t\bar{t}$) predicted in the type-II Two-Higgs-Doublet Model (2HDM), and a reinterpretation analysis of BSM $t\bar{t}t\bar{t}$ search in a 2HDM+a combination analysis.

The first is the observation of four-top-quark production with same-sign dilepton and multilepton final states in an integrated luminosity of 140 fb^{-1} of proton-proton collision data at a center-of-mass energy of 13 TeV collected using the ATLAS detector. The analysis is based on the $t\bar{t}t\bar{t}$ evidence analysis with additional optimizations on object selection, background estimation, and a novel multivariate technique. Looser lepton identification requirements and lower jet p_T criteria are employed to maximize the $t\bar{t}t\bar{t}$ signal acceptance. A new $t\bar{t}W$ data-driven background estimation is utilized to improve the modeling of $t\bar{t}W$ jet multiplicity distribution. A novel graph neural network is used to separate the signal from the background. A simultaneous fit to both signal and control regions is

performed to extract the signal strength and constrain various background contributions. The $t\bar{t}t\bar{t}$ cross section is measured to be $22.5^{+6.6}_{-5.5}$ fb, consistent with the SM prediction of 12.0 ± 2.4 fb within 1.8 standard deviations. The corresponding observed (expected) significance of $t\bar{t}t\bar{t}$ production is found to be 6.1 (4.3) standard deviations with respect to the background-only hypothesis. Additional interpretations are explored, including limits on three-top-quark production, constraints on the Higgs-top Yukawa coupling, and effective field theory operator coefficients affecting $t\bar{t}t\bar{t}$ production.

The second is the search for a new heavy scalar or pseudo-scalar Higgs boson (H/A) predicted by the type-II 2HDM. The heavy Higgs boson is produced in association with a pair of top quarks ($t\bar{t}H/A$), with the Higgs boson decaying into a pair of top quarks ($H/A \to t\bar{t}$), leading to $t\bar{t}t\bar{t}$ production ($t\bar{t}H/A \to t\bar{t}t\bar{t}$). This analysis (referred to as the BSM $t\bar{t}t\bar{t}$ analysis) targets same-sign dilepton and multilepton final states with data corresponding to an integrated luminosity of 139 fb^{-1}. The analysis is based on the $t\bar{t}t\bar{t}$ evidence analysis with improved jet and b-jet algorithms. Two classifiers using Boosted Decision Trees are utilized to discriminate the signal and backgrounds. No significant excess of events is observed over the SM prediction. The observed (expected) upper limit at 95% confidence level on the $t\bar{t}H/A$ cross section times the branching ratio of $H/A \to t\bar{t}$ ranges between 14 (10) fb and 6 (5) fb for a heavy Higgs boson mass of 400 GeV and 1000 GeV. Constraints on $\tan\beta$ are derived under different scenarios. Assuming only one particle, either H or A, contributes to $t\bar{t}t\bar{t}$ production, $\tan\beta$ values below 1.2 or 0.5 are excluded for a heavy Higgs mass of 400 GeV or 1000 GeV. Assuming both H and A particles contribute to $t\bar{t}t\bar{t}$ production, $\tan\beta$ values below 1.6 or 0.6 are excluded for a heavy Higgs mass of 400 GeV or 1000 GeV.

The third is the combination of BSM searches to constrain the parameters of type-II 2HDM with an additional pseudo-scalar (a) mediating the interaction between ordinary matter and dark matter. The $t\bar{t}t\bar{t}$ process can be produced either from an s-channel diagram through a heavy Higgs boson ($H/A/a$) decaying to a pair of top quarks or a t-channel

diagram coupling with a heavy Higgs boson. This analysis follows the same strategy as the BSM $t\bar{t}t\bar{t}$ analysis to reinterpret with $t\bar{t}t\bar{t}$ production predicted in 2HDM+a, but uses different final discriminating distributions in the signal region. Constraints on the parameters of 2HDM+a are derived in several benchmark scenarios.

CHAPTER I

Introduction

What is our universe made of? This profound question was first posed a long time ago by the ancient Greek philosophers. Prior to the late 19th century, substantial developments in classical mechanics, electromagnetism, and thermodynamics initiated a transformative period in the understanding of the physical world. The dawn of the 20th century opened a new chapter in particle physics with groundbreaking discoveries and theoretical advancements. These included the discoveries of the radioactivity beta decay, electron, and proton, and the establishment of the atomic model. Subsequently, Quantum Mechanics and the Theory of Relativity were developed to describe the physics of microscopic and macroscopic worlds, respectively. Paul Dirac's pioneering work unified Quantum Mechanics with Special Relativity, leading to the prediction of antiparticles. In the 1940s, Quantum Electrodynamics (QED) [1–6] was formulated as the first quantum relativistic perturbation theory of electromagnetism. Contrary to expectations, the beta decay was anticipated to yield a discrete energy solution for the electrons. However, the observed energy spectrum of the electrons was surprisingly found to be continuous [7], which violated the conservation law. This paradox prompted the hypothesis of the neutrino to elucidate the mechanism of beta decay [8; 9]. Simultaneously, advancements in gauge theory using non-abelian groups [10; 11] laid the groundwork towards understanding the weak interaction. These collective works unify the electromagnetic and weak

forces, forming the electroweak (EW) theory [12–14]. Subsequently, the Higgs mechanism [15–17] was developed to explain the origin of the mass of elementary particles. In the 1960s, the discovery of numerous particles at high-energy accelerators led to what was known as the 'particle zoo', a chaotic period in particle physics. This complexity was later explained by Quantum Chromodynamics (QCD), which predicts how the strong force binds gluons and quarks together, resulting in various particle states. In the 1970s, these advancements of EW and QCD led to the establishment of a comprehensive theory of particle physics known as the Standard Model (SM). Many SM particles were verified experimentally since its establishment, but some particles were not yet observed. In the 1980s, $W^{\pm}$ and Z bosons, predicted in the SM EW theory, were observed by the UA1 and UA2 experiments using the Super Proton–Antiproton Synchrotron at the European Organization for Nuclear Research (CERN) [18–20]. In 1995, the top quark, the heaviest quark predicted in the SM, was discovered by the CDF and D∅ experiments at the Tevatron proton-anitproton ($p\bar{p}$) collider at Fermilab [21; 22]. Finally, the Higgs boson, the last important piece of the SM, was discovered in 2012 by the A Toroidal LHC Apparatus (ATLAS) and Compact Muon Solenoid (CMS) experiments at the Large Hadron Collider (LHC) [23; 24]. The SM is the most successful theoretical framework for describing the fundamental constituents and the forces of the universe. Despite its remarkable achievements, the SM is not without its unresolved problems. These include the accommodation of neutrino masses [25–27], the hierarchy problem [28; 29], the integration of gravity, matter-antimatter asymmetry, and other significant quandaries. New physics is needed to solve these problems.

The same-sign dilepton and multilepton (SSML) final states provide a great portal to examine the SM and explore new physics at the LHC. Both SM and beyond the Standard Model (BSM) processes can produce the SSML final states with different b-jet multiplicities. The SM predicts several rare but important processes that can produce the SSML final states, including the four-top-quark ($t\bar{t}t\bar{t}$) production, three-top-quark ($t\bar{t}t$)

production, $t\bar{t}$ associated production with bosons ($t\bar{t}X$), di-boson and multi-boson (VV and VVV), Higgs pair production with $t\bar{t}$ and vector bosons ($t\bar{t}HH$ and VHH), and multiple Higgs production (HHH and $HHHH$). Additionally, BSM scenarios can contribute to SSML final states with production such as the seesaw mechanism [30–34], supersymmetry (SUSY) [35–40], vector-like quarks [41–50], and interactions involving dark matter (DM). Any observed deviation from SM predictions could indicate new physics, which makes the accurate measurement of these rare SM processes crucial. Subsequent investigations can determine whether these deviations align with a specific BSM model.

The SSML final states are produced with low cross sections due to the small branching fraction of the leptonic decays. However, this characteristic results in a higher signal-to-background ratio than in hadronic channels. In the latter, hadronic final states from the same SM processes are associated with significantly higher cross sections, leading to substantial background rates. Due to the low rates of SSML events, dedicated measurements in the SSML final states became more feasible and precise after the Run 2 operation of LHC (detailed in Section 3.1) due to increased statistics. Measurements of SM processes decaying into SSML have shown small deviations from SM predictions, such as $t\bar{t}W$ [51] and $t\bar{t}t\bar{t}$ [52] production, on the order of 2 standard deviations (σ). Furthermore, the kinematics of these processes have not been extensively studied.

In 2020, evidence for the SM $t\bar{t}t\bar{t}$ production was achieved with the measured cross section twice of the SM prediction [52]. Further investigations are essential to understand the discrepancies. This analysis also identified limitations in the $t\bar{t}W$ modeling. A region with charge asymmetry, enriched by $t\bar{t}W$, had shown an unexpectedly higher number of data events, with positive total electric charges of the leptons, than the SM prediction. Similar discrepancies on $t\bar{t}W$ production were found in $t\bar{t}H$ and $t\bar{t}W$ measurements [51]. This discrepancy on the $t\bar{t}W$ production results in large ad-hoc $t\bar{t}W$ systematic uncertainties assigned to $t\bar{t}W$ backgrounds at high jet multiplicities, which limit the sensitivity

of the analysis.

This dissertation describes three analyses focusing on the $t\bar{t}t\bar{t}$ production. These include the first observation of SM $t\bar{t}t\bar{t}$ production (referred to as the SM $t\bar{t}t\bar{t}$ analysis), a search of BSM $t\bar{t}t\bar{t}$ production predicted by the type-II Two-Higgs-Doublet Model (2HDM) (referred to as the BSM $t\bar{t}t\bar{t}$ analysis), and a combination of BSM searches within the type-II 2HDM with a pseudo-scalar mediator a (2HDM+a) (referred to as the 2HDM+a combination analysis). The dissertation is organized as follows. Chapter II introduces the SM and BSM theories. The LHC and the phenomenology of LHC physics are discussed in Chapter III. Chapter IV outlines an overview of the ATLAS detector. Chapter V discusses an overview of particle identification and reconstruction in the ATLAS detector. Chapter VI introduces the common strategies for the SSML analyses. Chapter VII presents the first observation of the SM $t\bar{t}t\bar{t}$ production in the SSML final states. Chapter VII presents the search of BSM $t\bar{t}t\bar{t}$ production in the SSML final states. Chapter IX presents the 2HDM+a combination analysis reinterpreted from BSM $t\bar{t}t\bar{t}$ analysis. Finally, the summary and outlook are discussed in Chapter X.

CHAPTER II

Standard Model and Beyond

2.1 Standard Model

The SM describes the fundamental elementary particles and their interactions that build the universe. The elementary particles of SM are categorized into fermions and bosons: fermions are particles with half-integer spin following Fermi-Dirac statistics, while bosons are particles with integral spin obeying Bose–Einstein statistics. In the SM, quarks and leptons are fermions and serve as the building blocks of the matter, while bosons are force carriers and serve as the mediator for the interactions. A schematic summary of SM is shown in Figure 2.1.

Quarks, with a spin of 1/2, contain six flavors: up (u), down (d), charm (c), strange (s), bottom (b), and top (t). They are further grouped into three generations of doublets, with each doublet formed with an up (electric charge of $+2/3$) and down (electric charge of $-1/3$) type of quark. Each quark carries a color charge, which can be one of three colors: red (R), green (G) and blue (B). Due to the color confinement, quarks are never found in isolation. Instead, the bound state of quarks, known as hadron, is observed. A hadron can only be a neutral color charge, with a total color charge of white. The white color can be formed with a set of (R,G,B) or a pair of colors and anticolors, for example, ($R, \bar{R}$). Quarks are the only elementary particles that interact with all forces in SM.

Leptons, similar to quarks with a spin of 1/2, contain six flavors and three generations of doublets: electron (e), electron neutrino (ν_e), muon (μ), muon neutrino (ν_μ), tau (τ) and tau neutrino (ν_τ). Each charged lepton (e, μ, and τ) carries an electric charge of -1, while its antiparticle carries an electric charge of $+1$. Neutrinos (ν_e, ν_μ and ν_τ) are charge neutral. The charged leptons undergo electromagnetic and weak interactions, while neutrinos only experience weak interactions.

Bosons act as mediators for all types of interactions. There are two types of bosons in the SM: the scalar boson with spin 0 and the vector gauge boson with spin 1. In the SM, the only scalar boson is the Higgs boson, while the vector gauge bosons are gluons (g), photon (γ), $W^\pm$ and Z bosons. The gluons serve as mediators for the strong force, with each gluon carrying a color charge from one of eight color states. In total, there are eight gluons of different color states. The photon is the mediator for the electromagnetic interactions, with each photon carrying an electric charge of 0. Both gluons and photons are massless. The $W^\pm$ and Z bosons are massive mediators for the weak force with a $W^\pm$ boson carrying an electric charge of ±1 and a Z boson carrying an electric charge of 0. Finally, the Higgs boson provides the rest mass of the elementary particles through the Higgs mechanism. The Higgs boson is massive and has no electric or color charge.

2.1.1 Formalism of Standard Model

The SM is described by a Lagrangian ($\mathcal{L}$) in the formalism of Quantum Field Theory (QFT) under global Poincaré symmetry [54] and local symmetry of $SU(3)_C \times SU(2)_L \times U(1)_Y$ group. By Noether's theorem [55], each symmetry provides invariant quantities due to the invariance of a Lagrangian under transformations. The global Poincaré symmetry indicates that the Lagrangian of SM is invariant under the space-time transformations: translation, rotation, and Lorentz boost. These symmetries imply energy, momentum, and angular momentum conservation laws. The local symmetry of $SU(3)_C \times SU(2)_L \times U(1)_Y$ implies the three fundamental interactions of the strong, weak, and electromagnetic forces.

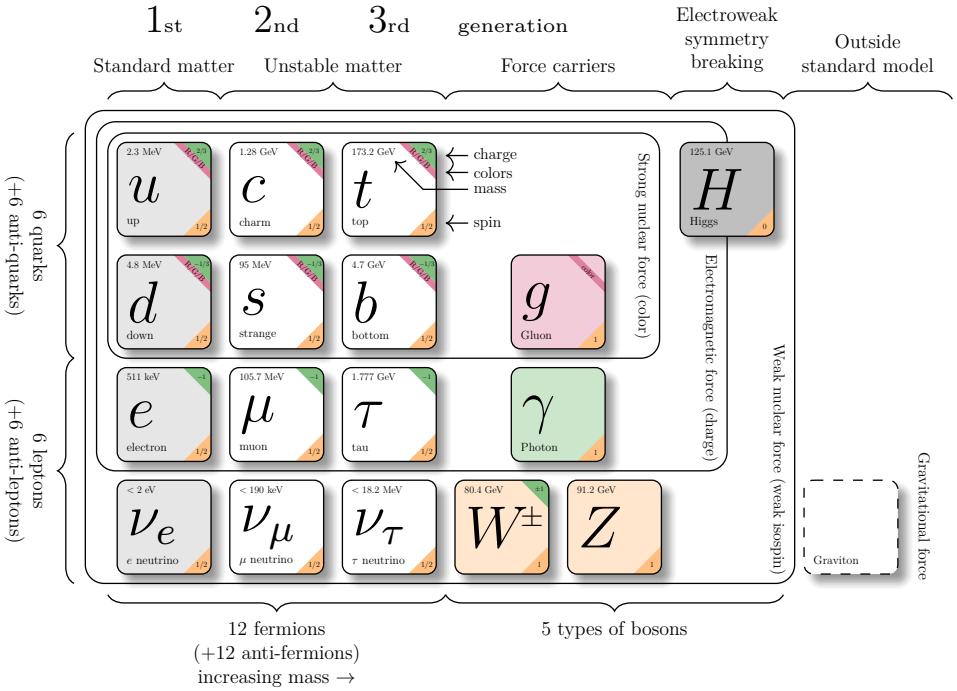

Figure 2.1: The building blocks of the SM [53].

The SM Lagrangian can be separated into QCD and EW terms,

$$\mathcal{L}_{\text{SM}} = \mathcal{L}_{\text{QCD}} + \underbrace{\mathcal{L}_{\text{gauge}} + \mathcal{L}_{\text{fermion}} + \mathcal{L}_{\text{Higgs}} + \mathcal{L}_{\text{Yukawa}}}_{\mathcal{L}_{\text{EW}}} . \tag{2.1}$$

QCD theory is described in Section 2.1.1.1, and EW theory is presented in Section 2.1.1.2 and Section 2.1.1.3.

2.1.1.1 Quantum Chromodynamics

QCD describes the strong interactions, which is based on the Yang-Mills theory [10; 11] with the $SU(3)_C$ gauge group. The symbol C represents the color charge, conserved with the $SU(3)_C$ symmetry. The quark is represented by a 3-dimensional field of $SU(3)_C$ under the basis of color charges of R, G, and B. The fields of quark (ψ) are under the $SU(3)_C$ transformation as,

$$\psi \rightarrow e^{ig_1\theta(x)T_a}\psi, \tag{2.2}$$

where $T_a = \lambda^a/2$ are the generators of $SU(3)_C$ with λ^a being the Gell-Mann matrices and index a is a discrete integer in a range of 1 to 8. The g_1 represents the QCD coupling constant, and $\theta(x)$ is an arbitrary function of space-time. The free Dirac Lagrangian,

$$\mathcal{L} = \bar{\psi}(i\gamma^\mu\partial_\mu - m)\psi, \tag{2.3}$$

is invariant under global $SU(3)$ transformation. However, it is no longer invariant under the local $SU(3)_C$ group. To construct an invariant Lagrangian under local $SU(3)_C$ transformations, a covariant derivative (D_μ) on the field is introduced,

$$D_\mu\psi = (\partial_\mu - ig_1G^a_\mu T^a)\psi, \tag{2.4}$$

where G^a_μ is the vector field of gluons. In addition, the kinematic term for the gauge fields is introduced as,

$$\mathcal{L}_{gauge} = -\frac{1}{4}G^a_{\mu\nu}G^{a\,\mu\nu}, \tag{2.5}$$

where the $G^a_{\mu\nu}$ is the color field tensor written as,

$$G^a_{\mu\nu} = \partial_\mu G^a_\nu - \partial_\nu G^a_\mu - g_1 f^{abc}G^b_\mu G^c_\nu, \tag{2.6}$$

where f^{abc} is the structure constant of $SU(3)_C$ group. The QCD Lagrangian can be written as,

$$\mathcal{L}_{QCD} = \underbrace{-\frac{1}{4}G^a_{\mu\nu}G^{a\,\mu\nu}}_{\text{Gluon self-coupling}} + \sum_{f=\text{quarks}} \underbrace{\bar{\psi}_f(i\gamma^\mu\partial_\mu - m)\psi_f}_{\text{Kinematic term}} + \underbrace{\bar{\psi}^\alpha_f g_1\gamma^\mu(T^a)_{\alpha\beta}G^a_\mu\psi^\beta_f}_{\text{Quark-gluon interaction}}, \tag{2.7}$$

where α and β are the color indices ($\alpha = 1, 2, 3$ and $\beta = 1, 2, 3$). This Lagrangian describes the interactions between quarks and gluons and the gluon self-interaction.

2.1.1.2 Electroweak Theory

The weak and electromagnetic interactions are unified as an EW theory, which is based on the $SU(2)_L \times U(1)_Y$ gauge group. The symbol L represents the left-handed chirality of weak interactions. This implies that the weak force only interacts with left-handed fermions, which was experimentally confirmed by Wu experiment [56]. The corresponding quantum number is the weak isospin (I). On the other hand, the symbol Y stands for the weak hypercharge, which is another quantum number associated with the EW theory. The electric charge (Q) is related to the $SU(2)_L$ and $U(1)_Y$ symmetry through Gell-Mann-Nishijima relation [57],

$$Q = I_3 + \frac{1}{2}Y, \tag{2.8}$$

where I_3 is the third component of weak isospin. This relation ensures the electric charge conservation under $SU(2)_L \times U(1)_Y$ symmetry. The fermion fields are divided into left-handed doublets and right-handed singlets under the $SU(2)_L$ group. The left-handed doublets with isospin $I = 1/2$ are written as,

$$\begin{pmatrix} \nu_e \\ e_L \end{pmatrix}, \begin{pmatrix} \nu_\mu \\ \mu_L \end{pmatrix}, \begin{pmatrix} \nu_\tau \\ \tau_L \end{pmatrix} \begin{pmatrix} u \\ d_L \end{pmatrix}, \begin{pmatrix} c \\ s_L \end{pmatrix}, \begin{pmatrix} t \\ b_L \end{pmatrix}, \tag{2.9}$$

where the neutrinos are left-handed only in the SM. The I_3 of the up (down) type in the doublet is +1/2 (-1/2). The right-handed singlets with isospin $I = 0$ are written as,

$$e_R, \mu_R, \tau_R, u_R, d_R, c_R, s_R, t_R, b_R, \tag{2.10}$$

where the I_3 is 0 for right-handed fermions. These properties of the fermions are summarized in Table 2.1.

Fermion family	Left-chiral fermions				Right-chiral fermions			
	Particles	Q	I_3	Y	Particles	Q	I_3	Y
Leptons	ν_e, ν_μ, ν_τ	0	$+\frac{1}{2}$	-1	ν_R (not exist in SM)			
	e^-, μ^-, τ^-	-1	$-\frac{1}{2}$	-1	e_R^-, μ_R^-, τ_R^-	-1	0	-2
Quarks	u, c, t	$+\frac{2}{3}$	$+\frac{1}{2}$	$+1$	u_R, c_R, t_R	$+\frac{2}{3}$	0	$+\frac{4}{3}$
	d, s, b	$-\frac{1}{3}$	$-\frac{1}{2}$	-1	d_R, s_R, b_R	$-\frac{1}{3}$	0	$-\frac{2}{3}$

Table 2.1: The properties of fermions in terms of the electric charge Q, the third component of weak isospin I_3, and hypercharge Y. The quantities follow the Gell-Mann-Nishijima relation.

The fermion fields are transformed under $U(1)_Y$ as,

$$L = \begin{pmatrix} \nu_e \\ e_L \end{pmatrix} \rightarrow e^{iY\theta(x)/2} \begin{pmatrix} \nu_e \\ e_L \end{pmatrix}, R = e_R \rightarrow e^{iY\theta(x)/2} e_R. \tag{2.11}$$

The invariance under the local $U(1)_Y$ transformation is achieved by introducing a covariant derivative with a vector boson gauge field (B_μ). The transformation of B_μ under $U(1)_Y$ group is defined as,

$$B_\mu \rightarrow B_\mu + \frac{1}{g_2}\partial_\mu \theta(x), \tag{2.12}$$

where g_2 is the coupling constant between B_μ and the fermions. The covariant derivative for $U(1)_Y$ is introduced as,

$$D_\mu \psi = (\partial_\mu - i g_2 \frac{Y}{2} B_\mu)\psi \tag{2.13}$$

On the other side, the fermion fields are transformed under $SU(2)_L$ as,

$$L = \begin{pmatrix} \nu_e \\ e_L \end{pmatrix} \rightarrow e^{i\vec{I}_3 \theta(\vec{x})\cdot\vec{\sigma}/2} \begin{pmatrix} \nu_e \\ e_L \end{pmatrix}, R = e_R \rightarrow e_R, \tag{2.14}$$

where $\vec{I_3}$ represents the projection of the weak isospin at the third component. The $\vec{\sigma}/2$ are generators of $SU(2)_L$, which are proportional to the Pauli matrices ($\vec{\sigma}$). The invariance of the Lagrangian under the local $SU(2)_L$ transformation is preserved by introducing the covariant derivative with three additional gauge fields, W_μ^a ($a = 1, 2, 3$), which transform as,

$$W_\mu^a \to W_\mu^a + \frac{2}{g_3}\partial_\mu \theta^a(x) + \epsilon^{abc}\theta^b(x)W_\mu^c, \tag{2.15}$$

where g_3 is the coupling constant between W_μ^a and the fermions, and ϵ^{abc} is the structure constant for $SU(2)_L$ which is total asymmetric. The covariant derivative for $SU(2)_L$ is written as,

$$D_\mu \begin{pmatrix} \nu_e \\ e_L \end{pmatrix} = (\partial_\mu - ig_3\frac{\sigma^i}{2}W_\mu^i) \begin{pmatrix} \nu_e \\ e_L \end{pmatrix}. \tag{2.16}$$

Under the $SU(2)_L \times U(1)_Y$ symmetry, the covariant derivatives acting on the fermion fields are

$$D_\mu \begin{pmatrix} \nu_e \\ e_L \end{pmatrix} = (\partial_\mu - ig_2\frac{Y_{\ell_L}}{2}B_\mu - ig_3\frac{\sigma^i}{2}W_\mu^i) \begin{pmatrix} \nu_e \\ e_L \end{pmatrix}, D_\mu e_R = (\partial_\mu - ig_2\frac{Y_{\ell_R}}{2}B_\mu)e_R, \tag{2.17}$$

where Y_{ℓ_L} and Y_{ℓ_R} are the weak hypercharges of left-handed and right-handed fermions. With the covariant derivative from Equation (2.17), the fermion Lagrangian can be written as,

$$\mathcal{L}_{fermion} = \sum_{f=L_L,L_R,Q_L,u_R,d_R} \bar{\psi}_f i\gamma^\mu \partial_\mu \psi_f \tag{2.18}$$

$$+ \underbrace{\sum_{f=L_L,L_R,Q_L,u_R,d_R} \bar{\psi}_f i\gamma^\mu (ig_2\frac{Y}{2}B_\mu)\psi_f - \sum_{f=L_L,Q_L} \bar{\psi}_f i\gamma^\mu (ig_3\frac{\sigma^i}{2}W_\mu^i)\psi_f}_{\text{Interaction term}}, \tag{2.19}$$

where L_L and Q_L represent left-handed doublets of each generation of leptons and quarks. The L_R denotes the singlet of leptons, while u_R and d_R denote the singlets of the up

and down type of the quark. The interaction terms of the Lagrangian, as presented in Equation (2.18), and following the treatment in Ref. [58], can be rewritten with an example using the first generation doublet as,

$$\begin{aligned}\mathcal{L}_{\nu_e,e} = & \underbrace{\sum_{f=\nu_e,e} eQ\bar{\psi}_f\gamma^\mu\psi_f A_\mu}_{\text{Electromagnetic interaction}} \\ & + \underbrace{\frac{e}{2\sin\theta_W\cos\theta_W}\sum_{f=\nu_e,e}\bar{\psi}_f\gamma^\mu(v_f - a_f\gamma_5)\psi_f Z_\mu}_{\text{Neutral current interaction}} \\ & + \underbrace{\frac{g_3}{\sqrt{2}}(\bar{\nu_e}\gamma^\mu e_L W_\mu^+ + \bar{e_L}\gamma^\mu\nu_e W_\mu^-)}_{\text{Charged current interaction}},\end{aligned} \tag{2.20}$$

where $a_f = I_3$ and $v_f = I_3(1 - 4|Q|\sin^2\theta_W)$. Equation (2.20) is a result of reparameterization from Equation (2.33) and Equation (2.34), described in Section 2.1.1.3. The interaction term contains the electromagnetic interaction with photons and fermions, neutral current interaction with Z bosons and fermions, and charged current interaction with W bosons and fermions. The kinematic term for the gauge field is introduced as,

$$\mathcal{L}_{gauge} = -\frac{1}{4}W^a_{\mu\nu}W^{a\,\mu\nu} - \frac{1}{4}B_{\mu\nu}B^{\,\mu\nu}, \tag{2.21}$$

where

$$W^a_{\mu\nu} = \partial_\mu W^a_\nu - \partial_\nu W^a_\mu - g_3\epsilon^{abc}W^b_\mu W^c_\nu, \tag{2.22}$$

$$B_{\mu\nu} = \partial_\mu B_\nu - \partial_\nu B_\mu, \tag{2.23}$$

are the field strength of $SU(2)_L$ and $U(1)_Y$.

In the EW theory, the mass term would connect the left-handed and right-handed fields. The introduction of the mass term would result in either fermion or gauge fields

breaking the local $SU(2)_L$ gauge invariance. The construction of the mass terms is later solved by the introduction of the Higgs mechanism.

2.1.1.3 The Higgs Mechanism

The Brout-Englert-Higgs mechanism [15–17], known as the Higgs mechanism, is introduced to include the mass terms of the fermions and gauge bosons in the SM Lagrangian. The Higgs field Φ is introduced as,

$$\Phi = \begin{pmatrix} \phi^+ \\ \phi^0 \end{pmatrix}, \tag{2.24}$$

where Φ is a $SU(2)_L$ doublet, and ϕ^+ and ϕ^0 are complex scalar fields carrying the electric charges of +1 and 0. The Higgs Lagrangian is defined as

$$\mathcal{L}_{\text{Higgs}} = (D_\mu \Phi)^\dagger (D^\mu \Phi) - V(\Phi^\dagger \Phi), \tag{2.25}$$

where D_μ is the covariant derivative in the EW theory shown in Equation (2.17). The Higgs potential $V(\Phi^\dagger \Phi)$ is described as

$$V(\Phi^\dagger \Phi) = \mu^2 \Phi^\dagger \Phi + \lambda (\Phi^\dagger \Phi)^2, \tag{2.26}$$

where μ^2 and λ are independent parameters, with requirement of $\lambda > 0$. If $\mu^2 > 0$, the potential would become stable equilibrium with a minimum at $\Phi = 0$, and the W and Z boson would remain massless. If $\mu^2 < 0$, the Higgs potential is no longer stable equilibrium at $\Phi = 0$. Instead, the minimum of the Higgs potential is located at

$$\Phi^\dagger \Phi = -\frac{\mu^2}{\lambda} \equiv v^2, \tag{2.27}$$

where v is the Vacuum Expectation Value (VEV). Therefore, the stable equilibrium point of the Higgs potential is at

$$\Phi = \frac{1}{\sqrt{2}} \begin{pmatrix} 0 \\ v \end{pmatrix}. \tag{2.28}$$

Figure 2.2 illustrates the Higgs potential in the case of $\mu^2 > 0$ and $\mu^2 < 0$. The Higgs field acquires the vacuum state and results in the electroweak symmetry breaking (EWSB).

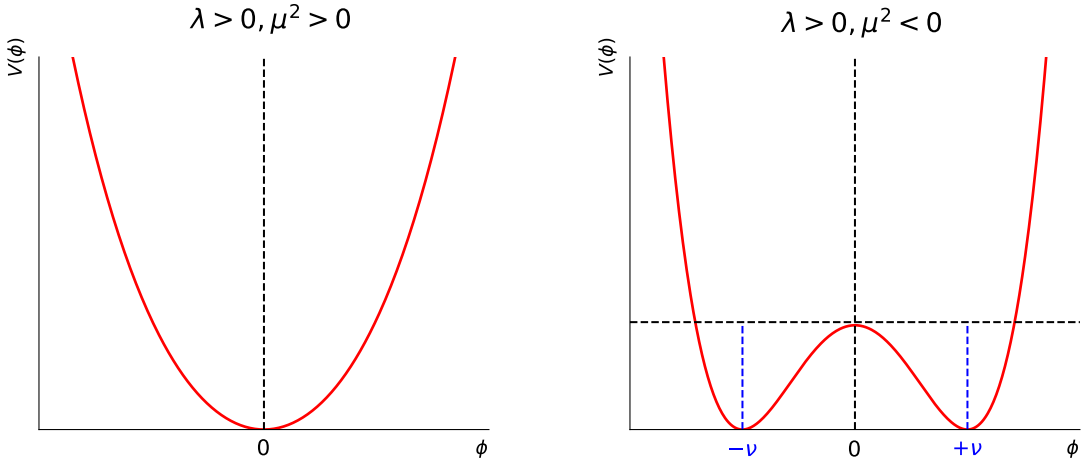

(a) (b)

Figure 2.2: The potential V of the scalar field ϕ in the case of $\mu^2 > 0$ (left) and $\mu^2 < 0$ (right).

The EWSB breaks the $SU(2)_L \times U(1)_Y$ symmetry into $U(1)_{EM}$ symmetry, which conserves the electric charge. Therefore, the component of Φ obtaining the VEV must be an electric charge of 0. The Higgs field with perturbations around the VEV, in the unitary gauge, can be written as

$$\Phi = \frac{1}{\sqrt{2}} \begin{pmatrix} 0 \\ v + h \end{pmatrix}, \tag{2.29}$$

where h represents the excitation of the Higgs field, which is the Higgs boson. The Higgs

potential around the vacuum state becomes

$$V(\Phi^\dagger\Phi) = \lambda v^2 h^2 + \lambda v h^3 + \frac{\lambda}{4}h^4 + \text{constant}, \tag{2.30}$$

where $\lambda v^2 h^2$ represents the mass term of the Higgs boson with $m_h = \sqrt{2\lambda v^2} = \sqrt{-2\mu^2}$. Moreover, the kinematic term of Higgs Lagrangian, shown in Equation (2.25), becomes

$$(D_\mu\Phi)^\dagger(D^\mu\Phi) = \frac{1}{2}(\partial_\mu h)^2 + \frac{g_3^2}{8}(W_\mu^1 + iW_\mu^2)(W^{1\mu} - iW^{2\mu})(v+h)^2 \tag{2.31}$$

$$+ \frac{1}{8}(g_3 W_\mu^3 - g_2 B_\mu)(g_3 W^{3\mu} - g_2 B^\mu)(v+h)^2, \tag{2.32}$$

where the gauge fields of B_μ and W_μ^a do not correspond to the physical $W^\pm$, Z and γ bosons. A reparameterization is performed to satisfy charge conservation and to convert them to mass eigenstates. Charged vector gauge bosons $W^\pm$ can be written as a linear combination of W_μ^1 and W_μ^2,

$$W_\mu^\pm = \frac{1}{\sqrt{2}}(W_\mu^1 \mp iW_\mu^2). \tag{2.33}$$

The gauge fields of B_μ and W_μ^3 are both electrically neutral and the mass eigenstates of the photon field A_μ and massive Z boson vector field Z_μ are mixed due to the spontaneous symmetry breaking,

$$A_\mu = \frac{1}{\sqrt{g_2^2 + g_3^2}}(g_2 W_\mu^3 + g_3 B_\mu), \tag{2.34}$$

$$Z_\mu = \frac{1}{\sqrt{g_2^2 + g_3^2}}(g_3 W_\mu^3 - g_2 B_\mu). \tag{2.35}$$

The couplings can be written as,

$$e = \frac{g_2 g_3}{\sqrt{g_2^2 + g_3^2}}, \quad \cos\theta_W = \frac{g_3}{\sqrt{g_2^2 + g_3^2}}, \quad \sin\theta_W = \frac{g_2}{\sqrt{g_2^2 + g_3^2}}, \tag{2.36}$$

where θ_W is the weak mixing angle, which is the relation between gauge and mass eigenstates. The Higgs Lagrangian can be written as

$$\begin{aligned}\mathcal{L}_{\text{Higgs}} = & \underbrace{\frac{1}{2}(\partial_\mu h)^2}_{\text{Kinematic term}} + \underbrace{0^2 A_\mu A^\mu}_{\text{Massless photon}} + \underbrace{\frac{g_3^2 v^2}{4} W_\mu^- W^{+\mu}}_{\text{Mass term of } W \text{ boson}} + \underbrace{\frac{(g_2^2+g_3^2)v^2}{8} Z_\mu Z^\mu}_{\text{Mass term of } Z \text{ boson}} \\ & + \underbrace{\frac{g_3^2 v}{2}(h W_\mu^- W^{+\mu})}_{hWW \text{ coupling}} + \underbrace{\frac{(g_2^2+g_3^2)v}{4}(h Z_\mu Z^\mu)}_{hZZ \text{ coupling}} \\ & + \underbrace{\frac{g_3^2}{4}(hh W_\mu^- W^{+\mu})}_{hhWW \text{ coupling}} + \underbrace{\frac{(g_2^2+g_3^2)}{8}(hh Z_\mu Z^\mu)}_{hhZZ \text{ coupling}} \\ & - \underbrace{\lambda v^2 h^2}_{\text{Mass term of Higgs boson}} - \underbrace{\lambda v h^3}_{\text{Trilinear Higgs self-coupling}} - \underbrace{\frac{\lambda}{4} h^4}_{\text{Quartic Higgs self-coupling}} ,\end{aligned} \tag{2.37}$$

where masses of W and Z bosons are defined as

$$m_W = \frac{g_3 v}{2}, \quad m_Z = \frac{\sqrt{g_2^2+g_3^2}\,v}{2}. \tag{2.38}$$

The fermions obtain mass through the interaction with the Higgs field. The Yukawa Lagrangian around the minimum is written as

$$\mathcal{L}_{\text{Yukawa}} = \sum_f \underbrace{\frac{y_f v}{\sqrt{2}} \bar{f} f}_{\text{Fermion mass}} + \underbrace{\frac{y_f}{\sqrt{2}} h \bar{f} f}_{\text{Higgs-Fermion interaction}} , \tag{2.39}$$

where y_f represents the Yukawa coupling of fermions. The fermion mass is defined as $m_f = \frac{y_f v}{\sqrt{2}}$, and the coupling between Higgs and fermions is proportional to the fermion mass.

2.1.2 Open Questions of the Standard Model

The SM has been a successful theory predicting numerous phenomena in particle physics. However, there are several problems that cannot be answered by the SM. A list

of open questions and limitations of SM related to studies included in this dissertation are outlined in the following.

2.1.2.1 Hierarchy problem

The hierarchy problem indicates the large discrepancy in the scales between the weak force and gravity. To be more specific, quantum corrections to the Higgs mass-squared parameter become quadratically divergent at the Planck scale in contradiction to the observed Higgs mass. A fine-tuning on the bare mass is required to make cancellations that result in the observed Higgs mass. Several BSM scenarios are proposed to resolve the hierarchy problem such as SUSY [35–40], extra dimensions [59; 60], Composite Higgs [42; 43] and Little Higgs [45; 61] models.

2.1.2.2 Dark Matter

Several astrophysical measurements supports the existence of DM including rotational speed of stars in galaxies [62–64], cosmic microwave background [65; 66], and gravitational lensing [67–69]. Nonetheless, the fundamental mechanism of the DM remains unknown. A few BSM scenarios are proposed to explain the DM, such as axions [70–74] or Weakly Interacting Massive Particles (WIMPs) [75]. In addition, a portal connecting the SM and DM sectors is needed to observe. This dissertation introduces a pseudo-scalar mediator to link these two sectors, detailed in Section 2.2.1.

2.1.2.3 Matter-antimatter asymmetry

Equal amounts of matter and antimatter are expected to be produced from the Big Bang, but an observable imbalance between matter and antimatter is found in our current universe. Andrei Sakharov proposed three necessary conditions for the matter and anti-matter asymmetry [76]. These include violations of baryon number conservation, charge symmetry, charge-parity (CP) symmetry, and deviations from thermal equilibrium.

2.2 Physics beyond the Standard Model

After discovering the Higgs boson, multiple studies have been conducted to explore the possibility of new physics. Exploration of new physics categorizes precise measurements with model-independent interpretation and model-dependent BSM searches. Measurements aim to examine the SM precisely to check if there is any deviation from the SM. The measured cross section can be interpreted with model-independent parameters to search for anomalies. This approach can potentially discover unexpected new physics, but it might lack the precision to detect subtle effects. Alternatively, the model-dependent BSM searches provide a clear theoretical hypothesis with analysis strategies that aim to extract the signal as best as possible. This approach is sensitive to the studied model but can be insensitive to other new physics. Therefore, both strategies are important to have complete pictures to explore new physics.

Several BSM models are proposed for the model-dependent approaches. The most famous one is SUSY, proposing a supersymmetric partner for each boson and fermion in the SM. This results in the cancellation of quadratically divergent terms and the preservation of the small Higgs mass in a natural way. A significant assumption of SUSY is the introduction of a new Higgs doublet. The presence of an extended Higgs sector provides a clear pathway to explore new physics before the SUSY itself. The 2HDM [77] provides a simple extension to include an additional Higgs doublet. An additional Higgs doublet is not just a solution for solving the hierarchy problem. It can also address the strong CP problem in Peccei–Quinn model [77; 78] and the matter-antimatter asymmetry [77; 79]. The theoretical framework will be discussed in Section 2.2.1.

For the model-independent approach, Effective Field Theory (EFT) can be used to establish model-independent constraints on BSM physics when the energy scale Λ characterizing new physics is larger than what LHC can directly probe. An overview of EFT is summarized in Section 2.2.2.

2.2.1 Two-Higgs-Doublet Model and its Extension

An additional Higgs doublet is introduced in the 2HDM, following Ref. [77]. This results in the scalar potential for two doublets Φ_1 and Φ_2 to be,

$$\begin{aligned} V = & m_{11}^2 \Phi_1^\dagger \Phi_1 + m_{22}^2 \Phi_2^\dagger \Phi_2 - m_{12}^2 (\Phi_1^\dagger \Phi_2 + \Phi_2^\dagger \Phi_1) + \frac{\lambda_1}{2} (\Phi_1^\dagger \Phi_1)^2 + \frac{\lambda_2}{2} (\Phi_2^\dagger \Phi_2)^2 \\ & + \lambda_3 \Phi_1^\dagger \Phi_1 \Phi_2^\dagger \Phi_2 + \lambda_4 \Phi_1^\dagger \Phi_2 \Phi_2^\dagger \Phi_1 + \frac{\lambda_5}{2} \left[(\Phi_1^\dagger \Phi_2)^2 + (\Phi_2^\dagger \Phi_1)^2 \right]. \end{aligned} \tag{2.40}$$

The minimization of this potential leads to the following VEV,

$$\langle \Phi_1 \rangle_0 = \frac{1}{\sqrt{2}} \begin{pmatrix} 0 \\ v_1 \end{pmatrix}, \langle \Phi_2 \rangle_0 = \frac{1}{\sqrt{2}} \begin{pmatrix} 0 \\ v_2 \end{pmatrix}, \tag{2.41}$$

where the combination of v_1 and v_2 gives the SM electroweak VEV as,

$$\frac{v}{\sqrt{2}} = \sqrt{(\frac{v_1}{\sqrt{2}})^2 + (\frac{v_2}{\sqrt{2}})^2}. \tag{2.42}$$

The two scalar $SU(2)$ doublets can be expanded around their VEVs in terms of eight real scalar fields:

$$\Phi_a = \begin{pmatrix} \phi_a^+ \\ (v_a + \rho_a + i\eta_a)/\sqrt{2} \end{pmatrix}, \quad a = 1, 2. \tag{2.43}$$

After EWSB, the eight real scalar fields mix into five physical scalar mass eigenstates and three Goldstone bosons. Three Goldstone bosons become the longitudinal components of the SM $W^\pm$ and Z bosons. The five physical Higgs bosons correspond to two CP-even (h, H) scalars, one CP-odd (A) scalar , and two charged ($H^\pm$) scalars. The 2HDM model has six free parameters: four Higgs masses (m_h, m_H, m_A and $m_{H^\pm}$), the ratio of two VEVs ($\tan\beta = v_2/v_1$), and the mixing angle (α) that diagonalizes the matrix of mass squares of the scalars.

A wide range of parameter spaces are available within the current experimental con-

straints. To be consistent with the SM theory, an additional constraint is required to avoid Flavor Changing Neutral Currents (FCNC) at the tree level. This results in four possible sets of Yuakwa couplings between the Higgs doublets and SM fermions, listed in Table 2.2. The type-II 2HDM is the most studied model, as the coupling of 2HDM contains the Minimal Supersymmetric Standard Model (MSSM) as a subset. In type-II 2HDM, Φ_1 couples to down-type fermions and Φ_2 couples only to up-type fermions. The Yukawa couplings depend on the α and β, outlined in Table 2.3.

The experimental results constrain 2HDM parameter space to lie in the alignment limit. Figure 2.3 presents the exclusion limit from the ATLAS experiment [80]. This indicates the alignment limit to be $\cos(\beta - \alpha) \to 0$, where the mass eigenbasis of the CP-even scalar sector of the 2HDM aligns with the SM gauge eigenbasis. Consequently, the lightest CP-even scalar behaves like the SM Higgs boson.

The type-II 2HDM is utilized in both BSM $t\bar{t}t\bar{t}$ and 2HDM+a combination analyses shown in Chapter VIII and Chapter IX. In addition, 2HDM+a combination analysis targets to include a portal to the DM χ [81]. An additional pseudo-scalar (CP-odd) mediator a is introduced with Yukawa-like couplings to both the SM fermions and the Dirac DM particles. This allows for interactions between SM and DM sectors. The interaction terms [81] are included as

$$V_P = \frac{1}{2}m_P^2 P^2 + P\left(ib_P H_1^\dagger H_2 + \text{h.c.}\right) + P^2\left(\lambda_{P1} H_1^\dagger H_1 + \lambda_{P2} H_2^\dagger H_2\right), \tag{2.44}$$

where m_P and b_P are parameters with dimensions of mass. This portal coupling b_P mixes the two neutral CP-odd weak eigenstates with a mixing angle θ. The charged mass eigenstates ($H^\pm$) are assumed to be equal mass and to be identical to the mass of CP-odd Higgs boson (A).

Model	u_R^i	d_R^i	e_R^i
Type I	Φ_2	Φ_2	Φ_2
Type II	Φ_2	Φ_1	Φ_1
Lepton-specific	Φ_2	Φ_2	Φ_1
Flipped	Φ_2	Φ_1	Φ_2

Table 2.2: Coupling relations between Higgs doublets and right-handed fermions in different types of 2HDM [77]. The coupling scheme with right-handed fermion is considered to suppress the FCNC at the tree level.

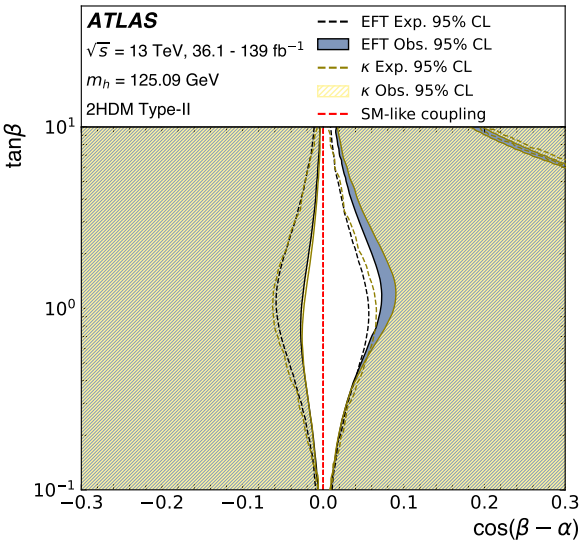

Figure 2.3: Exclusion contour in two-dimension of $\cos(\beta-\alpha)$ and $\tan\beta$ within the context of the type-II 2HDM parameter space [80]. The SM Higgs measurements are interpreted with κ- and EFT-frameworks, with coupling modifiers shown in Table 2.2 and Wilson coefficients on the dimensional-6 operators in the SMEFT Lagrangian [82], respectively. A small allowed region for large $\tan\beta$ and $\cos(\beta-\alpha) \approx 0.2$ is presented due to the opposite sign of fermion couplings in the same magnitude, which is not sufficiently well constrained by current experimental measurements. Details can be found in Ref. [80].

Model	Type II
ξ_h^u	$\cos\alpha/\sin\beta$
ξ_h^d	$-\sin\alpha/\cos\beta$
ξ_h^ℓ	$-\sin\alpha/\cos\beta$
ξ_H^u	$\sin\alpha/\sin\beta$
ξ_H^d	$\cos\alpha/\cos\beta$
ξ_H^ℓ	$\cos\alpha/\cos\beta$
ξ_A^u	$\cot\beta$
ξ_A^d	$\tan\beta$
ξ_A^ℓ	$\tan\beta$

Table 2.3: Coupling modifiers of fermions (u, d, ℓ) to the neutral Higgs bosons (h, H, A) in the type-II 2HDM model [77]. These modifiers alter coupling strengths relative to that in the SM.

2.2.2 Effective Field Theory

The SMEFT [83] expands the SM Lagrangian with higher-order operators, including composite operators of SM fields. The EFT Lagrangian can be written as

$$\mathcal{L}_{EFT} = \mathcal{L}_{SM}^{(4)} + \frac{1}{\Lambda}\sum_k C_k^{(5)} Q_k^{(5)} + \frac{1}{\Lambda^2}\sum_k C_k^{(6)} Q_k^{(6)} + ..., \tag{2.45}$$

where $\mathcal{L}_{SM}^{(4)}$ is the SM Lagrangian which consists of dimension-2 and dimension-4 operators. The Λ represents the scale of new physics, with each term suppressed by Λ with order $n-4$. The $Q_k^{(n)}$ represents dimension-n operators, and $C_k^{(n)}$ the dimensionless coupling parameters, known as Wilson coefficients, associated with each $Q_k^{(n)}$. The operators with odd dimensions violate baryon and lepton number conservation [84], resulting in the leading baryon and lepton number conserving term being the dimension-6 operator. This dissertation focuses on the interpretation with dimension-6 operators. In addition, the dimension-6 operator can be expressed in terms of different bases, such as Warsaw basis [85], HISZ basis [86], and SILH basis [87]. In this dissertation, the Warsaw basis is used for EFT interpretation and can provide a complete set of dimension-6 operators allowed by SM gauge symmetries [85]. The SM $t\bar{t}t\bar{t}$ cross section is interpreted with SMEFT

dimension-6 four-fermion operators [88–91] and Higgs oblique parameter [92], discussed in Section 3.2.2.1 and Section 7.6.

CHAPTER III

Phenomenology of LHC Physics

3.1 Large Hadron Collider

The LHC [93] is the world's largest particle collider built by CERN. It is located underground on the border between France and Switzerland, with a circumference of 27 kilometers. The LHC collides proton-proton (pp), proton-lead (pPb), and lead-lead ($PbPb$) beams at the TeV scale, with collisions happening at the center of four major experiments. The ATLAS [94] and CMS [95] detectors are general-purpose detectors built to explore SM, BSM and heavy-ion physics. A Large Ion Collider Experiment (ALICE) [96] focuses on dedicated heavy-ion physics. Large Hadron Collider beauty (LHCb) [97] experiment measures the properties of b-hadrons such as the CP violation to understand the matter-antimatter asymmetry.

The LHC has been collecting pp and heavy-ion collision data since 2010. The LHC's schedule is divided into data-taking periods, referred to as 'Runs', and shutdown periods, known as 'Long Shutdowns' (LS). The first two data-taking periods, Run 1 and Run 2, have finished. Run 1 operation started from 2010 to 2012 with center-of-mass energies ($\sqrt{s}$) of 7 TeV and 8 TeV. Run 2 operated from 2015 to 2018 with $\sqrt{s} = 13$ TeV, followed by LS2 to upgrade the detectors for increased luminosity. Run 3 operation started in 2022 and will continue through 2025 at $\sqrt{s} = 13.6$ TeV. The High-Luminosity (HL) LHC will

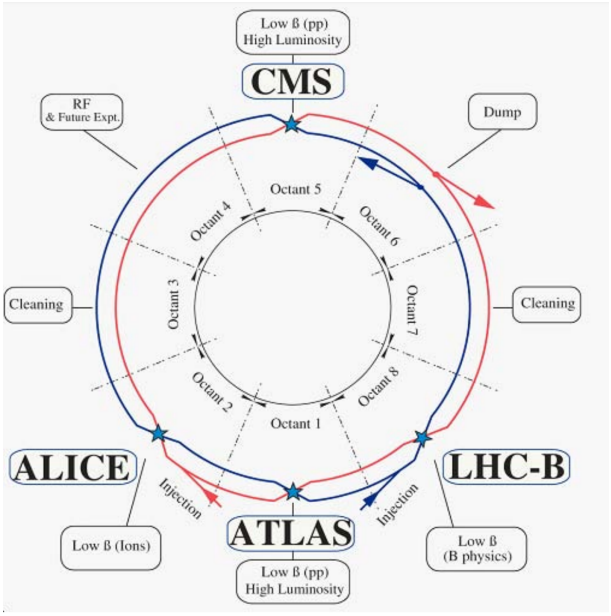

Figure 3.1: Layout of LHC and four major experiments [93].

begin an approximated 10-year data-taking period in 2029 onwards with $\sqrt{s} = 13.6 - 14$ TeV, after the detector upgrades in LS3.

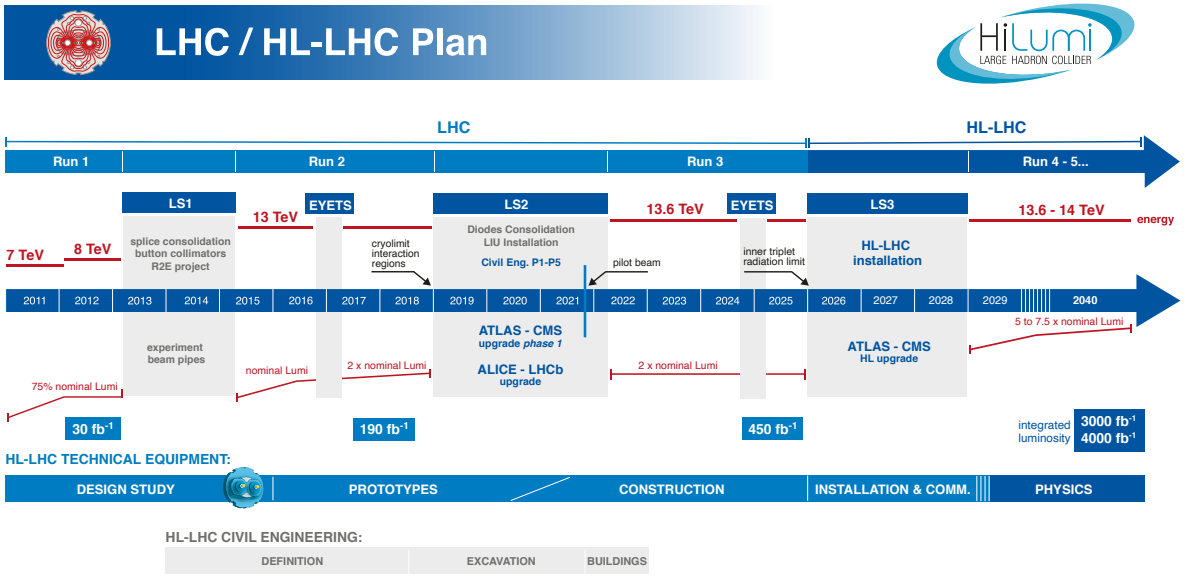

Figure 3.2: The schedule of LHC and HL LHC with the expected beam energy of pp collisions and proposed luminosity [98].

For the LHC to reach the collision energy, sections of accelerators sequentially increase proton beam energy, as shown in Figure 3.3. The injection complex is changed after 2020 (the latter is shown in parentheses). The proton beam sources start from Linac 2 (Linac 4), accelerating hydrogen ions up to 50 MeV (160 MeV). The ions are stripped of their electrons to leave only protons, which are injected into the Proton Synchrotron Booster. After injection, the proton beams are accelerated up to 1.6 (2) GeV for another injection into the Proton Synchrotron. The beam energy is further increased to 25 (26) GeV and injected into the Super Proton Synchrotron, increasing the energy to 450 GeV. Finally, the proton beams are injected into the LHC beam pipes in opposite directions. The beams are further ramped up to 6.5 TeV per beam to achieve a center-of-mass energy of 13 TeV for the collisions in Run 2.

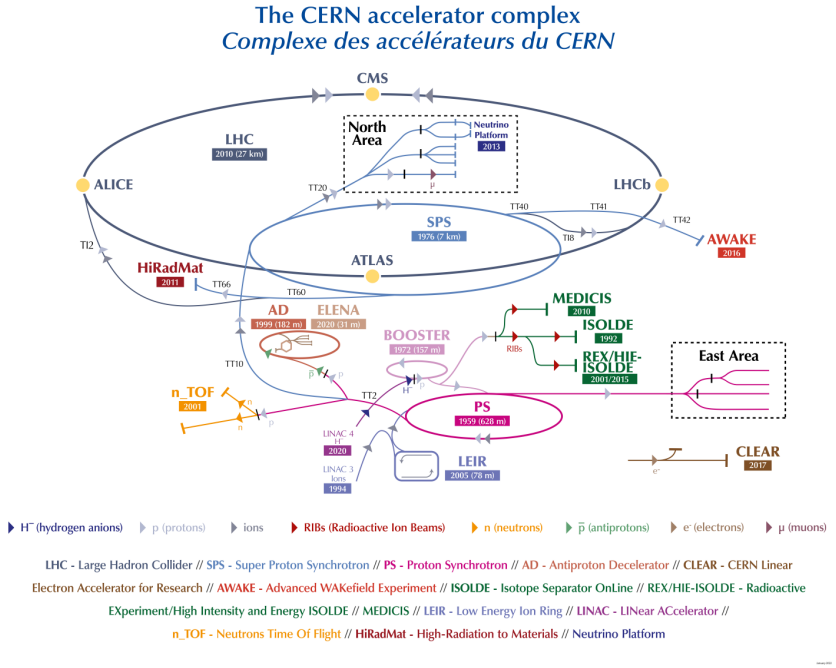

Figure 3.3: The layout of accelerator complex of LHC in 2022 following Ref. [99]. The layout in 2016 can be found in Ref. [100].

3.1.1 Luminosity

The instantaneous luminosity (L) is an important indicator of the LHC performance [101]. It is defined through

$$\frac{dR}{dt} = L \cdot \sigma_p, \tag{3.1}$$

where $\frac{dR}{dt}$ represents the number of events per unit time, and σ_p is the cross section of a particular process. Following Ref. [102], the luminosity of the collisions of proton beams, assuming a Gaussian beam profile, can be written as

$$L = \frac{N_b^2 n f_r \gamma}{4\pi\epsilon_n \beta^*} F, \tag{3.2}$$

where N_b is the number of protons per bunch, n is the number of bunches per beam, f_r is the revolution frequency, γ is the relativistic factor, ϵ_n is the normalized transverse emittance, β^* is the beta function at the collision point, and F is the geometry luminosity reduction factor accounting for the crossing angle at the interaction point (IP). The F is defined as

$$F = \frac{1}{\sqrt{1 + \left(\frac{\theta_c \sigma_z}{2\sigma^*}\right)}}, \tag{3.3}$$

where θ_c is the full crossing angle at the IP, θ_z is the Root Mean Square (RMS) bunch length, and σ^* is the transverse RMS beam size at the crossing point. The conditions for pp collisions in the LHC Run 2 operation [103] are shown in Table 3.1.

The integrated luminosity is taken by integrating the instantaneous luminosity over time to represent the accumulated data size from the data-taking periods. The integrated luminosity is written as

$$L_{int} = \int L dt, \tag{3.4}$$

where the unit is proportional to the inverse of the cross section. The typical unit of integrated luminosity is the inverse femtobarn (fb^{-1}). The total integrated luminosity

Parameter	2015	2016	2017	2018
Maximum number of colliding bunch pairs (n_b)	2232	2208	2544/1909	2544
Bunch spacing [ns]	25	25	25/8b4e	25
Typical bunch population [10^{11} protons]	1.1	1.1	1.1/1.2	1.1
β^* [m]	0.8	0.4	0.3	0.3–0.25
Peak luminosity L_{peak} [10^{33} cm^{-2}s^{-1}]	5	13	16	19
Peak number of inelastic interactions/crossing ($\langle\mu\rangle$)	~ 16	~ 41	$\sim 45/60$	~ 55
Luminosity-weighted mean inelastic interactions/crossing	13	25	38	36
Total delivered integrated luminosity [fb^{-1}]	4.0	39.0	50.6	63.8

Table 3.1: Beam conditions for pp collisions in the Run 2 LHC operation [103]. The '8b4e' presents a pattern of eight bunches separated by 25 ns followed by a four bunch-slot gap.

delivered by LHC and recorded by the ATLAS detector in Run 2 is summarized in Figure 3.4. An integrated luminosity of $139 \pm 1.7\%$ fb^{-1} in pp collisions at $\sqrt{s} = 13$ TeV in Run 2 had been measured with good data quality, reported in Ref. [104]. A dedicated legacy measurement [103] of the integrated luminosity of Run 2 has been updated to be $140 \pm 0.83\%$ fb^{-1}, superseding Ref. [104].

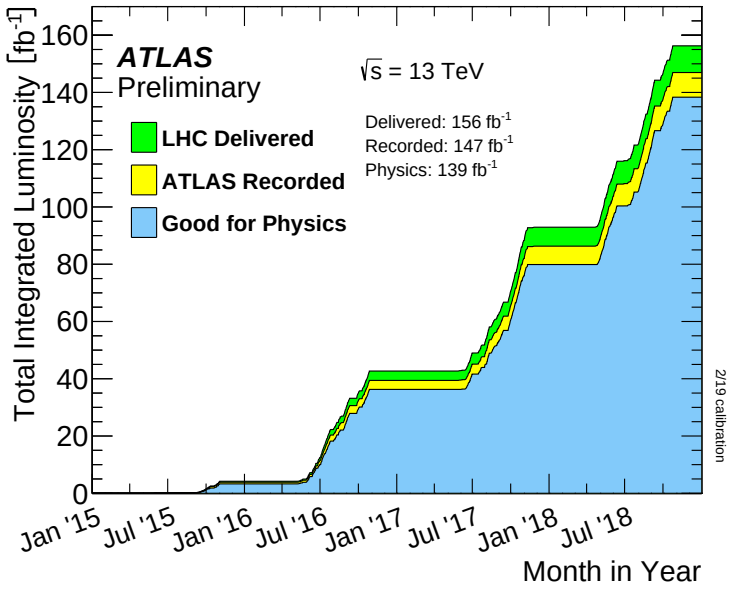

Figure 3.4: The integrated luminosity delivered by LHC (green), recorded by ATLAS (yellow), and certificated with good data quality (blue) during the stable beam of pp collisions at $\sqrt{s} = 13$ TeV from 2015 to 2018 [104].

3.1.2 Proton-Proton Collisions

The *pp* collisions at the LHC can be described by the physics of scattering of quarks and gluons [105], which are collectively named partons. Scattering of partons can be categorized as hard or soft. Hard scattering involves a large momentum exchange between two partons, which can be predicted using perturbation theory. Soft scattering is a low energy exchange between two partons in the non-perturbative QCD regime.

As illustrated in Figure 3.5, when two protons collide, protons emit partons to exchange momentum, which is described by the parton distribution function (PDF) shown in Section 3.1.2.1. The emitted partons are highly accelerated, and radiation can be emitted before or after hard scattering, known as initial-state radiation (ISR) and final-state radiation (FSR), described in Section 3.1.2.2. The remaining partons in the proton, which do not participate in the primary collision, can also interact. These interactions are named underlying events (UE). Finally, the probability of producing a physics process from the hard scattering is quantified by a cross section, discussed in Section 3.1.2.3.

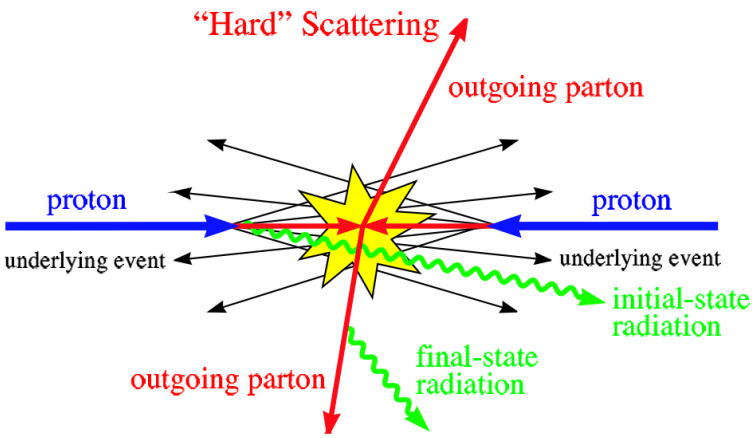

Figure 3.5: The schematic diagram of the *pp* collision [105; 106].

3.1.2.1 Parton Distribution Function

The PDF, $f_i(x, Q^2)$, describes the probability function to interact with a particular parton (labeled i) carrying a momentum fraction x of the proton, with a momentum exchange Q^2. The PDF is extracted from global fits to data from scattering and collider experiments since it is not calculable in non-perturbative QCD [107]. Various PDF sets are available from different collaborations such as CTEQ [108], MSTW2008 [109], and NNPDF [110]. A PDF uncertainty is commonly assigned to account for the difference between the PDF sets. Figure 3.6 illustrates the PDF of the gluon and quarks in NNPDF3.0 at next-to-next-to-leading order (NNLO) QCD.

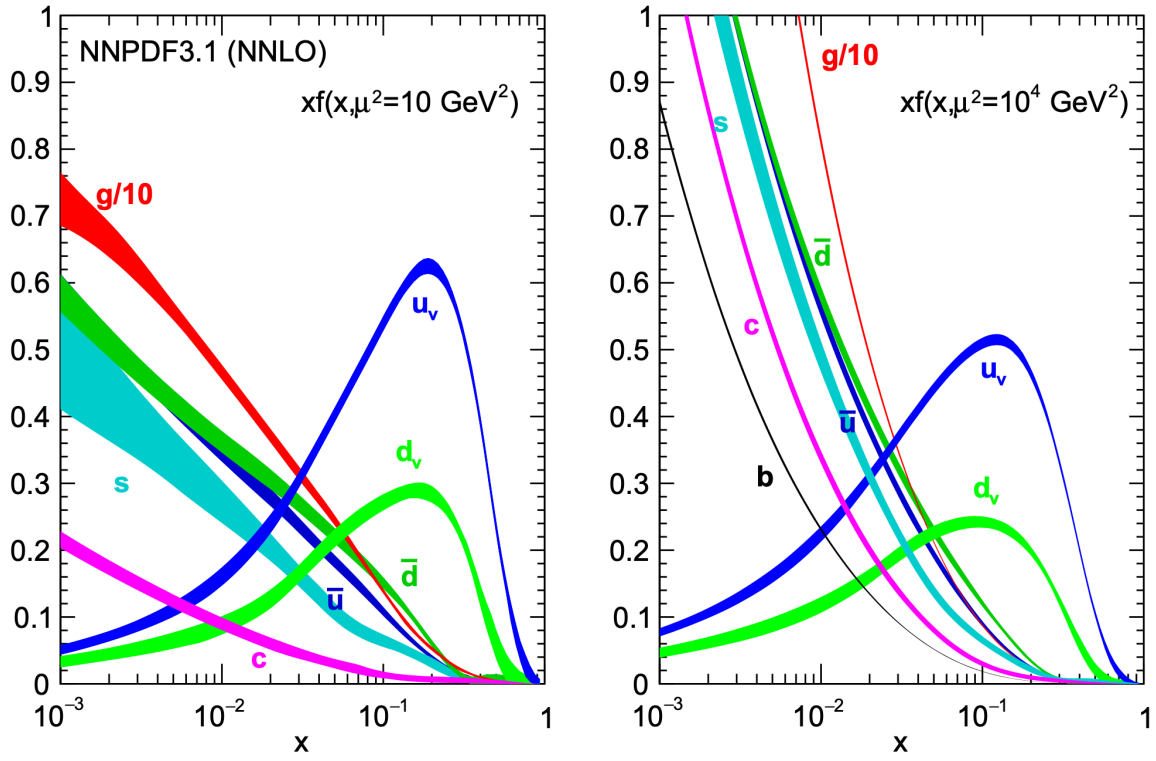

Figure 3.6: PDF of gluon and quarks, $xf(x, Q^2)$, in NNPDF3.0 at NNLO QCD accuracy with energy scale $Q^2 = 10$ GeV^2 and $Q^2 = 10^4$ GeV^2 [107].

3.1.2.2 Parton Shower and Hadronization

Hard scattering provides highly accelerated and unstable particles that result in additional radiation in the initial or final states, known as ISR and FSR, respectively. These radiated particles can undergo further QCD and QED radiations, leading to a cascade known as a parton shower (PS). QCD showers further combine into colorless hadrons, a process known as fragmentation and hadronization.

3.1.2.3 Cross section

At the LHC, the most common physical observable is the cross section, which is typically measured and used to compare with the theoretical prediction. The cross section of the particular physics process in hard scattering can be described by QCD factorization theorem [106] with leading logarithm corrections. The cross section of pp collision [105] can be written as

$$\sigma_{p_A p_B \to X} = \int dx_a dx_b f_{a/A}(x_a, \mu_F^2) f_{b/B}(x_b, \mu_F^2) \times \left[\hat{\sigma}_0 + \alpha_s(\mu_R^2)\hat{\sigma}_1 + \ldots\right]_{p_A p_B \to X}, \quad (3.5)$$

where $f_{a/A}(x_a, \mu_F^2)$ and $f_{b/B}(x_b, \mu_F^2)$ represent the PDF in terms of the fraction of momentum in the hadron (x_a and x_b) and the factorization scale (μ_F), which separates the long- and short-distance physics and is used to minimize the logarithms in perturbative calculations. The last term represents the parton-level cross section calculated in the perturbation theory, with the dependency on the QCD running coupling α_s in a function of renormalization scale (μ_R). In the absence of the complete set of corrections, the choices of the μ_R and μ_F become important to calculate predictions. Typically, the μ_R and μ_F are set to be equal at the order of hard scattering scales. In addition, the different choices of μ_R and μ_F are commonly used as uncertainties to account for missing higher-order corrections.

3.2 Physics at the LHC

The cross sections of the SM processes in pp collisions measured by ATLAS at the LHC are summarized in Figure 3.7. Overall, good agreement has been found between measurements and SM predictions. However, several measurements exhibit mild deviations from the SM and warrant further investigation.

This dissertation focuses on the $t\bar{t}t\bar{t}$ production with its decay to the SSML final states with multiple b-jets. The other important SM processes are $t\bar{t}X$, where X can be a top quark or a $H/W/Z$ boson. These SM processes produce the SSML final states with multiple b-jets and have relatively small cross sections at the LHC. The phenomenology of these processes is discussed in the following sections.

3.2.1 Higgs Boson Phenomenology at the LHC

The Higgs boson was discovered by the ATLAS and CMS collaborations at the LHC in 2012 [23; 24]. The Higgs boson is predicted to be a scalar particle characterized by its CP-even property ($J^{CP} = 0^{++}$) and has a predicted total width of 4.1 MeV. Within the SM, the Higgs mass is a free parameter that must be measured. Recent measurements showed the Higgs mass to be 125.11 ± 0.11 GeV [112]. In addition, the total width of the Higgs boson was measured to be $4.5^{+3.3}_{-2.5}$ MeV [113], agreeing with the prediction. The spin of the Higgs boson has been determined to be 0, consistent with SM expectations [114; 115]. Moreover, the Higgs boson is measured to be a CP-even quantum state, but the admixtures of CP-even and CP-odd states are not completely excluded [114; 115].

The Higgs boson can be produced in pp collisions at the LHC with four leading production processes: gluon fusion (ggF), vector boson fusion (VBF), associated production with a vector boson (VH), associated production with a pair of top quarks ($t\bar{t}H$). The associated production with a pair of bottom quarks ($b\bar{b}H$) is experimentally indistinguishable from the ggF production due to the low identification efficiency of b-jets. The

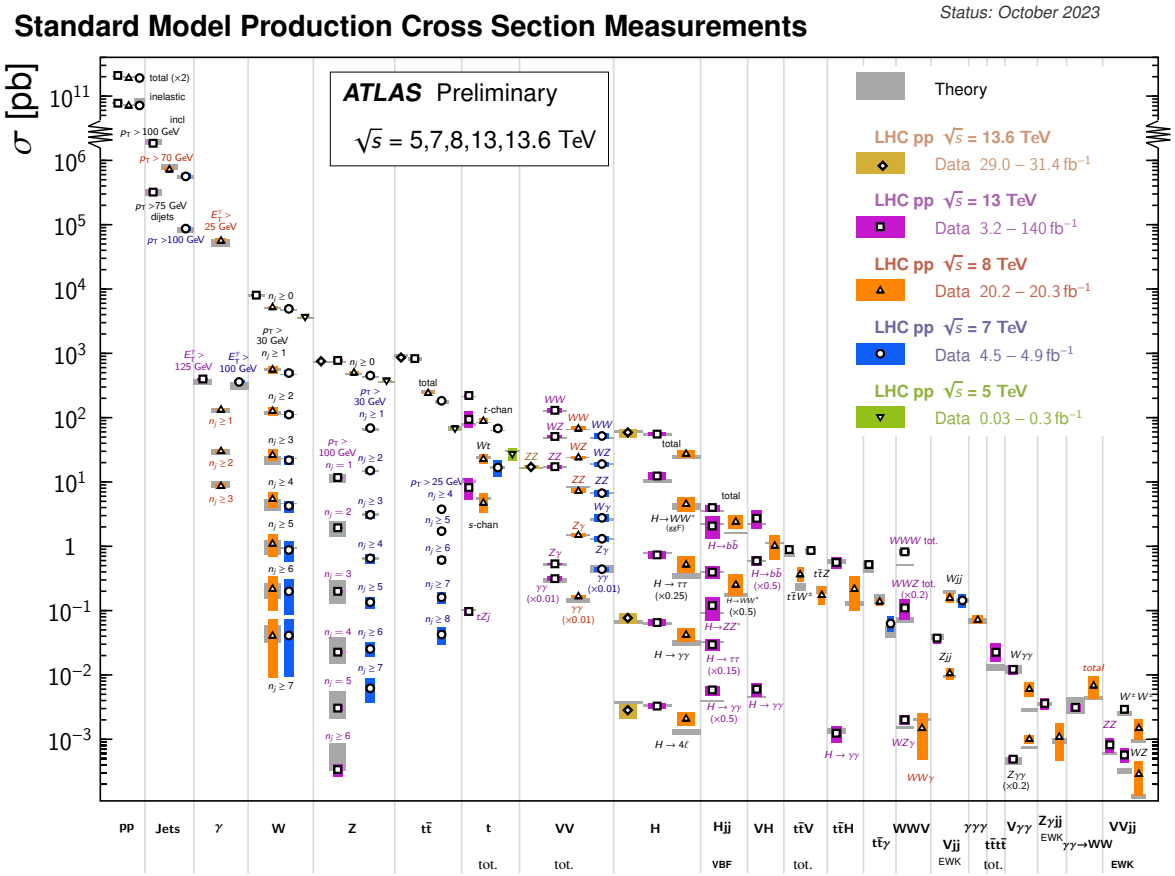

Figure 3.7: Summary of the cross sections of the SM processes from inclusive and fiducial measurements in different center-of-mass energies [111].

associated production with a single top quark (tH) production can also produce the Higgs boson but has a smaller cross section than the leading processes. Examples of Feynman diagrams for Higgs production and decay mode are shown in Figure 3.8.

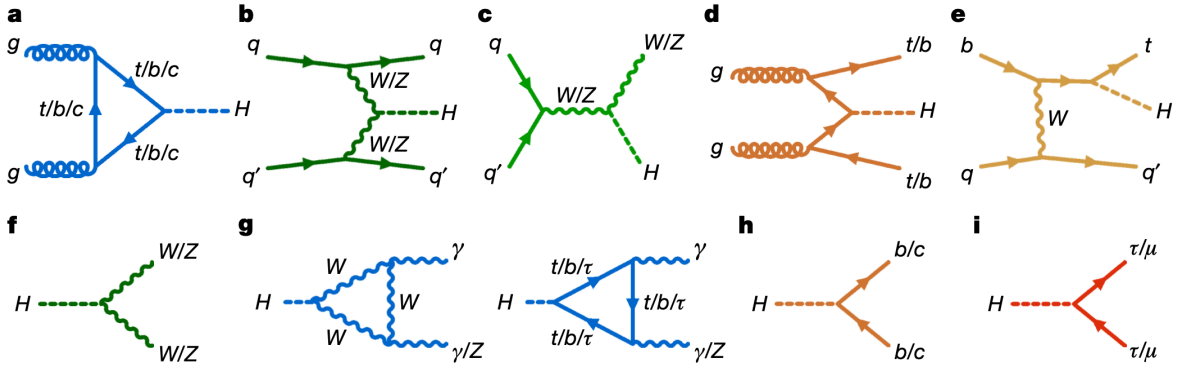

Figure 3.8: Examples of Feynman diagrams for Higgs production and decay mode [116].

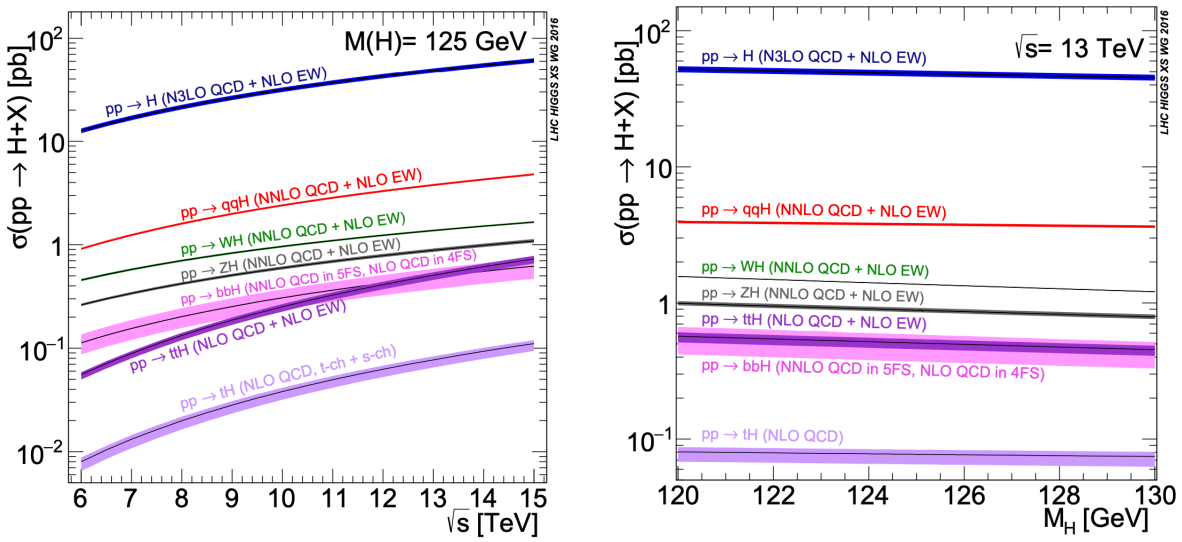

(a) (b)

Figure 3.9: The predicted Higgs boson production cross sections in term of (a) $\sqrt{s}$ with $m_H = 125$ GeV and (b) m_H at $\sqrt{s} = 13$ TeV [117].

ggF production is a dominant process at the LHC with 90% of the total production cross section of the Higgs boson. Since the Higgs boson does not directly couple to the gluon, a fermion loop is required in this process. The fermion loop is dominated by the

top quark, given its largest coupling with the Higgs boson. Therefore, ggF production is sensitive to the Higgs-top Yukawa coupling. VBF production has the second largest cross section, with the Higgs boson, produced from the fusion of W/Z bosons. VBF production is characterized by two forward jets. The VH process is produced with a W/Z radiating the Higgs boson. $t\bar{t}H$ production has a smaller cross section due to the large energy required to produce a $t\bar{t}$ pair and a Higgs boson. This mechanism is sensitive to Higgs-top Yukawa coupling due to the direct couplings between the Higgs boson and the top quark. The tH process is associated with a single top quark and a light quark or a W boson (tHq or tHW), respectively. It provides a cross section smaller than $t\bar{t}H$ due to electroweak coupling instead of QCD couplings in $t\bar{t}H$ production.

Couplings with Higgs bosons are proportional to the mass of the particles. Therefore, the Higgs bosons predominately decay to heavier particles kinematically allowed. The Higgs decay modes are summarized in Figure 3.10. The $H \to b\bar{b}$ decay provides the largest branching ratio. However, identifying a b-jet is relatively difficult compared to the leptons. This results in difficulty measuring the Higgs boson with $b\bar{b}$ final states. The $H \to WW^*$ has the second largest branching fraction. The leptonic decay of the W boson ($W \to \ell\nu$) provides cleaner final states to explore the coupling between Higgs and W bosons. However, the leptonic decay of the W boson also produces neutrinos, which cannot be detected. This results in a limitation of the sensitivity. The $H \to \gamma\gamma$ and $H \to ZZ^* \to 4\ell$ provide clear signatures with good mass resolution and high signal-to-background ratios despite the low branching ratios of these decays.

For the SSML and multiple b-jets final states, the $t\bar{t}H$ production is the most important background compared to other Higgs production. The $H \to WW^*$ decay is the dominant decay for the $t\bar{t}H$ production to produce the SSML final state. The $t\bar{t}H$ production in SSML final states is discussed in the following.

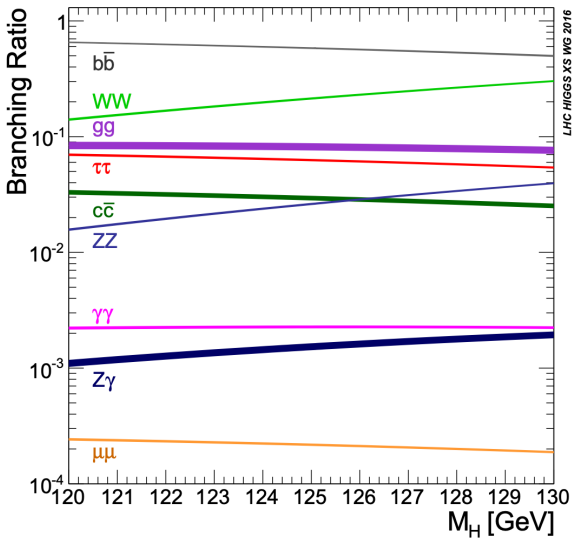

Figure 3.10: Branching ratios of Higgs boson decays and their uncertainties [117].

3.2.1.1 $t\bar{t}H$ Production

The most accurate theoretical $t\bar{t}H$ cross section is computed at NNLO QCD and next-to-leading order (NLO) EW [118] providing

$$\sigma_{t\bar{t}H} = 507\,^{+5}_{-15}\ \text{fb}. \tag{3.6}$$

A significant reduction in the scale uncertainties is achieved with the NNLO QCD calculation compared to the prediction at NLO [117]. Dedicated measurements on $t\bar{t}H$ in SSML final states by the ATLAS [51] and CMS [119] collaborations show consistent results between theoretical and measured $t\bar{t}H$ cross section, as reported in Figure 3.11. The combined signal strength (μ), defined as the ratio of the measured cross section to the theoretical prediction, of $t\bar{t}H$ in the SSML is consistent with the SM prediction and within the uncertainties. However, the central value of the ATLAS measurement deviates slightly from the SM prediction due to the large correlation between $t\bar{t}H$ and $t\bar{t}W$ production.

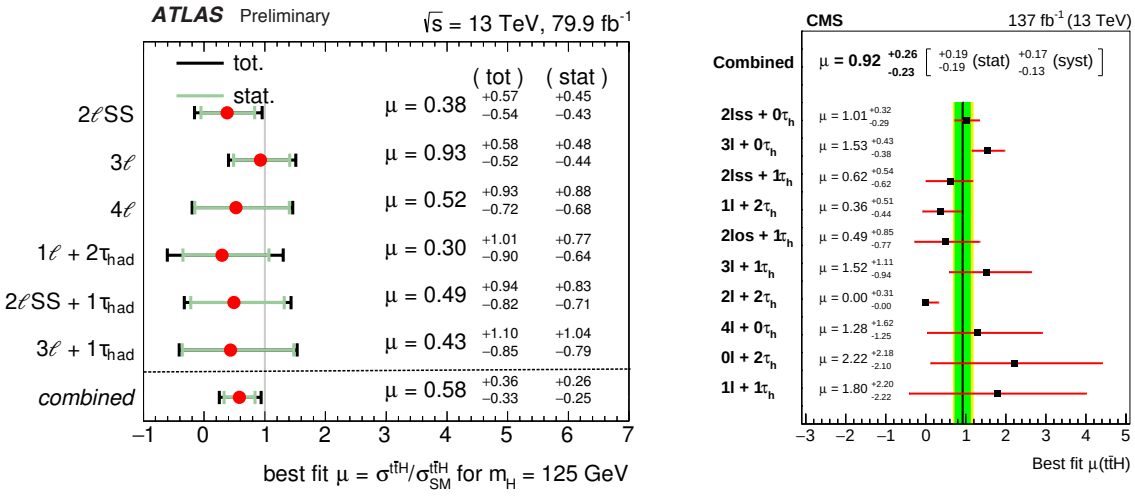

(a) ATLAS (b) CMS

Figure 3.11: Comparisons between signal strengths μ of $t\bar{t}H$ production in different final states by the ATLAS [51] and CMS [119] collaborations. The μ is defined as the ratio of the measured cross section to the theoretical prediction.

3.2.2 Top Quark Phenomenology at the LHC

The top quark was discovered by the CDF and D∅ experiments at Tevatron $p\bar{p}$ collider at Fermilab in 1995 [21; 22]. Since then, a variety of its properties have been measured. They include mass, couplings to vector bosons and the Higgs boson, spin correlation and entanglement in $t\bar{t}$ production, and the top-related production and decays. With its large mass, the top quark has the largest coupling to the Higgs boson. This is the reason that the leading Higgs production at LHC comes from the gluon fusion via a top-quark loop and $t\bar{t}H$ production. In addition, the top-quark mass and Higgs-top Yukawa coupling play an important role in the stability of the universe. A small variation can lead to a new minimum of the effective potential at large values of the Higgs field, which would lead to our vacuum being metastable [120]. Figure 3.12 presents the SM phase diagram in terms of the Higgs boson and the top quark mass [121].

The following sub-sections introduce the important processes associated with top quarks: $t\bar{t}t\bar{t}$, $t\bar{t}t$, $t\bar{t}W$, and $t\bar{t}Z$ production processes. The processes are important to be

precisely measured since BSM physics can introduce a modification of the top-quark couplings, resulting in deviations from the SM. In the SSML and multiple b-jets final states, $t\bar{t}W$ and $t\bar{t}Z$ are dominant background sources, similar to $t\bar{t}H$ production described in Section 3.2.1.1. The latest experimental results of these production processes are summarized in Figure 3.13.

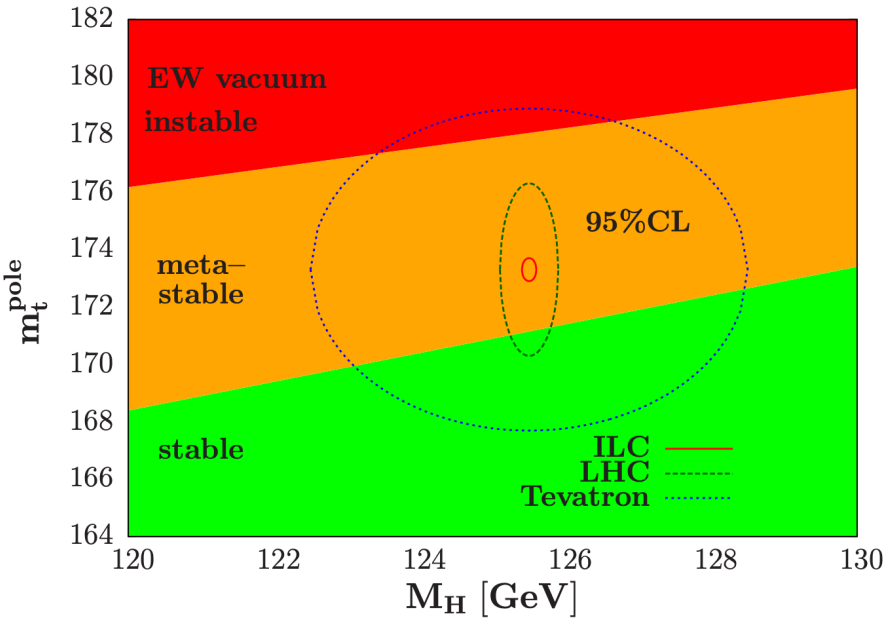

Figure 3.12: The 2σ contour of m_H and m_t^{pole} with experimental results from Tevatron and LHC with areas showing the SM vacuum to be absolutely stable, metastable and unstable up to the Planck scale. A projection is also performed for the potential new collider, the International Linear Collider (ILC). Figure comes from Ref. [120].

3.2.2.1 Four-top-quark production

Four-top-quark production is a rare process in the SM with a predicted cross section of $\sigma_{t\bar{t}t\bar{t}} = 12 \pm 2.4$ fb at NLO including EW corrections [123]. By including threshold resummation at NLO, logarithmic accuracy increases the total production cross section by approximately 12% and significantly reduces the scale uncertainty, leading to $\sigma_{t\bar{t}t\bar{t}} = 13.4^{+1.0}_{-1.8}$ fb [124]. Examples of Feynman diagrams are shown in Figure 3.14. The $t\bar{t}t\bar{t}$ decays into four W bosons and four b quarks, as the top quark decays into a W boson

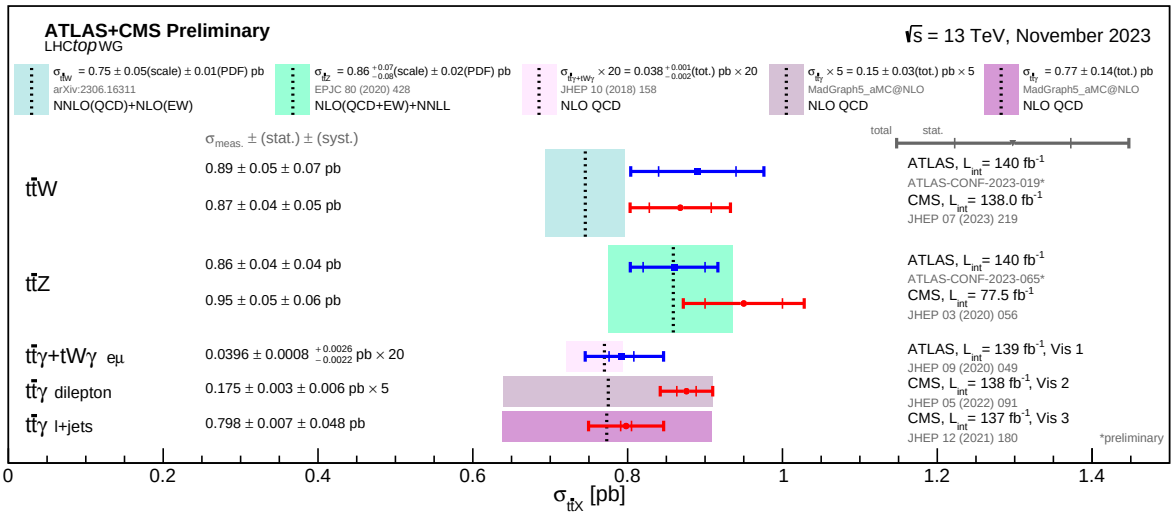

Figure 3.13: Comparison between observed and expected cross sections of $t\bar{t}X$ production, where $X = W$, Z or γ [122].

and a b quark with almost a 100% branching fraction. The final states depend on whether the W boson decays leptonically or hadronically, with the branching fraction for four W boson decays illustrated in Figure 3.15. These final states include all hadronic decays, one lepton or two leptons with opposite electric charge (1LOS) and SSML. While all hadronic and 1LOS final states have a high branching fraction, they suffer from significant background contamination from $t\bar{t}$. In contrast, despite its smaller branching fraction, the SSML channel has the advantage of lower background levels, offering better sensitivity compared to other channels due to reduced background contamination.

Both ATLAS and CMS experiments have reported evidence for $t\bar{t}t\bar{t}$ production in $\sqrt{s} =$ 13 TeV pp collisions at the LHC. The ATLAS result combined 1LOS and SSML channels using an integrated luminosity of 139 fb^{-1} at $\sqrt{s}$ =13 TeV. This combination results in a measured cross section of 24^{+7}_{-6} fb, corresponding to an observed (expected) significance of 4.7 (2.6) standard deviations over the background-only hypothesis. The CMS result also combined several measurements using an integrated luminosity of 138 fb^{-1} at $\sqrt{s}$ =13 TeV, in channels with all hadronic decays, 1LOS and SSML. The $t\bar{t}t\bar{t}$ cross section measured by the CMS collaboration is 17 ± 5 fb, yielding an observed (expected) significance of 4.0

(3.2) standard deviations. In 2023, the first observation of $t\bar{t}t\bar{t}$ production was achieved in the SSML channel by the ATLAS experiment using an integrated luminosity of 140 fb^{-1} [125]. This analysis will be presented in Chapter VII.

$t\bar{t}t\bar{t}$ production is also an excellent candidate to examine the properties of SM and is sensitive to potential BSM physics. First, the $t\bar{t}t\bar{t}$ can be produced via off-shell Higgs boson decaying to $t\bar{t}$, as illustrated in Fig. 3.14b. Therefore, the $t\bar{t}t\bar{t}$ cross section is sensitive to the Higgs-top Yukawa coupling and the Higgs CP properties [126; 127]. $t\bar{t}t\bar{t}$ can also be influenced by various four-fermion interactions [88–91] and the Higgs oblique parameter [92] within an EFT framework. Numerous BSM scenarios predict an increased $t\bar{t}t\bar{t}$ cross section. These include SUSY particle productions such as gluino pair production [128; 129] or scalar gluon pair production [130; 131]. Moreover, the associated production of BSM particles with $t\bar{t}$ can also contribute to $t\bar{t}t\bar{t}$ events. Examples of such contributions come from a heavy pseudoscalar (A) or scalar boson (H) from type-II 2HDM [77], or a top-philic vector resonance (Z') in the composite Higgs scenarios [43; 132–134]. The associated BSM particles will further decay into $t\bar{t}$ to produce $t\bar{t}t\bar{t}$ events.

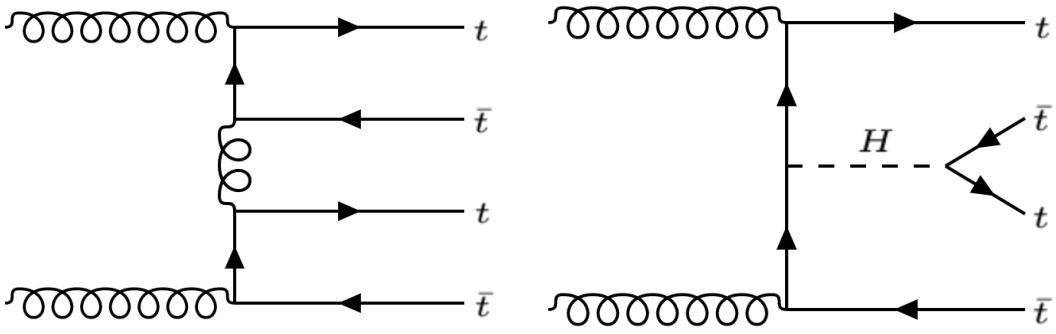

(a) QCD diagrams (b) EW diagrams

Figure 3.14: Examples of Feynman diagrams of the SM $t\bar{t}t\bar{t}$ production. The mediator connecting two top quarks can be a gluon, γ, Z, or a Higgs boson.

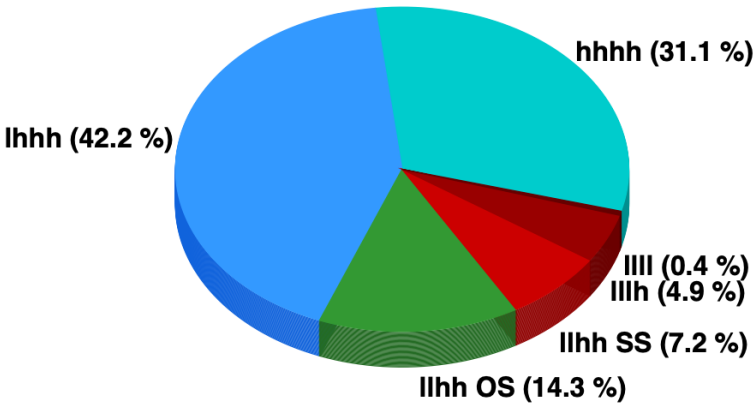

Figure 3.15: The branching fractions of the decays of four W bosons. The 'l' denotes the leptons, including an electron or a muon. The 'h' stands for the hadronic product from the decay. The 'OS' represents a dilepton event with opposite-sign electric charges, and 'SS' stands for a dilepton event with same-sign electric charges.

3.2.2.1.1 Higgs-Top Yukawa coupling and Higgs CP

The Lagrangian of the Higgs-top Yuakwa coupling of $t\bar{t}t\bar{t}$ takes the form,

$$\mathcal{L} = -\frac{m_t}{v}[\bar{\psi}_t \kappa_t \left(\cos\alpha + i \sin\alpha \gamma_5\right) \psi_t] H, \tag{3.7}$$

where m_t is the top quark mass, v is the Higgs VEV, κ_t is the Higgs-top Yukawa coupling strength modifier, and α is the mixing angle between the CP-even and CP-odd Higgs-top couplings. The SM corresponds to the CP-even coupling with $\kappa_t = 1$ and $\alpha = 0°$, while the non-SM pure CP-odd coupling has $\kappa_t = 1$ and $\alpha = 90°$. The dependence of the $t\bar{t}t\bar{t}$ cross section on the Yukawa coupling has been studied at leading order (LO) [127]:

$$\sigma_{t\bar{t}t\bar{t}} = 9.998 - 1.522 a_t^2 + 2.883 b_t^2 + 1.173 a_t^4 + 2.713 a_t^2 b_t^2 + 1.827 b_t^4 \text{ fb}, \tag{3.8}$$

where a_t (b_t) corresponds to $\kappa_t \cos\alpha$ ($\kappa_t \sin\alpha$). The SM corresponds to $a_t = 1$ and $b_t = 0$ in this parameterization. The $t\bar{t}t\bar{t}$ cross section is interpreted as a function of κ_t and α, discussed in Section 7.6.1.

3.2.2.1.2 Effective Field Theory

The $t\bar{t}t\bar{t}$ production cross section can be enhanced by EFT interactions between third-generation quarks. The four heavy-flavor fermion operators [88–91] affecting the $t\bar{t}t\bar{t}$ production are,

$$\mathcal{O}^1_{tt} = (\bar{t}_R\gamma^\mu t_R)(t_R\gamma_\mu \bar{t}_R) \tag{3.9}$$

$$\mathcal{O}^1_{QQ} = (\bar{Q}_L\gamma^\mu Q_L)(Q_L\gamma_\mu \bar{Q}_L) \tag{3.10}$$

$$\mathcal{O}^1_{Qt} = (\bar{Q}_L\gamma^\mu Q_L)(t_R\gamma_\mu \bar{t}_R) \tag{3.11}$$

$$\mathcal{O}^8_{Qt} = (\bar{Q}_L\gamma^\mu T^A Q_L)(t_R\gamma_\mu T^A \bar{t}_R). \tag{3.12}$$

where Q_L and t_R are left-handed third-generation quark doublet and right-handed top-quark singlet. The $t\bar{t}t\bar{t}$ cross section can be parameterized as,

$$\sigma_{t\bar{t}t\bar{t}} = \sigma^{SM}_{t\bar{t}t\bar{t}} + \frac{1}{\Lambda^2}\sum_k C_k\sigma^{(1)}_k + \frac{1}{\Lambda^4}\sum_{jk} C_jC_k\sigma^{(2)}_{j,k} \tag{3.13}$$

where $C_k\sigma^{(1)}_k$ is the linear term, representing the interference of dimension-6 operators with SM operators. The $C_jC_k\sigma^{(2)}_{j,k}$ is the quadratic term, which includes the square of one EFT operator or the interference of different EFT operators.

In addition, $t\bar{t}t\bar{t}$ can also be enhanced by the Higgs oblique parameter ($\hat{H}$). The $\hat{H}$ [92] is a self-energy correction applied to EW propagator in the SM. The self-energy correction to the Higgs boson can be parameterized by the $\hat{H}$, with $\hat{H} = 0$ corresponding to the SM. Similar to Yukawa coupling, the $\hat{H}$ parameter affects the $t\bar{t}t\bar{t}$ through the off-shell Higgs interaction. The deviation of the $t\bar{t}t\bar{t}$ cross section from the SM value from $\hat{H}$ at $\sqrt{s} = 14$ TeV is

$$\delta\sigma_{t\bar{t}t\bar{t}} \equiv \frac{\sigma_{\hat{H}} - \sigma_{SM}}{\sigma_{SM}} \approx 0.03\left(\frac{\hat{H}}{0.04}\right) + 0.15\left(\frac{\hat{H}}{0.04}\right)^2. \tag{3.14}$$

where $\sigma_{\hat{H}}$ represents the cross section enhanced by $\hat{H}$.

3.2.2.1.3 Type-II Two-Higgs-Doublet Model and its Extension

Type-II 2HDM includes heavy scalar and pseudo-scalar bosons after EWSB. $t\bar{t}t\bar{t}$ can be produced through a H or A boson production in association with $t\bar{t}$, in which H or A also decay into $t\bar{t}$. Furthermore, a light pseudo-scalar mediator (a) can be included associated with the type-II 2HDM, forming a 2HDM+a model. The light pseudo-scalar mediator provides a portal to couple with DM particles. Feynman diagrams of $t\bar{t}(H/A/a) \rightarrow t\bar{t}t\bar{t}$ production are shown in Figure 3.16, including both s- and t-channel diagrams. In the type-II 2HDM and 2HDM+a, the Yukawa couplings between $H/A/a$ bosons and the top quarks are dependent on β, summarized in Table 2.3. The $t\bar{t}t\bar{t}$ production is sensitive in the low $\tan\beta$ regime, which maximizes the branching fraction of $H/A/a \rightarrow t\bar{t}$.

A search of $t\bar{t}H/A \rightarrow t\bar{t}t\bar{t}$ production within type-II 2HDM in the SSML channel by the ATLAS experiment using an integrated luminosity of 139 fb^{-1} [135] will be presented in Chapter VIII. A combination of 2HDM+a searches will be summarized in Chapter IX.

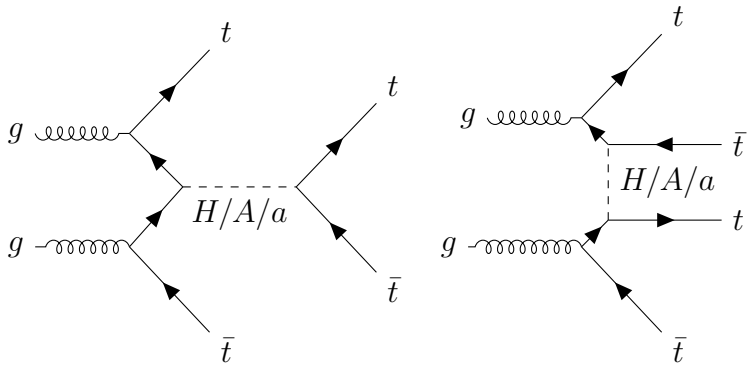

(a) s-channel (b) t-channel

Figure 3.16: Example of Feynman diagrams for $t\bar{t}(H/A/a) \rightarrow t\bar{t}t\bar{t}$ production in the (a) s-channel and (b) t-channel.

3.2.2.2 $t\bar{t}t$ Production

The $t\bar{t}t$ production, which includes $t\bar{t}tW$ and $t\bar{t}tq$ processes, is predicted to have a cross section of $O(1)$ fb at 13 TeV in the SM. Due to similar kinematics, the $t\bar{t}t$ production is hardly distinguishable from $t\bar{t}t\bar{t}$ production. At LO, the $t\bar{t}t\bar{t}$ overlaps the $t\bar{t}tW$ production in the 4-flavor scheme (FS). The 4FS treats the b quark as a massive particle at short distances, so it does not appear in the initial state. However, a gluon splitting ($g \to b\bar{b}$) can occur in the initial state, providing a b quark as an initial-state particle for $t\bar{t}tW$ production and emitting an additional b quark. Fig. 3.17a presents the example Feynman diagram of $t\bar{t}tW$ production at LO in 4FS. At short distances, the 5FS treats b quark as a massless particle, allowing for production with b-quark initial states. The overlap between $t\bar{t}t\bar{t}$ and $t\bar{t}tW$ at the LO are removed with 5FS. For the NLO prediction, the overlap becomes complicated. The $t\bar{t}t\bar{t}$ overlaps with the production of $t\bar{t}tW$ with an extra parton emission. In addition, the $t\bar{t}tW$ overlaps with the production of $t\bar{t}tq$ with an extra parton emission. These overlaps are removed using a diagram-removal scheme at NLO. The most accurate calculation of $t\bar{t}t$ production is predicted at NLO QCD and LO EW with diagram removal in the 5FS [125]. The $t\bar{t}tW$ and $t\bar{t}tq$ cross sections are 1.02 and 0.65 fb at NLO QCD, respectively. The LO EW correction provides additional 0.28 and 0.06 fb to $t\bar{t}tW$ and $t\bar{t}tq$ production, respectively. The LO EW was not included in $t\bar{t}t$ production. Instead, an uncertainty is assigned to account for this missing term.

The $t\bar{t}t$ production can be sensitive to the BSM physics. Moreover, it has never been studied. In this dissertation, a limit on $t\bar{t}t$ cross section is performed.

3.2.2.3 $t\bar{t}W$ Production

The most precise theoretical prediction of the $t\bar{t}W$ cross section, following Ref. [136], is

$$\sigma(t\bar{t}W) = 745 \pm 50 \text{ (scale)} \pm 13 \text{ (2-loop approx.)} \pm 19 \text{ (PDF, } \alpha_s\text{) fb.} \tag{3.15}$$

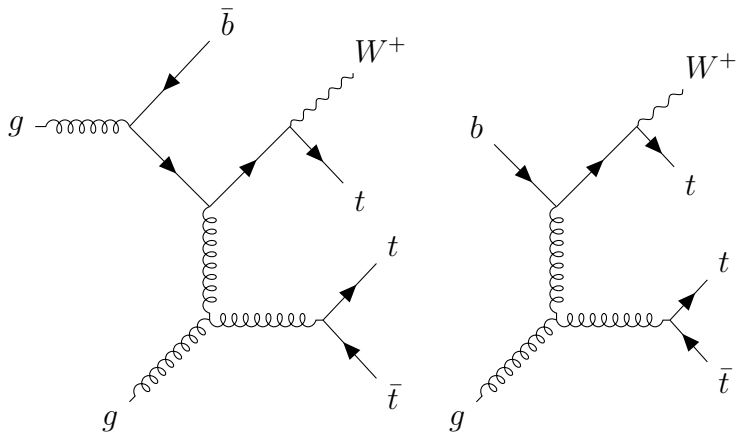

(a) 4FS (b) 5FS

Figure 3.17: Examples of Feynman diagrams for $t\bar{t}tW$ production in (a) 4FS and (b) 5FS.

This is calculated at NNLO in QCD, including NLO EW corrections. In addition, $t\bar{t}W$ cross section is also predicted by a NLO multileg-merged FxFx technique, following Ref. [137], to be

$$\sigma(t\bar{t}W) = 722\ ^{+70}_{-78}(\text{scale})\ \pm 7(\text{PDF})\ \text{fb}, \tag{3.16}$$

predicted at NLO QCD and NLO EW. The NLO FxFx technique captures a significant fraction of the NNLO QCD contributions to the cross section. Other calculations are available though provide less precision, as shown in Ref. [117; 123; 137–147]. The $t\bar{t}W$ cross section at different orders of correction is summarized in Table 3.2. Dedicated $t\bar{t}W$ cross section measurements are performed in the SSML final states using the full Run 2 data collected by the ATLAS [148] and CMS [149] detectors. The measured inclusive $t\bar{t}W$ cross sections from ATLAS and CMS, shown in Fig. 3.18a, are higher than the most accurate theoretical prediction. Given the nature of the charge asymmetry of the $t\bar{t}W$ process, it is important to understand the cross sections of $\sigma(t\bar{t}W^+)$ and $\sigma(t\bar{t}W^-)$. The $t\bar{t}W^+/t\bar{t}W^-$ ratio is shown in Fig. 3.18b. A two-dimensional contour of $\sigma(t\bar{t}W^+)$ and $\sigma(t\bar{t}W^-)$ is shown in Figure 3.19. The measured cross sections of $\sigma(t\bar{t}W^+)$ and $\sigma(t\bar{t}W^-)$ deviate from the prediction of $\text{NNLO}_{\text{QCD}} + \text{NLO}_{\text{EW}}$, but are within uncertainties [136].

As $t\bar{t}W$ is a dominant process in SSML, the kinematics of the $t\bar{t}W$ must be well understood. The jet multiplicity in the same-sign dilepton and trilepton final states are depicted in Figure 3.20. With the fit adjusting $t\bar{t}W$ to a higher normalization, the data and the post-fit predictions show good agreement. However, an excess of data over the post-fit predictions is observed in the high jet multiplicity region for events with positive total charges of 2ℓ and 3ℓ. This discrepancy highlights the difficulty of the $t\bar{t}W$ modeling in the signal enriched phase space for the $t\bar{t}t\bar{t}$ analyses.

NNLO [136]		FxFx [137]	
Order	σ [fb]	Order	σ [fb]
LO QCD: $\alpha_s^2\alpha$	$420\ ^{+106}_{-79}$		
NLO QCD: $+\alpha_s^3\alpha$	$622\ ^{+79}_{-72}$	$t\bar{t}W$+0,1,2j@NLO	$691\ ^{+66}_{-74}$
NNLO QCD: $+\alpha_s^4\alpha$	$711\ ^{+35}_{-46} \pm 14$		
NLO EW: $+\alpha_s\alpha^3 + \alpha_s^2\alpha^2 + \alpha^4$	$745 \pm 50 \pm 13$	$+\alpha_s\alpha^3$	$739\ ^{+75}_{-81}$
		$+\alpha_s^2\alpha^2 + \alpha^4$	$722\ ^{+70}_{-78}$

Table 3.2: Summary of the $t\bar{t}W$ cross section predicted at the $\mathrm{NNLO_{QCD}} + \mathrm{NLO_{EW}}$ [136] and at $\mathrm{NLO_{QCD}} + \mathrm{NLO_{EW}}$ using FxFx multijet merging [137]. In both calculations, the first uncertainty is from the choice of the μ_R and μ_F. The second uncertainty in the NNLO calculation corresponds to the approximation used in the 2-loop calculation. Uncertainties on PDF and α_s are omitted. Table comes from Ref. [148].

3.2.2.4 $t\bar{t}Z$ Production

The most accurate theoretical $t\bar{t}Z$ cross section is predicted at NLO QCD with NLO EW [117; 150]. A next-to-next-to-leading-logarithm (NNLL) calculation with a resummation of soft gluon corrections has been matched to NLO results at $\sqrt{s} = 13$ TeV [117], providing an NLO+NNLL cross section prediction [138],

$$\sigma_{t\bar{t}Z} = 0.86\,^{+0.07}_{-0.08}\,(\text{scale}) \pm 0.02\,(\text{PDF} \oplus \alpha_s)\,\text{pb}. \tag{3.17}$$

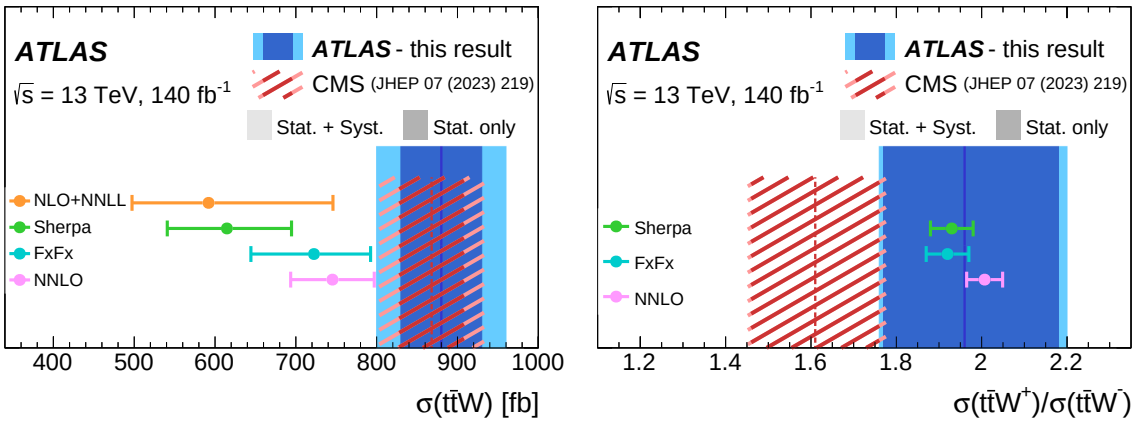

(a) (b)

Figure 3.18: Comparison between measurements from ATLAS [148] and CMS [149] experiments and various theoretical predictions [136; 137; 140] on (a) the inclusive $t\bar{t}W$ cross section and (b) the $t\bar{t}W^+/t\bar{t}W^-$ cross-section ratio. Figure comes from Ref. [148].

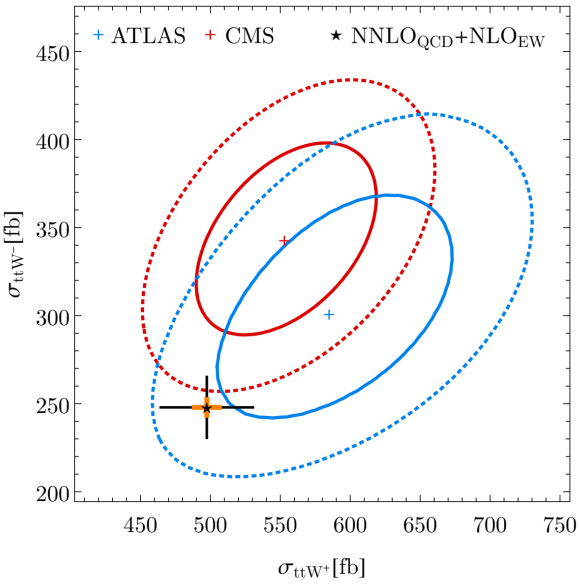

Figure 3.19: Comparison between theoretical prediction, at $\mathrm{NNLO_{QCD}} + \mathrm{NLO_{EW}}$, and measured cross sections from ATLAS and CMS at 68% (solid) and 95% (dashed) CL. Figure comes from Ref. [136].

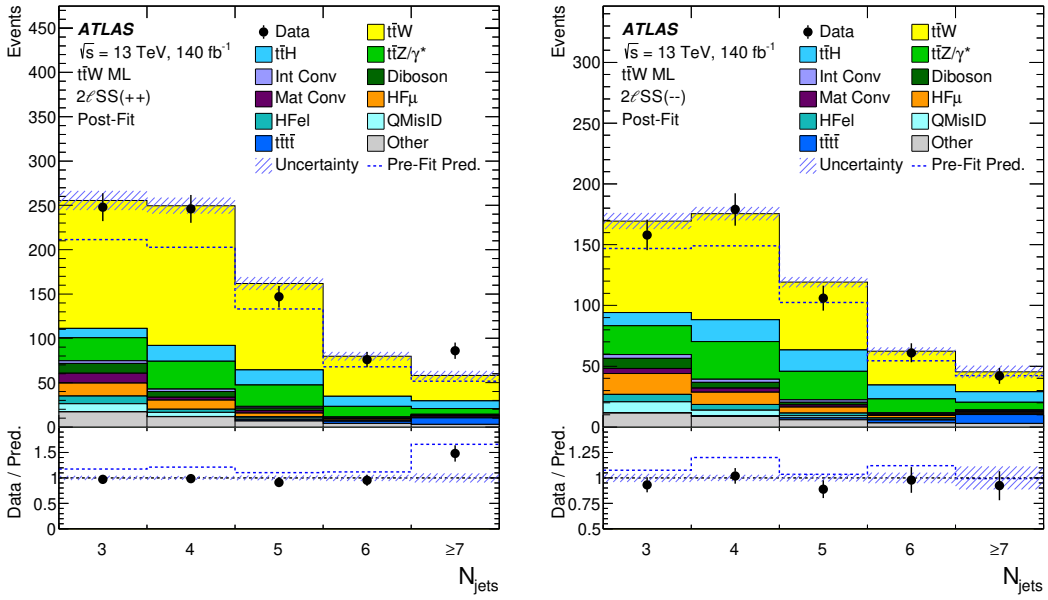

(a) $2\ell(++)$

(b) $2\ell(--)$

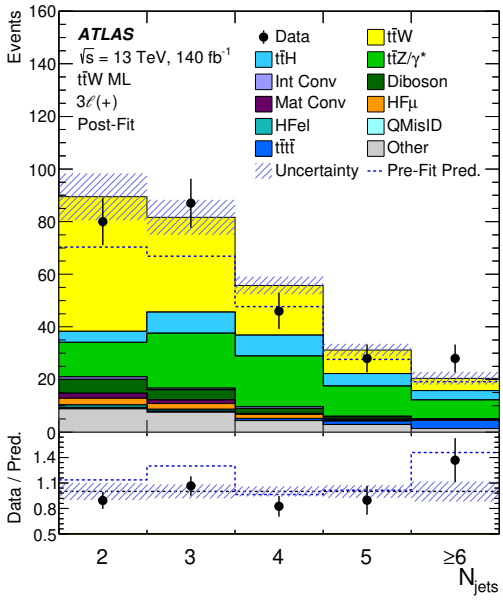

(c) $3\ell(+)$

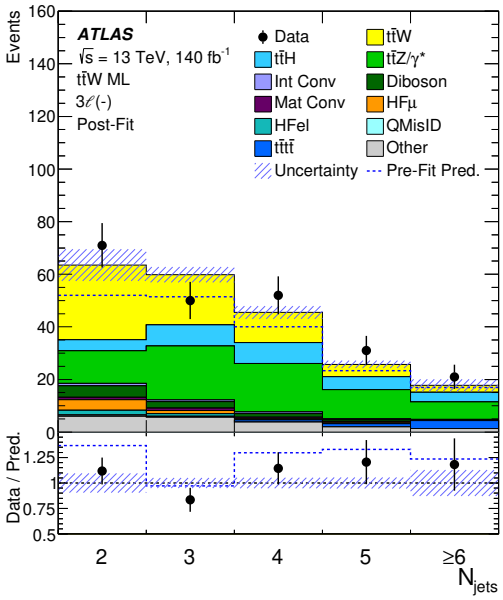

(d) $3\ell(-)$

Figure 3.20: Comparisons on the jet multiplicity between data and post-fit predictions in the same-sign dilepton and trilepton regions with different total charges of leptons [148].

Dedicated measurements from ATLAS [151] and CMS [152] show consistent results between theoretical and measured $t\bar{t}Z$ cross section, as reported in Figure 3.13.

CHAPTER IV

The ATLAS Detector

The ATLAS detector [94] is a multipurpose detector designed to study the physics of SM and BSM in pp and heavy-ion collisions at the TeV scale. The ATLAS detector is the world's largest detector for a particle collider, 44 meters long and 25 meters in diameter. Figure 4.1 presents the schematic view of the ATLAS detector. It is designed to be cylindrical symmetric, covering almost 4π solid angle around the IP, with multiple layers of sub-detector to identify and reconstruct individual types of particles. Four major sub-detectors and two magnetic systems from the innermost to outermost are the inner detector (ID), the solenoid magnet, electromagnetic (EM) calorimeters, hadronic calorimeters, toroid magnets, and the muon spectrometer (MS). Table 4.1 summarizes the performance of sub-detectors in the ATLAS detector. Different sub-detectors are discussed in separate sections in the following.

Detector component	Required resolution	η coverage	
		Measurement	Trigger
Tracking	$\sigma_{p_T}/p_T = 0.05\% \oplus 1\%$	± 2.5	
EM calorimeter	$\sigma_E/E = 10\%/\sqrt{E} \oplus 0.7\%$	± 3.2	± 2.5
Hadronic calorimeter (jets)			
Barrel and end-cap	$\sigma_E/E = 50\%/\sqrt{E} \oplus 3\%$	± 3.2	± 3.2
Forward	$\sigma_E/E = 100\%/\sqrt{E} \oplus 10\%$	$3.1 < \lvert\eta\rvert < 4.9$	$3.1 < \lvert\eta\rvert < 4.9$
Muon spectrometer	$\sigma_{p_T}/p_T = 10\%$ at $p_T = 1$ TeV	± 2.7	± 2.4

Table 4.1: General performance of the sub-detectors in the ATLAS detector [94].

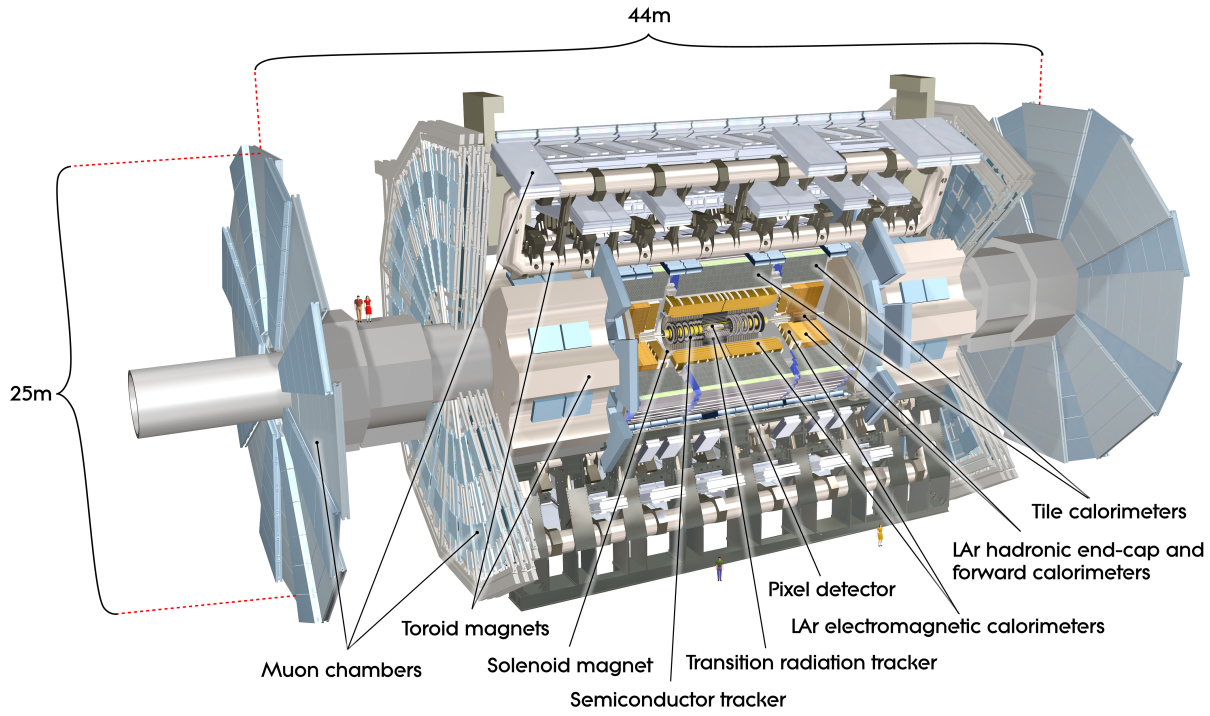

Figure 4.1: Schematic view of the ATLAS detector [94].

As reported in Ref. [94], the ATLAS detector uses a right-handed cartesian coordinate system, with the IP defined as the origin of the coordinate system. The beam direction is the z-axis, while the transverse plane to the beam direction is the x-y plane. The positive x-axis is defined as pointing from the IP to the center of the LHC ring. Therefore, with the right-handed cartesian coordinate system, the y-axis points upwards. The ATLAS detector also utilizes polar coordinates (r, θ, ϕ), with θ representing the polar angle from the beam axis and ϕ standing for the azimuthal angle in the x-y plane.

Several observables can describe the characteristics of the particles in the ATLAS detector. The rapidity (y) describes the location within the detector for massive particles. The y is defined as

$$y = \frac{1}{2} \ln \left(\frac{E + p_z}{E - p_z} \right). \tag{4.1}$$

For massless or ultra-relativistic particles, the rapidity can be approximately expressed

by pseudorapidity (η). The η is defined as

$$\eta = \frac{1}{2} \ln \left(\frac{|\vec{p}| + p_z}{|\vec{p}| - p_z} \right) = - \ln \left[\tan \left(\frac{\theta}{2} \right) \right]. \tag{4.2}$$

Based on the pseudorapidity, the ATLAS detector is separated into barrel and end-cap regions, emphasizing different physics regimes. The separation in the detector between two physics objects is measured using the angular distance (ΔR) defined as

$$\Delta R = \sqrt{(\Delta\eta)^2 + (\Delta\phi)^2}. \tag{4.3}$$

The observables in the transverse plane are also crucial in collider physics. The transverse energy (E_T) of the particle is defined as $E_T = E \sin\theta = \sqrt{p_T^2 + m^2}$, where the transverse momentum (p_T) of the particle is defined as $p_T = \sqrt{p_x^2 + p_y^2}$.

4.1 Inner Detector

The ID [94], the innermost sub-detector in the ATLAS detector, provides measurements on the charged particles with excellent momentum resolution and primary and secondary vertex reconstruction for charged tracks with p_T above 0.5 GeV and within $|\eta| < 2.5$. It also identifies electrons with a p_T range between 0.5 GeV and 150 GeV with $|\eta| < 2.0$. The ID layout is presented in Figure 4.2. The ID contains three independent layers of sub-detector from the innermost to the outermost: Pixel Detector, Semiconductor Tracker (SCT), and Transition Radiation Tracker (TRT). A solenoid magnet surrounding the ID provides a 2 tesla (T) magnetic field to bend the charged particles. Figure 4.3 shows the structures of the ID sub-systems in detail.

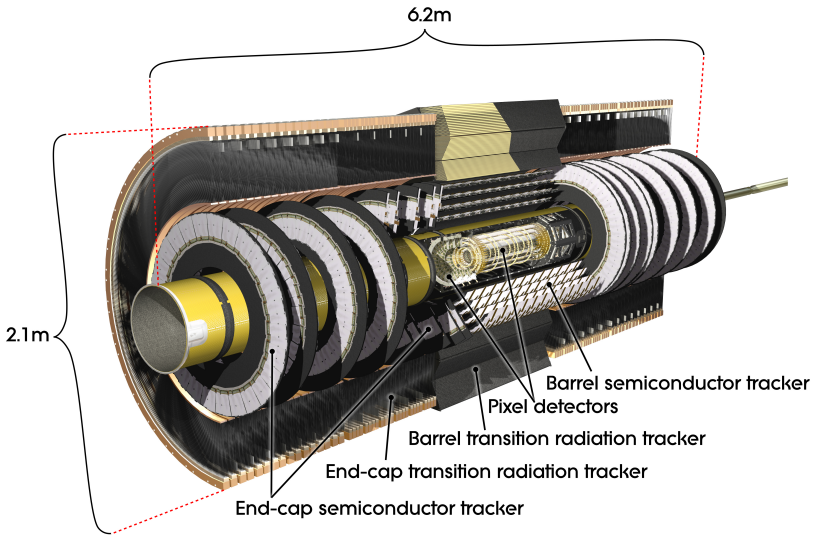

Figure 4.2: Cut-away view of the ID in the ATLAS detector [94].

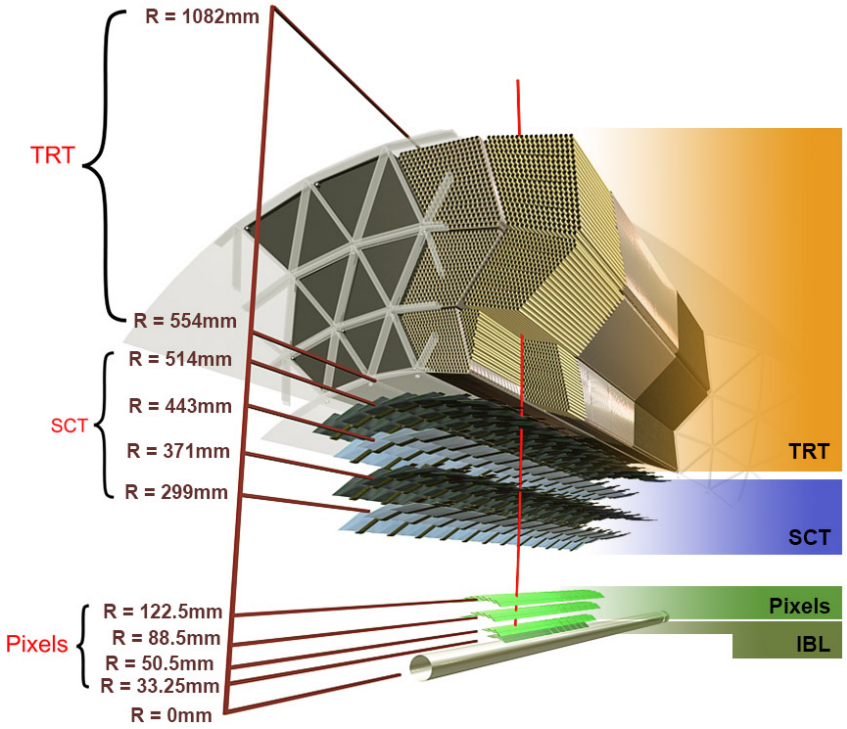

Figure 4.3: Schematic view of sensors and structural elements traversed by a charged track with p_T of 10 GeV in the barrel ID ($\eta = 0.3$) [94].

4.1.1 Pixel Detector and Insertable B-Layer

The pixel detector [94] utilizes the semiconductor pixel structure, with 250 μm thick silicon for the detector and sensor. The detection in the pixel relies on the electron-hole pair production when charged particles pass through. The produced electron would drift to an electrode under the applied electric field, resulting in an electric signal. The pixel detector provides high-efficiency and high-resolution measurements of charged particles due to the low energy required to create an electron-hole pair in silicon, as well as the small volume of pixels.

The pixel detector determines the impact parameter resolution and the vertex identification for the reconstruction of the short-lived particles such as b quarks and τ leptons. In the Run 2 operation of the LHC, the pixel detector consists of four cylindrical layers in the barrel region and three disk layers in the end-cap region of both sides. These layers ensure at least three space points for the tracks and cover the full η range of $|\eta| < 2.5$. Four layers in the barrel region are Insertable B-Layer (IBL) [153], B-layer, layer 1, and layer 2. The IBL was inserted in the LS1 to improve hit and vertex resolutions. Figure 4.3 shows the radii of pixel layers in the barrel region. The pixel layers are segmented in R-ϕ and z with a minimum size in R-$\phi \times z$ to be 50×400 μm^2, while the IBL has a smaller size of 50×250 μm^2. There are about 86 million readout channels in total for the pixel detector, including 6 million for the IBL. The typical spatial hit resolution reaches 10 (10) μm in R-ϕ plane and 67 (115) μm along z for IBL (rest of the layers) [94; 154].

4.1.2 Semiconductor Tracker

The SCT [94] is positioned around the pixel detector and employs a semiconductor microstrip structure. Utilizing a technology similar to the pixel system, the SCT precisely measures charge particles' momentum, impact parameters, and vertex position. The SCT consists of four layers in the barrel region and nine disks on both sides of the end-cap

region, covering the range of $|\eta| < 2.5$. Both barrel and end-cap regions utilize the stereo strips inclined at a small angle of 40 milliradians to measure both R-ϕ and z coordinates. The strip pitch is 80 μm in the barrel region and is approximately the same in the end-cap regions. The SCT is equipped with roughly 6.3 million channels for the readout. The intrinsic accuracies per layer reach 17 μm in the R-ϕ plane and 580 μm along the z (R) axis in the barrel (disks of end-cap) region [94].

4.1.3 Transition Radiation Tracker

The TRT [94] utilizes straw tubes of 4 mm diameter to provide tracking measurements in the outermost area of the ID system. The straw tube is filled with a xenon-based gas mixture (70% Xe + 27% CO_2 + 3% O_2) with a 30 μm gold-plated wire placed in the center. The gas mixture can be ionized with charged particles passing through the tubes, producing free electrons. The electrons drift toward the wire under an electric field, producing electric signals. The TRT consists of 52544 straw tubes of 1.5 m in length in the barrel region ($|\eta| < 1$) and 122880 straw tubes of 0.4 m long on each side of the end-cap region ($1 < |\eta| < 2$). The TRT provides an average of 36 space-point measurements per track on R-ϕ coordinates with an intrinsic accuracy of 130 μm per straw tube [94]. In addition to the tracking measurements, the xenon-based gas mixture allows the detection of the transition-radiation photons, enhancing the electron identification capability.

4.2 Calorimeters

The ATLAS calorimeter system, surrounding the ID and the solenoid magnet, is divided into two sub-detectors: EM and hadronic calorimeters. The calorimeter system covers a wide range of $|\eta| < 4.9$. Figure 4.4 presents a schematic view of the ATLAS calorimeter system.

The ATLAS calorimeter system uses sampling calorimeters. The sampling calorimeter

follows a destructive method by alternating passive and active material layers, with the passive material stopping the incoming particles and the active material providing signals for readout. When an incoming particle passes through the calorimeters, it initiates a cascade of EM or hadronic interactions. The energies are further deposited in the calorimeters and converted into electric signals for readout. Therefore, the calorimeters provide energy measurements of the showers from both electrically charged and neutral particles.

The shower structure can be described with longitudinal and angular profiles. In the context of the EM shower, a gamma function can be used to describe the longitudinal shower profile

$$\frac{dE}{dt} = E_0 t^{\alpha} e^{-\beta t}, \tag{4.4}$$

where α and β are model parameters, t is the depth, and E_0 is the energy of incoming particle. The length of the shower is then approximately determined as

$$X = X_0 \frac{\ln(E_0/E_c)}{\ln 2}, \tag{4.5}$$

where X_0 is the radiation length of the matter, and E_c is the critical energy when bremsstrahlung and ionization rates are equal. The Moliere radius (R_M) is defined as the radius of a cylinder to contain 90% of the energy deposition of an EM shower. It describes the angular profile as

$$R_M = X_0 \left(\frac{21.2 \text{ MeV}}{E_c} \right). \tag{4.6}$$

On the other hand, the nuclear interaction length (λ_I) is used to describe the hadronic shower. The λ_I is defined as the mean path length required to reduce the particle intensity by a factor of exponential when the showers pass through the material. The λ_I can be

approximately written as

$$\lambda_I = 35 \cdot A^{1/3}\ g/cm^2, \tag{4.7}$$

where A is the atomic mass number. The λ_I is approximately larger than the X_0 with a factor of $A^{4/3}$. Two primary active detector mediums are used in the ATLAS calorimeter system: liquid-argon (LAr) [155] and scintillator tiles [156].

The energy resolution of the calorimeter [157] can be described as

$$\frac{\sigma(E)}{E} = \frac{a}{\sqrt{E}} \oplus \frac{b}{E} \oplus c, \tag{4.8}$$

where $\oplus$ represents a quadratic sum. The first term, $\frac{a}{\sqrt{E}}$, stands for the stochastic term, including the shower intrinsic fluctuations. The second term, $\frac{b}{E}$, is the noise term depending on the detector technique, which is generally related to the electronic readout noise. The third term is the constant term related to the instrumental effects such as nonuniform response and mechanical imperfections.

4.2.1 Electromagnetic Calorimeter

The EM calorimeter [94] provides precision energy measurements of electrons and photons covering the η region matched to the ID and the full ϕ range. It utilizes lead as the passive medium and LAr as the active medium. An electron or a photon initiates a cascade, dominated by pair production and bremsstrahlung processes, in both LAr and lead absorber. The LAr is ionized, producing signals that can be measured.

The EM calorimeter is divided into a barrel ($|\eta| < 1.475$) and two end-cap parts ($1.375 < |\eta| < 3.2$). The transition region between the barrel and end-cap regions ($1.375 < |\eta| < 1.52$) contains additional material for the cooling system for the ID. This region is generally excluded from analyses requiring precision measurement with electrons. Each end-cap calorimeter is divided into an outer wheel ($1.375 < |\eta| < 2.5$) and an inner wheel

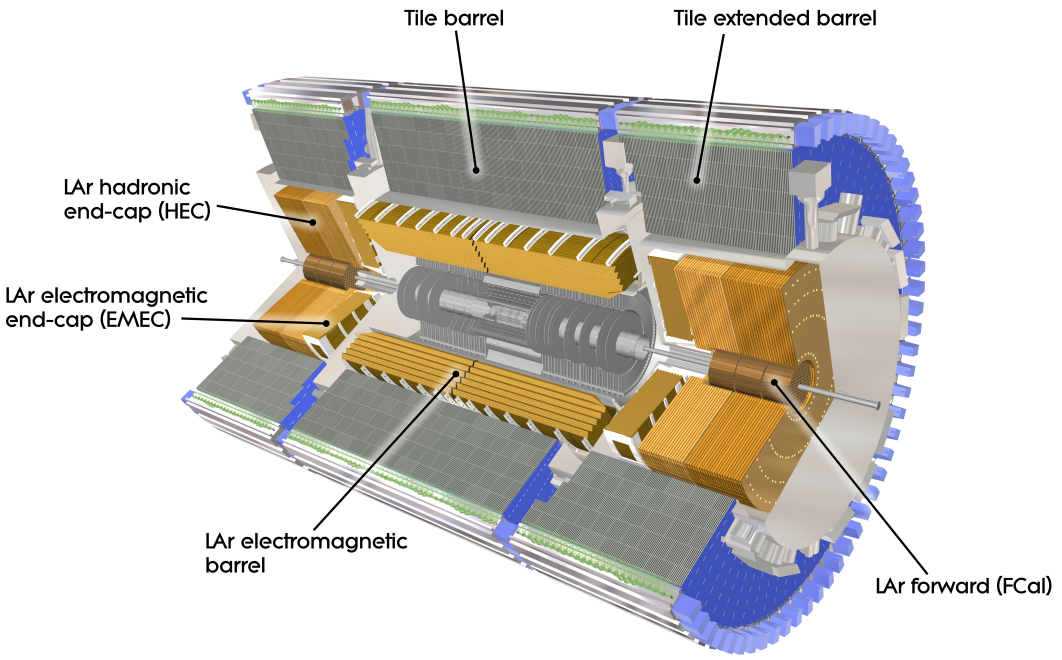

Figure 4.4: Cut-away view of the calorimeter systems in the ATLAS detector [94].

($2.5 < |\eta| < 3.2$). In the EM calorimeter, the region of $|\eta| < 2.5$ is often used for precision physics.

The total thickness of the EM calorimeter is > 22 X_0 in the barrel region and > 24 X_0 in the end-cap regions to ensure the majority of electrons and photons are contained within the EM calorimeter [94]. The lead thickness has been optimized as a function of η to improve energy resolution. The design energy resolution of the EM calorimeter [94] is

$$\frac{\sigma(E)}{E} = \frac{10\%}{\sqrt{E}} \oplus 0.7\%. \tag{4.9}$$

4.2.2 Hadronic Calorimeter

The hadronic calorimeter [94] measures the energy of the hadronic showers, covering the range of $|\eta| < 4.9$ and the full ϕ range. Hadronic showers are from a series of inelastic QCD interactions, including multi-particle production and nuclear decay of excited nuclei.

Similar to the EM calorimeter, a passive material is used to stop the hadrons and an active material to measure the energy deposits. The hadronic calorimeter has a total thickness of $11\lambda_I$ at $\eta = 0$ [158]. This allows most particle showers to be contained in the calorimeters and prevents punch-through to the muon detector. The hadronic calorimeter includes the tile calorimeter, the liquid-argon hadronic end-cap calorimeter (HEC), and the liquid-argon forward calorimeter (FCal).

The tile calorimeter is positioned outside the EM calorimeter with the barrel region of $|\eta| < 1.0$ and the end-cap region of $0.8 < |\eta| < 1.7$. It uses steel as the passive medium and plastic scintillating tiles as the active medium. The charged particles would produce fluorescence photons passing through the plastic scintillators, creating electric signals with the photomultiplier.

The HEC contains two independent wheels on each side of the end-cap, placed outside the end-cap EM calorimeter. The HEC covers a region of $1.5 < |\eta| < 3.2$, which overlaps with the tile calorimeter and FCal to reduce the drop off of material density in the transition region. The HEC uses copper plates as the absorber and LAr as the active medium.

The FCal provides the uniformity of the calorimeter coverage in a range of $3.1 < |\eta| < 4.9$. This also reduces radiation backgrounds in the muon system. The FCal consists of three modules in each end-cap region: the first uses copper and the other two use tungsten. The module with copper is optimized for the EM measurements, while the modules with tungsten predominantly measure the hadronic interactions.

The designed energy resolution of the hadronic calorimeter [94] in the barrel and end-cap regions is

$$\frac{\sigma(E)}{E} = \frac{50\%}{\sqrt{E}} \oplus 3\%, \tag{4.10}$$

while the resolution in forward regions is

$$\frac{\sigma(E)}{E} = \frac{100\%}{\sqrt{E}} \oplus 10\%. \tag{4.11}$$

4.3 Muon Spectrometer

The MS [94], the outermost subsystem of the ATLAS detector, measures the momenta and charge of muons in a range of $|\eta| < 2.7$. The momentum measurements of muons depend on their deflection from the magnetic field produced by toroid magnets. The magnetic fields are provided with a large barrel toroid ($|\eta| < 1.4$) and two smaller end-cap toroids ($1.6 < |\eta| < 2.7$). The barrel toroid provides approximately 0.5 T, and the end-cap toroid provides about 1 T. In the transition region of $1.4 < |\eta| < 1.6$, the magnetic bend is determined by a combination of fields from the barrel and enc-cap magnets. The muon detector includes separate high-precision tracking chambers and trigger detectors in different η ranges: Monitored Drift Tubes (MDT) and Cathode Strip Chambers (CSC) for the tracking system, and Resistive Plate Chambers (RPC) and Thin Gap Chambers (TGC) for the trigger system. In addition, an alignment system of the muon chambers is designed using optical alignment. The accuracy of the posistions of the muon chambers is generally around 50 μm, allowing for the track resolution being around 10% in the muon momentum measurements with $p_T = 1$ TeV [159]. Figure 4.5 shows the schematic view of the ATLAS muon system. Table 4.2 presents the performance and configurations of the four sub-detectors in the ATLAS muon system.

Type	Function	Chamber resolution (RMS) in			Measurements/track		Number of	
		z/R	ϕ	time	barrel	end-cap	chambers	channels
MDT	tracking	35 μm (z)	—	—	20	20	1088 (1150)	339k (354k)
CSC	tracking	40 μm (R)	5 mm	7 ns	-	4	32	30.7k
RPC	trigger	10 mm (z)	10 mm	1.5 ns	6	—	544 (606)	359k (373k)
TGC	trigger	2–6 mm (R)	3–7 mm	4 ns	-	9	3588	318k

Table 4.2: Performances and configurations of the four sub-detectors in the ATLAS muon system [94].

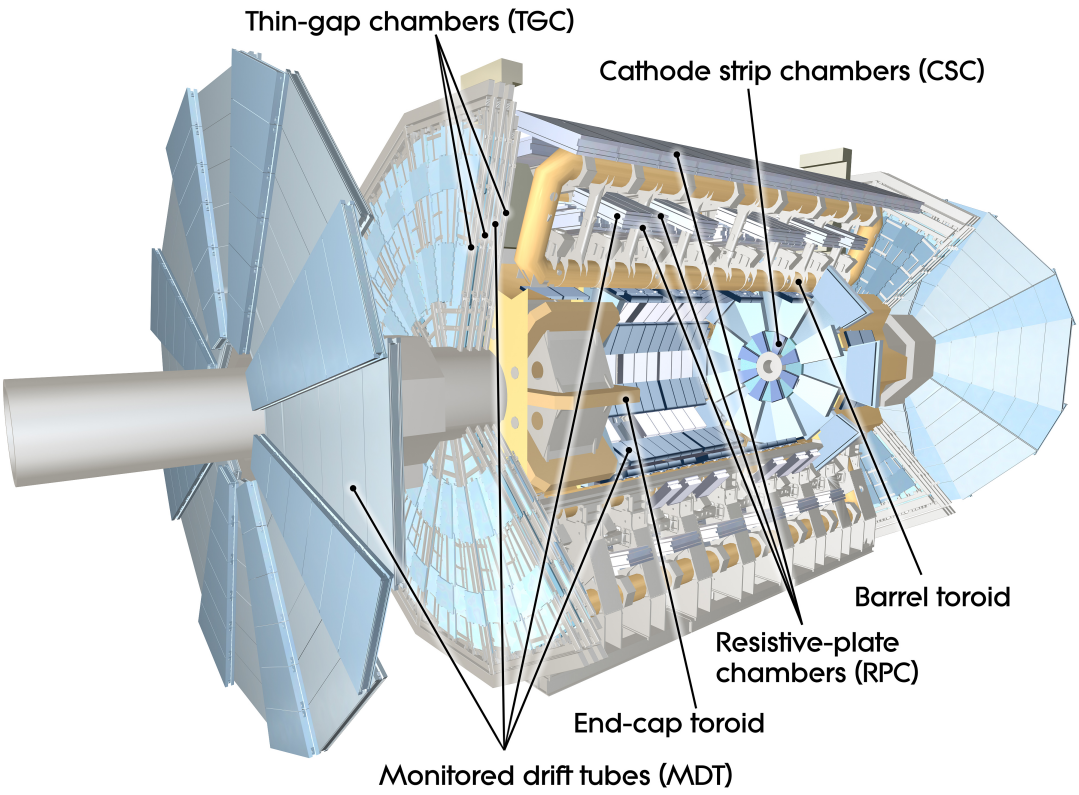

Figure 4.5: Cut-away view of the MS in the ATLAS detector [94].

The MDT system [94] provides precision tracking measurements of the muons, covering the range of $|\eta| < 2.7$. They consist of multiple layers of drift tubes of a 30 mm in diameter filled with a gas mixture of Ar (93%) and CO_2 (7%) at a pressure of 3 bar. A tungsten-rhenium wire of 50 μm in diameter is placed at the center of each tube and is applied with a potential of 3080 V. When a muon passes through the MDT, it will ionize the gas in the tubes, producing the electric signals. The tubes that provide the electric signal would form the track in the MDT. The average resolutions are 35 μm per chamber and 80 μm per tube [94].

The CSC [94] are multiwire proportional chambers filled with a similar gas mixture of Ar (80%) and CO_2 (20%) as the MDT chambers. The CSC provides a better capability of dealing with high background rates than the MDT due to its shorter drift time. Therefore, the CSC system is placed in the innermost tracking layer ($2.0 < |\eta| < 2.7$) to provide high-precision tracking measurements in a region with high background rates. The spatial resolution of CSC is 40 μm in the bending plane and 5 μm in the transverse plane.

The RPC [94] provides fast triggering and position measurements of η and ϕ in the barrel region of $|\eta| < 1.05$. The RPC is a gaseous parallel electrode-plate detector with a gas mixture of $C_2H_2F_4$ (94.7%), C_4H_{10} (5%), and SF_6 (0.3%). High voltage is applied between the plates, creating a uniform electric field. Avalanches would be produced by the passing of a charged particle, leading to an instantaneous signal after the passage. This provides the capability to deal with high background rates and rate-independent time resolution.

The TGC [94] provides the triggering and position measurements of η and ϕ in the end-cap region of $1.05 < |\eta| < 2.5$. The TGC are multiwire proportional chambers with a gas mixture of CO_2 and C_5H_{12}. The TGC is structured with small wire-to-wire distances, with a high electric field applied around TGC wires. This results in good time resolution, 4 ns, for most tracks.

The momentum resolution of the muon system [160] depends on the η. For a given η,

the muon momentum resolution can be further parameterized as

$$\frac{\sigma_{p_T}}{p_T} = \frac{p_0^{MS}}{p_T} \oplus p_1^{MS} \oplus p_2^{MS} \cdot p_T, \tag{4.12}$$

where the $\oplus$ represents the quadratic sum. The p_0^{MS}, p_1^{MS}, and p_2^{MS} are the coefficients related to the energy loss in the calorimeter material, multiple scattering, and intrinsic resolution terms, respectively [160]. The ATLAS muon spectrometer is optimized to provide the resolution to be

$$\frac{\sigma_{p_T}}{p_T} \approx 10\% \text{ at } p_T = 1 \text{ TeV}. \tag{4.13}$$

4.4 Magnetic systems

The ATLAS magnetic system [94] provides magnetic fields to bend charged particles. The system includes solenoid and toroid magnets, which are superconducting systems cooled by liquid helium to around 4.5 K.

The solenoid magnet has a diameter of 2.56 m and an axial length of 5.8 m. It provides a 2 T magnetic field enclosing the inner detector. The toroid magnet has a barrel toroid and two end-cap toroids. The barrel toroid contains eight superconducting coils, with 25.3 m in length and inner and outer diameters of 9.4 m and 20.1 m, providing magnetic fields of approximately 0.5 T. The end-cap toroid is assembled as a cold mass, containing eight racetrack-like coils and eight keystone wedges. The overall size of the end-cap toroid is 5.0 m in length, and its inner and outer diameters are 1.65 m and 10.7 m, respectively. The end-cap toroid provides approximately 1 T magnetic field. Figure 4.6 shows the schematic view of the magnetic field direction in the ATLAS detector.

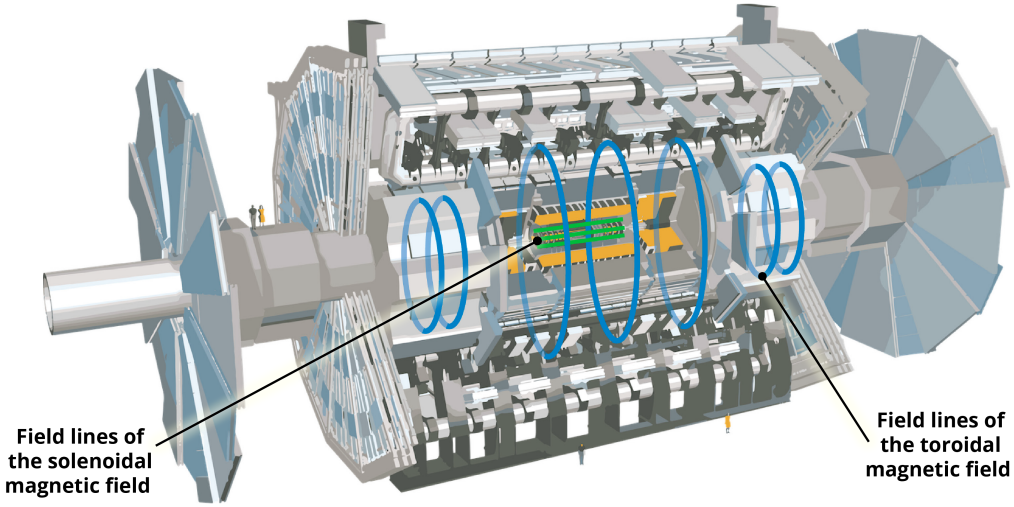

Figure 4.6: Illustration of the directions of the magnetic field from the solenoid and toronoid magnets in the ATLAS detector [161].

4.5 Trigger and Data Acquisition

The ATLAS Trigger and Data Acquisition (TDAQ) system [162] handles online processing, selecting, and recording interested events. It is crucial to skim data sizes to keep events potentially from interesting physics processes for offline analyses. The TDAQ system in Run 2 has two stages: Level-1 (L1) trigger and High-Level Trigger (HLT). Figure 4.7 shows the data of the ATLAS TDAQ system. The L1 trigger utilizes electronics hardware for triggering in both calorimeter and muon systems. The HLT is a software-based trigger with dedicated fast trigger algorithms taking inputs from L1 triggers. The L1 triggers are separated into two main parts: the L1 calorimeter (L1Calo) and the L1 muon (L1Muon) triggers. The L1Calo trigger collects the calorimeter information as input and sends it to the preprocessors to identify particle objects. The L1Calo is responsible for rapidly selecting relatively high-p_T objects such as electrons, muons, photons, jets, and hadronic τ, and the missing transverse momentum (E_T^{miss}). The L1Muon trigger selects with the hit information from RPC and TGC. An additional L1 topological (L1Topo)

trigger integrates the information from L1Calo and L1Muon and provides a topological selection with L1Calo and L1Muon objects. Results from L1Calo, L1Muon, and L1Topo are further processed by the Central Trigger Processor (CTP). The CTP forms the final trigger decisions within a latency of 2.5 μs. The L1 triggers also identify Regions of Interest (ROIs) in η and ϕ, which are processed by the HLT. The information of L1 accepted events is read out by the Front-End (FE) detector electronics. Those data are sent to the ReadOut Drivers (RODs) to preprocess the data and then to the ReadOut System (ROS) to buffer the data. Finally, the data are propagated to the HLT for offline-level selections on a dedicated computing farm. The computing farm would make the decisions within a few hundred milliseconds. The HLT is primarily based on the ATLAS Athena framework [163]. Once the HLT selects the events, the data will be sent to the storage for the offline physics analysis. The events failing the HLT selections are permanently lost.

With the sequence of selections from TDAQ, the collision data rate can be reduced from 40 MHz (with a 25 ns bunch crossing) to 100 kHz with L1 triggers. The rates are further reduced to 1 kHz with the HLT triggers. In addition, the data size is further reduced with L1 triggers and HLT. The original collision data size rate is approximate $\mathcal{O}(10)$ TB/s, assuming a single raw event has an $\mathcal{O}(1)$ MB size. The rates can be reduced to $\mathcal{O}(1)$ GB/s with the selections of L1 triggers and HLT.

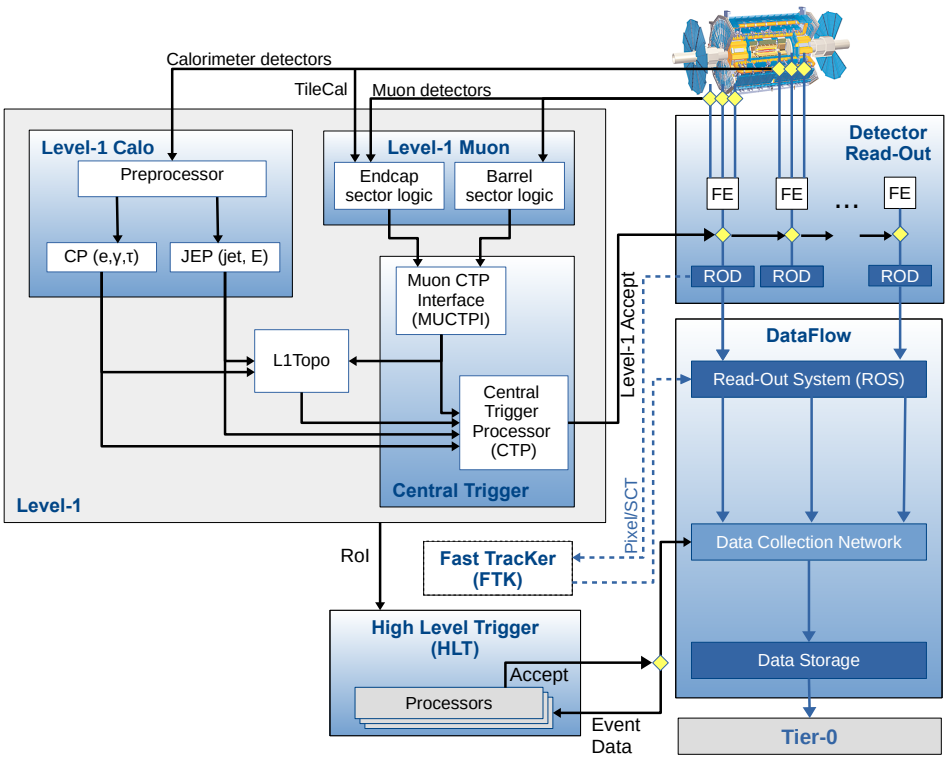

Figure 4.7: Schemtic view of the ATLAS TDAQ system in the Run 2 operation of LHC [162].

CHAPTER V

Particle Reconstruction and Identification

The ATLAS detector records physics events as different formations of electronic signals. This chapter describes the reconstruction and identification of physics objects from the detector signals in the triggered events, including light leptons (electrons and muons), jets, and E_T^{miss}. Figure 5.1 illustrates the particle identification in the ATLAS detector.

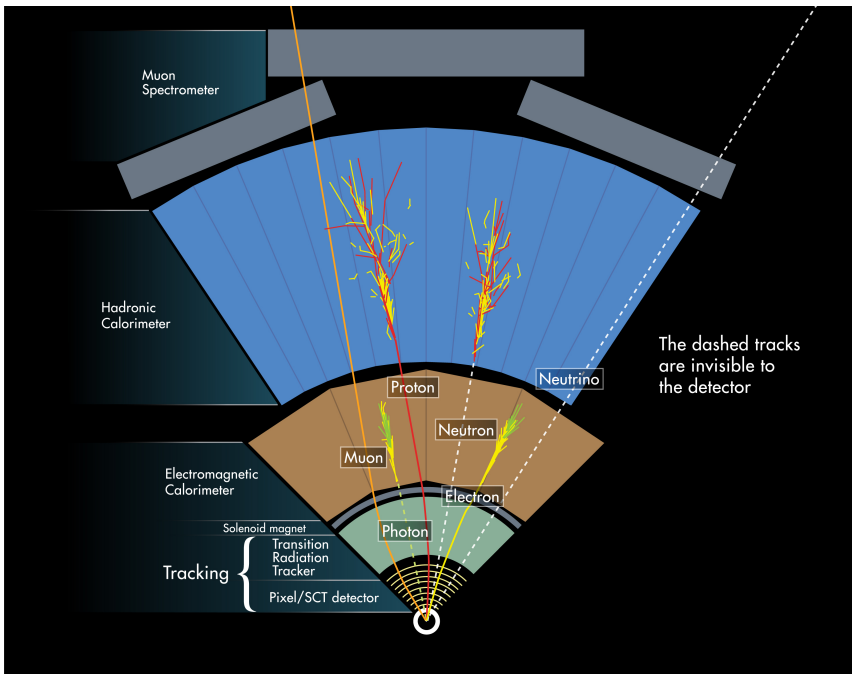

Figure 5.1: Particle identification in the ATLAS detector [164].

5.1 Tracking of Charged Particles

Charged-particle tracks are reconstructed with data recorded by the ID or MS. A track reconstruction software [165] was designed to provide a common event data model [166; 167] and detector description [168] to perform both the ID and MS reconstructions.

The ID track reconstruction contains two algorithm chains: inside-out and outside-in track reconstructions [165; 169]. The inside-out track reconstruction starts with forming space points in the pixel and SCT and drift circles in the TRT. A combinatorial Kalman filter [170] is used to find and form the track candidates with the space points from pixel and SCT, followed by a track scoring strategy [171] to resolve the shared hits in different tracks and reject fake tracks. Finally, the track candidates are further extended to the matching drift circles in the TRT to form the final tracks. Followed by the inside-out algorithm, an outside-in algorithm starts from the segments in the TRT. It extends inward to the pixel and SCT to improve the tracking efficiency for secondary tracks from conversions or decays of long-lived particles.

The tracks in the ID are described in perigee representation [166] with five parameters $(d_0, z_0, \phi, \theta, q/p)$ and a reference point. Figure 5.2 presents the schematic view of the track. The reference point is the beam spot position, the average position of the pp collision. The d_0 and z_0 are the transverse and longitudinal impact parameters relative to the beam spot position. The ϕ and θ are the azimuthal and polar angles of the track, respectively. The q/p represents the ratio of the track's charge to the track's momentum.

The MS track reconstruction is performed independently in the ID and MS. The information from both detectors is combined to form muon tracks for physics analysis. Muon reconstruction in the ID follows the abovementioned approaches. Muon reconstruction in the MS [172] begins with segment reconstruction from hits in different muon sub-detectors. The segment reconstruction of MDT fits straight-line functions to the hits found in each layer. Separate combinatorial searches are performed in the η and ϕ de-

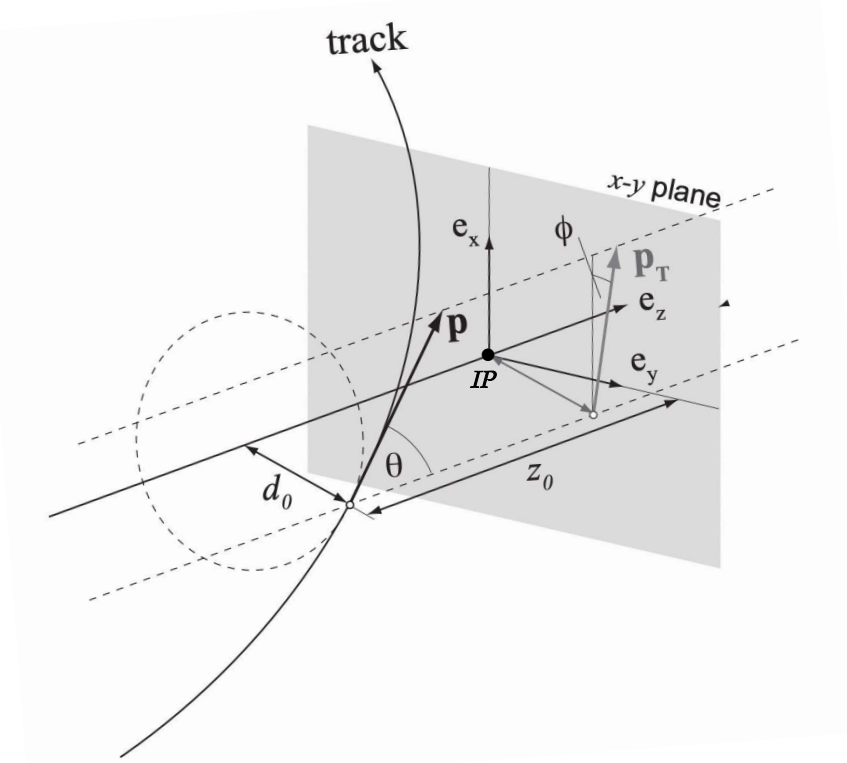

Figure 5.2: Illustration of the track parameters in the perigee representation [167].

tector planes to build the segments in the CSC. The RPC and TGC hits determine the coordinate perpendicular to the bending plane. The muon track candidates are further built with fits to the hits from the segments in different layers. Once the MS track candidate is formed, the hits associated with the track candidate are further fitted with a global χ^2 fit. Track candidates are then selected based on the χ^2 quality. Track fits are performed iteratively for hit removal and recovery procedures to remove unwanted hits and recover the necessary hits for tracks.

5.2 Primary Vertex and Pile-up

The primary vertices (PVs) are defined as the *pp* interaction points in space. The reconstruction of PVs is essential to the reconstruction of the complete kinematic properties of an event, allowing the proper assignment of charged-particle trajectories to the

hard-scattering PV [173]. Multiple inelastic pp interactions can occur in an pp collision event and produce many PVs. These additional PVs are usually from the soft QCD interactions, called pile-up. The mean number of inelastic pp collisions per bunch crossing, $\langle\mu\rangle$, quantifies the pile-up effects [174]. The $\langle\mu\rangle$ is directly related to the instantaneous luminosity, introduced in Section 3.1.1. Figure 5.3 presents the $\langle\mu\rangle$ for Run 2 pp collisions at $\sqrt{s} = 13$ TeV.

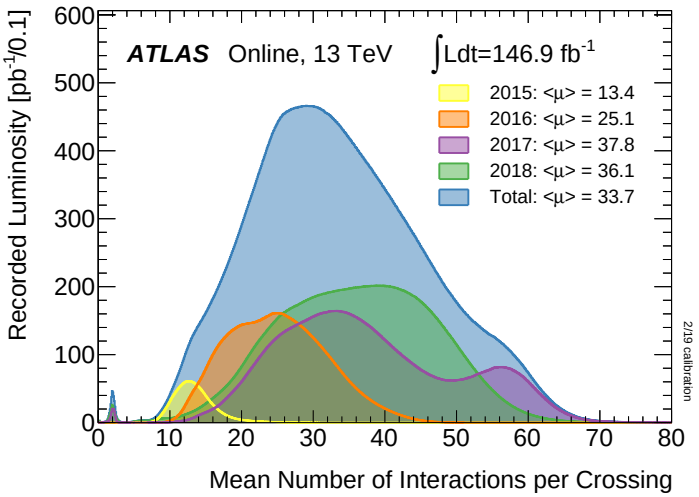

Figure 5.3: The integrated luminosity as a function of $\langle\mu\rangle$ for Run 2 2015-2018 pp collisions at $\sqrt{s} = 13$ TeV. The $\langle\mu\rangle$ corresponds to the mean of Poisson distribution of the number of inelastic interactions per bunch crossing [174].

The reconstruction of PVs is performed in two stages: vertex finding and vertex fitting [175]. The vertex-finding stage associates the reconstructed tracks with vertex candidates, and the vertex-fitting stage reconstructs the correct vertex position and covariance matrix with an adaptive vertex-fitting algorithm [176]. Ref. [173] summarizes this strategy in detail. A vertex is considered a valid PV if the vertex has at least two associated tracks.

5.3 Leptons: Electrons and Muons

Electrons and muons, collectively called leptons, can be produced from the heavy-particle decays, such as W, Z, or Higgs bosons from the hard scattering. These leptons

are known as the prompt leptons. On the other side, leptons can also arise from photon conversions and b/c-hadron decays, which are denoted as non-prompt leptons. Therefore, the reconstruction and identification of these leptons are significant to comprehending the underlying physics. The following sections will discuss the reconstruction and identification of the leptons and the suppression of the non-prompt lepton.

5.3.1 Electrons

5.3.1.1 Electron Reconstruction

When an electron passes through, it interacts with the detector materials, radiating photons through Bremsstrahlung. The emitted photon may produce an electron-positron pair with interaction with detector mediums. These processes would lead to a collimated object, which can typically be reconstructed in the same EM cluster. Such interactions can leave multiple tracks in the ID and produce EM showers in the calorimeter. Therefore, the electron reconstruction in the ATLAS detector is based on the following characteristics: localized clusters of energy deposits in the EM calorimeter, the tracks left in the ID, and close matching in $\eta \times \phi$ space of the tracks to the clusters [177].

The electron reconstruction, in a range of $|\eta| < 2.47$, starts with forming the clusters of calorimeter cells, known as topo-clusters, with a dynamic and variable-size topological cell clustering algorithm [178; 179]. The variable-size clusters allow energy recovery from bremsstrahlung photons or electrons from photon conversions. An electron candidate is reconstructed as the topo-cluster matched to the ID track, not associated with a conversion vertex. The track is re-fitted once the match is found to account for the Bremsstrahlung. An unconverted photon is defined when topo-clusters are matched to neither an electron ID track nor a conversion vertex. A converted photon is determined when a cluster matches a conversion vertex (or vertices). The fraction of converted photons varies from 20% in the barrel region to 65% in the end-cap regions.

5.3.1.2 Electron Identification

The electron identification is performed with a multivariate analysis (MVA) method using likelihood (LH) [177; 178]. This LH-based identification allows the suppression of the background from hadronic jets or converted photons being reconstructed as electrons. The inputs for the LH discriminant contain measurements from the ID and calorimeter systems and quantities combined with information from both systems. In the building of the LH, the signal is the prompt leptons, while the background is from the electrons arising from jets, photon conversions, or decay of heavy-flavor (HF) hadrons.

Three major working points (WPs) for physics analysis are Loose, Medium, and Tight. These WPs are optimized in bins of E_T and $|\eta|$ to meet the efficiency requirement. The WPs are defined based on the LH discriminant with a trade-off between signal efficiency and background rejection. Figure 5.4 presents the efficiencies of different WPs. These efficiencies are estimated from $J/\Psi \to ee$ and $Z \to ee$ with tag-and-probe methods [177]. The analyses discussed in this dissertation use the Tight WP.

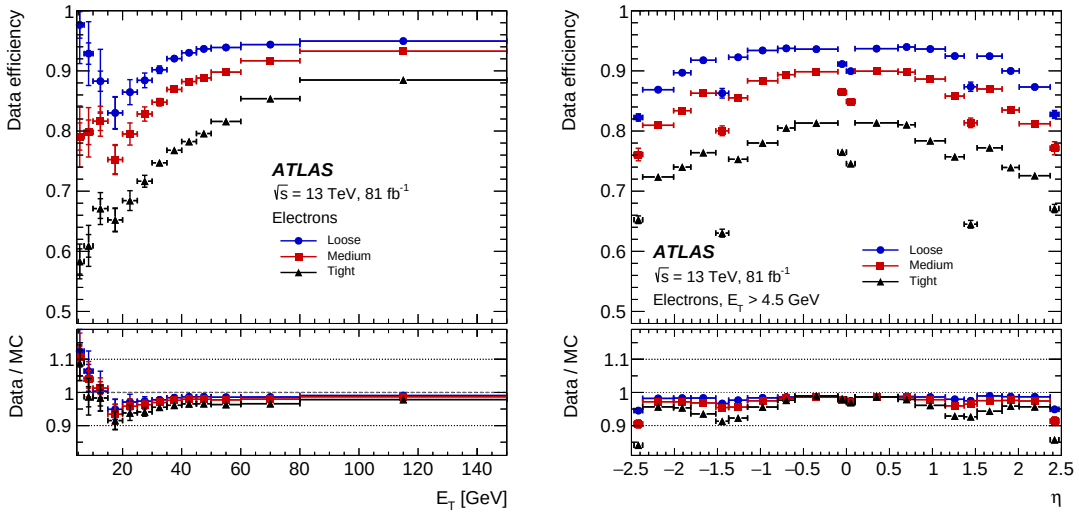

(a) (b)

Figure 5.4: The efficiency of electron identification measured from the $Z \to ee$ data events as a function of (a) E_T and (b) η for different WPs [178].

5.3.1.3 Electron Charge Identification

The electric charge of an electron is identified through the curvature of its associated tracks within the ID. However, misidentification can occur for two primary reasons. Firstly, electrons with high momentum have very slight track curvatures, which can lead to incorrect charge determination. Secondly, when an electron undergoes Bremsstrahlung, it can produce 'trident' electrons through electron-positron pair production, which may result in the misattribution of the track with an incorrect charge to the electron. Such background is named as Charge mis-assigned electrons (QmisID). The QmisID background can be further suppressed with an MVA discriminant based on Boosted Decision Trees (BDT) trained with the TMVA toolkit [180], known as Electron Charge ID Selector (ECIDS). The ECIDS is trained with data from $Z \to ee$ events using input variables, including observables from ID and EM calorimeter and their combined quantities [178]. Using data events instead of Monte Carlo (MC) simulation, used in the previous version of BDT [177], minimizes efficiency losses due to the mismodeling of input variables. The efficiency of BDT is 98% in the $Z \to ee$ events for electrons satisfying the Tight WPs. Figure 5.5 shows the charge misidentification probability with and without the BDT selection.

5.3.1.4 Electrons from Photon Conversion

Electrons originating from photon conversion can arise through internal or material conversions. Electrons can be produced at the hard-scattering level with photon radiation followed by the electron-positron pair production, referred to as internal conversions. Electrons can also originate from photon radiations that interact with the detector material, known as material conversions. These conversions can be selected as electrons due to the features from the ATLAS conversion reconstruction [181]. First, a conversion vertex is reconstructed if the radius of a pair of tracks containing at least seven hits in the silicon

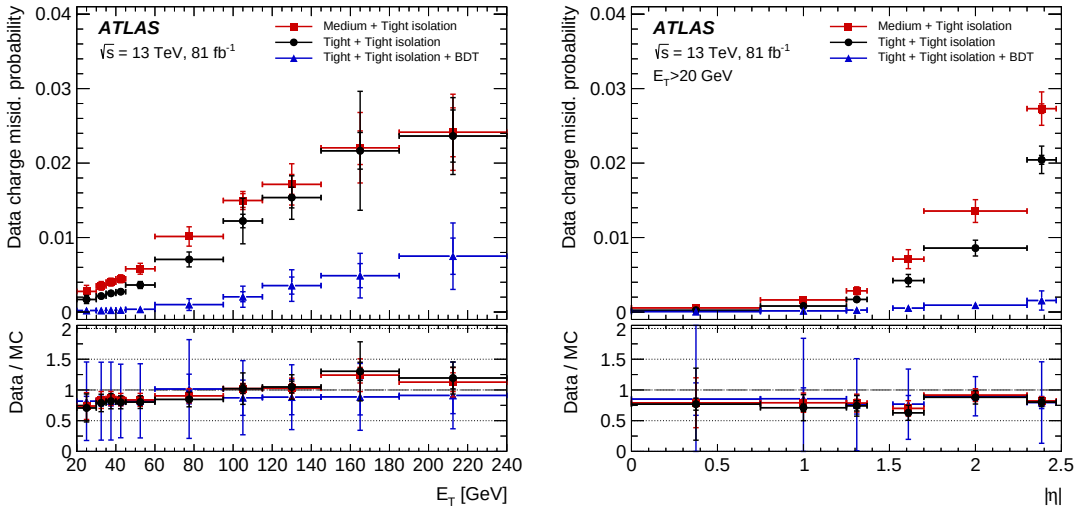

(a) (b)

Figure 5.5: Charge misidentification probabilities in $Z \to ee$ data as a function of (a) E_T and (b) $|\eta|$ [178].

pixel detector and best matched to the electron candidate is larger than 20 mm. The conversions with a radius less than 20 mm are considered electrons, whereas the internal conversion is likely to fall into this category. Secondly, the conversion candidates with two tracks are regarded as electrons when one track has a hit on the innermost silicon layer, and the other does not, where a hit is expected. This feature matches the properties of the material conversion. Therefore, the reconstruction and identification of these converted electrons are essential to reject these backgrounds.

The converted electrons tend to have more than one track associated with the cluster [51; 182]. The conversion can be reconstructed with this feature by pairing the electron best-match track and the second-best-match silicon track of opposite charge. An invariant mass of this track pair at the hard-scattering PV ($m_{trk,trk}$@PV) is calculated. This invariant mass identifies the internal conversions, providing a narrow peak from the reconstruction of massless photons from internal conversions. The $m_{trk,trk}$@PV distribution of material conversions is wider than that of internal conversions, given material conversions are not reconstructed at their actual vertices. Thus, another vertex is built as the

conversion vertex for material conversion by finding a point where two tracks are parallel in the transverse plane. An invariant mass of the track pair at the conversion vertex ($m_{trk,trk}$@CV) is calculated, which provides a narrow peak for the massless converted photons from material conversions. The radius of the conversion vertex (R_{CO}) is also used to separate the internal and material conversions. These observables are shown in Figure 5.6.

An additional photon conversion tagger is built to categorize events with electrons to be prompt leptons, internal conversions, and material conversions based on the conversion observables ($m_{trk,trk}$@PV, $m_{trk,trk}$@CV and R_{CO}). An electron is declared prompt lepton if a second track or conversion vertex is not found. An electron would be classified as from internal or material conversions if the second track and conversion vertex are found. The material conversion is first identified with $R_{CO} > 20$ mm and $m_{trk,trk}$@CV < 0.1 GeV. The internal conversion is defined as failing the material conversion selection and passing the selection with $m_{trk,trk}$@PV < 0.1. This allows a rejection of 40% of photon conversion in the electrons. The BSM $t\bar{t}t\bar{t}$ analysis directly uses the conversion variables ($m_{trk,trk}$@PV and $m_{trk,trk}$@CV), while the SM $t\bar{t}t\bar{t}$ analysis utilizes the photon conversion tagger to identify the converted electrons.

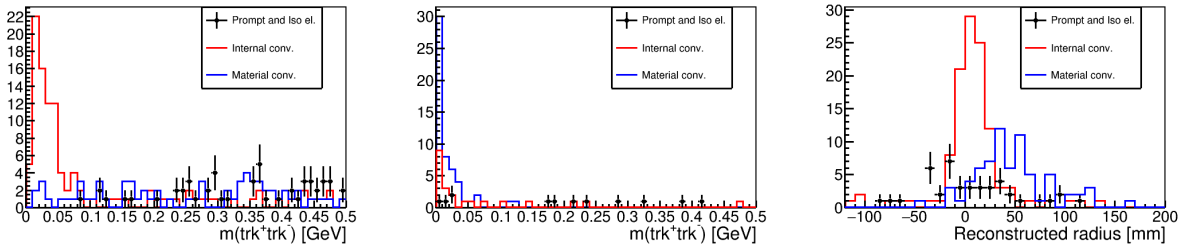

(a) $m_{trk,trk}$@PV (b) $m_{trk,trk}$@CV (c) R_{CO}

Figure 5.6: Conversion observables used to define the photon conversion tagger: (a) $m_{trk,trk}$@PV, (b) $m_{trk,trk}$@CV, and (c) R_{CO} [51; 182; 183].

5.3.2 Muons

5.3.2.1 Muon Reconstruction

The muon reconstruction is performed with various algorithms, taking information from the ID, calorimeters, and MS. Four types of muon reconstructions [172; 184] are shown below,

- Combined (CB) muon: The CB muon is the primary reconstruction method in ATLAS. Track reconstructions are performed independently in the ID and MS, followed by a global re-fit to form the combined track from hits in the MS and ID. The muons are reconstructed with the outside-in method as the default. The muons are first reconstructed in the MS and extrapolated to the ID. An inside-out method is used as the complementary method.

- Segment-tagged (ST) muons: The ST muons are used when the muon p_T is low or in the regions with low MS acceptance, where the muons only cross one layer of the MS chambers. The muon is reconstructed if the ID track matches at least one local track segment in the MDT or CSC chambers.

- Calorimeter-tagged (CT) muons: The CT muons are reconstructed for the region where the MS is partially instrumented due to the cabling and services of ID or calorimeters. The CT muons are reconstructed with an ID track matched to the energy deposit in the calorimeter compatible with a minimum-ionizing particle. This muon type is optimized for $|\eta| < 0.1$ and $15 < |p_T| < 100$ GeV.

- Extrapolated (ME) muons: The ME muon extends the MS acceptance in $2.5 < |\eta| < 2.7$, where no ID is available. The ME muons are reconstructed only with MS tracks with loose requirements to be compatible with originating from the IP.

The overlaps between these four muon types are resolved before forming the muon collections for physics analyses.

5.3.2.2 Muon Identification

Muon identification [172; 184] is performed to select the prompt leptons with high efficiency and ensure a robust momentum measurement. Muons are identified with several quality requirements to suppress backgrounds from pion and kaon decays. Muon candidates from the in-flight hadron decays can be characterized by the reconstructed track's distinctive 'kink' topology. This results in the incompatibility of the track's momentum measured in the ID and MS and a poor fit quality of the combined track. The identification utilizes the ID and MS track quantities to discriminate the prompt muons from the backgrounds shown below for CB muons:

- q/p significance is defined as

$$\frac{q}{p}\text{ significance} = \frac{\left|\frac{q}{p_{T,\mathrm{ID}}} - \frac{q}{p_{T,\mathrm{MS}}}\right|}{\sqrt{\sigma^2_{p_{T,\mathrm{ID}}} + \sigma^2_{p_{T,\mathrm{MS}}}}}, \tag{5.1}$$

  where $\frac{q}{p_{T,\mathrm{ID}}}$ ($\frac{q}{p_{T,\mathrm{MS}}}$) is the ratio of the charge and momentum of the muons measured in the ID and MS, and $\sigma_{p_{T,\mathrm{ID}}}$ ($\sigma_{p_{T,\mathrm{MS}}}$) is the corresponding uncertainty.

- ρ' is defined as

$$\rho' = \frac{p_{T,\mathrm{ID}} - p_{T,\mathrm{MS}}}{p_{T,\mathrm{CB}}}, \tag{5.2}$$

  where the $p_{T,\mathrm{ID}}$ ($p_{T,\mathrm{MS}}$) is the p_T measured in the ID (MS), and $p_{T,\mathrm{CB}}$ is the p_T of the combined track.

- Normalized χ^2 of the combined track fit.

- Number of hits in ID and MS.

Three major WPs are available for physics analysis: Loose, Medium, and Tight. The Loose WP, designed for analyses with multiple leptons, is optimized to maximize the reconstruction efficiency with less purity. The Tight WP maximizes prompt muons' purity and limits the non-prompt muon background. The Medium WP is optimized to minimize systematic uncertainties and balances efficiency and purity. The Medium WP is the default selection for muons in ATLAS. Figure 5.7 shows the reconstruction and identification efficiencies with different WPs.

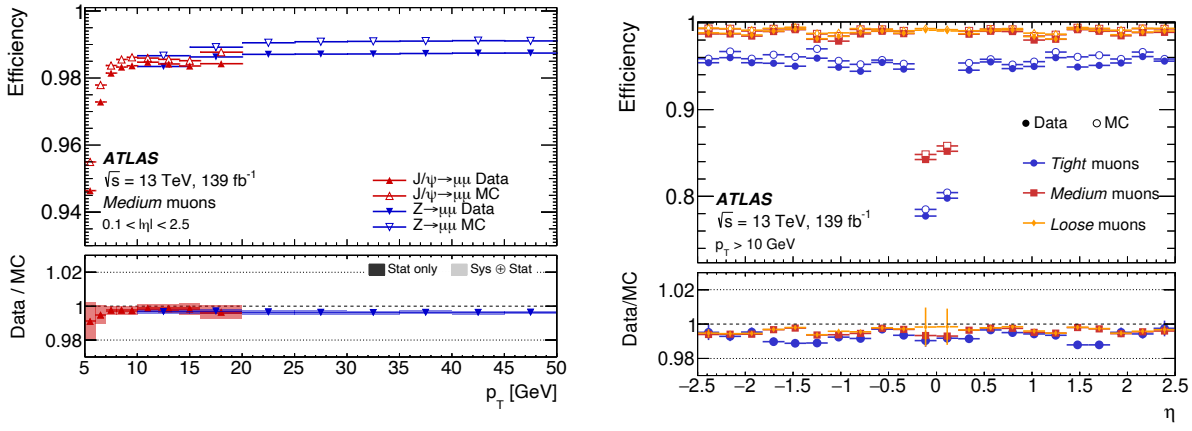

(a) (b)

Figure 5.7: Efficiencies of muon reconstruction and identification for Loose, Medium, and Tight criteria as a function of (a) p_T and (b) η [184]. The efficiencies are evaluated using (a) both $J/\Psi \to \mu\mu$ and $Z \to \mu\mu$, and (b) $Z \to \mu\mu$ events. The predicted efficiencies are illustrated as open markers, while filled markers show the measured results from the collision data.

5.3.3 Lepton Isolation

The lepton isolation [172; 178; 184; 185] measures the detector activity around leptons. Both eletron and muon isolations are based on a track-based isolation variable ($p_T^{\text{varconeXX}}$) and a calorimeter-based isolation variable ($E_T^{\text{topoconeXX}}$), where XX refers to the cone size. The $p_T^{\text{varconeXX}}$ is the scalar sum of the p_T of the selected tracks with $p_T > 1$ GeV within a variable cone size ΔR around the lepton, excluding the lepton itself. The variable ΔR

is defined as

$$\Delta R = \min\left(\frac{10}{p_T[\text{GeV}]}, \Delta R_{\text{max}}\right), \tag{5.3}$$

where ΔR_{max} is the maximum cone size, defined by XX in the variable name. This cone size is chosen to be p_T-dependent to improve the performance of lepton with large p_T. The $p_T^{\text{varconeXX}}$ is primarily independent of the pile-up effects due to the track rejection from pile-up or large d_0 relative to PV. The $E_T^{\text{topoconeXX}}$ is the sum of the E_T of topological cell clusters around the lepton in ΔR, with subtraction of the contribution from the lepton itself and the correction for pile-up effects. The BSM $t\bar{t}t\bar{t}$ analysis uses the Tight WP, defined in Table 5.1.

Isolation WP	Definition	Lepton
FixedCutTight	$p_T^{\text{varcone20}}/p_T < 0.06, E_T^{\text{topocone20}}/p_T < 0.06$	e
FixedCutTightTrackOnly	$p_T^{\text{varcone30}}/p_T < 0.06$	μ

Table 5.1: Definitions of the lepton isolation used in the BSM $t\bar{t}t\bar{t}$ analysis [172; 178; 184; 185].

An MVA discriminant, the prompt lepton BDT, is developed for the $t\bar{t}H$ measurement [182] to reject the non-prompt lepton backgrounds. An improved version of the BDT discriminant, Prompt Lepton Improved (PLImproved) BDT, is studied for electrons and muons [148; 186]. Three BDT are trained for muons, eletrons in barrel region ($|\eta| < 1.37$) and eletrons in end-cap region ($|\eta| > 1.37$). The $t\bar{t}$ MC simulation is used for the prompt and non-prompt lepton samples. The input variables for BDT include information related to the lepton-track relationship, isolation variables, lifetime variables, and lepton p_T bin number. The lepton p_T bin number parameterizes the p_T dependence of the BDT. The PLImproved WPs (PLImprovedTight and PLImprovedVeryTight) are defined with the prompt lepton BDT cuts in bins of lepton p_T. The PLImprovedTight trades off the prompt efficiency but provides better rejection of non-prompt lepton background than the FixedCutTight, defined in Table 5.1. The PLImprovedTight provides the prompt muons (barrel/end-cap electrons) with an efficiency of around 60% (60%/70%) for p_T around

20 GeV and reaching a plateau of 95% (95%/90%) for p_T around 40 (40/65) GeV. The corresponding rejection factor is defined as the reciprocal of the efficiency. The rejection factor against muons (electrons) from the b-hadron decays ranges from 33 to 50 (20 to 50) for the PLImprovedTight WP, depending on p_T and η [148]. The PLImprovedTight WP is used in the SM $t\bar{t}t\bar{t}$ analysis.

5.4 Jets

Given the nature of color confinement in QCD, quarks and gluons cannot be observed individually in detectors. They undergo the hadronization process, producing a narrow and collimated cone of color-neutral hadrons, known as a jet. The jet reconstruction [187] is performed by forming the topo-clusters from the calorimeter cells using a nearest-neighbor algorithm at the EM scale [179], referred to as EMTopo jets. An additional particle flow (PFlow) algorithm [187] was introduced by combining the information from ID and calorimeter systems for the jet reconstruction. The energy deposited in the calorimeter by charged particles is subtracted from the topo-cluster calculation and replaced by the momenta of tracks matched to the topo-clusters. This results in the PFlow jets having improved energy and angular resolutions, reconstruction efficiency, and pile-up stability compared to EMTopo jets [179; 187]. The jets used in this dissertation are reconstructed with PFlow and anti-k_t algorithms [188] using a radius parameter $R = 0.4$.

Jets are reconstructed at the energy of the EM scale, which does not accurately account for the energy scale of hadronic interactions. To correct the reconstructed jets to have a reasonable energy scale to that of jets reconstructed at the particle level, a jet energy scale (JES) calibration [189] is performed. A sequence of the calibrations is taken, as shown in Figure 5.8. In addition, the jet energy resolution (JER) calibration is also performed to match the jet resolution in simulation to data with dijet events [190].

Pile-up interactions are often reconstructed as jets in the final states. However, these

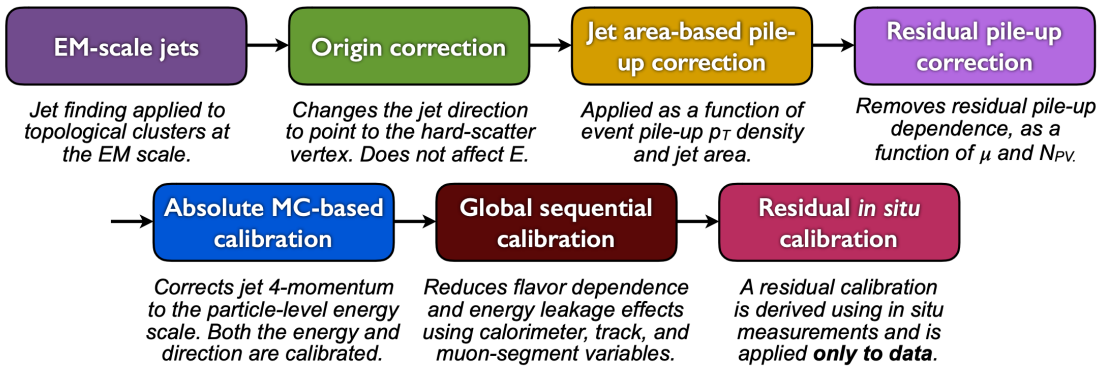

Figure 5.8: The JES calibration procedure for the EM-scale jets [189].

jets are not associated with the hard-scattering PV. A jet vertex tagger (JVT) algorithm [191] is introduced to discriminate the hard-scattering and pile-up jets. The JVT uses two-dimensional likelihood with observables built from tracking information associated with the reconstructed jet from PV or pile-up interactions. The JVT is applied to reconstructed jets with $p_T < 60$ GeV and $|\eta| < 2.4$ in both SM and BSM $t\bar{t}t\bar{t}$ analyses in this dissertation.

5.4.1 Flavor Tagging

The jets containing HF hadrons, including b- and c-hadrons, likely originate from the hadronization of the b and c quarks, known as b-jets and c-jets, respectively. On the other hand, the jets arising from the light-flavor (LF) quarks are referred to as light-flavor jets (or simply light jets). Identifying b-jets and c-jets is called 'flavor tagging'. The flavor tagging is essential to many aspects of the physics programs in the ATLAS experiment. For example, the leading Higgs boson decay mode is the $H \to b\bar{b}$ channel, or the top quark decays to a W boson and a b quark with a branching ratio of almost 100%. The production with final states, including c quarks, has a small cross section or branching ratio. However, the identification of c-jet plays a vital role in the $H \to c\bar{c}$ measurement.

The b- and c-hadrons have a larger mass, higher decay multiplicity of b- and c-hadrons, longer lifetime, and intrinsic properties of heavy-quark fragmentation. The typical life-

time of b-hadron is about 1.5 ps ($\langle c\tau \rangle \approx 450\ \mu m$), which leads to at least one vertex displaced by a few mm from the hard-scattering PV for b-jets with $p_T > 20$ GeV. Various low-level flavor tagging algorithms are designed to reconstruct the characteristic features of b-jets [192]. These algorithms use the information from impact parameters of the tracks originating from the b-hadron decays [193], track impact parameters with Recurrent Neural Network (RNN) [194], secondary vertex reconstruction [195], reconstruction of b- and c-hadron entire decay chains [196]. The outputs of these low-level algorithms are further fed into deep-learning classifiers with multi-layer feed-forward neural networks (NNs), referred to as the DL1r algorithm. The DL1r classifier has 3-dimensional outputs corresponding to the probabilities for a jet to be a b-jet (p_b), a c-jet (p_c), or a light jet (p_{light}). The final DL1r b-tagging discriminant output is defined as

$$D_{\text{DL1r}} = \ln\left(\frac{p_b}{\sqrt{f_c \cdot p_c + (1 - f_c) \cdot p_{\text{light}}}}\right), \tag{5.4}$$

where f_c is the c-jet fraction in the background. The f_c is optimized with a posteriori ($f_c = 0.018$) [192] to ensure good rejection factors for both c-jet and light jets in a considerable b-tagging efficiency (ϵ_b) range across several analyses, such as $VH, H \to b\bar{b}$ [197] and $t\bar{t}H, H \to b\bar{b}$ [198] measurements. Figure 5.9 shows the raw output of p_b and final DL1r b-tagging discriminant output. The DL1r has a higher efficiency and better rejection of the c-jets and light jets than the previous ATLAS MV2 b-tagging algorithm [199]. Figure 5.10 presents the comparisons between DL1r and MV2 algorithms.

The flavor tagging is available for the jets with $p_T > 20$ GeV and $|\eta| < 2.5$. Different WPs are provided based on the selections of the DL1r final discriminant. These include the WPs with average b-jet efficiencies of 60%, 70%, 77%, and 85%. Figure 5.11 shows the b-jet efficiency and background rejections with different WPs. In addition, pseudo-continuous b-tagging (PCBT) scores are defined to provide dedicated information to quantify how likely the jet is a b-jet by giving an integer score to the jet. A jet is assigned a score of

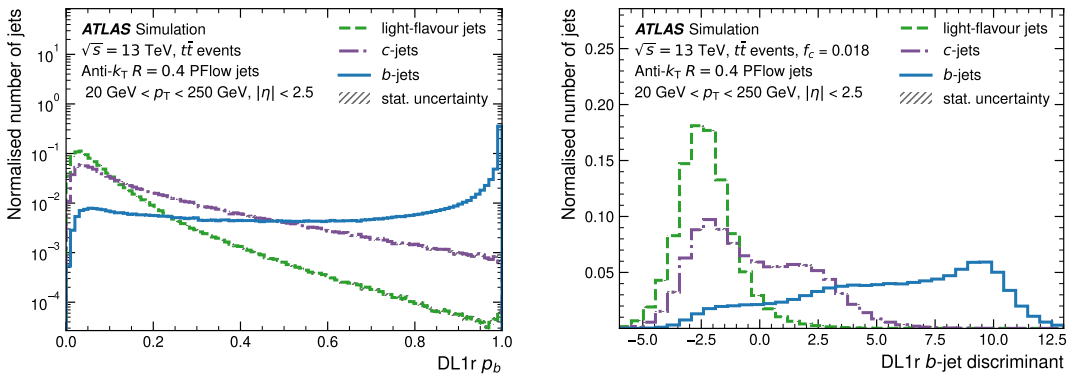

(a) DL1r p_b (b) DL1r b-tagging discriminant

Figure 5.9: Distributions of (a) DL1r p_b output and (b) final DL1r b-tagging discriminant for b-jets, c-jets, and light jets in the $t\bar{t}$ simulated sample [192].

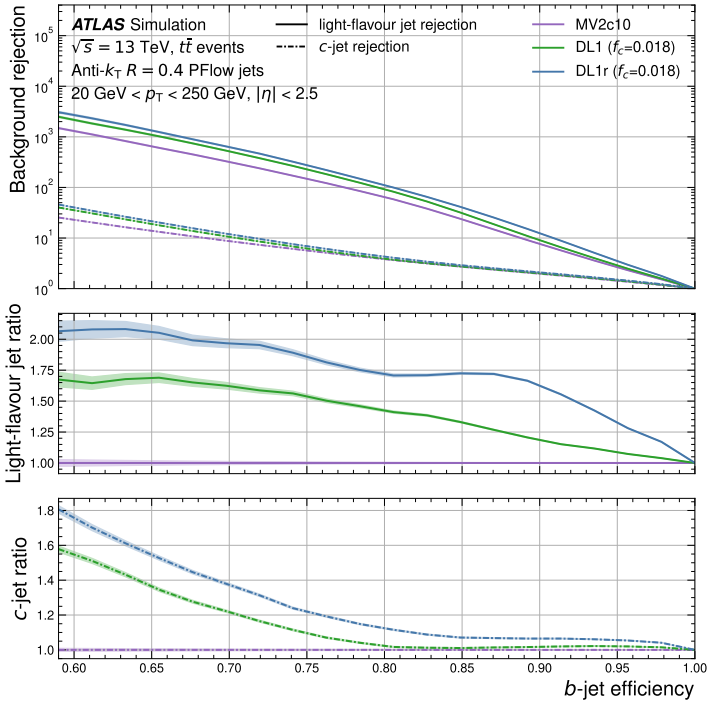

Figure 5.10: The light-jet and c-jet rejection factors as a function of b-jet efficiency for different high-level b-tagging algorithms. The lower two panels show the ratio of the light-jet rejection and c-jet rejection of the algorithms to the MV2 algorithms [192].

five, four, three, two, and one if the jet passes a b-tagging WP of 60%, 70%, 77%, 85%, and none of WP, respectively. Both SM and BSM $t\bar{t}t\bar{t}$ analyses optimize the choices of the WP and use 77% as the WP to define b-tagged jets. In addition, both analyses utilize the PCBT scores in the MVA.

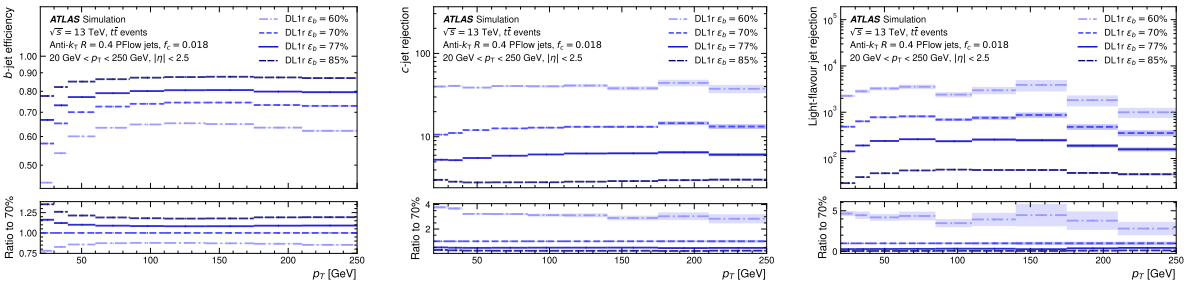

(a) (b) (c)

Figure 5.11: The (a) b-tagging efficiency, as well as (b) c-jet and (c) light-jet rejection factors as a function of jet p_T [192].

Additional calibrations for the flavor tagging are required due to the imperfect description of the detector response and physics modeling effects in MC simulation. Two efficiencies are measured to calibrate the difference between data and MC simulations [200] and between MC simulations with different configurations [201]. The calibration measures the b-jet efficiency with data using events enriched with $t\bar{t}$ dilepton decays. The events are further categorized into different bins of p_T of the two jets, invariant masses ($m_{j1,\ell}$ and $m_{j2,\ell}$) of the lepton and jet which are paired to be from the same top decay, and DL1r b-tagging discriminant. A log-likelihood function is built with control and signal regions to simultaneously estimate the b-tagging probabilities and flavor compositions. The scale factors (SFs), defined as the efficiency ratio between data and MC simulation ($\text{SF} = \epsilon_{\text{data}}/\epsilon_{\text{MC}}$), are derived in bins of p_T and η. The p_T ranges of calibration are different for b-jet, c-jet, and light-jet tagging: $20 \leq p_T \leq 400$ GeV for b-jets, $20 \leq p_T \leq 250$ GeV for c-jets, $20 \leq p_T \leq 300$ GeV for light jets. The SFs are then applied to the MC simulations on a per-jet basis in the physics analysis. Figure 5.12 shows the SFs for

b-tagging efficiency, c-jet mistag rate, and light-jet mistag rate.

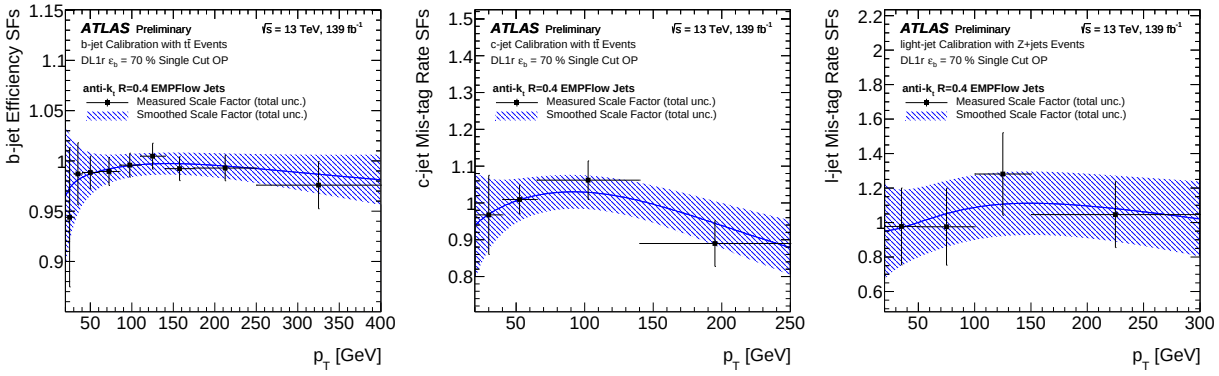

(a) (b) (c)

Figure 5.12: The data/MC SFs for (a) b-tagging efficiency, (b) c-jet mistag rate, and (c) light-jet mistag rate of the DL1r tagger with PFlow jets using 70% WP. The calibration is performed with $t\bar{t}$ simulated events for b-tagging efficiency and c-jet mistag rate and with Z boson + jets simulated events for light-jet mistag rate [192; 202].

5.5 Missing Transverse Momentum

At the LHC, the proton beams collide in opposite directions along the z direction of the ATLAS coordinate. Because of the momentum conservation, the momenta of all final state particles should be conserved in the transverse plane to the beam axis. Therefore, the vector sum of the momenta of all particles in the transverse plane should be zero. A momentum imbalance can be produced due to invisible particles, which are not detectable by the ATLAS detectors. The known invisible particles in the SM are neutrinos, which are charge-neutral and only interact through weak interaction. Potential momentum imbalance can also arise from the unknown new particles introduced by the BSM. This momentum imbalance is reconstructed as the missing transverse momentum (E_T^{miss}).

The reconstruction of E_T^{miss} [203] is performed by calculating the missing p_T with the calibrated objects in the detectors. These objects include electrons, photons, muons, hadronically decaying τ leptons, and jets. The x and y components of missing transverse

momentum vector ($\vec{E}_T^{miss}$) are defined as

$$E_{x(y)}^{\text{miss}} = E_{x(y)}^{\text{miss},e} + E_{x(y)}^{\text{miss},\gamma} + E_{x(y)}^{\text{miss},\mu} + E_{x(y)}^{\text{miss},\tau} + E_{x(y)}^{\text{miss,jets}} + E_{x(y)}^{\text{miss,soft}}, \tag{5.5}$$

where the terms are calculated as the negative vectorial sum of p_T of the calibrated objects. Additional soft term ($E_{x(y)}^{\text{miss,soft}}$) is included to account for the reconstructed tracks originating from hard-scattering PV that are not associated with the reconstructed objects. The $\vec{E}_T^{miss}$ can be further separated as two terms, the magnitude (E_T^{miss}) and azimuthal angle ϕ^{miss}, which are defined as

$$E_T^{\text{miss}} = \sqrt{(E_x^{\text{miss}})^2 + (E_y^{\text{miss}})^2}, \tag{5.6}$$

$$\phi^{\text{miss}} = \arctan\left(E_y^{\text{miss}}/E_x^{\text{miss}}\right). \tag{5.7}$$

Due to the uses of reconstructed objects to reconstruct E_T^{miss}, several factors can also impact the E_T^{miss}, such as the detector noise, detector mismodeling, the coverage of the detector, or the miscalibration of the reconstructed objects.

5.6 Overlap Removal

An overlap removal procedure is employed to avoid the same calorimeter energy deposit or the same track being reconstructed as different objects in the same event. Table 5.2 summarizes the sequence of criteria applied to remove objects. This method is used in all analyses shown in this dissertation.

Reject	Against	Criteria
Electron	Electron	Shared track, $p_{\mathrm{T},1} < p_{\mathrm{T},2}$
Muon	Electron	Is CT Muon and shared ID track
Electron	Muon	Shared ID track
Jet	Electron	$\Delta R < 0.2$
Electron	Jet	$\Delta R < 0.4$
Jet	Muon	Number of tracks < 3 and (ghost-associated or $\Delta R < 0.2$)
Muon	Jet	$\Delta R < \min(0.4, 0.04 + 10\ \mathrm{GeV}/p_T(\mu))$

Table 5.2: Overlap removal procedure used in the analyses of this dissertation. The procedure starts from the top to the bottom.

CHAPTER VI

Common Features for the Same-sign Dilepton and Multilepton Final States

This chapter discusses common elements for the SSML final states used in SM and BSM $t\bar{t}t\bar{t}$ analyses[1]. The two analyses largely share the same strategy with subtle differences because they target the same phase space in the SSML final states. The same trigger selections used in both analyses are shown in Section 6.1. The physics processes can be categorized into signal and background in an analysis. The signal is the physics process of interest in an analysis, while the backgrounds are the other physics processes that can produce the same final states. Both analyses share the same background processes, and mostly the same MC simulations are used to describe these backgrounds. Section 6.2 summarizes the common MC simulations. Moreover, the same data-driven approach is used in the background estimation strategy for mis-reconstructed or misidentified leptons. Section 6.3 describes common approaches for background estimations. In addition, the two analyses share the common sources of systematic uncertainties. Section 6.4 introduces the configurations of systematic uncertainties. Finally, both analyses utilize statistical methods to quantify the consistency between observed data and theoretical predictions. Section 6.5 presents the statistical methods used in both analyses.

[1]The 2HDM+a combination analysis reinterprets the BSM $t\bar{t}t\bar{t}$ analysis using the same strategy, so the following sections will only focus on the setups in the SM and BSM $t\bar{t}t\bar{t}$ analyses.

6.1 Trigger Selection

The SM and BSM $t\bar{t}t\bar{t}$ analyses use the same HLT strategy following $t\bar{t}t\bar{t}$ evidence analysis [52]. Single lepton and dilepton triggers are used in both analyses. Table 6.1 summarizes the HLT triggers in the different data periods. A matching between online objects firing the trigger and the offline reconstructed object is required. The trigger efficiency uncertainties are summarized in Section 6.4.1.

Trigger name	Data periods			
	2015	2016	2017	2018
Single electron triggers				
e24_lhmedium_L1EM20VH	✓	-	-	-
e26_lhtight_nod0_ivarloose	-	✓	✓	✓
e60_lhmedium	✓	-	-	-
e60_lhmedium_nod0	-	✓	✓	✓
e120_lhloose	✓	-	-	-
e140_lhloose_nod0	-	✓	✓	✓
Single muon triggers				
mu20_iloose_L1MU15	✓	-	-	-
mu26_ivarmedium	-	✓	✓	✓
mu50	✓	✓	✓	✓
Di-electron triggers				
2e12_lhloose_L12EM10VH	✓	-	-	-
2e17_lhvloose_nod0	-	✓	-	-
2e17_lhvloose_nod0_L12EM15VHI	-	-	-	✓
2e24_lhvloose_nod0	-	-	✓	✓
Di-muon triggers				
2mu10	✓	-	-	-
2mu14	-	✓	✓	✓
mu18_mu8noL1	✓	-	-	-
mu22_mu8noL1	-	✓	✓	✓
Electron-muon triggers				
e7_lhmedium_mu24	✓	-	-	-
e7_lhmedium_nod0_mu24	-	✓	✓	✓
e17_lhloose_mu14	✓	-	-	-
e17_lhloose_nod0_mu14	-	✓	✓	✓

Table 6.1: List of single lepton and dilepton HLT triggers used in the analyses per data period. A logical OR is used for a given data period year.

6.2 Monte Carlo Simulation

MC simulations [204] rely on random sampling to produce the possible output following certain probability density functions. The MC simulations provide a statistical framework to model the physics of the *pp* collisions. The MC simulations of the physics processes from *pp* collisions can be broken down into a few parts: matrix element (ME), PDF, PS, and hadronization, UE, and detector response simulation.

The ME describes dynamical information of the physics process from particle interactions. The squared matrix element provides the probability density function of a given physics process. The matrix element of a physics process in an available phase space describes the partonic cross section under QCD perturbation theory. The ME MC generators use the complete matrix element to offer reliable physics descriptions in the perturbative QCD regime. These generators include MadGraph5_aMC@NLO [205] and PowhegBox [206–208]. They are integrated with different PDF sets, described in Section 3.1.2.1, to describe the probability of interacting with specific partons from a proton. Three PDF sets are commonly used: CTEQ [108], MSTW2008 [109], and NNPDF [110]. In this dissertation, the samples are produced with the NNPDF sets.

Collinear and soft emissions are the so-called parton showers. Fragmentation or hadronization refers to the process that quarks and gluons turn into colorless hadrons. The PS generator is designed to describe the collinear and soft emissions of the radiative process following the primary process. The PS algorithm is further integrated with the ME calculation via jet matching and merging techniques to prevent double counting in the multi-jet phase space. There are three General-purpose Monte Carlo (GPMC) generators providing both the ME calculation and computations of PS and UE [204]: Herwig [209–211], Pythia [212; 213], and Sherpa [214; 215]. The Herwig and Pythia are commonly used as PS generators only, combined with the ME generators such as MadGraph5_aMC@NLO and PowhegBox. This is most of the cases in this dissertation.

On the other hand, SHERPA is commonly used to provide both the ME and PS calculations.

The PS generator models contain several free parameters when modeling the PS, hadronization, and UE. These parameters are tuned to experimental data with the observables sensitive to the PS, hadronization, and UE physics. The ATLAS experiment provides a standalone tune for PYTHIA8, 'A14' tune, with different PDF sets [216]. Default tunes are provided by HERWIG [211], named as H7UE, and SHERPA [214; 215].

Generated MC events are processed with GEANT4 [217; 218] or ATLFAST2 [219] to simulate the geometry and response of the ATLAS detector. This allows the MC simulations to have the correct description and to compare with the real data observed in the ATLAS detector. The detector simulation with GEANT4 is known as the 'full simulation', and it provides the complete description of the ATLAS detector. However, the full simulations with GEANT4 take a huge amount of computational time. The ATLFAST2 algorithm, known as AF2, had been developed to provide faster detector simulation with reasonable precision and accuracy. After the detector simulations, MC events are further processed by the reconstruction algorithms, described in Chapter V. Finally, theoretical cross sections are used to normalize the simulated MC events to describe the physics processes in the analyses. Table 6.2 summarizes the MC generator configurations used in the analyses of this dissertation. The following sections discuss the MC simulations of the SM processes used in both analyses. The BSM signal samples ($t\bar{t}H/A \to t\bar{t}t\bar{t}$ and $t\bar{t}(H/A/a) \to t\bar{t}t\bar{t}$) are discussed in Section 8.1 and Section 9.1, respectively.

6.2.1 $t\bar{t}t\bar{t}$

The $t\bar{t}t\bar{t}$ production is simulated using MADGRAPH5_AMC@NLO 2.6.2 at NLO in QCD with NNPDF3.1NLO PDF set. The μ_R and μ_F scales are set to $m_T/4$, with m_T being the scalar sum of the transverse mass ($\sqrt{m^2 + p_T^2}$) of the particles generated from the ME [123]. Top quark decays are simulated at LO with MADSPIN, preserving spin

Process	Generator	ME order	PDF	PS	Tune	Detector	Analysis
$t\bar{t}H/A \to t\bar{t}t\bar{t}$	MadGraph5	LO	NNPDF3.1LO	Pythia8	A14	AF2	BSM $t\bar{t}t\bar{t}$
$t\bar{t}(H/A/a) \to t\bar{t}t\bar{t}$	MadGraph5	LO	NNPDF3.0NLO	Pythia8	A14	AF2	2HDM+a
$t\bar{t}t\bar{t}$	MadGraph5_aMC@NLO	NLO	NNPDF3.1NLO	Pythia8	A14	AF2	Both
	(MadGraph5_aMC@NLO)	(NLO)	(NNPDF3.1NLO)	(Herwig7)	(H7UE)	(AF2)	Both
	(Sherpa 2.2.10)	(NLO)	(NNPDF3.0NNLO)	(Sherpa)	(Sherpa)	(Full)	BSM $t\bar{t}t\bar{t}$
	(Sherpa 2.2.11)	(NLO)	(NNPDF3.0NNLO)	(Sherpa)	(Sherpa)	(Full)	Both
	(MadGraph5)	(LO QCD)	(NNPDF3.1LO)	(Pythia8)	(A14)	(AF2)	Both
$t\bar{t}t\bar{t}$ κ_t	MadGraph5	LO	(NNPDF3.1LO)	Pythia8	A14	AF2	SM $t\bar{t}t\bar{t}$
$t\bar{t}t\bar{t}$ EFT	MadGraph5	LO	(NNPDF3.1LO)	Pythia8	A14	AF2	SM $t\bar{t}t\bar{t}$
$t\bar{t}t$	MadGraph5	LO in 5 FS	NNPDF2.3LO	Pythia8	A14	Full	SM $t\bar{t}t\bar{t}$
	(MadGraph5)	(LO in 4 FS)	(NNPDF2.3LO)	(Pythia8)	(A14)	(Full)	BSM $t\bar{t}t\bar{t}$
$t\bar{t}W$	Sherpa 2.2.10	MEPS@NLO	NNPDF3.0NNLO	Sherpa	Sherpa	Full	Both
	(MadGraph5_aMC@NLO)	(NLO)	(NNPDF3.0NLO)	(Pythia8)	(A14)	(Full)	BSM $t\bar{t}t\bar{t}$
	(MadGraph5_aMC@NLO)	(FxFx)	(NNPDF2.3LO)	(Pythia8)	(A14)	(Full)	SM $t\bar{t}t\bar{t}$
$t\bar{t}W$ EW	Sherpa 2.2.10	LO	NNPDF3.0NNLO	Sherpa	Sherpa	Full	Both
	(MadGraph5)	(LO)	(NNPDF2.3LO)	(Pythia8)	(A14)	(Full)	Both
$t\bar{t}Z/\gamma^*$	[MadGraph5_aMC@NLO]	[NLO]	[NNPDF3.0NLO]	[Pythia8]	[A14]	[Full/AF2]	Both
	Sherpa 2.2.1	MEPS@NLO	NNPDF3.0NNLO	Sherpa	Sherpa	Full	BSM $t\bar{t}t\bar{t}$
	(Sherpa 2.2.11)	(MEPS@NLO)	(NNPDF3.0NNLO)	(Sherpa)	(Sherpa)	(Full)	SM $t\bar{t}t\bar{t}$
$t\bar{t}H$	PowhegBox	NLO	NNPDF3.0NLO	Pythia8	A14	Full	Both
	(PowhegBox)	(NLO)	(NNPDF3.0NLO)	(Herwig7)	(H7UE)	(Full)	SM $t\bar{t}t\bar{t}$
	(MadGraph5_aMC@NLO)	(NLO)	(NNPDF3.0NLO)	(Pythia8)	(A14)	(Full)	Both
$t\bar{t}$	PowhegBox	NLO	NNPDF3.0NLO	Pythia8	A14	Full	Both
tW	PowhegBox	NLO	NNPDF3.0NLO	Pythia8	A14	Full	Both
tWZ	MadGraph5_aMC@NLO	NLO	NNPDF3.0NLO	Pythia8	A14	Full	Both
tZq	MadGraph5	LO	NNPDF2.3LO	Pythia8	A14	Full	Both
$t\bar{t}VV$	MadGraph5	LO	NNPDF2.3LO	Pythia8	A14	AF2	Both
$t\bar{t}HH$	MadGraph5	LO	NNPDF2.3LO	Pythia8	A14	AF2	Both
V	Sherpa 2.2.1	MEPS@NLO	NNPDF3.0NNLO	Sherpa	Sherpa	Full	Both
VV,VVV	Sherpa 2.2.2	MEPS@NLO	NNPDF3.0NNLO	Sherpa	Sherpa	Full	Both
VH	Pythia8	LO	NNPDF23LO	Pythia8	A14	Full	Both

Table 6.2: Summary of the MC generator configurations used in SM $t\bar{t}t\bar{t}$, BSM $t\bar{t}t\bar{t}$, and 2HDM+a combination analyses. The 2HDM+a combination analysis uses exactly the same MC generators as BSM $t\bar{t}t\bar{t}$ except for the additional signal samples. The samples with parentheses are used to estimate the systematic uncertainties, while those with brackets are used as either nominal or alternative samples for systematic uncertainties in different analyses. The symbol V refers to an EW boson (W or Z/γ^*). The ME order refers to the order in QCD of the perturbative calculation. The FS is specified in $t\bar{t}t$ samples, to highlight the FS choice used in the PDF. The PDF used for the ME is shown in the table. Tune refers to the UE tune of the PS generator. The MEPS@NLO and FxFx refer to the methods used to match the ME to the PS in Sherpa [220–223] and in MadGraph5_aMC@NLO [224], respectively. Detector refers to the detector simulation, where 'Full' represents full simulation and 'AF2' represents ATLFAST2 simulation. The analysis column summarizes in which analyses the sample is used, where 'Both' stands for SM and BSM $t\bar{t}t\bar{t}$ analyses. The table is modified from Ref. [125].

Process	SM $t\bar{t}t\bar{t}$	BSM $t\bar{t}t\bar{t}$	Unit	Reference	Note
$t\bar{t}t\bar{t}$	11.97	11.97	fb	[123]	Inclusive
$t\bar{t}t$	1.67	1.64	fb	[125]	Inclusive
$t\bar{t}W$ QCD+EW	722.48	639.11	fb	[123; 137]	Inclusive
$t\bar{t}Z$	878.30	878.30	fb	[117]	Inclusive
$t\bar{t}H$	507.01	507.01	fb	[117]	Inclusive
$t\bar{t}$	831.77	831.77	pb	[109; 225–236]	Inclusive
tW	71.71	71.71	pb	[237–239]	Inclusive
tWZ	16.05	16.05	fb	[205; 239]	Leptonic Z-boson decay
tZq	240.37	240.37	fb	[205]	Non all-hadronic decays
$t\bar{t}ZZ$	1.83	1.83	fb	[117]	Inclusive
$t\bar{t}WW$	9.88	9.88	fb	[117]	Inclusive
$t\bar{t}WZ$	3.90	3.90	fb	[117]	Inclusive
$t\bar{t}HH$	0.75	0.75	fb	[117]	Inclusive
$t\bar{t}WH$	1.58	1.58	fb	[117]	Inclusive
V	240.86	240.86	nb	[111; 240; 241]	Inclusive
VV	40.03	40.03	pb	[242]	Non all-hadronic decays
VVV	14.88	14.88	fb	[242]	Only leptonic decays
VH	2.25	2.25	fb	[117]	Inclusive

Table 6.3: Summary of cross sections used in the SM and BSM $t\bar{t}t\bar{t}$ analyses.

correlations. Events are interfaced with PYTHIA8.2 for PS and hadronization, using A14 tune and NNPDF2.3LO PDF.

An alternative sample is produced by using the alternative HERWIG7.04 showering model with the H7UE tune and NNPDF3.1NLO to evaluate PS and hadronization effects. For generator uncertainty, $t\bar{t}t\bar{t}$ events are simulated at NLO in QCD using SHERPA 2.2.11 with NNPDF3.0NNLO PDF for SM $t\bar{t}t\bar{t}$ analysis and SHERPA 2.2.10 for BSM $t\bar{t}t\bar{t}$ analysis. The μ_R and μ_F scales are set to $H_T/2$, where H_{T} is the scalar sum of the transverse momentum of all final state particles. SHERPA 2.2.11 $t\bar{t}t\bar{t}$ sample includes EW contributions (LO2+LO3+NLO2) [123], but only part of EW NLO2 is remained due to cancellations. EW contribution is considered as an additional uncertainty in the BSM $t\bar{t}t\bar{t}$ analysis but omitted in the SM $t\bar{t}t\bar{t}$ analysis due to negligible impact.

An additional $t\bar{t}t\bar{t}$ sample is generated at LO in QCD using MADGRAPH5 with the same configuration as the nominal sample to prevent negative weights in the MVA training. Additional samples are produced to simulate BSM effects, such as various non-SM Higgs-top Yukawa couplings (denoted as $t\bar{t}t\bar{t}$ κ_t) and EFT operators (denoted as $t\bar{t}t\bar{t}$ EFT). The EFT operators include four-fermion and Higgs oblique parameters. Different Universal FeynRules Output (UFO) models [243] are implemented in MADGRAPH5 with FeynRules [243; 244] to simulate the BSM physics. The $t\bar{t}t\bar{t}$ κ_t sample is simulated with the Higgs Characterization model [245]. The $t\bar{t}t\bar{t}$ EFT samples are generated with the SMEFT@NLO model [246] and the Higgs oblique UFO model [92]. These BSM samples are produced with MADGRAPH5 at LO in QCD with NNPDF3.1LO. Events are showered by PYTHIA8 with A14 tune and NNPDF2.3LO.

6.2.2 $t\bar{t}t$

The $t\bar{t}t$ production, including $t\bar{t}tW$ and $t\bar{t}tq$, is modeled using MADGRAPH5 at LO in QCD with NNPDF3.0NLO. Two samples are produced in 4FS and 5FS, discussed in Section 3.2.2.2. The simulated events are showered using PYTHIA8 with A14 tune

and NNPDF2.3LO. The μ_R and μ_F scales are set to the default choice in MADGRAPH5, which is the transverse mass of the $2 \to 2$ system resulting from the k_t clustering algorithm [247]. The BSM $t\bar{t}t\bar{t}$ analysis uses the 4FS $t\bar{t}t$ with a cross section from MADGRAPH5. The SM $t\bar{t}t\bar{t}$ analysis utilizes the 5FS $t\bar{t}t$ to prevent the overlap with $t\bar{t}t\bar{t}$ at LO. The $t\bar{t}tW$ and $t\bar{t}tq$ are normalized to cross sections of 1.02 fb and 0.65 fb, respectively, calculated at NLO in QCD with MADGRAPH5_AMC@NLO using $H_T/2$ dynamical scales and NNPDF2.3NLO [125].

6.2.3 $t\bar{t}W$

The $t\bar{t}W$ production process is simulated with SHERPA 2.2.10 at NLO in QCD with NNPDF3.0NNLO, including up to one extra parton at NLO and two at LO, matched and merged with PS based on Catani-Seymour dipole factorization [222] in SHERPA. MEPS@NLO prescription [223; 248–250] with a 30 GeV merging scale is used. The virtual QCD correction for ME at NLO is provided by OpenLoops [220; 251; 252]. The μ_R and μ_F scales are set to $m_T/2$. The cross section is predicted to be 597 fb from sample production.

Higher-order corrections [215; 253; 254] are included as internal weights, combining NLO in QCD and EW contributions (NLO2+LO3) following Ref. [137]. A separate SHERPA 2.2.10 sample at LO covers sub-leading EW NLO3 corrections, presenting a cross section of 42.1 fb. The $t\bar{t}W$ sample in BSM $t\bar{t}t\bar{t}$ analysis includes NLO in QCD and sub-leading EW NLO3 corrections, with a cross section of 639.11 fb. The $t\bar{t}W$ sample in SM $t\bar{t}t\bar{t}$ analysis includes NLO in QCD and higher-order corrections (NLO2+LO3+NLO3), normalized to 722 fb calculated with hard non-logarithmically enhanced radiation at NLO in QCD [137].

Systematic models vary between SM and BSM $t\bar{t}t\bar{t}$ analyses, with separate samples covering generator differences at NLO in QCD and sub-leading EW NLO3 corrections. The BSM $t\bar{t}t\bar{t}$ analysis uses an alternative $t\bar{t}W$ sample at NLO in QCD without additional partons using MADGRAPH5_AMC@NLO 2.3.3 and NNPDF3.0NLO. Events are inter-

faced with PYTHIA8.210 using A14 tune and NNPDF2.3LO. For the SM $t\bar{t}t\bar{t}$ analysis, a separate NLO $t\bar{t}W$ sample with up to one extra parton at NLO and up to two at LO is generated using MADGRAPH5_aMC@NLO, merged using the FxFx prescription [224] with a 30 GeV merging scale. Events are interfaced with PYTHIA8.210 using A14 tune and NNPDF2.3LO. Both analyses use MADGRAPH5 to simulate the $t\bar{t}W$+jets sample for EW NLO3 correction with NNPDF2.3LO, showered by PYTHIA8.2 using A14 tune and NNPDF2.3LO.

6.2.4 $t\bar{t}Z$ and $t\bar{t}H$

The $t\bar{t}Z/\gamma^*$ samples used for the SM and BSM $t\bar{t}t\bar{t}$ analyses are produced from different generators covering on-shell and off-shell Z and γ^* contributions with dilepton invariant mass ($m_{\ell\ell}$) exceeding 1 GeV. For the BSM $t\bar{t}t\bar{t}$ analysis, $t\bar{t}Z/\gamma^*$ for $m_{\ell\ell} > 5$ GeV is modeled with SHERPA 2.2.1 at NLO using NNPDF3.0NNLO. For $1 < m_{\ell\ell} < 5$ GeV, $t\bar{t}Z/\gamma^*$ is simulated with MADGRAPH5_aMC@NLO 2.3.3 at NLO interfaced with PYTHIA8.210 using A14 tune and NNPDF2.3LO. An alternative $m_{\ell\ell} > 5$ GeV sample is generated using MADGRAPH5_aMC@NLO 2.3.3 interfaced with PYTHIA8 to account for the generator uncertainty. In the SM $t\bar{t}t\bar{t}$ analysis, $t\bar{t}Z/\gamma^*$ NLO production, including off-shell Z/γ^* contributions ($m_{\ell\ell} > 1$ GeV), is generated with MADGRAPH5_aMC@NLO 2.8.1 and NNPDF3.0NLO. Events are interfaced with PYTHIA8.210 using A14 tune and NNPDF2.3LO. $t\bar{t}Z/\gamma^*$ with SHERPA 2.2.11 at NLO using the NNPDF3.0NNLO is simulated for the generator uncertainty.

The $t\bar{t}H$ production process is produced using POWHEGBOX [208; 255] at NLO with NNPDF3.0NLO, showered using PYTHIA8.230 with A14 tune and NNPDF2.3LO. An alternative MADGRAPH5_aMC@NLO 2.3.3 sample with NNPDF3.0NLO is simulated for generator uncertainty. Both analyses use the same nominal and alternative MC samples. In SM $t\bar{t}t\bar{t}$ analysis, an additional NLO sample is simulated by showering the nominal POWHEGBOX sample with HERWIG7.04 to evaluate the PS and hadronization impacts.

6.2.5 Other Backgrounds

The $t\bar{t}$ and single-top (tW) production processes [256] are simulated using POWHEG-BOX [208; 257] at NLO in QCD with NNPDF3.0NLO. The h_{damp} parameter[2] is set to 1.5 m_{top} [258]. The tW can be produced with an additional b-quark at NLO in QCD. This tW process overlaps with $t\bar{t}$ production at LO. A diagram removal scheme is performed to the tW to remove the interference with $t\bar{t}$ production [258; 259]. For both samples, events are interfaced with PYTHIA8.230 using the A14 tune and NNPDF2.3LO.

V+jets, VV, and VVV are modeled with SHERPA 2.2.1 and 2.2.2 at NLO in QCD [242]. V+jets is normalized to NNLO [240], while VV and VVV are normalized to NLO calculations [242]. The VH process, where $V = W, Z$, is generated with PYTHIA8.230 using A14 tune and NNPDF2.3LO and normalized to theoretical cross sections at NNLO in QCD and NLO in EW [117].

Rare production processes of tZq, $t\bar{t}WW$, $t\bar{t}HH$, $t\bar{t}WH$, $t\bar{t}ZZ$, and $t\bar{t}WZ$ are generated with MADGRAPH5 at LO interfaced with PYTHIA8 using the A14 tune. The tWZ is generated with MADGRAPH5_AMC@NLO 2.3.3 at NLO using NNPDF3.0NLO, interfaced with PYTHIA8.212 using the A14 tune and NNPDF2.3LO. These rare processes are normalized to their NLO theoretical cross sections [117; 205].

6.3 Background Estimation

Several SM processes can decay into the SSML final state, resulting in different types of background processes. These backgrounds can be divided into two categories: irreducible and reducible. Irreducible backgrounds are characterized by SM processes that lead to the SSML final states, with all selected leptons being prompt. These prompt leptons primarily originate from the decays of $H/W/Z$ bosons, τ-leptons, or internal conversions (discussed in Section 5.3.1.4). Major contributions to irreducible backgrounds include

[2]The h_{damp} parameter controls ME and PS matching and regulates the high-p_T radiation [258].

$t\bar{t}t\bar{t}$ (for the BSM $t\bar{t}t\bar{t}$ analysis only), $t\bar{t}W$+jets, $t\bar{t}Z$+jets and $t\bar{t}H$+jets production where jets include both light-flavor jets and b-jets. Smaller contributions come from VV, VVV, VH, and rare processes including $t\bar{t}VV$, tWZ, tZq and $t\bar{t}t$. Irreducible backgrounds are estimated using MC simulations normalized to their theoretical cross sections, as described in Section 6.2. Additional corrections are applied to $t\bar{t}W$ and internal conversion. The $t\bar{t}W$ background is estimated using either a floating normalization or a N_{jets} parameterized function in different analyses, summarized in Section 6.3.3. The internal conversion is estimated with the template method [51; 52], described in Section 6.3.2, in both SM and BSM $t\bar{t}t\bar{t}$ analyses.

The reducible background primarily arises from $t\bar{t}$+jets, V+jets, and tW+jets. These processes do not inherently produce SSML final states but are reconstructed as SSML due to misidentified and mis-reconstructed leptons. The background sources are summarized into three categories: QmisID, fake leptons, and non-prompt leptons. The QmisID background is from reconstructed electrons with a sign flip of electrical charge, described in Section 5.3.1.3. This background is evaluated using a data-driven method for the charge flip rates, as outlined in Section 6.3.1. On the other hand, the fake/non-prompt lepton background, discussed in Section 5.3.1.4 and Section 5.3.3, mainly arises from the following sources:

- Events with one non-prompt electron (muon) originating from semi-leptonic decays of b- and c-hadrons are known as HF decays, HF e (HF μ).
- Events with one non-prompt electron originating from photon conversion in the detector material are named material conversion (Mat. Conv.).
- Events with a virtual photon (γ^*) leading to an e^+e^- pair are referred to as internal conversion (Low m_{γ^*}).

Minor components of the fake/non-prompt lepton background, originating from events

with a lepton arising from LF meson decays or with a jet misidentified as a lepton (referred to as 'other fakes'), are determined from the MC simulations. The intricate nature of these sources presents challenges in accurately simulating the fake/non-prompt lepton background. Consequently, data-driven methods are predominantly employed with common approaches, including the matrix method [182] and the template method, to model the fake/non-prompt lepton backgrounds. Both SM and BSM $t\bar{t}t\bar{t}$ analyses utilize the template method instead of the matrix method due to its sensitivity to $t\bar{t}W$ contribution variations. The variations of $t\bar{t}W$ can significantly affect the fake efficiency calculations with large correlations between $t\bar{t}W$ and fake contributions. Section 6.3.2 summarizes the template method to estimate the fake/non-prompt lepton backgrounds.

6.3.1 Charge Misidentification

Lepton charge is determined from track curvature. The charge misidentification is mainly caused by bremsstrahlung, resulting in trident leptons, or due to incorrect charge assignment. The charge misidentification is primarily relevant for electrons (see Section 5.3.1.3), as it is significantly rare for muons due to the infrequency of bremsstrahlung and precise charge determination facilitated by the ID and MS. The primary source of QmisID background in electrons is trident electron production, influenced by the material amount traversed by the electrons in the detector, which varies with $|\eta|$. In addition, the misidentification is particularly significant at high transverse momentum due to track curvature mismeasurement. Therefore, in both SM and BSM $t\bar{t}t\bar{t}$ analyses, a data-driven method using a Poisson likelihood fit based on p_T and $|\eta|$ is utilized to estimate the QmisID background [260]. The electron charge flip rate (ϵ) is determined from $Z \to e^+e^-$ events within a Z-boson mass window cut, without requirement on the charge of the electron tracks. It is assumed that the charge flip rates of electrons in an event are uncorrelated and independent of (p_T,$|\eta|$) bins. Therefore, the number of measured same-sign events N_{ij}^{SS}, where one electron is in the i^{th} bin of (p_T,$|\eta|$) and the other is j^{th} bin of (p_T,$|\eta|$), is

expected to be

$$N_{ij}^{SS} = N_{ij}(\epsilon_i(1-\epsilon_j) + \epsilon_j(1-\epsilon_i)), \tag{6.1}$$

where N_{ij} is the total number of events in i^{th} bin and j^{th} bin regardless of electric charges. The charge flip rates are estimated by maximizing the Poisson likelihood function, equivalently as minimizing the negative logarithm of the likelihood function,

$$-\ln[L(\epsilon|N^{SS}, N)] = -\ln\left(\prod_{ij} \frac{N_{ij}^{N_{ij}^{SS}} \cdot e^{N_{ij}}}{N_{ij}^{SS}!}\right) \tag{6.2}$$

$$= \sum_{ij} -N_{ij}^{SS} \ln[N_{ij}(\epsilon_i(1-\epsilon_j) + \epsilon_j(1-\epsilon_i))] + N_{ij}(\epsilon_i(1-\epsilon_j) + \epsilon_j(1-\epsilon_i)), \tag{6.3}$$

where N^{SS} represents the number of observed events where both electrons are with the same electric charge, and N represents the number of dielectron events without any specific charge requirement. Since the electron requirement varies in different regions, the charge flip rates are extracted from likelihood fits with different region definitions using opposite-sign (OS) events. The following weight is then applied to OS ee and $e\mu$ events to account for the same-sign (SS) events that pass the region definition in an analysis,

$$w = \frac{\epsilon_i + \epsilon_j - 2\epsilon_i\epsilon_j}{1 - \epsilon_i - \epsilon_j + 2\epsilon_i\epsilon_j}. \tag{6.4}$$

Additional setups are used given different object and region definitions, with details shown in Section 7.2.1 for SM $t\bar{t}t\bar{t}$ analysis and Section 8.3.1 for BSM $t\bar{t}t\bar{t}$ analysis. The common approaches for systematic uncertainties on QmisID are shown in Section 6.4.2.

6.3.2 Fake and Non-prompt Lepton

The template method is a semi-data-driven approach used to estimate fake/non-prompt lepton background in the $t\bar{t}H$ multilepton analysis [51] and the subsequent $t\bar{t}t\bar{t}$ evidence analysis [52]. It relies on the general kinematic description of MC, while the normalizations of various fake/non-prompt backgrounds are determined with fits to data. In this method, events with fake/non-prompt leptons are classified based on their truth information, and each main contribution is assigned a free-floating normalization factor (NF). Both SM and BSM $t\bar{t}t\bar{t}$ analyses use the same set of NFs in the fit to adjust the fake/non-prompt lepton backgrounds:

- $\mathrm{NF}_{\mathrm{HF}\ e}$: NF applied to events with one non-prompt electron from HF decay.
- $\mathrm{NF}_{\mathrm{HF}\ \mu}$: NF applied to events with one non-prompt muon from HF decay.
- $\mathrm{NF}_{\mathrm{Mat.\ Conv.}}$: NF applied to events with one non-prompt electron originating from photon conversion in the detector material (Mat. Conv.).
- $\mathrm{NF}_{\mathrm{Low}\ m_{\gamma^*}}$: NF applied to events with a virtual photon (γ^*) leading to an e^+e^- pair (Low m_{γ^*}).

Dedicated control regions (CRs) have been established to measure and constrain NFs for fake/non-prompt lepton backgrounds. Additionally, validation regions (VRs) are employed to evaluate the modeling of the main backgrounds. The definitions of the CRs and VRs of SM and BSM $t\bar{t}t\bar{t}$ analyses are summarized in Section 7.2 and Section 8.3, respectively. Moreover, the template method relies significantly on MC simulations to describe the kinematics of processes. Consequently, systematic uncertainties are necessary to address potential bias in the kinematic distributions. These systematic uncertainties used in SM and BSM $t\bar{t}t\bar{t}$ analyses are summarized in Section 7.4 and Section 8.5, respectively.

6.3.3 $t\bar{t}W$ Estimation

The $t\bar{t}W$ cross section has been consistently measured higher than the current predictions in $t\bar{t}H$ and $t\bar{t}W$ multilepton measurements [51; 148] and $t\bar{t}t\bar{t}$ evidence analysis [52]. The $t\bar{t}W$ NF was left free-floating in these analyses, allowing for adjustment of the $t\bar{t}W$ normalization. In the $t\bar{t}t\bar{t}$ evidence analysis, the $t\bar{t}W$ modeling was checked in a $t\bar{t}W$ VR defined based on the charge asymmetry of the $t\bar{t}W$ process. However, a discrepancy in the $t\bar{t}W$ VR, particularly at high jet multiplicity (N_{jets}), emerged between the data and the post-fit $t\bar{t}W$ background after applying with $t\bar{t}W$ NF. Substantial uncertainties of 125% and 300% are applied to $t\bar{t}W$ events with $N_{\text{jets}} = 7$ and $N_{\text{jets}} \geq 8$ to cover the observed discrepancy. These uncertainties have become one of the most significant systematic uncertainties.

In both SM and BSM $t\bar{t}t\bar{t}$ analyses, $t\bar{t}W$ production is a significant source of background contamination. In the BSM $t\bar{t}t\bar{t}$ analysis, the $t\bar{t}W$ estimation follows $t\bar{t}t\bar{t}$ evidence analysis, where a $t\bar{t}W$ NF is kept free-floating, and large ad-hoc uncertainties are assigned to $t\bar{t}W$ events with high jet multiplicity due to the mis-modelings. Conversely, the SM $t\bar{t}t\bar{t}$ analysis introduces a new data-driven method for $t\bar{t}W$, which was employed in the R-parity-violating SUSY search [261] for describing the $t\bar{t}V$ and $t\bar{t}$ backgrounds. The $t\bar{t}W$ data-driven method is a semi-data-driven approach with kinematic distributions from $t\bar{t}W$ MC simulation corrected by N_{jets} distribution from a fitted parameterized function. By adopting this data-driven method, the dominant systematic uncertainties in the analysis shift from modeling uncertainties to those inherent in the data-driven method, which is now predominantly statistical. The details of setups are described in Section 7.2.3 and Section 8.3.2 for SM and BSM $t\bar{t}t\bar{t}$ analyses, respectively.

6.4 Systematic Uncertainties

The uncertainties in measuring a physics process contain two sources: statistical and systematic uncertainties. The statistical uncertainties arise from the sampling size of the MC simulation and observed data and the uncertainties of free parameters in the likelihood fits, discussed in Section 6.5. The systematic uncertainties originate from theoretical modeling ('theoretical uncertainties') and experimental effects ('experimental uncertainties'). The SM and BSM $t\bar{t}t\bar{t}$ analyses study similar physics phase space and use the common objects for the SSML final states. Both analyses share common sources of systematic uncertainties. This section will discuss the systematic uncertainties used in both studies. Section 6.4.1 summarizes the experimental uncertainties. Section 6.4.2 presents the QmisID systematic uncertainties. The theoretical uncertainties are summarized in Section 7.4 and Section 8.5 for different analyses, respectively.

6.4.1 Experimental Uncertainties

The experimental uncertainties can be categorized into luminosity, pile-up reweighting, and reconstruction and identification of the physics objects. Table 6.4 summarizes the experimental uncertainties used in both analyses and their typical sizes.

6.4.1.1 Luminosity and Pile-up Reweighting

Both luminosity and pile-up reweighting uncertainties are independent of the physics processes. The luminosity measurements are performed with the LUCID-2 Cherenkov detector [262], complemented by the ID and calorimeters. The uncertainty on the integrated luminosity of the entire Run 2 dataset is initially measured to be 1.7% with the preliminary measurement [104], which is used in the BSM $t\bar{t}t\bar{t}$ analysis. The final uncertainty is reduced to 0.83% in the legacy measurement with improved calibrations [103]. This reduced uncertainty is used in the SM $t\bar{t}t\bar{t}$ analysis. The luminosity uncertainty is

Systematic uncertainty	Application	SM $t\bar{t}t\bar{t}$	BSM $t\bar{t}t\bar{t}$	Typical size [%]
Luminosity	Normalization	1	1	$O(1)$
Pile-up reweighting	Weight	1	1	$O(1) \sim O(10)$
Electrons				
Electron trigger efficiency	Weight	1	1	$O(10^{-2}) \sim O(10^{-1})$
Electron reconstruction efficiency	Weight	1	1	$O(10^{-1}) \sim O(1)$
Electron identification efficiency	Weight	1	1	$O(10^{-1}) \sim O(1)$
Electron isolation efficiency	Weight	1	1	$O(10^{-1}) \sim O(1)$
Electron energy scale	Kinematics	$1^{\dagger}$	$1^{\dagger}$	$O(10^{-2}) \sim O(10^{-1})$
Electron energy resolution	Kinematics	1	1	$O(10^{-2}) \sim O(10^{-1})$
Electron ECIDS efficiency	Weight	1	1	$O(10^{-1}) \sim O(1)$
Muons				
Muon trigger efficiency (stat & syst)	Weight	2	2	$O(10^{-1}) \sim O(1)$
Muon track-to-vertex efficiency (stat & syst)	Weight	2	2	$O(10^{-2}) \sim O(10^{-1})$
Muon identification efficiency (stat & syst)	Weight	2	2	$O(10^{-1}) \sim O(1)$
Muon isolation efficiency (stat & syst)	Weight	2	2	$O(10^{-1}) \sim O(1)$
Muon momentum resolution (ID & MS)	Kinematics	-	2	$O(10^{-1}) \sim O(1)$
Muon momentum resolution (CB)	Kinematics	1	-	$O(10^{-2}) \sim O(10^{-1})$
Muon charge-independent momentum scale	Kinematics	1	1	$O(10^{-2}) \sim O(10^{-1})$
Muon charge-dependent momentum scale	Kinematics	1	2	$O(10^{-2}) \sim O(10^{-1})$
Muon charge-dependent corrections (stat)	Kinematics	1	-	$O(10^{-2}) \sim O(10^{-1})$
Jets				
JES effective NP	Kinematics	15	15	$O(10^{-2}) \sim O(1)$
JES η intercalibration	Kinematics	6	6	$O(10^{-1}) \sim O(1)$
JES flavor composistion and response	Kinematics	2^{*}	2^{*}	$O(1) \sim O(10)$
JES pile-up	Kinematics	4	4	$O(10^{-1}) \sim O(10)$
JES punch-through	Kinematics	$1^{\dagger}$	$1^{\dagger}$	$< O(10^{-2})$
JES AF2 non-closure	Kinematics	1	1	$O(10^{-2}) \sim O(10^{-1})$
JES high-p_T single-particle	Kinematics	1	1	$< O(10^{-2})$
JES b-jet response	Kinematics	1	1	$O(10^{-1}) \sim O(1)$
JER effective NP	Kinematics	12	7	$O(10^{-1}) \sim O(1)$
JER data/MC	Kinematics	$1^{\dagger}$	$1^{\dagger}$	$O(10^{-1}) \sim O(1)$
JVT efficiency	Weight	1	1	$O(10^{-1}) \sim O(1)$
b-tagging efficiencies for b-jets	Weight	45	45	$O(10^{-2}) \sim O(1)$
b-tagging efficiencies for c-jets	Weight	20	20	$O(10^{-2}) \sim O(1)$
b-tagging efficiencies for light jets	Weight	20	20	$O(10^{-2}) \sim O(1)$
b-tagging efficiencies for high p_T	Weight	3	-	$O(10^{-2}) \sim O(10^{-1})$
Missing transverse momentum				
E_T^{miss} scale and resolution on soft term	Kinematics	3	3	$O(10^{-2}) \sim O(10^{-1})$

Table 6.4: Summary of the experimental systematic uncertainties in the analyses. The 'application' column indicates the implementation of the systematic uncertainties. The 'weight' stands for the event reweighting of an event. The 'kinematics' represents rescaling the object's kinematics in an event such as p_T or energy corrections. The 'normalization' represents the overall uncertainty applied to an event. The symbol † represents the systematic uncertainty that is decorrelated for samples simulated with AF2 or full detector simulations. The value with $*$ symbol represents the flavor composition systematic uncertainty is decorrelated into signal and background terms, where $t\bar{t}t\bar{t}$ ($t\bar{t}t\bar{t}$ and BSM signal) events are considered in the signal term in the SM (BSM) $t\bar{t}t\bar{t}$ analysis. The 'Typical size' summarizes ranges of uncertainty sizes in the signal region. Both analyses have similar levels of uncertainties.

applied to all MC simulated samples, affecting their overall normalization. The pile-up modeling in MC simulations matches the data through pile-up reweighting, with an SF of 1.0/1.03 applied to the number of PVs in the data. Variations of the SF are assigned as the pile-up reweighting uncertainty. These uncertainties correspond to an up variation of 1.0/1.07 and a down variation of 1.0/0.99 to the nominal value. The pile-up reweighting uncertainties are applied to all MC simulated samples, affecting overall normalization and kinematics.

6.4.1.2 Uncertainties on Physics Objects

6.4.1.2.1 Electrons and Muons

The reconstruction, identification, isolation, and trigger efficiencies of electrons and muons differ between data and MC simulations. Additional SFs are applied to correct the differences. These SFs are measured with the tag-and-probe method using $Z \to \ell\ell$ and $J/\Psi \to \ell\ell$ samples in data and MC simulations [172; 178]. The uncertainties arising from these corrections are evaluated by varying the SFs. Moreover, additional uncertainty is applied to the electrons to account for the efficiency of ECIDS. These uncertainties result in five independent components for electrons and eight for muons with decorrelated statistical and systematic effects.

The scale and resolution of electron energy and muon momentum are corrected in MC simulations to match those in the data. The associated uncertainties are estimated by re-simulating the events with varying energy/momentum scale and resolution with $\pm 1\sigma$. The uncertainty of muon momentum resolution can be derived in different schemes, ID+MS and CB schemes. The uncertainty in the CB scheme, used for SM $t\bar{t}t\bar{t}$ analysis, is evaluated by varying the CB muon track resolution, resulting in one component. The uncertainties in the ID+MS scheme, used for BSM $t\bar{t}t\bar{t}$ analysis, are derived by varying the ID and MS track resolution, resulting in two independent components. The uncertainties of the muon momentum scale include three components in both SM and BSM $t\bar{t}t\bar{t}$ analyses. SM $t\bar{t}t\bar{t}$

analysis considers the uncertainties from the charge-independent and charge-dependent momentum scales and the statistical uncertainty on the charge-dependent corrections. BSM $t\bar{t}t\bar{t}$ analysis considers one term for the charge-independent momentum scale and two for the charge-dependent momentum scale. The uncertainties of electron energy scale and resolution result in two components. As a result, two independent components are considered for electron energy scale and resolution. Four (five) components are considered for the muon momentum scale and resolution in the SM (BSM) $t\bar{t}t\bar{t}$ analysis.

6.4.1.2.2 Jets

The uncertainties on jets arise from the calibration of the JES and JER [190; 263; 264] and the SFs applied to correct the JVT selection efficiency difference between data and MC [265].

The JES and its associated uncertainties are estimated with information from MC simulations and data from test-beam and collisions at the LHC [189; 190]. The JES uncertainties are estimated by varying the JES measurements with a shift of $\pm 1\sigma$. Therefore, the uncertainties can vary the p_T and η in the MC simulation, resulting in different kinematics of an event. The JES uncertainties arise from eight various sources with definitions from Ref. [190],

- **p_T-dependent *in situ* uncertainty components (denoted as Effective nuisance parameters (NPs))** are grouped into 15 reduced components based on their origin (detector, statistical, modeling, or mixed) using the category reduction.

- **η intercalibration** corrects the forward jets ($0.8 \leq |\eta_{det}| < 4.5$) to have the same energy scale as the central jets ($|\eta_{det}| < 0.8$). The uncertainties of η intercalibration contain six terms: systematic effects, statistical uncertainties, and non-closure terms.

- **Flavor dependence uncertainties** contain two components accounting for rela-

tive flavor compositions and differing responses to quark- and gluon-initiated jets [266; 267].

- **Pile-up effect uncertainties** contain four components accounting for offset and p_T dependence in $\langle\mu\rangle$ and N_{PV} and event topology dependence of the density metric ρ.

- **Punch-through uncertainties** account for the mis-modeling of the correction to jets, which pass through the calorimeters and into the muon system. The difference in jet response between data and MC simulation is estimated as uncertainty. This is decorrelated as two terms applied to samples with AF2 and full detector simulations.

- **Non-closure uncertainty** is applied to AF2 MC simulated samples to account for the difference between samples simulated with AF2 and those with full detector simulations.

- **High-p_T 'single particle' uncertainty** accounts for the response to individual hadrons in the high p_T region.

- ***b*-jet response uncertainty** accounts for the difference in response between jets from light- versus heavy-flavor quarks.

The JER was measured with the dijet events in the Run 2 data of the LHC in bins of p_T and η [190]. Smearing procedures match the JER in MC simulation ($\mathrm{JER_{MC}}$) to that in data ($\mathrm{JER_{data}}$) when $\mathrm{JER_{data}}$ is larger than $\mathrm{JER_{MC}}$. The JER-associated uncertainties are evaluated by the quadratic difference (or difference) between data and MC simulations when $\mathrm{JER_{data}} > \mathrm{JER_{MC}}$ ($\mathrm{JER_{data}} < \mathrm{JER_{MC}}$). The JER uncertainties are provided in two reduction schemes, full and simple correlation schemes. The full correlation scheme contains 13 components, while the simple correlation scheme provides eight components. In both schemes, the uncertainties are categorized into one term accounting

for the difference between data and MC simulations and the rest accounting for various sources. Similar to JES, the JER uncertainties affect the p_T and η of an event, resulting in different kinematics. The SM $t\bar{t}t\bar{t}$ analysis uses the full correlation scheme, and the BSM $t\bar{t}t\bar{t}$ analysis utilizes the simple correlation scheme.

The JVT uncertainty [265] is considered by varying the SFs up and down within their uncertainties to correct the JVT efficiencies in the MC simulations. A single component is considered for this uncertainty.

6.4.1.2.3 Flavor-tagging for Jets

The flavor-tagging efficiencies are corrected in simulated samples to match the data using SFs [200]. Section 5.4.1 describes the SFs as a function of the p_T for the b-jets, c-jets, and light jets. The uncertainties of the b-tagging efficiencies are evaluated through the impacts on the SFs, containing $O(100)$ independent components from a mixture of the statistical, experimental, and modeling uncertainties. An eigenvector reduction is performed by an eigenvalue decomposition of the covariance matrix of systematic and statistical variations [268]. It results in 45, 20, and 20 independent components of uncertainties for b-jets, c-jets, and light jets, respectively.

Three additional components are evaluated to account for b-tagging efficiency for high p_T jets due to the lack of calibration in this region. The uncertainties are derived by independently extrapolating the highest p_T bins below the threshold from the simulations for b-/c-/light jets. These uncertainties are considered only in the SM $t\bar{t}t\bar{t}$ analysis.

6.4.1.2.4 Missing Transverse Momentum

The uncertainties on the E_T^{miss} [269] arise from the possible miscalibration of its soft-track component. Three components are estimated with the scale and resolution of the soft term. The scale uncertainty for E_T^{miss} varies the scale of the soft term up and down in the direction of p_T of the hard object (p_T^{Hard}). The hard objects include electrons,

photons, muons, hadronically decaying τ leptons, and jets. Two resolution uncertainties are considered parallel or perpendicular to the p_T^{Hard}.

6.4.2 Charge Misidentification

The sources of systematic uncertainties on the charge flip rates are considered in both SM and BSM $t\bar{t}t\bar{t}$ analyses:

- The statistical uncertainty from the Poisson likelihood fit.
- Variation in the size of the side-band regions used to subtract the background from the Z-boson mass window.
- Difference between the rates with the likelihood method and the truth-matching method using MC $Z \to ee$ simulation.

The total uncertainty is calculated with a quadrature sum of different sources of uncertainties. The final QmisID systematic uncertainty is estimated with a variation of the weight Δw defined as

$$\Delta w = \frac{\sqrt{(1-2\epsilon_1)^2\Delta\epsilon_2^2 + (1-2\epsilon_2)^2\Delta\epsilon_1^2 + (1-2\epsilon_1)(1-2\epsilon_2)\rho_{12}\Delta\epsilon_1\Delta\epsilon_2}}{(1-\epsilon_1-\epsilon_2+2\epsilon_1\epsilon_2)^2}, \tag{6.5}$$

where $\Delta\epsilon_1$ and $\Delta\epsilon_2$ stand for the uncertainties on the charge flip rates of the first and the second electron, and the ρ_{12} stands for the correlation between ϵ_1 and ϵ_2. Section 7.2.1 and Section 8.3.1 summarize the final systematic uncertainties for SM and BSM $t\bar{t}t\bar{t}$ analyses.

6.5 Statistical Interpretation

6.5.1 Likelihood Function

The statistical interpretation aims to estimate the unknown physics parameters with a collection of data and MC simulated samples. The interpretation relies on the maximum

likelihood method with a set of independent measured quantities x_i from the probability density function $f(x_i;\alpha)$, where α represents an unknown set of parameters. This method maximizes the joint probability density functions in the likelihood function defined as

$$L(\alpha) = \prod_i f(x_i;\alpha). \tag{6.6}$$

The estimate of α can be obtained with the derivative of α to be zero. However, it is more usual to take the derivative on $\ln L(\alpha)$, which can turn the products into summations. Therefore, the estimate of α is written as

$$\frac{\partial \ln L(\alpha)}{\partial \alpha} = 0. \tag{6.7}$$

In the large sample case, the $L(\alpha)$ follows Gaussian distribution, leading $\ln L(\alpha)$ to be a parabola with s standard-deviation errors as

$$\ln L(\alpha') = \ln L_{\max} - \frac{s^2}{2}, \tag{6.8}$$

where $L_{\max}$ is the value at the solution point.

The parameter α to be measured in the analyses of this dissertation contains the parameter of interest (POI), NPs ($\boldsymbol{\theta}$), and background NFs. The POI is the quantity that the analysis targets to measure. In this dissertation, the POI is the μ of a physics process, defined as the ratio of the measured cross section to its theoretical prediction. The NPs are considered to estimate the impact of the systematic uncertainties on the signal and background simulations. In addition, background normalizations, known as the NFs, correct the overall yields of background processes that do not have a well-known cross section. The background NFs are simultaneously measured with the signal strength.

Both SM and BSM $t\bar{t}t\bar{t}$ analyses use a binned likelihood function, which divides the total number of events into bins of signal and control regions based on kinematics. The

probability in each bin i follows a Poisson distribution to estimate the probability of observing exactly N_i events when the event rate is expected to be n_i,

$$\mathcal{P}_{\text{Poisson}} = \frac{n_i^{N_i} e^{-n_i}}{N_i!}. \tag{6.9}$$

The Poisson distribution can be rewritten by dividing the expected event rate into events from signal and background with parameters to be measured,

$$\mathcal{P}_{\text{Poisson}}\left(N_i|\mu s_i(\boldsymbol{\theta}) + \sum_j \kappa_j b_{ij}(\boldsymbol{\theta})\right) = \frac{e^{-\left(\mu s_i(\boldsymbol{\theta}) + \sum_j \kappa_j b_{ij}(\boldsymbol{\theta})\right)}}{N_i!}\left(\mu s_i(\boldsymbol{\theta}) + \sum_j \kappa_j b_{ij}(\boldsymbol{\theta})\right)^{N_i}, \tag{6.10}$$

where $s_i(\boldsymbol{\theta})$ is the signal yields in the bin i of all regions, and b_{ij} represents the background yields in the bin (index i) of all regions for different background sources (index j). The NPs $\boldsymbol{\theta}$ can modify the normalization and/or kinematics on either a single process or multiple processes depending on the construction of the associated systematic uncertainties. The μ stands for the signal strength of the signal process, and the κ_j represents the background NFs for different sources of backgrounds for which the theoretical predictions are not fully reliable.

The NPs are estimated from auxiliary measurements [270]. The probability function $f(a_p|\alpha_p, \sigma_p)$ of the auxiliary measurement of NP can be generally described by a Gaussian function as

$$f_p(a_p|\alpha_p, \sigma_p) = \frac{1}{\sqrt{2\pi\sigma_p^2}} \exp\left[-\frac{(a_p - \alpha_p)^2}{2\sigma_p^2}\right], \tag{6.11}$$

where α_p is the parameter to be measured, a_p is the maximum likelihood esimate of the α_p, and σ_p is the standard error. However, using the Gaussian function is problematic for the non-negative parameters, such as event yields and energy scale uncertainties. A log-

normal distribution is used to describe the constraint term for positive-only parameters,

$$f_p(a_p|\alpha_p,\sigma_p) = \frac{1}{\sqrt{2\pi}\ln\kappa}\frac{1}{a_p}\exp\left[-\frac{(\ln(a_p/\alpha_p))^2}{2(\ln\kappa)^2}\right], \tag{6.12}$$

where $\kappa = 1+\sigma_p/\alpha_p$.

The full likelihood function is built with products of Poisson distributions and the auxiliary measurements of NPs, and written as

$$L(\boldsymbol{N}|\mu,\boldsymbol{\theta},\boldsymbol{\kappa}) = \left(\prod_{i\in\text{bin,reg}} \mathcal{P}_{\text{Poisson}}(N_i|\mu s_i(\boldsymbol{\theta}) + \sum_j \kappa_j b_{ij}(\boldsymbol{\theta}))\right)\cdot\prod_{\theta\in\boldsymbol{\theta}} f(\tilde{\theta}|\theta), \tag{6.13}$$

where the additional arguments are described below,

- $\boldsymbol{N} = (N_0,...,N_{N_{\text{bin}}\times N_{\text{reg}}})$ is the pseudo- or observed data in every bins of every region.
- $\boldsymbol{\theta} = (\theta_0,...,\theta_{N_{syst}})$ is the NPs associated to the systematic uncertainties with total number N_{syst}.
- $\boldsymbol{\kappa} = (\kappa_0,...,\kappa_{N_{bkg}})$ is the NFs of background sources with not well known cross-section predictions.
- $\mathcal{P}_{\text{Poisson}}(n|\lambda)$ is the Poisson probability to observe n events while λ events are expected.
- $f(\tilde{\theta}|\theta)$ is the probability function from auxiliary measurements with $\tilde{\theta}$ being the maximum likelihood estimate for θ.

In the likelihood, the μ for signal and $\boldsymbol{\kappa}$ for backgrounds are unconstrained parameters, which are free-floating in the likelihood fit. Conversely, the NPs are included as constrained terms.

6.5.2 Statistical Test

The sensitivity of a new physics process is set with a statistical test following Ref. [271]. A null hypothesis (H_0) is defined as known background processes to test against an alternative hypothesis (H_1) that includes background and new signals. While setting the limits, the signal-plus-background hypothesis model is treated as the H_0 and tested against the background-only hypothesis H_1. A p-value describes the probability of incompatibility between the observed data and the hypothesis model. The p-value is commonly converted into the Z-value, known as the signal significance, to describe the number of standard deviations away from the mean in a Gaussian distribution. The relation between p-value and Z-value is defined as

$$Z = \Phi^{-1}(1 - p), \tag{6.14}$$

where Φ^{-1} is the quantile of the standard Gaussian. Table 6.5 summarizes the relation between the area of tail α (corresponding to p-value) and standard deviation δ (corresponding to Z-value), assuming the area of tails on both sides. However, the μ has a non-negative value leading to a one-side Gaussian distribution. Therefore, the one-side assumption leads to half of the α values in Table 6.5. Discovery of a physics process is defined as having a $Z = 5$ to reject the background-only hypothesis, corresponding to a p-value of 2.87×10^{-7}. The exclusion of a signal hypothesis at a 95% confidence level (CL) is set with a p-value of 0.05, corresponding to $Z = 1.64$.

The likelihood-ratio test, known as a profile likelihood ratio, is performed to quantify the goodness of fit between two statistical models. The profile likelihood ratio is defined to test a hypothesized μ as

$$\lambda(\mu) = \frac{L(\mu, \hat{\hat{\theta}})}{L(\hat{\mu}, \hat{\theta})}, \tag{6.15}$$

where $\hat{\hat{\theta}}$ is the conditional maximum-likelihood estimator of θ, which maximizes the likelihood for a specific μ. The $\hat{\mu}$ and $\hat{\theta}$ are the maximum-likelihood estimators for the un-

α	δ	α	δ
0.3173	1σ	0.2	1.28σ
4.55×10^{-2}	2σ	0.1	1.64σ
2.7×10^{-3}	3σ	0.05	1.96σ
6.3×10^{-5}	4σ	0.01	2.58σ
5.7×10^{-7}	5σ	0.001	3.29σ
2.0×10^{-9}	6σ	10^{-4}	3.89σ

Table 6.5: The area of tail α outside $\pm\delta$ from the mean of a Gaussian distribution. The tail area is halved for the one-side Gaussian distribution [204].

conditional maximized-likelihood function. The $\lambda(\mu)$ ranges between 0 to 1, with $\lambda = 1$ ($\lambda = 0$) indicating good (bad) agreement between data and the hypothesized value of μ.

The test statistic (t_μ) is defined with the profile likelihood ratio as

$$t_\mu = -2 \ln \lambda(\mu) \tag{6.16}$$

to evaluate the compatibility between observed data and the hypothesis model. In large statistics, the distribution of t_μ can be approximated as a chi-square (χ^2) distribution by Wilks' Theorem [272] and written as

$$t_\mu = -2 \ln \lambda(\mu) = \left(\frac{\mu - \hat{\mu}}{\sigma_\mu} \right)^2 . \tag{6.17}$$

The lower value of t_μ means the good compatibility between data and the hypothesized μ, while the higher values of t_μ indicate the incompatibility between data and the hypothesized μ. The disagreement between the data and hypothesis model is quantified as p-value calculated as

$$p_\mu = \int_{t_{\mu,\mathrm{obs}}}^{\infty} f(t_\mu|\mu) dt_\mu, \tag{6.18}$$

where $t_{\mu,\mathrm{obs}}$ is the observed test statistic from data and $f(t_\mu|\mu)$ is the probability density

function of t_μ with the assumption of μ.

The Gaussian distributed data allows the relation of the least χ^2 method and maximum likelihood method as

$$2\Delta \ln L = \Delta\chi^2 = F^{-1}_{\chi^2_M}(1-\alpha), \tag{6.19}$$

where the $F^{-1}_{\chi^2_M}$ is the chi-square quantile for M degree of freedom [204]. Table 6.6 summarizes the relation between probability and values of $2\Delta \ln L$ or $\Delta\chi^2$.

$(1-\alpha)$ (%)	$M=1$	$M=2$	$M=3$
68.27	1.00	2.30	3.53
90.	2.71	4.61	6.25
95.	3.84	5.99	7.82
95.45	4.00	6.18	8.03
99.	6.63	9.21	11.34
99.73	9.00	11.83	14.16

Table 6.6: Values of $2\Delta \ln L$ or $\Delta\chi^2$ corresponding to a coverage probability $1-\alpha$ for M degree of freedom [204].

6.5.2.1 Signal Significance

The presence of the signal process increases the event rate compared to the event rate from the background alone, resulting in an assumption of the $\mu \geq 0$. Therefore, a test statistic is constructed for $\mu \geq 0$, where if the $\hat{\mu} < 0$, the best agreement with data occurs when $\mu = 0$. The profile likelihood ratio $\tilde{\lambda}(\mu)$ [271] with the assumption of $\mu \geq 0$ is defined as

$$\tilde{\lambda}(\mu) = \begin{cases} \frac{L(\mu, \hat{\hat{\theta}}(\mu))}{L(\hat{\mu}, \hat{\theta})} & \text{if } \hat{\mu} \geq 0, \\ \frac{L(\mu, \hat{\hat{\theta}}(\mu))}{L(0, \hat{\hat{\theta}}(0))} & \text{if } \hat{\mu} < 0, \end{cases} \tag{6.20}$$

where $\hat{\hat{\theta}}(0)$ and $\hat{\hat{\theta}}(\mu)$ are the conditional maximum-likelihood estimators of θ given the signal strength to be 0 and μ, respectively. The $\tilde{t}_\mu$ is then defined as

$$\tilde{t}_\mu = -2\ln\tilde{\lambda}(\mu) = \begin{cases} -2\ln\left(\frac{L(\mu,\hat{\hat{\theta}}(\mu))}{L(\hat{\mu},\hat{\theta})}\right) & \text{if } \hat{\mu} \geq 0, \\ -2\ln\left(\frac{L(\mu,\hat{\hat{\theta}}(\mu))}{L(0,\hat{\hat{\theta}}(0))}\right) & \text{if } \hat{\mu} < 0. \end{cases} \tag{6.21}$$

The test statistic to discover a positive signal is to test and reject the $\mu = 0$ hypothesis. This special case of test statistic with $\mu = 0$ is defined as

$$\tilde{t}_0 = q_0 = \begin{cases} -2\ln\lambda(0) & \text{if } \hat{\mu} \geq 0, \\ 0 & \text{if } \hat{\mu} < 0. \end{cases} \tag{6.22}$$

The probability of incompatibility between the data and the background-only hypothesis $\mu = 0$ using the observed value of q_0 is

$$p_0 = \int_{q_{0,\text{obs}}}^{\infty} f(q_0|0)dq_0. \tag{6.23}$$

The $f(q_0|0)$ can be further approximated with Gaussian distribution with the form as

$$f(q_0|0) = \frac{1}{2}\delta(q_0) + \frac{1}{2\sqrt{2\pi q_0}}e^{-q_0/2}. \tag{6.24}$$

This leads to the p-value of background hypothesis $\mu = 0$ to be

$$p_0 = 1 - \Phi(\sqrt{q_0}), \tag{6.25}$$

where the corresponding signal significance is defined as

$$Z_0 = \sqrt{q_0}. \tag{6.26}$$

6.5.2.2 Upper Limit

To establish the exclusion upper limits on μ with the assumption of $\mu \geq 0$, a test statistic is based on the CL_s prescription [273] and defined as

$$q = -2\ln\frac{L_{s+b}}{L_b} = -2\ln\frac{L(\mu=1,\hat{\hat{\theta}}(1))}{L(\mu=0,\hat{\hat{\theta}}(0))} = -2\ln\lambda(1) + 2\ln\lambda(0), \tag{6.27}$$

where L_{s+b} is the likelihood function of the signal-plus-background model ($\mu = 1$), and L_b is the likelihood function of the background-only model ($\mu = 0$). The p-values of signal-plus-background and background-only hypothesis models are calculated as

$$p_{s+b} = p(q > q_{obs}|s+b) = \int_{q_{\mathrm{obs}}}^{\infty} f(q|s+b)\,dq = 1 - \Phi\left(\frac{q_{\mathrm{obs}} + 1/\sigma_{s+b}^2}{2/\sigma_{s+b}}\right), \tag{6.28}$$

$$p_b = p(q > q_{obs}|b) = \int_{-\infty}^{q_{\mathrm{obs}}} f(q|b)\,dq = \Phi\left(\frac{q_{\mathrm{obs}} - 1/\sigma_b^2}{2/\sigma_b}\right). \tag{6.29}$$

The upper limit is defined as

$$\mathrm{CL}_s \equiv \frac{\mathrm{CL}_{s+b}}{\mathrm{CL}_b} = \frac{p_{s+b}}{p_b}. \tag{6.30}$$

The upper limit on μ at 95% CL is set when CL_s is less than 5%.

CHAPTER VII

Observation of Standard Model Four-Top-Quark Production

This chapter presents the first observation of the SM $t\bar{t}t\bar{t}$ production in the SSML final states, using 140 fb^{-1} of pp collision data collected with the ATLAS detector at $\sqrt{s}$ =13 TeV [125]. The $t\bar{t}t\bar{t}$ event topology is characterized by a complex signature with numerous jets and b-jets assoicated with the SSML. This analysis employs a Graph Neural Network (GNN) to extract signals from backgrounds. A complementary BDT method is used to cross-check the final results. A likelihood fit is then conducted in the signal region, using the distribution of multivariate discriminant, and various control regions. This approach simultaneously determines $t\bar{t}t\bar{t}$ signal strength, the normalizations of fake/non-prompt backgrounds, and the parameterized function of $t\bar{t}W$.

This chapter is structured as follows: Section 7.1 outlines the selection criteria for physics objects and event selection. Section 7.2 details the background estimation on data-driven methods for charge misidentification and $t\bar{t}W$, as well as the template method for the fake/non-prompt contributions. The uses of GNN and BDT to extract the $t\bar{t}t\bar{t}$ signal are discussed in Section 7.3. Section 7.4 describes the systematic uncertainties affecting the signal and background modelings. Finally, Section 7.5 summarizes the results of the $t\bar{t}t\bar{t}$ production cross section and its interpretation with BSM physics.

7.1 Object and Event Selection

The object selections are optimized for the $t\bar{t}t\bar{t}$ evidence analysis [52], upgraded to the PFlow jet algorithm and the DL1r b-tagging algorithm, discussed in Section 5.4. Looser p_T selections are utilized to increase the signal acceptance compared to $t\bar{t}t\bar{t}$ evidence analysis. The physics objects considered in the measurement are electrons, muons, jets, b-jets, and the missing transverse momentum. Section 6.1 summarizes the trigger selections. Section 5.3 presents the identification and reconstruction of electrons and muons. Table 7.1 summarizes the reconstructed objects and identification criteria used in this measurement.

	Electrons	Muons	Jets	b-jets
p_T [GeV]	> 15 ($p_{\mathrm{T}}(\ell_0) > 28$)	> 15 ($p_{\mathrm{T}}(\ell_0) > 28$)	> 20	> 20
$\lvert\eta\rvert$	< 1.37 or $1.52 - 2.47$	< 2.5	< 2.5	< 2.5
Identification quality	Tight ECIDS (ee, $e\mu$)	Medium	JVT	DL1r 77%
Isolation	PLImprovedTight	PLImprovedTight		
Track vertex :				
$-\ \lvert d_0/\sigma_{d_0}\rvert$	< 5	< 3		
$-\ \lvert z_0 \sin\theta\rvert$ [mm]	< 0.5	< 0.5		

Table 7.1: Summary of object identifications and definitions. The ECIDS and PLImproved WPs are introduced in Section 5.3. The JVT and DL1r algorithm are summarized in Section 5.4.

Events are required to have exactly one same-sign dilepton or at least three leptons without charge requirement (± 1 or ± 3). Events with at least one b-tagged jet are preselected. Additional selections are applied depending on the lepton flavor combination. Events with a same-sign electron pair are required to have di-electron invariant mass $m_{ee} >$ 15 GeV and $|m_{ee} - 91\ \mathrm{GeV}| > 10$ GeV to suppress the charge misidentified background coming from low mass resonances and the Z bosons. Events with at least three leptons are required, with all opposite-sign same-flavor lepton pairs being $|m_{ee} - 91\ \mathrm{GeV}| > 10$ GeV.

This would reduce the contamination from the Z-boson decays.

The $t\bar{t}t\bar{t}$ production provides high jet and b-jet multiplicities, and a overall large scalar sum of the transverse momentum of the leptons and jets (H_T) in an event. The signal region is further selected according to the property of $t\bar{t}t\bar{t}$ requiring at least six jets, at least two b-jets, and $H_T > 500\,\text{GeV}$.

7.2 Background Estimation

As outlined in Section 6.3, several techniques were developed to improve background modeling in this analysis. The estimation of QmisID is performed using a data-driven strategy to derive the charge flip rates, summarized in Section 7.2.1. Section 7.2.2 summarizes the template method for different fake and non-prompt lepton background sources. Section 7.2.3 discusses the novel $t\bar{t}W$ data-driven method to improve the $t\bar{t}W$ modeling. Section 7.2.4 presents the results of the simultaneous fits with the template and $t\bar{t}W$ data-driven methods.

Several control regions are constructed to achieve the highest possible purity for the specific background of interest. This analysis uses control regions to estimate fake/non-prompt background and $t\bar{t}W$. Table 7.2 summarizes the definitions of signal and control regions. Figure 7.1 presents the $t\bar{t}t\bar{t}$ and background compositions in different regions.

7.2.1 Charge Misidentification

Charge misidentification is assessed using a data-driven method with a Poisson likelihood fit, as detailed in Section 6.3.1, to determine the charge flip rate. A Z-boson mass window, identified through fitting the m_{ee} spectrum to a Breit-Wigner function, sets the range of [67,112] GeV for SS and [72,109] GeV for OS events, encompassing most Z-peak events.

Charge flip rates are calculated separately for the signal region (SR) and various

Region	Channel	N_{jets}	N_b	Other selection	Fitted variable
CR Low m_{γ^*}	SS, ee or eμ	$4 \leq N_{\text{jets}} < 6$	≥ 1	ℓ_0 or ℓ_1 is from internal conversion ℓ_0 and ℓ_1 are not from material conversion	event yield
CR Mat. Conv.	SS, ee or eμ	$4 \leq N_{\text{jets}} < 6$	≥ 1	ℓ_0 or ℓ_1 is from material conversion	event yield
CR HF μ	e$\mu\mu$ or $\mu\mu\mu$	≥ 1	$= 1$	ℓ_0, ℓ_1 and ℓ_2 are not from photon conversion $100 < H_T < 300$ GeV $E_{\text{T}}^{\text{miss}} > 50$ GeV total charge $= \pm 1$	$p_{\text{T}}(\ell_2)$
CR HF e	eee or eeμ	≥ 1	$= 1$	ℓ_0 and ℓ_1 are not from photon conversion $100 < H_T < 275$ GeV $E_{\text{T}}^{\text{miss}} > 35$ GeV total charge $= \pm 1$	$p_{\text{T}}(\ell_2)$
CR $t\bar{t}W^+$	SS, eμ or $\mu\mu$	≥ 4	≥ 2	$\lvert\eta(e)\rvert < 1.5$ when $N_b = 2$: $H_T < 500$ GeV or $N_{\text{jets}} < 6$ when $N_b \geq 3$: $H_T < 500$ GeV total charge > 0	N_{jets}
CR $t\bar{t}W^-$	SS, eμ or $\mu\mu$	≥ 4	≥ 2	$\lvert\eta(e)\rvert < 1.5$ when $N_b = 2$: $H_T < 500$ GeV or $N_{\text{jets}} < 6$ when $N_b \geq 3$: $H_T < 500$ GeV total charge < 0	N_{jets}
CR 1b(+)	SS+3L	≥ 4	$= 1$	ℓ_0 and ℓ_1 are not from photon conversion $H_T > 500$ GeV total charge > 0	N_{jets}
CR 1b(-)	SS+3L	≥ 4	$= 1$	ℓ_0 and ℓ_1 are not from photon conversion $H_T > 500$ GeV total charge < 0	N_{jets}
SR	SS+3L	≥ 6	≥ 2	$H_T > 500$ GeV	GNN score

Table 7.2: Definition of the control and signal regions. The N_{jets} (N_b) indicates the jet (b-tagged jet) multiplicity in the event. The H_T is defined as the scalar sum of the p_T of the leptons and jets. The ℓ_0, ℓ_1 and ℓ_2 refer to the highest p_T, second-highest p_T and third-highest p_T leptons, respectively. The η(e) refers to the electron pseudorapidity. Total charge is the sum of charges for all leptons. The photon conversion represents material and internal conversions.

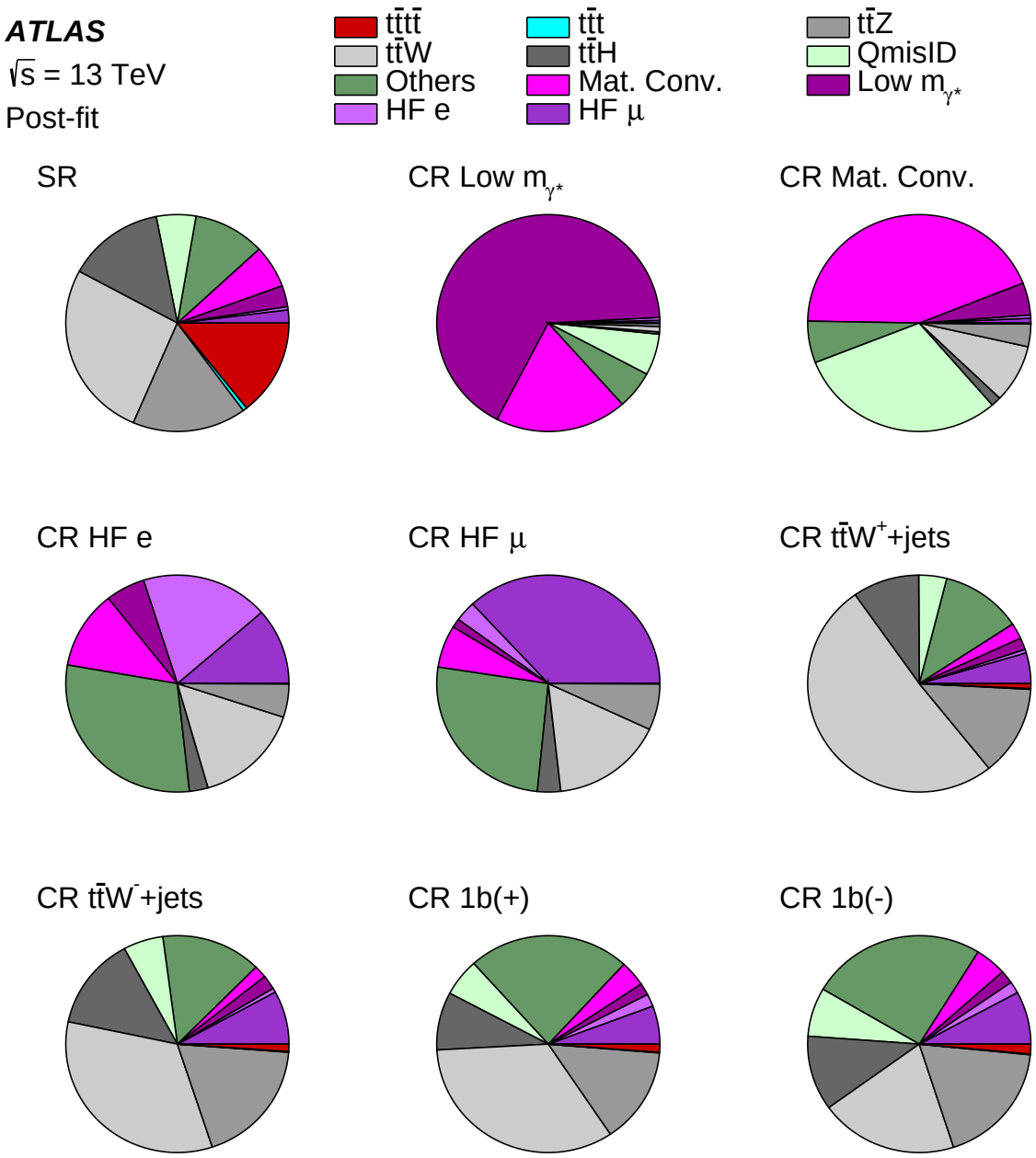

Figure 7.1: Post-fit pie chart for the background composition in each analysis region.

CRs based on specific electron selections with ECIDS applied. These regions include CR Low m_{γ^*}, CR Mat. Conv., and CR $t\bar{t}W$. The region definitions are elaborated in Section 7.2.2 and Section 7.2.3. The p_T and $|\eta|$ bins for estimating charge flip rates are selected to ensure fit convergence and maintain a total relative uncertainty below 30% in each bin.

Figure 8.4 summarizes the charge flip rates and their total uncertainties in the SR. Variations in charge flip rates are observed across CR Low m_{γ^*}, CR Mat. Conv., and CR $t\bar{t}W$ regions, ranging from 10^{-2} to 10^{-5}, with uncertainties varying from a few percent up to 30%. The charge flip rates increase with larger values of p_T and $|\eta|$ due to smaller curvature and denser materials, respectively. The low p_T and $|\eta|$ bins have larger uncertainties due to the limited QmisID contribution.

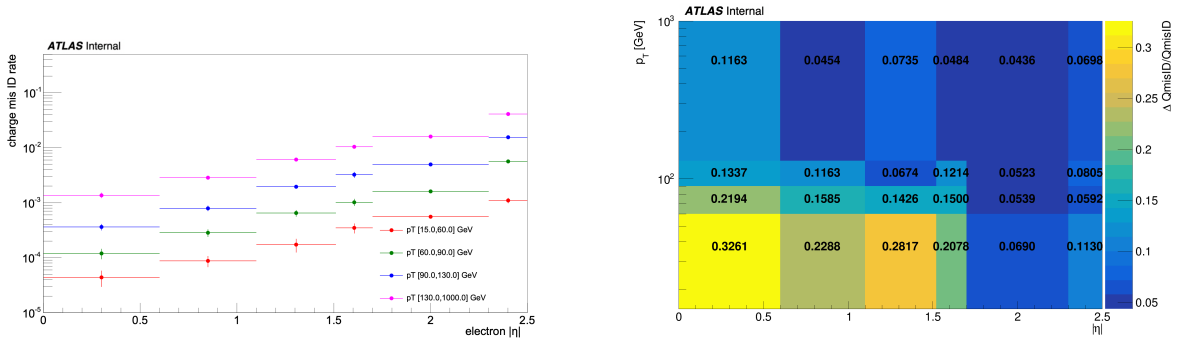

(a) Charge flip rate

(b) Total uncertainty

Figure 7.2: Charge misidentification rate and total relative uncertainty in the signal region.

7.2.2 Template Method

As detailed in Section 6.3.2, the template method estimates fake/non-prompt backgrounds, adjusting MC kinematics through floating normalizations. Control regions are designed to maximize the targeted background's purity and minimize contamination from other sources, thus reducing correlations between normalization factors. These regions

and their fitted distributions are included in a likelihood fit with the signal region. This allows simultaneous adjustment of background normalizations and signal strength. The results of simultaneous fits are summarized in Section 7.2.4. The control regions related to fake estimation are defined as follows:

- CR Mat. Conv.: A same-sign di-electron or electron-muon pair is required, with at least an electron being a material conversion candidate, detailed in Section 5.3.1.4. Jet multiplicity is selected as 4 or 5 jets to be orthogonal to the SR, with at least one b-jet among the jets. $\mathrm{NF}_{\text{Mat. Conv.}}$ is constrained using counting only.

- CR Low m_{γ^*}: A same-sign di-electron or electron-muon pair is required, with all electrons not from material conversion but with at least one of the electrons being an internal conversion candidate. Jet multiplicity is selected as 4 or 5 jets to be orthogonal to the SR, with at least one b-jet among the jets. $\mathrm{NF}_{\text{Low } m_{\gamma^*}}$ is constrained using counting only.

- CR HF e: Trilepton events featuring at least two electrons (eee and $ee\mu$) and a total lepton charge of ± 1 are selected, with the leading two leptons being non-conversion candidates. Exactly one b-jet is required to be orthogonal to the SR. Kinematic selections are imposed to increase purity: $100 < H_T < 275$ GeV, and $E_T^{miss} > 35$ GeV. The transverse momentum of the third lepton $p_{\mathrm{T}}(\ell_2)$ is utilized in a fit to constrain the $\mathrm{NF}_{\text{HF } e}$.

- CR HF μ: Trilepton events featuring at least two muons ($\mu\mu\mu$ and $\mu\mu e$) and a total lepton charge of ± 1 are selected, with all leptons being non-conversion candidates. Exactly one b-jet is required to be orthogonal to the SR. Kinematic selections are imposed to increase purity: $100 < H_T < 300$ GeV, and $E_T^{miss} > 50$ GeV. The $p_{\mathrm{T}}(\ell_2)$ is utilized in a fit to constrain the $\mathrm{NF}_{\text{HF } \mu}$.

7.2.3 $t\bar{t}W$ Data-driven Method

A $t\bar{t}W$ data-driven method, outlined in Section 6.3.3, is employed to improve the modeling of $t\bar{t}W$+jets, especially the showering part of $t\bar{t}W$+jets. A parameterized function that describes the scaling patterns for QCD jets is utilized following Ref. [274]. The scaling patterns for QCD jets can be described as the ratio of successive exclusive jet cross sections,

$$R_{(n+1)/n} = e^{-b} + \frac{\bar{n}}{n+1} = a_0 + \frac{a_1}{1+(j'-4)}, \tag{7.1}$$

where n is the number of jets in addition to the hard process. The e^{-b} represents the staircase scaling with a constant ratio between the successive multiplicity cross sections. The $\frac{\bar{n}}{n+1}$ describes the Poisson scaling with a ratio of Poisson distribution with an expectation value $\bar{n}$ between the successive multiplicity cross sections. Staircase and Poisson scaling can be re-parameterized with a_0 and a_1 to describe the showering of $t\bar{t}W$+jets. The j' is defined as the inclusive number of jets with $j' \geq 4$, and $n \equiv j' - 4$ is defined as the number of jets in the showering part of $t\bar{t}W$ for the dominant SS channel at the tree level. As the studies in Ref. [274], the staircase scaling (a_0) is sensitive to the high jet multiplicity events, and the Poisson scaling (a_1) is sensitive to the low jet multiplicity events.

The N_{jets} distribution of $t\bar{t}W$+jets can be described by the product of the ratios of successive multiplicity cross sections,

$$\text{Yield}_{\text{t}\bar{\text{t}}\text{W}(j)} = \text{Yield}_{\text{t}\bar{\text{t}}\text{W}(4\text{jet})} \times \Pi_{j'=4}^{j'=j-1} \left(a_0 + \frac{a_1}{1+(j'-4)} \right), \tag{7.2}$$

where j is required to be larger than 4. Two normalization factors ($\text{NF}_{\text{t}\bar{\text{t}}\text{W}^{\pm}(4\text{jet})}$) are applied to $t\bar{t}W^{\pm}$ MC at 4-jet bin to control the normalizations for $t\bar{t}W^{+}$ and $t\bar{t}W^{-}$, respectively. The $\text{Yield}_{\text{t}\bar{\text{t}}\text{W}(4\text{jet})}$ is re-parameterized as $\text{NF}_{\text{t}\bar{\text{t}}\text{W}(4\text{jet})} \times \text{MC}(4\text{jet})$. Given the small impact when splitting into $t\bar{t}W^{+}$ and $t\bar{t}W^{-}$, the same scaling of the N_{jets} distri-

butions in $t\bar{t}W^+$ and $t\bar{t}W^-$ productions are used. Therefore, a_0 and a_1 simultaneously control $t\bar{t}W^+$ and $t\bar{t}W^-$ N_{jets} distributions. The final $t\bar{t}W$ N_{jets} parameterized function is encoded in $\text{NF}_{\text{t}\bar{\text{t}}\text{W}(j)}$, where the $\text{NF}_{\text{t}\bar{\text{t}}\text{W}(j)}$ for $t\bar{t}W$ events with $j > 4$ is defined as

$$\text{NF}_{\text{t}\bar{\text{t}}\text{W}(j)} = \left(\text{NF}_{\text{t}\bar{\text{t}}\text{W}^+(4\text{jet})} + \text{NF}_{\text{t}\bar{\text{t}}\text{W}^-(4\text{jet})}\right) \times \Pi_{j'=4}^{j'=j-1}\left(a_0 + \frac{a_1}{1+(j'-4)}\right). \tag{7.3}$$

The $t\bar{t}W$ events with $1 \leq N_{\text{jets}} \leq 3$ are fitted by propagating the normalization used at the 4-jet bin without additional shape corrections due to negligible contributions. The $t\bar{t}W$ events with $N_{\text{jets}} \geq 10$ is represented by summing up the overflow from $N_{\text{jets}} = 10$ to $N_{\text{jets}} = 12$, which is $\Sigma_{j=10}^{j=12}\Pi_{j'=4}^{j'=j-1}[a_0 + \frac{a_1}{1+(j'-4)}]$. Events with $N_{\text{jets}} \geq 13$ are negligible, which are lower than $O(10^{-3})$ events.

The $t\bar{t}W$ N_{jets} parameterized function with two normalizations ($\text{NF}_{\text{t}\bar{\text{t}}\text{W}^\pm(4\text{jet})}$) and two scaling factors (a_0 and a_1) are simultaneously fitted with the fake NFs in the fit. Given that non-N_{jets} kinematics are based on the MC simulations, additional systematic uncertainties are applied to $t\bar{t}W$ to consider various MC setups, shown in Section 7.4.2.2. Four additional control regions, shown in Table 7.2, were built to parameterize the $t\bar{t}W$+jets scaling with N_{jets} as fitted distribution. The control regions for $t\bar{t}W$ data-driven method are defined as follows:

- CR $t\bar{t}W^+$ and CR $t\bar{t}W^-$: two same-sign muons or electron-muon are selected with total lepton charge being either positive (CR $t\bar{t}W^+$) or negative (CR $t\bar{t}W^-$). To be orthogonal to the CR Mat. Conv. and CR Low m_{γ^*} regions, both leptons are required to be non-conversion candidates, and the absolute value of electron pseudo-rapidity is selected to be less than 1.5. To be enriched by $t\bar{t}W$ and close to the SR, at least four jets and two b-jets are required. The orthogonality with the SR is ensured by requiring $H_T < 500$ GeV or $N_{\text{jets}} < 6$ in the $N_{b\text{-jets}} = 2$ region and by requiring $H_T < 500$ GeV in the $N_{b\text{-jets}} \geq 3$ region. The N_{jets} distribution is fitted in these regions for $t\bar{t}W$ events with $N_{b\text{-jets}} \geq 2$. These regions are limited in low

N_{jets} due to the orthogonal cut.

- CR 1b(+) and CR 1b(-): same-sign dilepton and trilepton events, with at least four jets, exactly one b-jet, and $H_T > 500$ GeV are required to extend to high N_{jets} but orthogonal to the SR. This region is split into two regions with a positive (CR 1b(+)) or negative (CR 1b(-)) total lepton charge. The N_{jets} distribution is fitted in these regions to describe $t\bar{t}W$ N_{jets} parameterized function with high N_{jets} events using $N_{b\text{-jets}} = 1$, assuming similar N_{jets} shape between $N_{b\text{-jets}} = 1$ and $N_{b\text{-jets}} \geq 2$.

A statistical-only (stat-only) fit to the $t\bar{t}W$ MC prediction in CR 1b(+) and CR 1b(-) confirms the validity of parameterized function in Equation (7.3), as seen in Figure 7.3. Several injection studies are performed to fit the alternative pseudo-data of $t\bar{t}W$ from scale variations, different generators, or enhanced $t\bar{t}W$ contribution to match the data distribution in the $t\bar{t}W$ VR. The injection studies show that the $t\bar{t}W$ data-driven method can well describe the $t\bar{t}W$ MC simulations and does not introduce biases, with the maximum impact on the signal strength at a 2% level.

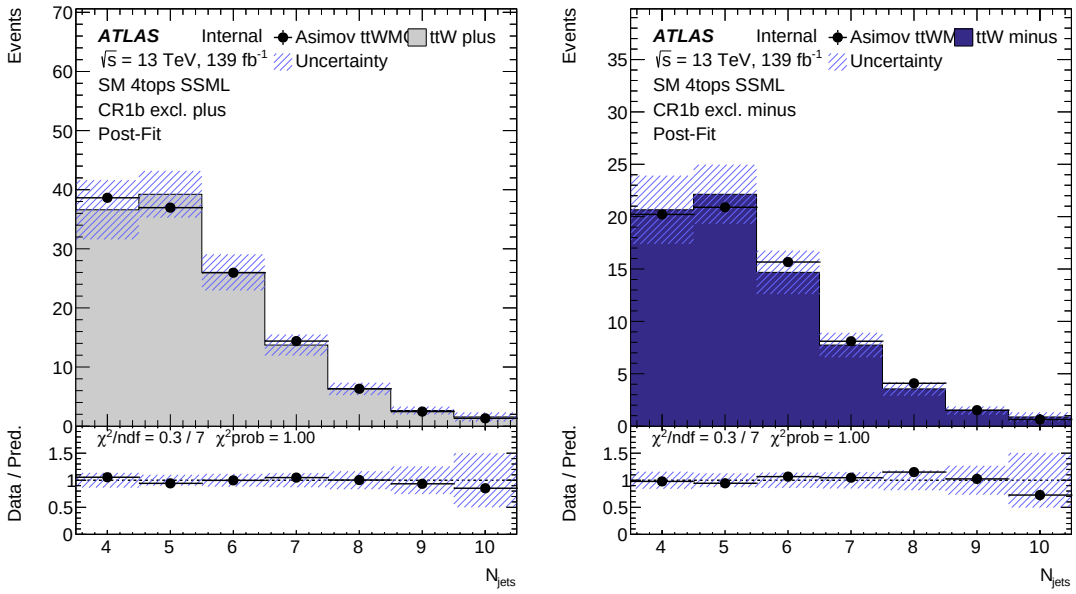

(a) CR 1b(+) (b) CR 1b(-)

Figure 7.3: N_{jets} distributions with post-fit estimation from a stat-only fit to $t\bar{t}W$ MC simulation with Equation (7.3) in the (a) CR 1b(+) and (b) CR 1b(-) regions.

7.2.4 Results

The final fit to the observed data, outlined in Section 7.5, is performed simultaneously in the signal and control regions with fake/non-prompt lepton background NF, $t\bar{t}W$ data-driven parameters, and $t\bar{t}t\bar{t}$ signal strength. The NFs of the different fake/non-prompt lepton background sources and the parameters of the $t\bar{t}W$ data-driven background model determined from the fit are shown in Table 7.3 and Table 7.4. Figure 7.4 and Figure 7.5 present the post-fit distributions in the control regions after the final fit to data. The $t\bar{t}W$ data-driven post-fit results are compatible with dedicated $t\bar{t}W$ unfolding analysis [148].

Fake/non-prompt background	$\mathrm{NF}_{\text{Mat. Conv.}}$	$\mathrm{NF}_{\text{Low } m_{\gamma^*}}$	$\mathrm{NF}_{\text{HF } e}$	$\mathrm{NF}_{\text{HF } \mu}$
Value	$1.80^{+0.47}_{-0.41}$	$1.08^{+0.37}_{-0.31}$	$0.66^{+0.75}_{-0.46}$	$1.27^{+0.53}_{-0.46}$

Table 7.3: The normalization factors for fake and non-prompt lepton background after the fit to data. The uncertainties include both statistical and systematic uncertainties. The nominal pre-fit value for these factors is 1.

$t\bar{t}W$ background	a_0	a_1	$\mathrm{NF}_{t\bar{t}W^+(\text{4jet})}$	$\mathrm{NF}_{t\bar{t}W^-(\text{4jet})}$
Value	0.51 ± 0.10	$0.22^{+0.25}_{-0.22}$	$1.27^{+0.25}_{-0.22}$	$1.11^{+0.31}_{-0.28}$

Table 7.4: The $t\bar{t}W$ modeling parameters after the fit to data. The uncertainties include both statistical and systematic uncertainties. The nominal pre-fit value for a_0 and a_1 is 0, while the nominal pre-fit value for $\mathrm{NF}_{t\bar{t}W^+(\text{4jet})}$ and $\mathrm{NF}_{t\bar{t}W^-(\text{4jet})}$ is 1.

The $t\bar{t}W$ VRs are defined to assess the $t\bar{t}W$ background modeling due to the charge asymmetric nature of $t\bar{t}W$ process. The difference between the number of events with a positive sum and those with a negative sum of the charges of the selected leptons ($N_+ - N_-$) is selected to define the $t\bar{t}W$ VR. This procedure constructs $t\bar{t}W$ dominant regions and removes charge symmetric processes, including $t\bar{t}t\bar{t}$ and most non-$t\bar{t}W$ backgrounds. The $t\bar{t}W$ VR is additionally required with selections of the sum of the four $t\bar{t}W$ CRs and the SR. Figure 7.6 shows good agreement between data and post-fit prediction. In addition, a

$t\bar{t}Z$ VR is defined with trilepton events within a Z-mass window, at least four jets, and at least two b-jets. Figure 7.7 presents the comparison between data and post-fit predictions in the $t\bar{t}Z$ VR.

7.3 Multivariate Analysis

The MVA techniques are used to separate the signal from the background in the SR. A GNN is used as the default method, while a BDT is employed as a separate but complementary approach for cross-checking. GNN and BDT trainings are conducted with events passing the SR requirement, as shown in Section 7.1.

7.3.1 Graph Neural Network

The GNN employs the graph_nets library [275] from TensorFlow [276] for event classification. Each event is depicted as a fully connected graph, with nodes representing the reconstructed jets, electrons, muons, and E_T^{miss}. Each node's features encompass the object's four-momentum, the jet PCBT score, the lepton charge, and an integer labeling the type of object represented by the node. The edges between these nodes are calculated to carry the angular separation between the objects, including $\Delta\eta$, $\Delta\phi$, and ΔR. Additionally, the jet multiplicity of the event is included as a global feature.

The GNN model comprises the encoder, graph network, and decoder. The encoder converts the input node, edge, and global features into a latent space. The graph network block, iterating four times, passes information between different graph features. The decoder places a multilayer perceptron (MLP) on the global latent space, which produces the binary output for the probability of an event ranging from 0 (background-like) to 1 ($t\bar{t}t\bar{t}$-like). The Receiver Operating Characteristic (ROC) curve is used as the metric to assess the performance of the MVA models. The node, edge, and global features, as well as the GNN hyperparameters, are optimized to maximize the area under the ROC

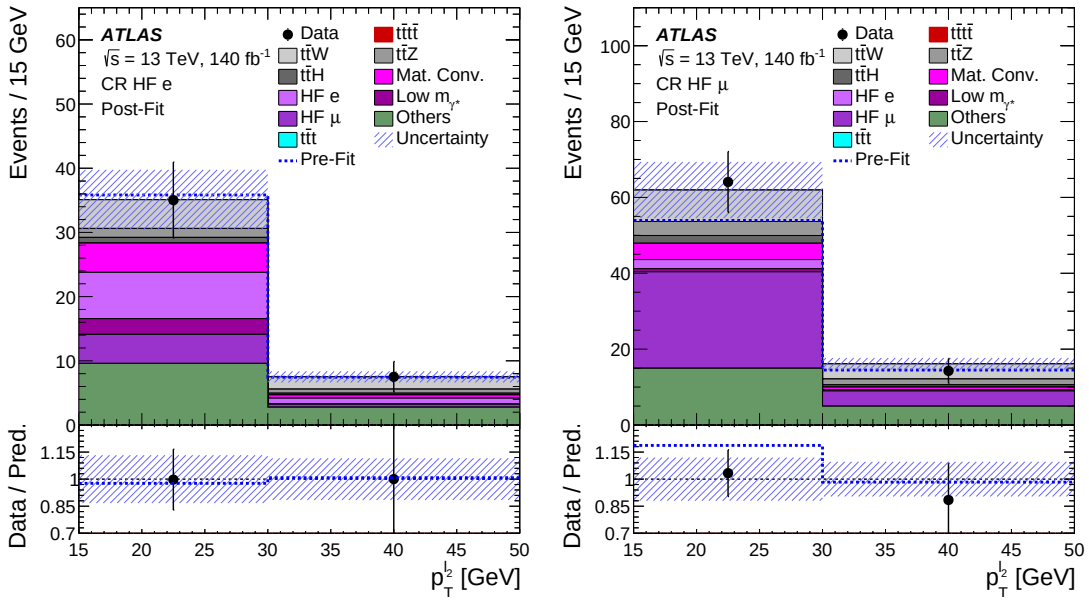

(a) CR HF e

(b) CR HF μ

(c) CR Mat. Conv.

(d) CR Low m_{γ^*}

Figure 7.4: Comparison between data and predictions in the fake/non-prompt lepton background CRs after the fit to data. Pre-fit distributions are added as the dashed line in each plot. The ratio of the data to the total post-fit prediction is shown in the lower panel. The shaded band represents the total post-fit uncertainty in the prediction.

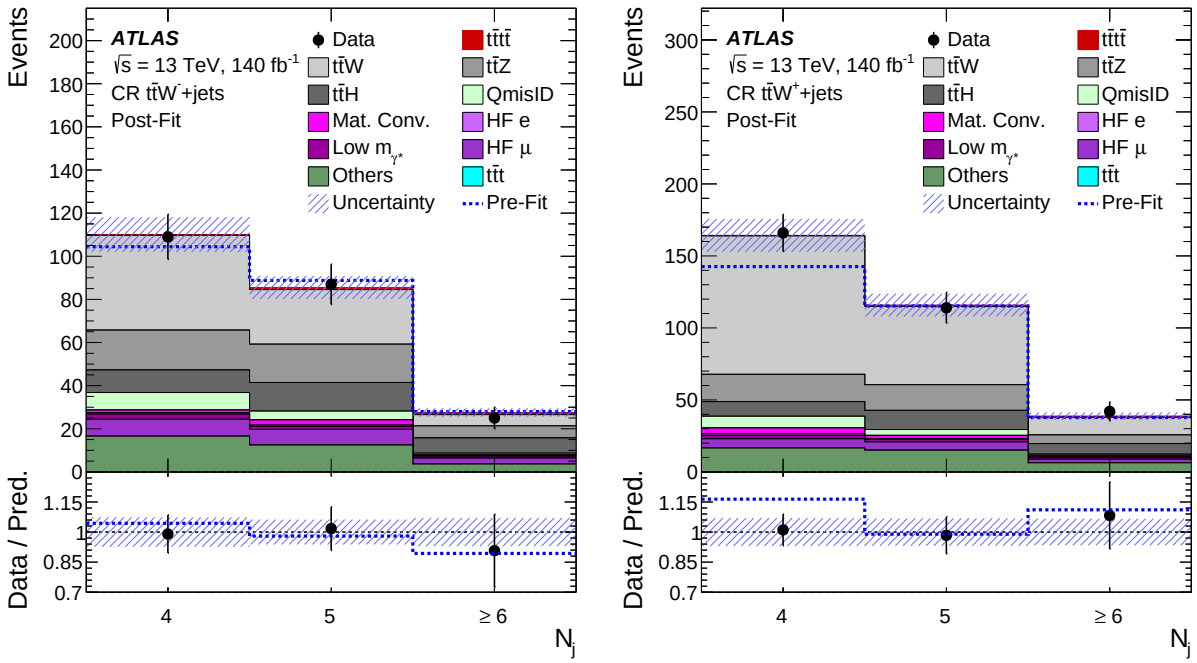

(a) CR $t\bar{t}W^-$

(b) CR $t\bar{t}W^+$

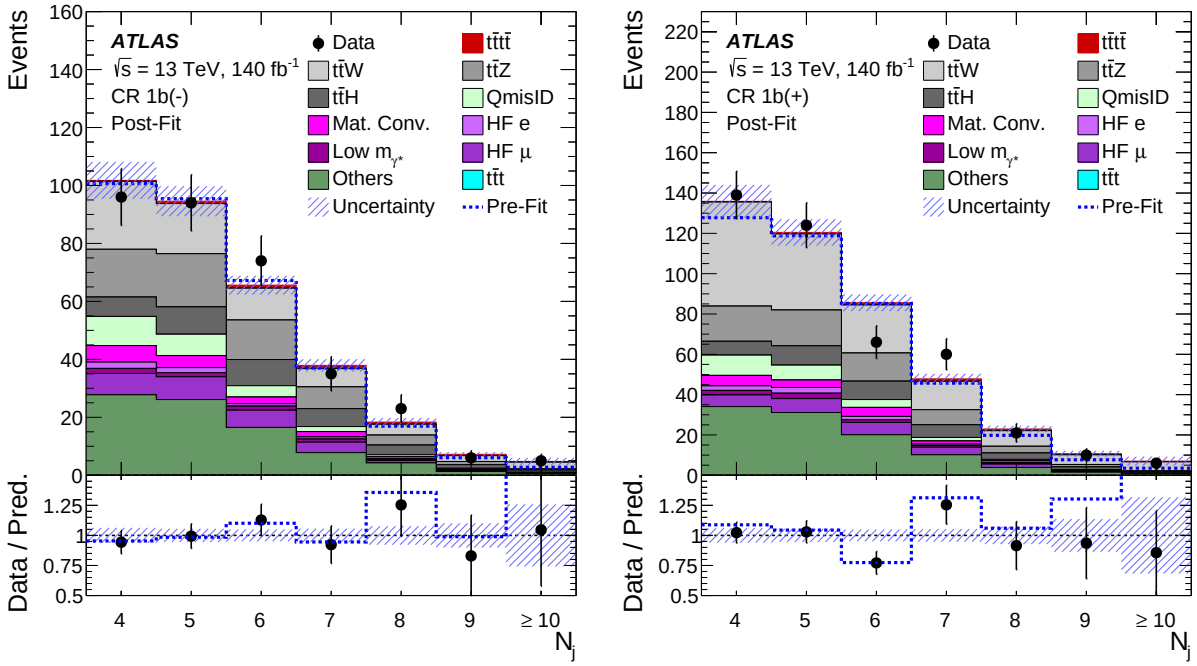

(c) CR 1b(-)

(d) CR 1b(+)

Figure 7.5: Post-fit distributions in the $t\bar{t}W$ CRs after the fit to data. Pre-fit distributions are added as the dashed line in each plot. The ratio of the data to the total post-fit prediction is shown in the lower panel. The shaded band represents the total post-fit uncertainty in the prediction.

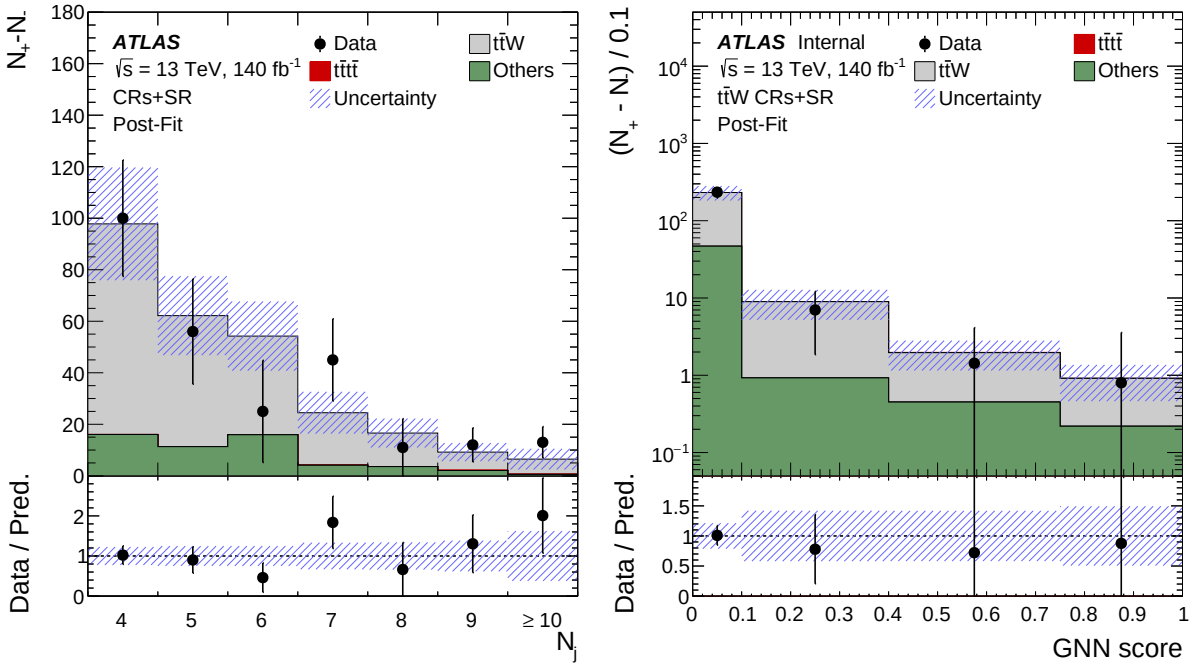

(a) (b)

Figure 7.6: Comparison between data and predictions for the (a) N_{jets} and (b) GNN (see Section 7.3) distributions in the $t\bar{t}W$ VR with the sum of the four $t\bar{t}W$ CRs and the SR after the fit to data. The y-axis label $N_+ - N_-$ represents the difference between the number of events with a positive sum and those with a negative sum of the charges of the selected leptons. The ratio of the data to the total post-fit prediction is shown in the lower panel. The shaded band represents the post-fit uncertainty from $t\bar{t}W$ data-driven parameters in the prediction.

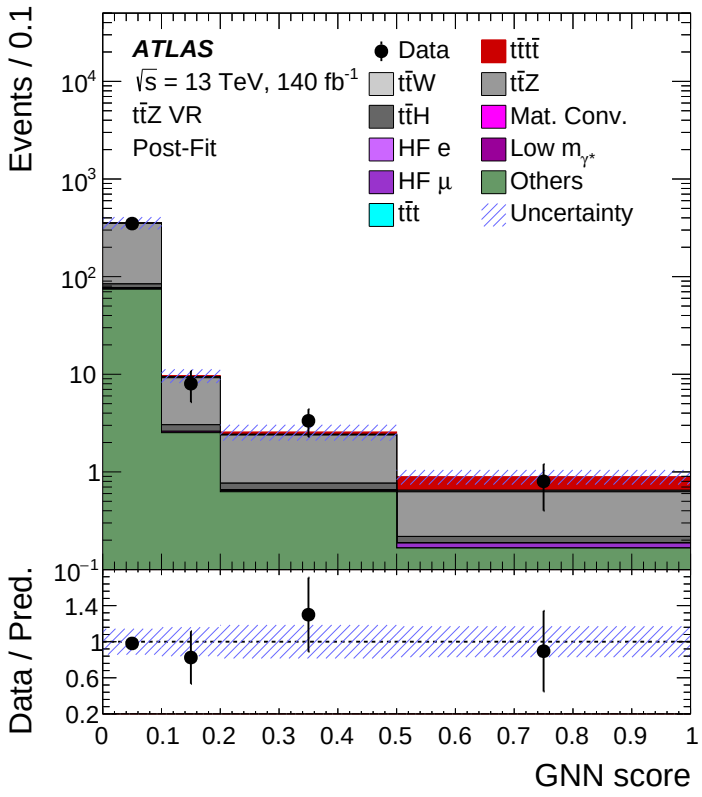

Figure 7.7: Comparison between data and predictions for the GNN (see Section 7.3) distributions in the $t\bar{t}Z$ VR after the fit to data. The ratio of the data to the total post-fit prediction is shown in the lower panel. The shaded band represents the total post-fit uncertainty in the prediction.

curve (AUC) of the GNN event classifier.

The LO $t\bar{t}t\bar{t}$ MC simulation is utilized as the signal, and MC simulations of all the backgrounds are used as the background. The application of MC event weights in the training reduces the GNN performance due to the loss of effective training statistics. Therefore, events are treated uniformly during training without applying any MC event weight. A flat weight of 1 is assigned to all events in the training dataset, except $t\bar{t}W$ events, which are applied with a higher flat weight of 3. The enhanced weight for $t\bar{t}W$ is used to improve the separation of the $t\bar{t}W$ background without sacrificing overall background separation. The yields of signal and background are reweighted to be the same in the training to prevent bias towards the majority class.

A k-fold cross-validation method is applied to increase the training statistics. The fold number is optimized to be 6, maximizing the AUC. The testing AUC, calculated with NLO $t\bar{t}t\bar{t}$ and backgrounds with MC weights applied, reaches 0.903. Figure 7.8 shows the GNN output distributions for the testing and training. Figure 7.9 compares data and post-fit predictions in the signal region with GNN ≤ 0.6. Figure 7.10 presents the GNN output distribution alongside the data and post-fit signal and background predictions. Good agreement on data and post-fit prediction is observed.

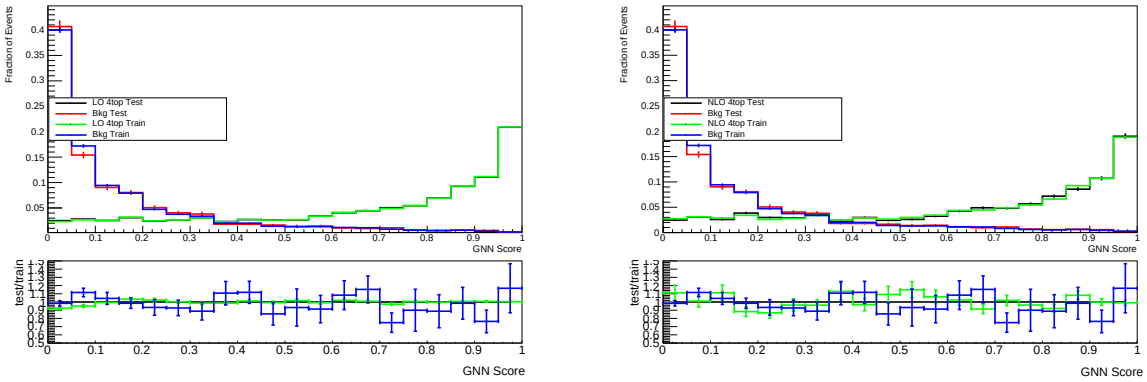

(a) (b)

Figure 7.8: (a) GNN distribution for training and testing using LO $t\bar{t}t\bar{t}$ and (b) GNN distribution for training and testing using NLO $t\bar{t}t\bar{t}$ in one of the folds.

7.3.2 Boosted Decision Trees

Following the strategy of the $t\bar{t}t\bar{t}$ evidence analysis [52], a BDT discriminant is employed as a cross-check method. The BDT is trained with the Extreme Gradient Boosting (XGBoost) algorithm [277]. The BDT model integrates high-level input features such as jet activities, lepton activities, missing transverse momentum, b-tagging information, and angular topologies. These features are derived from the topological characteristics of the events, with the detailed descriptions provided in Table 7.5. The hyperparameters of the BDT are optimized to maximize the AUC and enhance the significance of $t\bar{t}t\bar{t}$ derived from likelihood fits.

Similar to the setup for the GNN, both the LO $t\bar{t}t\bar{t}$ and background MC simulations are used in training. However, unlike the GNN approach, MC event weights are applied to each event during the BDT training, with events carrying negative weights excluded. Reweighting is performed to the $t\bar{t}W$ events with $N_{\text{jets}} = 7$ and $N_{\text{jets}} \geq 8$, adjusting relative contributions from 7% to 15% of total background, respectively. This reweighting enhances the discrimination between $t\bar{t}t\bar{t}$ and $t\bar{t}W$, thereby improving the significance of $t\bar{t}t\bar{t}$ signals. Additionally, the yields of signal and background are reweighted to be the same in the training to prevent bias towards the majority class.

A 2-fold cross-validation process is implemented to split backgrounds into training, testing, and validation data, allocating 40% of the events each to training and testing and 20% for validation. The $t\bar{t}t\bar{t}$ is trained with inclusive LO $t\bar{t}t\bar{t}$ samples without further splitting, and the optimization is evaluated with 80% of nominal SM $t\bar{t}t\bar{t}$ NLO events. Figure 7.11 presents the schematic summary of the strategy. The AUC evaluated in the testing and validation datasets are 0.873 and 0.874, respectively. Figure 7.12 illustrates the BDT distributions for training, testing, and validation, showing a good agreement among them. The consistency across training, testing, and validation indicates the absence of overtraining in the BDT models. Figure 7.13 presents the BDT distribution comparison

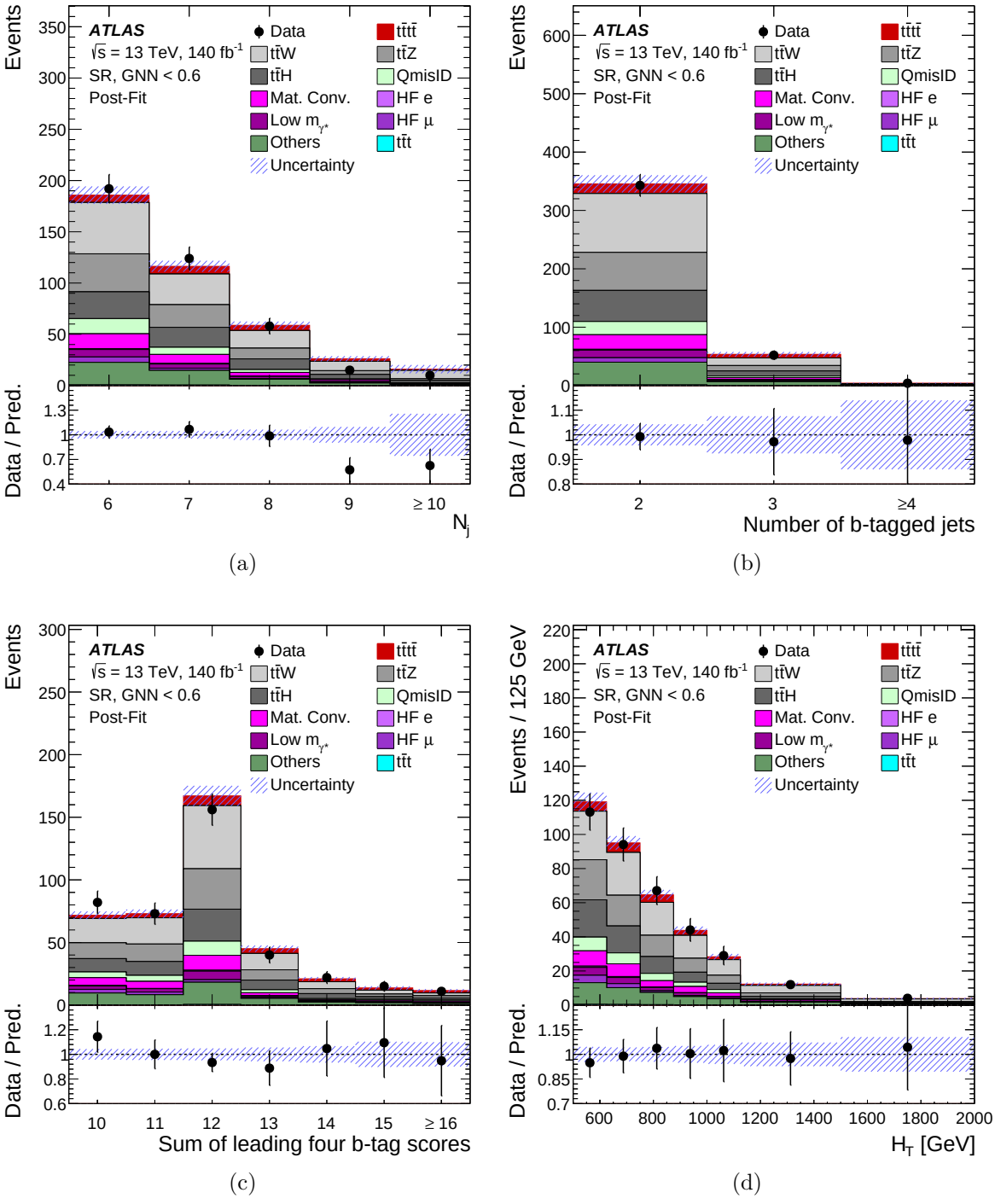

Figure 7.9: Comparison between data and post-fit predictions after the fit to data in the signal region with GNN < 0.6 for the distributions of (a) the number of jets, (b) the number of b-jets, (c) the sum of the four highest PCBT scores of jets in the event, and (d) the H_T. The uncertainty band includes the total uncertainty on the post-fit computation. The lower panel illustrates the ratio of the observed data to the total post-fit computation. The first and last bins contain the underflow and overflow events, respectively.

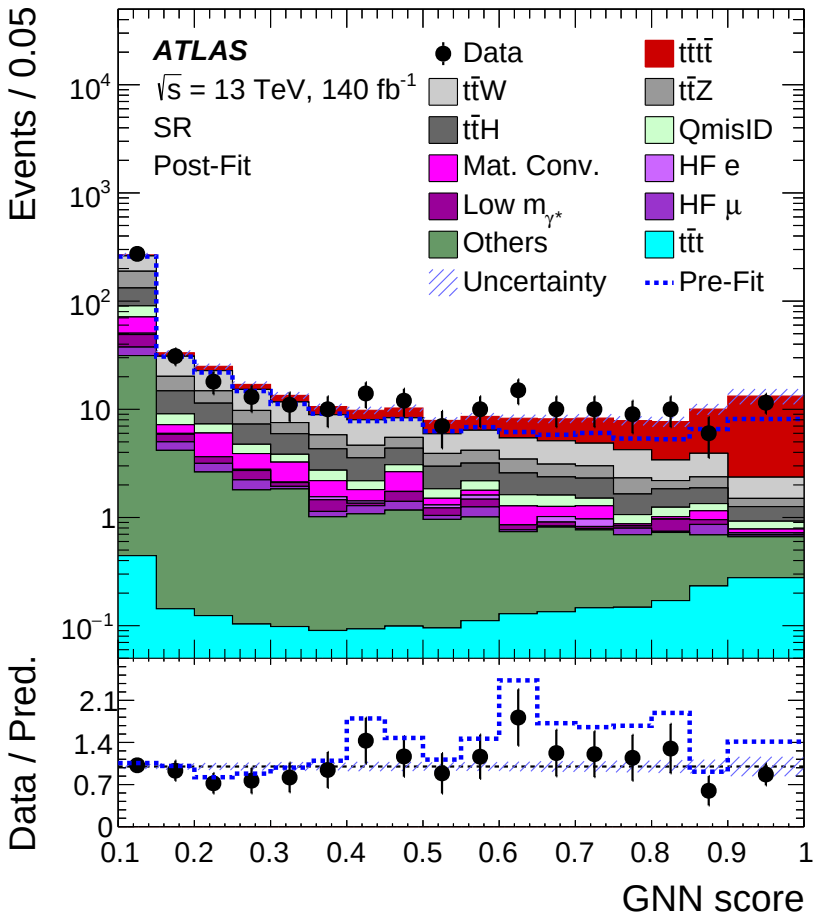

Figure 7.10: Comparison between data and predictions of GNN distribution in SR after the fit to data. The uncertainty band includes the total uncertainty on the post-fit computation. The lower panel illustrates the ratio of the observed data to the total post-fit computation. The dashed line represents the ratio of the observed data to the total pre-fit predictions.

between data and predictions after the fit to data using BDT distribution in the SR. Good agreement on data and post-fit modeling is observed.

Feature	Definition	SM	BSM
$\sum_{i=0}^{3} w_{\mathrm{PCBT}}$	Sum of PCBT scores over four jets with leading b-tagging raw scores	1	1
N_{jets}	Jet multiplicity	5	13
H_{T}(no lead jet)	Scalar sum of p_T of all leptons and jets except the leading jet	4	2
$p_{\mathrm{T}}(j_0)$	p_T of leading jet	8	4
$p_{\mathrm{T}}(j_1)$	p_T of sub-leading jet	11	7
$p_{\mathrm{T}}(j_5)$	p_T of 6th leading jet	2	6
$p_{\mathrm{T}}(b_0)$	p_T of leading b-tagged jet	6	9
$p_{\mathrm{T}}(\ell_0)$	p_T of leading lepton	12	10
E_T^{miss}	Missing transverse momentum	7	5
$\Delta R(\ell,\ell)_{\mathrm{min}}$	The minimum angular separation between any lepton pair	9	8
$\Delta R(\ell,b)_{\mathrm{max}}$	The maximum angular separation between leptons and b-tagged jets	10	11
$\Delta R(j,b)_{\mathrm{min}}$	The minimum angular separation between b-tagged jets and jets	13	12
$\sum \Delta R(\ell,\ell)$	Sum of the angular separation between all lepton pairs	3	3

Table 7.5: List of the input features to the BDT. The last two columns indicate the ranking of the feature importance evaluated with the XGBoost for the BDT in SM $t\bar{t}t\bar{t}$ analysis and the SM BDT in BSM $t\bar{t}t\bar{t}$ analysis.

Figure 7.11: The scheme summary of BDT training strategy, including the sample fractions and the 2-fold method with additional validation set.

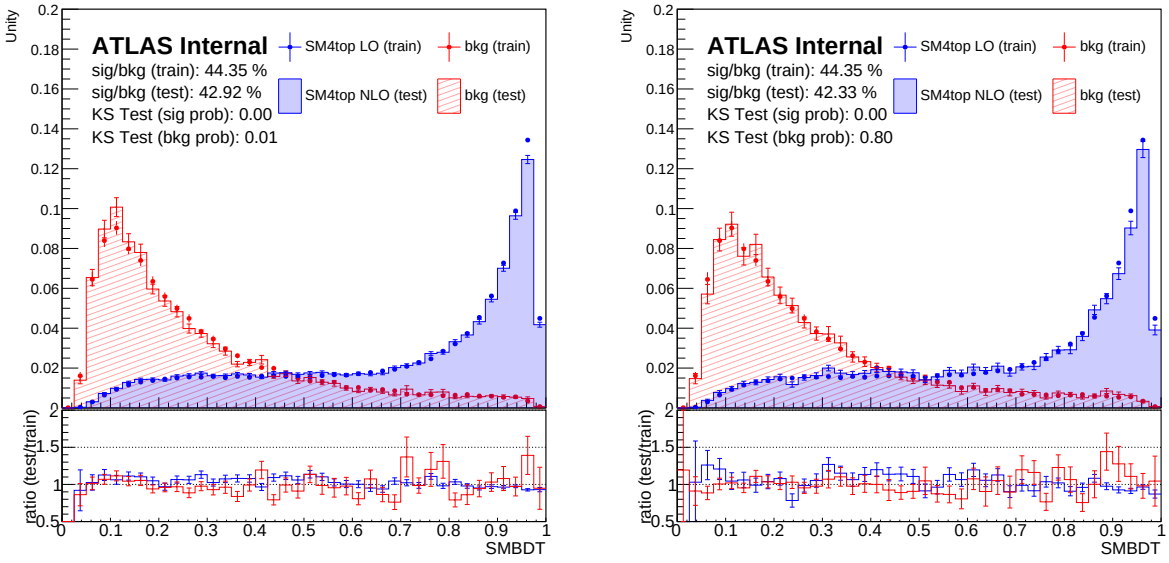

(a) (b)

Figure 7.12: BDT distributions for (a) training and testing datasets and (b) for training and validation datasets. The training data is with SM $t\bar{t}t\bar{t}$ LO events and backgrounds without negative weight events. The testing and validation datasets are with SM $t\bar{t}t\bar{t}$ NLO events and backgrounds with all weight included.

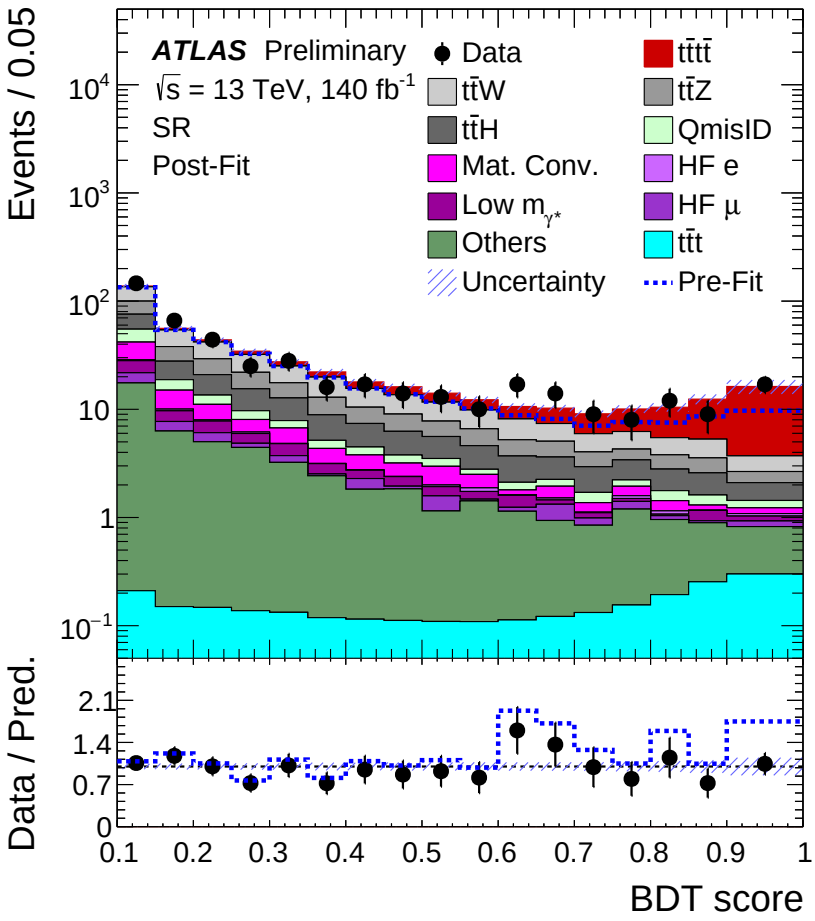

Figure 7.13: Comparison between data and predictions of BDT distribution in SR after the fit to data with BDT distribution. The uncertainty band includes the total uncertainty on the post-fit computation. The lower panel illustrates the ratio of the observed data to the total post-fit computation. The dashed line represents the ratio of the observed data to the total pre-fit predictions.

7.4 Systematic Uncertainties

A summary of the systematic uncertainties applied in this analysis is described in this section. Table 7.6 and Table 7.7 summarize the list of systematic uncertainties impacting the SM $t\bar{t}t\bar{t}$ analysis. This section focuses on the theoretical systematic uncertainties for signal and background modeling. The experimental systematic uncertainties are discussed in Section 6.4.

Systematic uncertainty	Components	Typical size [%]
Luminosity	1	0.83
Pile-up reweighing	1	$O(1) \sim O(10)$
Physical Objects		
Electron	7	$O(10^{-2}) \sim O(1)$
Muon	12	$O(10^{-2}) \sim O(1)$
Jet energy scale and resolution	44	$O(10^{-2}) \sim O(10)$
Jet vertex tagging	1	$O(10^{-1}) \sim O(1)$
Jet b-tagging	85	$O(10^{-2}) \sim O(1)$
Jet b-tagging for high p_T	3	$O(10^{-2}) \sim O(10^{-1})$
E_T^{miss}	3	$O(10^{-2}) \sim O(10^{-1})$
Total (Experimental)	157	
Electron charge misidentification	1	$10 \sim 15$
Fake/Non-prompt Lepton Uncertainty		
Material conversions	1	$O(1) \sim 20$
Internal conversions	1	$O(1) \sim 10$
HF non-prompt leptons	2	$8 \sim 13$
Other fake leptons	2	30 & 100
Additional heavy flavor jets on $t\bar{t}$	2	$O(1) \sim 30$
Total (Reducible Background)	9	

Table 7.6: Sources of experimental and fake/non-prompt lepton uncertainties considered in the analysis. The uncertainties from "Luminosity" and "Other fake leptons" are taken as normalization only in all regions. Other uncertainties affect the normalization and shape of the fitted distributions and/or the acceptance into the fit regions. The 'Components' column indicates the components of the systematic uncertainties. The decorrelations of experimental systematic uncertainties are summarized in Table 6.4. The 'Typical size' column summarizes ranges of uncertainty sizes in the signal region.

Systematic uncertainty	Components	Typical size [%]
$t\bar{t}t\bar{t}$ **modeling**		
Cross section	1	20
Generator choices	1	$O(1) \sim 20$
Parton shower and hadronization model	1	~ 6
Renormalization and factorization scales	1	$1 \sim 3$
PDF	1	1
$t\bar{t}t$ **modeling**		
Cross section	1	35
Renormalization and factorization scales	1	$O(10^{-1}) \sim 1$
Additional heavy flavor jets	1	$O(1) \sim 18$
$t\bar{t}H$ **modeling**		
Cross section	1	10
Generator choices	1	~ 8
Parton shower and hadronization model	1	$O(1) \sim 14$
Renormalization and factorization scales	1	$3 \sim 8$
PDF	1	1
Additional heavy flavor jets	2	$O(1) \sim 20$
$t\bar{t}W$ **modeling**		
Generator choices	1	$O(1) \sim 10$
Renormalization and factorization scales	1	$O(1) \sim 80$
Additional heavy flavor jets	2	$O(1) \sim 40$
$t\bar{t}Z$ **modeling**		
Cross section	1	12
Generator choices	1	$O(1) \sim 40$
Renormalization and factorization scales	1	$O(1) \sim 10$
PDF	1	1
Additional heavy flavor jets	2	$O(1) \sim 20$
VV **modeling**		
Cross section	3	60
Renormalization and factorization scales	1	~ 25
Additional heavy flavor jets	2	$O(1) \sim 50$
Other background modeling		
Cross section	3	30 & 50
Additional heavy flavor jets	2	$O(1) \sim 30$
Total (Signal and Irreducible Background)	36	
Total (Overall)	202	

Table 7.7: Sources of theoretical systematic uncertainty considered in the analysis. The uncertainties from "Luminosity", "Cross section", and "PDF" are taken as normalization only for all processes in all regions. Other uncertainties affect the normalization and shape of the fitted distributions and/or the acceptance into the fit regions. The 'Components' column indicates the components of the systematic uncertainties. The 'Typical size' column summarizes ranges of uncertainty sizes in the signal region.

7.4.1 Uncertainties on $t\bar{t}t\bar{t}$ Signal Modeling

Several factors influencing the modeling of $t\bar{t}t\bar{t}$ production are considered for various configurations. The uncertainty is evaluated with an alternative sample from SHERPA 2.2.11 to account for different ME, PS, and hadronization models. Additionally, a separate uncertainty specific to the choice of PS and hadronization models is estimated using samples from MADGRAPH5_aMC@NLO interfaced with HERWIG 7.04. Alternative samples are discussed in detail in Section 6.2.1. The uncertainty due to the missing higher-order QCD corrections is assessed by varying the μ_R and μ_F scales simultaneously by factors of 0.5 and 2 relative to the central values. The PDF uncertainty is evaluated as the RMS of the predictions from the 100 replicas of the `NNPDF30_nlo_as_0118` PDF set by the PDF4LHC prescription [278]. The effect of PDF variation on the shape of the fitted distributions was found to be negligible. A conservative uncertainty of 1% is considered. Additionally, an uncertainty of 20% on the total cross section, calculated from a prediction at NLO in QCD+EW [123], is considered when measuring the $t\bar{t}t\bar{t}$ signal strength.

7.4.2 Uncertainties on Background Modeling

7.4.2.1 Uncertainties on $t\bar{t}t$ Background

A cross-section uncertainty of 35% from the theoretical calculation is set for $t\bar{t}t$, including the effects of scale variations on the μ_R and μ_F [125], uncertainties from the PDF choices, acceptance difference between 5FS and 4FS MC simulations, and the missing EW LO contribution. An uncertainty of 50% is applied for $t\bar{t}t$ events with at least four truth b-jets. Uncertainties related to the μ_R and μ_F scale variations are computed by varying both μ_R and μ_F scales simultaneously by factors of 0.5 and 2 with respect to the central values.

7.4.2.2 Uncertainties on $t\bar{t}H$, $t\bar{t}W$ and $t\bar{t}Z$ Backgrounds

Theoretical uncertainties for $t\bar{t}H$, $t\bar{t}W$, and $t\bar{t}Z$ from various sources are assessed in a similar way. These include uncertainties related to the choice of different generators, scale variations, PDF variations, total cross section, and the presence of additional heavy-flavor jets.

Table 7.8 summarizes the generator uncertainties for $t\bar{t}H$, $t\bar{t}W$, and $t\bar{t}Z$ processes. These uncertainties are evaluated by comparing the nominal and alternative MC predictions, as outlined in Section 6.2.3 and Section 6.2.4. Specifically, for the $t\bar{t}W$ generator uncertainty, the alternative $t\bar{t}W$ is reweighed to align with the nominal $t\bar{t}W$ N_{jets} distribution in CR 1b(+) and CR 1b(-), described in Section 7.2.3. This avoids double-counting systematic effects in N_{jets} modeling, given that N_{jets} distribution is estimated using the data-driven method. For $t\bar{t}H$, an additional uncertainty associated with the PS is estimated by comparing $t\bar{t}H$ PowhegBox+Pythia8 with PowhegBox+Herwig 7.

Process	Nominal	Alternative	Purpose
$t\bar{t}H$	PowhegBox+Pythia8	MadGraph5_aMC@NLO+ Pythia8.210	Gen
		PowhegBox+Herwig 7	PS
$t\bar{t}W$	Sherpa 2.2.10	MadGraph5_aMC@NLO FxFx NLO QCD and MadGraph5_aMC@NLO EW	Gen
$t\bar{t}Z$	MadGraph5_aMC@NLO 2.8.1 + Pythia8.210	Sherpa 2.2.11	Gen

Table 7.8: Summary of alternative samples for generator and PS choices for $t\bar{t}H$, $t\bar{t}W$, and $t\bar{t}Z$ processes.

For $t\bar{t}W$ and $t\bar{t}H$, the uncertainty from missing higher-order QCD corrections is assessed by altering the μ_R and μ_F scales by factors of 0.5 and 2.0 with respect to their central values. No further reweighing is applied to the $t\bar{t}W$ with scale variations since the $t\bar{t}W$ scale variations are small. For the $t\bar{t}Z$, the scale variation uncertainties are computed by the envelope of the six-point variations of $(\mu_R, \mu_F) = (0.5, 0.5)$, $(0.5, 1)$, $(1, 0.5)$, $(1, 2)$, $(2, 1)$, and $(2, 2)$. A 1% PDF uncertainty, studied in $t\bar{t}t\bar{t}$ evidence analysis [52], is assigned to the $t\bar{t}Z$ and $t\bar{t}H$ processes. An uncertainty of 12% (10%) is applied to the $t\bar{t}Z$ ($t\bar{t}H$) total cross section [117]. No uncertainty is considered for $t\bar{t}W$ on the cross section and

PDF since its normalization and N_{jets} shape is estimated by $t\bar{t}W$ data-driven method.

The $t\bar{t}H$, $t\bar{t}W$, and $t\bar{t}Z$ background can enter the $t\bar{t}t\bar{t}$ signal region with additional heavy-flavor jets, which are difficult to model with MC simulation. An uncertainty of 50% is assigned to those with three truth b-jets and a separate 50% uncertainty to the events with four or more truth b-jets. These estimates are based on the measurement of the $t\bar{t}$+jets production with additional heavy-flavor jets [279] and on comparing data and prediction in $t\bar{t}\gamma$ events with three and four b-tagged jets.

7.4.2.3 Uncertainties on Fake and Non-prompt Backgrounds

Uncertainties related to fake/non-prompt backgrounds have a minor impact due to their small contributions in the signal region. These uncertainties are determined and treated as in Ref. [52]. The uncertainties on HF e and HF μ backgrounds are assessed based on the difference between data and MC simulations in the shape of distributions across signal and control regions. The assessment uses events where at least one lepton meets a loose lepton selection with relaxed isolation and identification requirements. These uncertainties range from 20% to 100% across different bins in the signal and control regions. The uncertainties on material and internal conversions are 30% and 21%, respectively, based on the comparison between data and simulation in a validation region of selected $Z \to \mu^+\mu^-\gamma(\to e^+e^-)$. Conservative uncertainties are applied to other smaller contributions, including an uncertainty of 100% for events with fake/non-prompt leptons from light jets and a 30% uncertainty for all other sources of fake/non-prompt background. These values are taken from previous analyses in a similar final state [51; 52; 260]. A final group of uncertainties is considered for $t\bar{t}+\text{HF}$ events, which can contribute to the signal region characterized by high b-jet multiplicities. The $t\bar{t}$+jets events are the primary source of the reducible background and can affect the shape of all reducible background components based on MC. Additional 30% uncertainties are assigned to $t\bar{t}$ events with three and four or more truth b-jets, separately, based on the observed discrepancies between

measured data and MC simulations [279].

7.4.2.4 Uncertainties on Other Backgrounds

A cross-section uncertainty of 30% is applied to tZq and tWZ processes [239; 280; 281]. The uncertainties on the VV are taken from the discrepancies between the measured differential cross section and the prediction of Sherpa 2.2.2 as a function of jet multiplicities [282]. For VV events with $\leq 3/4/\geq 5$ jets, an uncertainty of 20%/50%/60% is applied. The three components are considered to be uncorrelated. An uncertainty of 50% is considered for the $t\bar{t}WW$ based on the NLO prediction [205]. A converative uncertainty of 50% is assigned to VH although the precise measurement of $VH(\rightarrow b\bar{b})$ provides 20% uncertainty [283]. In addition, an uncertainty of 50% is also applied for all other minor background processes, including VVV, $t\bar{t}ZZ$, $t\bar{t}WZ$, $t\bar{t}HH$ and $t\bar{t}WH$. These uncertainties are based on the measurements in similar final states and the $t\bar{t}t\bar{t}$ evidence analysis [51; 52; 260] and are conservative enough to cover the different predictions shown in Ref. [205]. For the same reason as the heavy-flavor uncertainties for $t\bar{t}$ + HF [279], additional uncertainties of 50% are considered for all these small backgrounds with events containing three truth b-jets and four or more truth b-jets separately.

7.5 Results for the $t\bar{t}t\bar{t}$ Cross Section Measurement

A binned maximum-likelihood fit is performed to the GNN distribution in the SR and various CRs, defined in Table 7.2. The fit simultaneously determines the $t\bar{t}t\bar{t}$ signal strength, NFs of four fake/non-prompt lepton backgrounds, the parameterized function of $t\bar{t}W$, and systematic uncertainties. The $t\bar{t}t\bar{t}$ signal strength is defined as the ratio of the observed $t\bar{t}t\bar{t}$ cross section to the SM prediction of $\sigma_{t\bar{t}t\bar{t}} = 12.0 \pm 2.4$ fb computed at NLO QCD+EW with a 20% cross-section uncertainty [123]. The best-fit value of signal

strength is observed to be

$$\mu = 1.9 \pm 0.4(\text{stat})\,^{+0.7}_{-0.4}(\text{syst}) = 1.9\,^{+0.8}_{-0.5}, \tag{7.4}$$

and the corresponding measured cross section of $t\bar{t}t\bar{t}$ production is

$$\sigma_{t\bar{t}t\bar{t}} = 22.5^{+4.7}_{-4.3}(\text{stat})\,^{+4.6}_{-3.4}(\text{syst})\,\text{fb} = 22.5\,^{+6.6}_{-5.5}\,\text{fb}, \tag{7.5}$$

where the systematic uncertainty is determined by subtracting the statistical uncertainty in quadrature from the total uncertainty. The statistical uncertainty is computed from a fit with all NPs fixed to their post-fit values from the nominal fit.

The NFs of fake/non-prompt lepton backgrounds and $t\bar{t}W$ data-driven parameters are presented in Table 7.3 and Table 7.4. The NFs of fake/non-prompt lepton background agree with the MC predictions within the uncertainties except for $\text{NF}_{\text{Mat. Conv.}}$. The $t\bar{t}W$ data-driven parameters are determined by the observed data without priors, and the $t\bar{t}W$ modeling is checked by comparing pre-fit and post-fit predictions. Table 7.9 summarizes the post-fit predictions in SR or a high GNN score (GNN$\geq$ 0.6) before and after the fit to data. The post-fit $t\bar{t}W$ events with 6 and 7 jets are lower than the pre-fit predictions, while the $t\bar{t}W$ events with $\geq$9 jets are increased than the pre-fit predictions. The overall number of fitted $t\bar{t}W$ predictions agrees with the $t\bar{t}W$ cross section measurement [148; 284]. Figure 7.10 presents the good agreement between data and post-fit predictions of the GNN distribution in the SR. Figure 7.14 compares data and post-fit predictions in different kinematic distributions of a signal-enriched region with GNN $\geq$ 0.6 after the fit to data. Good agreements between data and post-fit predictions are observed.

The most significant theoretical uncertainties impacting the measured $\sigma_{t\bar{t}t\bar{t}}$ are from the $t\bar{t}t\bar{t}$ signal modeling, including the generator and PS uncertainties, as well as the $t\bar{t}W$ data-driven parameters. The largest experimental uncertainties impacting the $\sigma_{t\bar{t}t\bar{t}}$ are from

	Pre-fit		Post-fit	
	SR	GNN≥0.6	SR	GNN≥0.6
$t\bar{t}W$	130 ± 40	9 ± 4	127 ± 35	12 ± 4
$t\bar{t}Z$	72 ± 15	3.4 ± 1.8	79 ± 15	4.4 ± 2.0
$t\bar{t}H$	65 ± 11	4.6 ± 1.3	68 ± 10	5.0 ± 1.4
QmisID	27 ± 4	1.78 ± 0.26	27 ± 4	1.80 ± 0.24
Mat. Conv.	16.5 ± 2.3	0.73 ± 0.25	30 ± 8	1.4 ± 0.5
HF e	3.1 ± 1.0	0.4 ± 0.5	2.3 ± 2.4	0.3 ± 0.4
HF μ	7.1 ± 1.2	0.31 ± 0.15	9 ± 4	0.41 ± 0.22
Low m_{γ^*}	14.1 ± 2.0	0.52 ± 0.19	15 ± 5	0.56 ± 0.22
Others	47 ± 11	3.9 ± 1.2	50 ± 10	4.3 ± 1.2
$t\bar{t}t$	2.9 ± 0.9	1.5 ± 0.5	2.9 ± 0.9	1.5 ± 0.5
Total bkg	390 ± 50	26 ± 5	412 ± 21	32 ± 4
$t\bar{t}t\bar{t}$	38 ± 4	25.2 ± 3.2	69 ± 15	45 ± 10
Total	430 ± 50	51 ± 7	480 ± 19	77 ± 8
Data	482	83	482	83

Table 7.9: Pre-fit and post-fit predictions in the SR and for events with GNN ≥ 0.6 in the SR. The total systematic uncertainty differs from the sum in quadrature of the different uncertainties due to correlations.

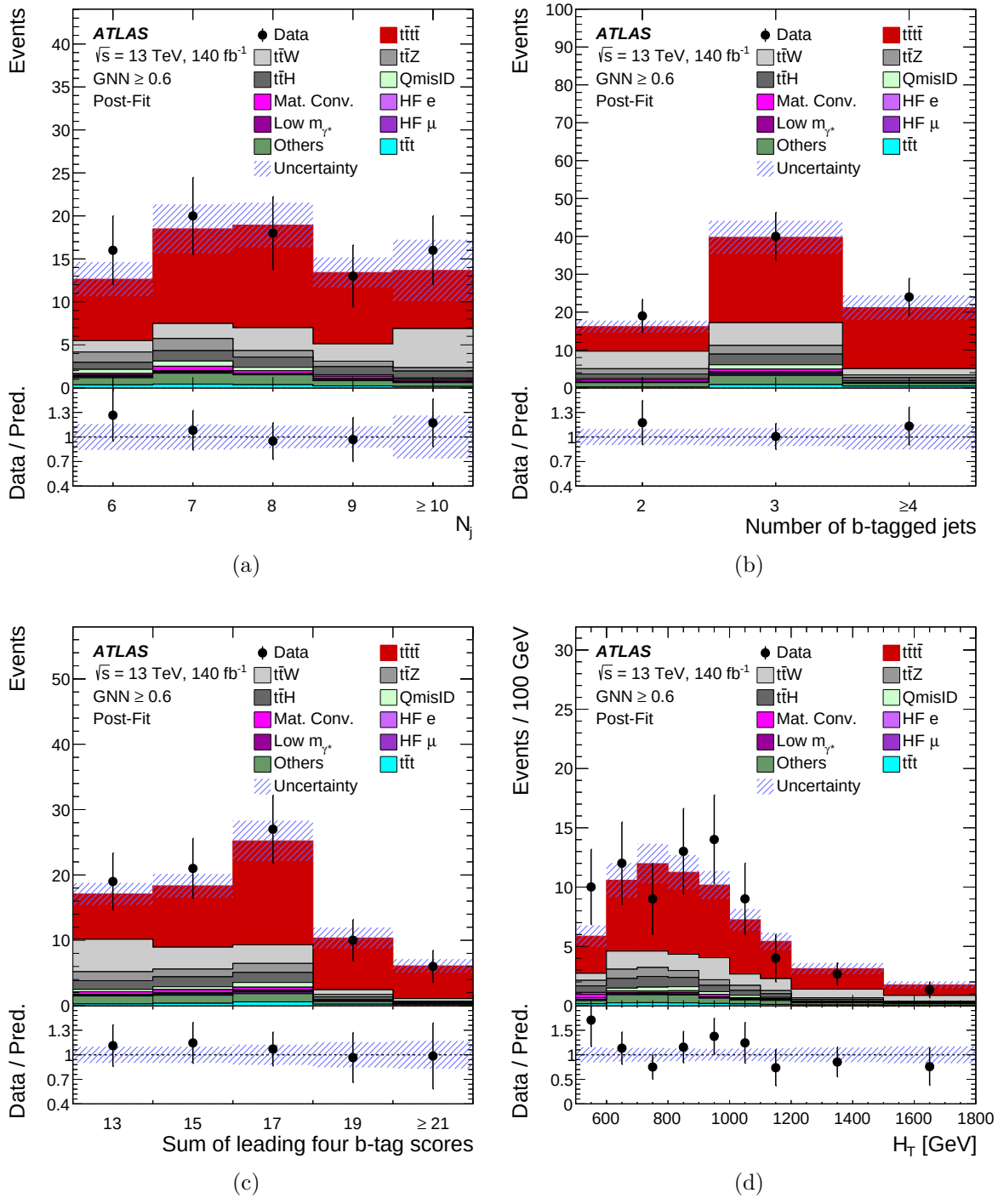

(a) (b)

(c) (d)

Figure 7.14: Comparison between data and post-fit predictions after the fit to data in the SR with GNN ≥ 0.6 for the distributions of (a) the number of jets, (b) the number of b-jets, (c) the sum of the four highest PCBT scores of jets in the event, and (d) the H_T. The uncertainty band contains the total uncertainty on the post-fit computation. The lower panel shows the ratio of the observed data to the total post-fit predictions. The underflow and overflow events are included in the first and last bins, respectively.

the b-tagging and the jet energy scale and resolution. A pull of $t\bar{t}t\bar{t}$ generator uncertainty by $-0.5\ \sigma$ is observed. No other nuisance parameters show significant constraints or pull from the fit. Table 7.10 presents the grouped impact of nuisance parameters on the $\sigma_{t\bar{t}t\bar{t}}$.

Uncertainty source	$\Delta\sigma$ [fb]		$\Delta\sigma/\sigma$[%]	
Signal modeling				
$t\bar{t}t\bar{t}$ generator choice	+3.7	−2.7	+17	−12
$t\bar{t}t\bar{t}$ parton shower model	+1.6	−1.0	+7	−4
Other $t\bar{t}t\bar{t}$ modeling	+0.8	−0.5	+4	−2
Background modeling				
$t\bar{t}H$+jets modeling	+0.9	−0.7	+4	−3
$t\bar{t}W$+jets modeling	+0.8	−0.8	+4	−3
$t\bar{t}Z$+jets modeling	+0.5	−0.4	+2	−2
Other background modeling	+0.5	−0.4	+2	−2
Non-prompt leptons modeling	+0.4	−0.3	+2	−2
$t\bar{t}t$ modeling	+0.3	−0.2	+1	−1
Charge misassignment	+0.1	−0.1	+0	−0
Instrumental				
Jet flavor tagging (b-jets)	+1.1	−0.8	+5	−4
Jet uncertainties	+1.1	−0.7	+5	−3
Jet flavor tagging (light-flavor jets)	+0.9	−0.6	+4	−3
Jet flavor tagging (c-jets)	+0.5	−0.4	+2	−2
Simulation sample size	+0.4	−0.3	+2	−1
Other experimental uncertainties	+0.4	−0.3	+2	−1
Luminosity	+0.2	−0.2	+1	−1
Total systematic uncertainty	+4.6	−3.4	+20	−16
Statistical				
Intrinsic statistical uncertainty	+4.2	−3.9	+19	−17
$t\bar{t}W$+jets normalization and scaling factors	+1.2	−1.1	+6	−5
Non-prompt leptons normalization (HF, Mat. Conv., Low m_{γ^*})	+0.4	−0.3	+2	−1
Total statistical uncertainty	+4.7	−4.3	+21	−19
Total uncertainty	+6.6	−5.5	+29	−25

Table 7.10: The grouped impact of the uncertainties to the $\sigma_{t\bar{t}t\bar{t}}$. The impacts are evaluated with the difference on $\sigma_{t\bar{t}t\bar{t}}$ derived from a nominal setup and an alternative setup by fixing a set of nuisance parameters in each category to the best value with $\pm1\sigma$. The total uncertainty differs from the quadratic sum of the components due to correlations among NPs.

The p-value of the background-only hypothesis resulting in a signal-like excess as observed data is derived with a profile-likelihood ratio [271]. The observed significance is found to be 6.1 standard deviations. The expected significance is calculated to be 4.3

standard deviations under the SM prediction of $\sigma_{t\bar{t}t\bar{t}} = 12.0 \pm 2.4$ fb [123], while 4.7 standard deviations using the $\sigma_{t\bar{t}t\bar{t}} = 13.4^{+1.0}_{-1.8}$ fb from Ref. [124]. Figure 7.15 presents the negative log-likelihood distribution as a function of the $t\bar{t}t\bar{t}$ cross section. The measured $t\bar{t}t\bar{t}$ cross section is consistent within 1.8 standard deviations with the SM prediction at NLO from Ref. [123], and within 1.7 standard deviations with the resummed $t\bar{t}t\bar{t}$ calculation at NLO+NLL' from Ref. [124]. The goodness-of-fit is evaluated to be a probability of 76% from a saturated model [285; 286]. Figure 7.16 presents the event display of the $t\bar{t}t\bar{t}$ candidate event from data collected in 2016. Compared to the $t\bar{t}t\bar{t}$ evidence analysis [52], the improvements in expected significance arise from the updated lepton and jet selection and uncertainties, the better separation power of the GNN classifier, and the improved treatment of the $t\bar{t}t$ background. This leads to a better acceptance and purity of the $t\bar{t}t\bar{t}$ signal and a smaller uncertainty on the background in the signal-enriched region.

The BDT discriminant is used as the complementary method to cross-check the results. A binned likelihood fit is performed in the same approach as the nominal fit but changes with BDT distribution in the SR for the fit to the data. The fit yields the same signal strength as the results using the GNN discriminant. The observed (expected) significance is 6.0 (3.9) standard deviations. In addition, a cut-based strategy is also studied without using an MVA discriminant. In the cut-based method, the SR is split into five sub-regions in terms of b-jet multiplicities, SS and multilepton (ML) final states, summarized in Table 7.11. The H_T is used as the fitted variable in each sub-region. A simultaneous fit with five sub-regions of the SR and CRs is performed. The fit yields the same strength as the results using the GNN discriminant. The observed (expected) significance is 5.0 (3.3) standard deviations. These two cross-checks reassure the observation of $t\bar{t}t\bar{t}$ process with a completely different technique on the MVA and a cut-based strategy.

As described in Section 3.2.2.2, the $t\bar{t}t\bar{t}$ and $t\bar{t}t$ have similar kinematics and are difficult to separate. Therefore, the $t\bar{t}t$ process can be studied in this $t\bar{t}t\bar{t}$ analysis with a simple extension. A simultaneous fit with both $t\bar{t}t\bar{t}$ and $t\bar{t}t$ normalization floating is performed

Region	Channel	N_{jets}	N_b	Other selection	Fitted variable
2bSS	SS	≥ 6	$= 2$	$H_T > 500$ GeV	H_T
2bML	3L	≥ 6	$= 2$	$H_T > 500$ GeV	H_T
3bSS	SS	≥ 6	$= 3$	$H_T > 500$ GeV	H_T
3bML	3L	≥ 6	$= 3$	$H_T > 500$ GeV	H_T
4b	SS+3L	≥ 6	≥ 4	$H_T > 500$ GeV	H_T

Table 7.11: Definition of the sub-regions from the signal region for the cut-based method. The N_{jets} (N_b) indicates the jet (b-tagged jet) multiplicity in the event. The H_T is defined as the scalar sum of the p_T of the leptons and jets.

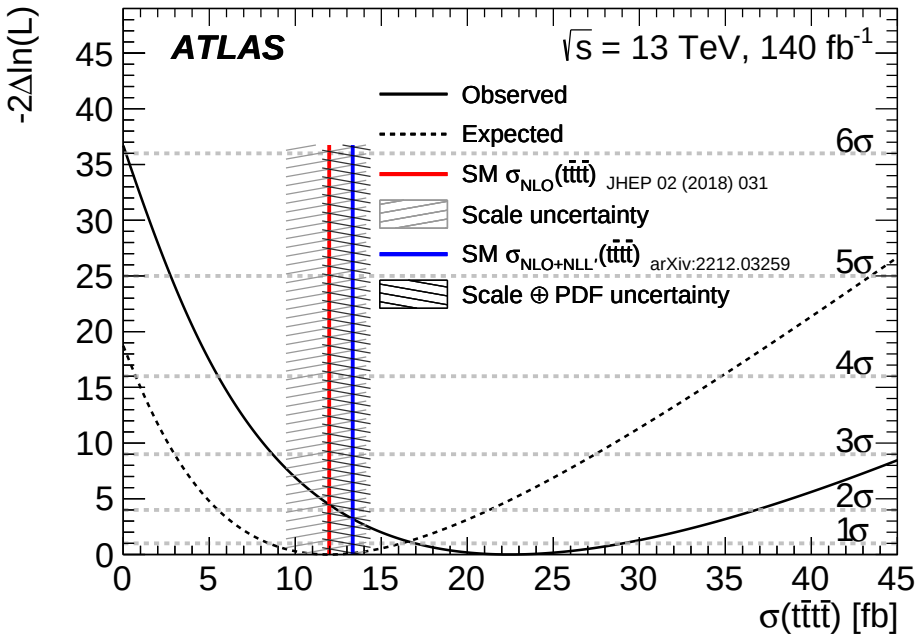

Figure 7.15: The negative log-likelihood distribution for the $t\bar{t}t\bar{t}$ cross section [125]. The solid curve denotes the observed likelihood, while the dashed curve represents the expected one. The red line presents the SM predictions calculated at NLO from Ref. [123] with its scale uncertainty as a light grey shaded area. The blue line shows the resummed $t\bar{t}t\bar{t}$ calculation at NLO+NLL' from Ref. [124] with its scale and PDF uncertainties as a dark grey shaded area.

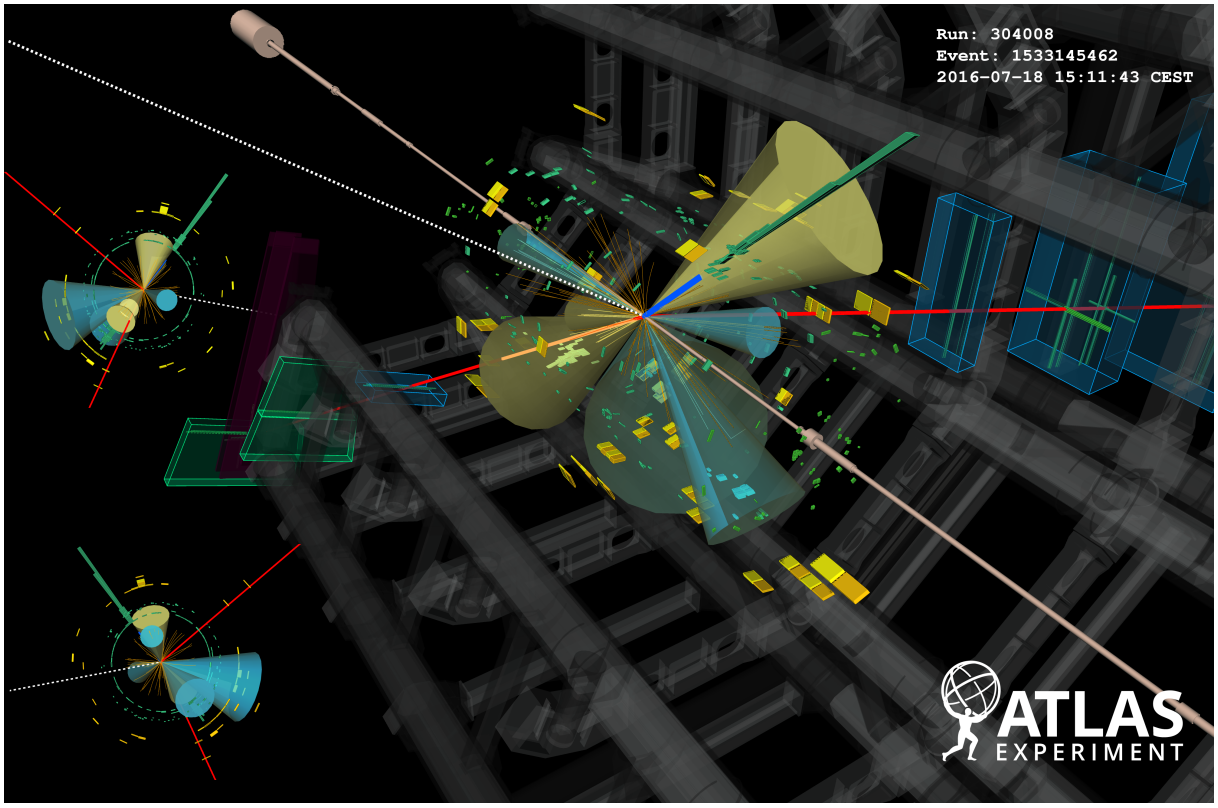

Figure 7.16: Event display of a candidate $t\bar{t}t\bar{t}$ event from data collected in 2016 [125]. The event consists of seven jets, four of them being b-tagged. Three of the top quarks produce leptons in their decay, including two muons (red) and one electron (blue). The fourth top quark decays into jets. Tracks of charged particles in the inner detector are visualized as orange lines. Green rectangles correspond to energy deposits in cells of the EM calorimeter, while yellow rectangles correspond to energy deposits in cells of the hadron calorimeter. Muon chambers associated with the two muon tracks are shown as blue and green boxes. The jets (b-tagged jets) are shown as yellow (azure) cones. The dotted line indicates the direction of the missing transverse momentum.

to investigate the sensitivity and correlations between $t\bar{t}t\bar{t}$ and $t\bar{t}t$. The fit shows a large anti-correlation of -93% between the two processes. Similar fits are performed with the BDT in the SR and with the cut-based method, showing similar levels of anti-correlation. Figure 7.17 presents the two-dimensional negative log-likelihood contours for the likelihood fits with free-floating $t\bar{t}t\bar{t}$ and $t\bar{t}t$ normalizations. The fit with the GNN in the SR prefers a $t\bar{t}t\bar{t}$ cross section of zero but with a large $t\bar{t}t$ cross section, deviating from the SM prediction at 2.1 standard deviations. However, the fit with the BDT in the SR (the cut-based method) prefers a large $t\bar{t}t\bar{t}$ cross section but with a $t\bar{t}t$ cross section of zero, deviating from the SM prediction at 1.9 (1.8) standard deviations. Different results from different fitting scenarios illustrate the challenges in separating $t\bar{t}t\bar{t}$ and $t\bar{t}t$ processes. The cut-based method provides better separation between $t\bar{t}t\bar{t}$ and $t\bar{t}t$ production. It shows consistent results with the nominal fit, providing a larger $t\bar{t}t\bar{t}$ cross section than the SM prediction. In addition, the two components of $t\bar{t}t$ ($t\bar{t}tW$ and $t\bar{t}tq$ processes) are sensitive to the possible BSM effects, such as the FCNC [287; 288]. The $t\bar{t}t$ production with FCNC can lead to the $t\bar{t}t$ production without the associated W boson in the final state. The studies of cross sections of $t\bar{t}t$ and its two components are essential to probe the potential BSM effects. Therefore, this analysis sets the 95% CL intervals on the cross section of the $t\bar{t}t$, $t\bar{t}tW$, and $t\bar{t}tq$ processes. Table 7.12 summarizes the sensitivities in different scenarios, assuming the $t\bar{t}t\bar{t}$ signal strength to be 1 or 1.9. The 95% CL intervals on the $t\bar{t}tq$ cross section are wider than the $t\bar{t}tW$ cross section due to lower selection efficiency with the lower lepton and jet multiplicities of the $t\bar{t}tq$ process.

7.6 Interpretations

This section interprets the measured $t\bar{t}t\bar{t}$ production cross section with Higgs-top Yukawa coupling, four heavy-flavor fermion EFT operators, or a Higgs oblique parameter. Limits and 95% CL intervals on these parameterizations are obtained.

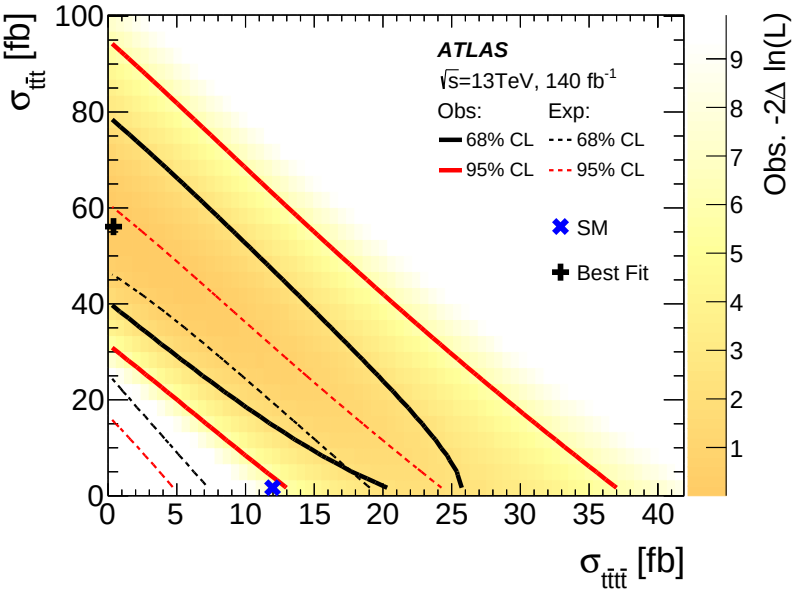

(a)

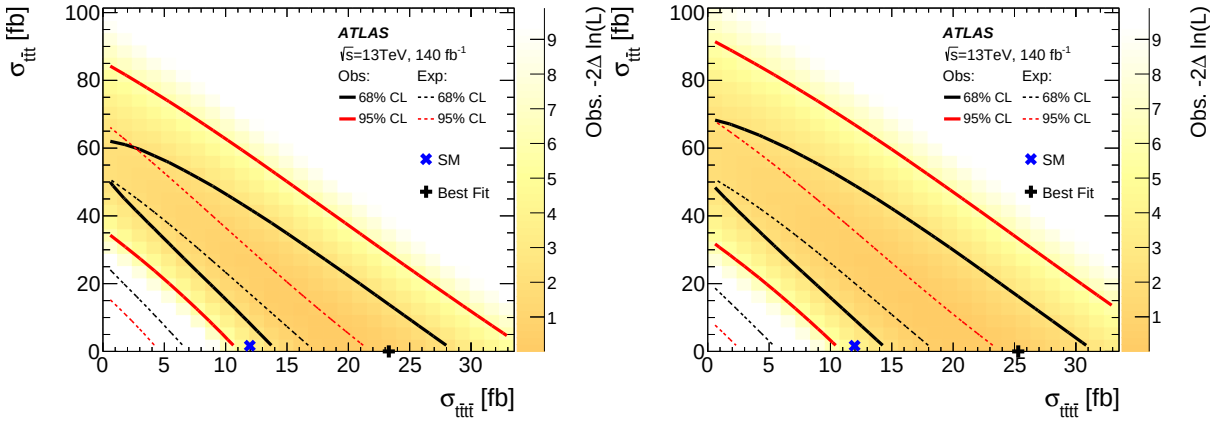

(b) (c)

Figure 7.17: The two-dimensional negative log-likelihood contours for the $t\bar{t}t\bar{t}$ and $t\bar{t}t$ cross sections when both cross sections are treated as free parameters in the fit [125]. Different fit scenarios are considered: (a) the nominal fit with the GNN in the SR, (b) the cross-check fit with the BDT in the SR, and (c) the cross-check fit with cut-based strategy. The blue cross represents the SM prediction of $\sigma_{t\bar{t}t\bar{t}} = 12$ fb [123] and $\sigma_{t\bar{t}t} = 1.67$ fb [125], computed at NLO. The black cross stands for the best-fit value from the likelihood fit. The observed (expected) exclusion contours at 68% (black) and 95% (red) CL are shown in solid (dashed) lines. The gradient-shaded area represents the observed likelihood value as a function of $\sigma_{t\bar{t}t\bar{t}}$ and $\sigma_{t\bar{t}t}$.

Processes	95% CL cross section interval [fb]	
	$\mu_{t\bar{t}t\bar{t}} = 1$	$\mu_{t\bar{t}t\bar{t}} = 1.9$
$t\bar{t}t$	[4.7, 60]	[0, 41]
$t\bar{t}tW$	[3.1, 43]	[0, 30]
$t\bar{t}tq$	[0, 144]	[0, 100]

Table 7.12: Observed 95% CL intervals for the $t\bar{t}t$, $t\bar{t}tq$, and $t\bar{t}tW$ cross sections assuming a $t\bar{t}t\bar{t}$ signal strength of 1 and 1.9 [125]. The $t\bar{t}tq$ ($t\bar{t}tW$) cross section is fixed to its SM prediction to derive the $t\bar{t}tW$ ($t\bar{t}tq$) cross section interval.

7.6.1 Higgs-top Yukawa Coupling

Modification of the Higgs-top Yukawa coupling and the Higgs CP property can result in deviation of the $t\bar{t}t\bar{t}$ cross section from SM. Following Section 3.2.2.1, the $t\bar{t}t\bar{t}$ cross section can be parameterized as a function of κ_t and α. Moreover, $t\bar{t}H$ production cross section also depends on these parameters, but the $t\bar{t}H$ kinematics can only be modified when $\kappa_t \sin\alpha$ is non-zero [127; 289]. The $t\bar{t}t\bar{t}$ and $t\bar{t}H$ yields are parameterized as a function of κ_t and α in each bin of the GNN distribution of the SR. In addition, an alternative approach is studied by treating the $t\bar{t}H$ cross section as a free parameter in the fit to probe the effects from the $t\bar{t}H$ process. Figure 7.19 shows the observed and expected 95% CL limits in a two-dimensional parameter space $(|\kappa_t \cos\alpha|, |\kappa_t \sin\alpha|)$ with parameterizing or floating $t\bar{t}H$ producion. Additional limits are studied to explore Yukawa coupling sensitivity by assuming only CP-even Yukawa coupling. Under this assumption, the observed (expected) 95% CL upper limit is extracted to be $|\kappa_t| < 1.9$ (1.6) when parameterizing $t\bar{t}H$, and to be $|\kappa_t| < 2.3$ (1.9) when floating $t\bar{t}H$. Figure 7.19 presents the negative log-likelihood distributions for the measurement on κ_t. The limits on κ_t show less stringent than that reported in Ref. [290] due to the higher measured $t\bar{t}t\bar{t}$ cross section than the SM prediction.

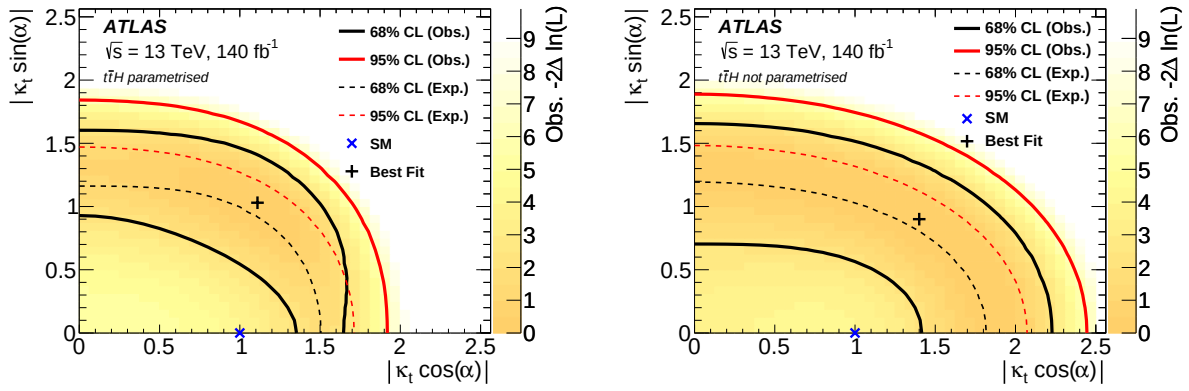

(a) $t\bar{t}H$ parameterized (b) $t\bar{t}H$ profiled

Figure 7.18: The two-dimensional negative log-likelihood contours for $|\kappa_t \cos(\alpha)|$ versus $|\kappa_t \sin(\alpha)|$ at 68% and 95% CL with (a) parameterizing or (b) floating $t\bar{t}H$. The κ_t is the Higgs-top Yukawa coupling strength parameter, and α is the mixing angle between the CP-even and CP-odd components [125]. The gradient-shaded area represents the observed likelihood value as a function of κ_t and α. The $t\bar{t}t\bar{t}$ signal and $t\bar{t}H$ background yields are parameterized as a function of κ_t and α in each fitted bin. The blue cross shows the expectation value of the SM, while the black cross shows the best-fit value.

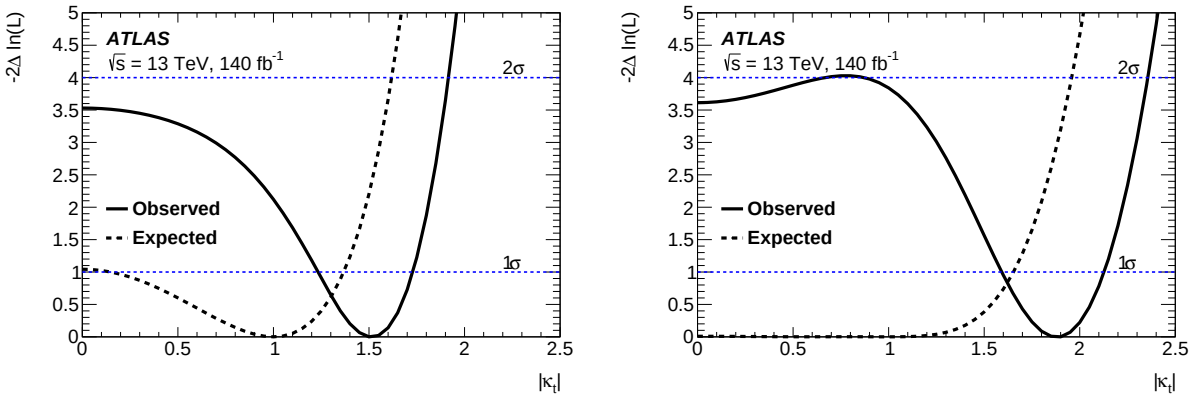

(a) $t\bar{t}H$ parameterized (b) $t\bar{t}H$ profiled

Figure 7.19: The negative log-likelihood distributions for the measurement on κ_t assuming purely CP-even contribution [125]. The events yield of the $t\bar{t}t\bar{t}$ signal and $t\bar{t}H$ background are parameterized as a function of κ_t in each fitted bin. The observed (expected) distribution is shown with the solid (dashed) line.

7.6.2 Effective Field Theory and Higgs Oblique Parameter

As described in Section 3.2.2.1, the four heavy-flavor fermion EFT operators can enhance the $t\bar{t}t\bar{t}$ cross section. The likelihood fits are performed with $t\bar{t}t\bar{t}$ yields parameterized as a quadratic function of the coefficient of the corresponding EFT operator (C_i/Λ^2). The fit is carried out assuming only one EFT operator contributing to the $t\bar{t}t\bar{t}$ cross section with other operators fixed at SM predictions of zero. Table 7.13 summarizes the expected and observed 95% CL intervals on the coefficients of EFT operators. The importance of the linear term is studied by parameterizing $t\bar{t}t\bar{t}$ with a linear function in the fit, resulting in the upper limits on the absolute values of the coefficients ($|C_i/\Lambda^2|$) of $\mathcal{O}^1_{QQ}$, $\mathcal{O}^1_{Qt}$, $\mathcal{O}^1_{tt}$, and $\mathcal{O}^8_{Qt}$ to be 6.6, 4.0, 2.8 and 10.8 TeV^{-2}, respectively. Comparable results on these EFT operators can be found in Ref. [290].

The Higgs oblique parameter is the self-energy correction term applied to the Higgs propagator in the SM. The $t\bar{t}t\bar{t}$ cross section can be enhanced by the Higgs oblique parameter through the off-shell Higgs interaction, following the relation shown in Equation (3.14). In addition, the $t\bar{t}H$ cross section can be affected by the Higgs oblique parameter as a function of $\hat{H}$:

$$\mu_{t\bar{t}H} = 1 - \hat{H}, \tag{7.6}$$

where $\mu_{t\bar{t}H}$ is the normalization with respect to the SM prediction. The limit on Higgs oblique parameter is extracted with $t\bar{t}t\bar{t}$ yields parameterized as a quadratic function of $\hat{H}$ and $t\bar{t}H$ parameterized with $\mu_{t\bar{t}H}$. Figure 7.20 presents the likelihood scan of the $\hat{H}$, resulting in the observed (expected) 95% CL upper limit on the $\hat{H}$ of 0.23 (0.11). The observed limit is higher than the expected limit due to the higher measured $t\bar{t}t\bar{t}$ cross section than the SM prediction. Refs. [92; 290; 291] reported the limits on the $\hat{H}$ parameter.

Operators	Expected C_i/Λ^2 [TeV^{-2}]	Observed C_i/Λ^2 [TeV^{-2}]
$\mathcal{O}^1_{QQ}$	[-2.5, 3.2]	[-4.0, 4.5]
$\mathcal{O}^1_{Qt}$	[-2.6, 2.1]	[-3.8, 3.4]
$\mathcal{O}^1_{tt}$	[-1.2, 1.4]	[-1.9, 2.1]
$\mathcal{O}^8_{Qt}$	[-4.3, 5.1]	[-6.9, 7.6]

Table 7.13: Expected and observed 95% CL intervals on coefficients of the EFT operators assuming only one EFT parameter variation in the fit [125] and others fixed at SM.

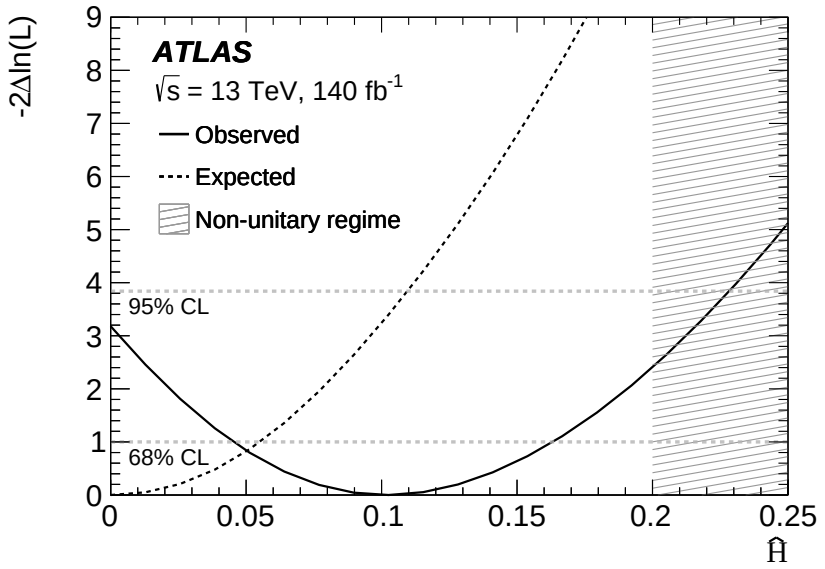

Figure 7.20: The negative log-likelihood values as a function of the Higgs oblique parameter $\hat{H}$ [125]. The solid curve represents the observed likelihood, while the dashed curve denotes the expected one. The dashed regions show the non-unitary regime in the perturbative theory.

CHAPTER VIII

Search for Beyond Standard Model Four-Top-Quark Production

This chapter describes searches for the heavy scalar or pseudoscalar Higgs bosons, predicted in the 2HDM model, produced in association with a top-quark pair ($t\bar{t}H/t\bar{t}A$). The heavy Higgs boson further decays into a $t\bar{t}$ pair, forming the $t\bar{t}t\bar{t}$ production. This analysis studies the $t\bar{t}H/A \to t\bar{t}t\bar{t}$ production in the SSML final states, using 139 fb^{-1} of pp collision data collected with the ATLAS detector at $\sqrt{s} = 13$ TeV [135]. The SSML final states have strongest exclusion limit of BSM parameter space than the other decaying final states of $t\bar{t}t\bar{t}$. This analysis mainly follows the strategies for the SM $t\bar{t}t\bar{t}$ evidence analysis [52] and shares many aspects of its successive analysis, the $t\bar{t}t\bar{t}$ observation analysis discussed in Chapter VII. These include the region definitions, background estimation, multivariate techniques, and statistical interpretation strategies.

This chapter is organized as follows. Section 8.1 summarizes the modeling of the BSM signal. Section 8.2 presents the object and event selections. Section 8.3 discusses the background estimation. Section 8.4 shows the MVA strategies used in this search. Section 8.5 summarizes the systematic uncertainties for this analysis. Section 8.6 summarizes the results of the BSM signals.

8.1 Signal Modeling

The $t\bar{t}H/A \to t\bar{t}t\bar{t}$ signal is simulated at LO in the 4FS using MadGraph5 2.3.3 with NNPDF3.1lo, generating complete $2 \to 12$ parton-level scattering to account for spin correlation in final state particles. Events are interfaced to Pythia8 with the A14 tune. The bottom and charm hadron decays are modeled with EvtGen 1.2.0 [292]. An additional filter is applied to increase statistics by selecting at least one lepton from $t\bar{t}$ decays, produced in association with the heavy Higgs boson.

The signal is generated with s-channel via CP-even heavy Higgs boson (H) using a type-II 2HDM model, excluding CP-odd heavy Higgs (A) and t-channel diagrams due to negligible kinematic difference shown in Figure 8.1. The sample is produced with $\tan\beta = 0.65$ at the alignment limit with $\cos(\beta - \alpha) = 0$. From Ref. [293], the kinematics is found to be generally independent of the choice of $\tan\beta$. For low $\tan\beta$ ($\tan\beta \lesssim 0.5$) and large Higgs boson mass ($m_H \geq 700$ GeV), the total width increases up to a few hundred GeV. The p_T of particle-level objects change in the order of $O(10\%)$ with different width setups, and other kinematics are unaffected. A narrow width is considered for each mass point, summarized in Table 8.1. The other free parameters of the model do not affect the kinematics and follow the default setting of MadGraph5.

Interference between BSM signals and SM $t\bar{t}t\bar{t}$ is neglected due to limited impact, with at most 20% at the parton level [293]. The interference mainly affects the invariant mass of the $t\bar{t}$ system from Higgs decay with large width scenario, as shown in Figure 8.2.

The theoretical cross sections are evaluated in the relevant parameter space of the type-II 2HDM benchmark model. The cross section of CP-even and CP-odd heavy Higgs boson productions are obtained from the ATLAS theoretical calculation[1]. Figure 8.3 summarizes the cross sections at the alignment limit.

[1]https://twiki.cern.ch/twiki/bin/viewauth/AtlasProtected/HiggsBSM2HDMRecommendations

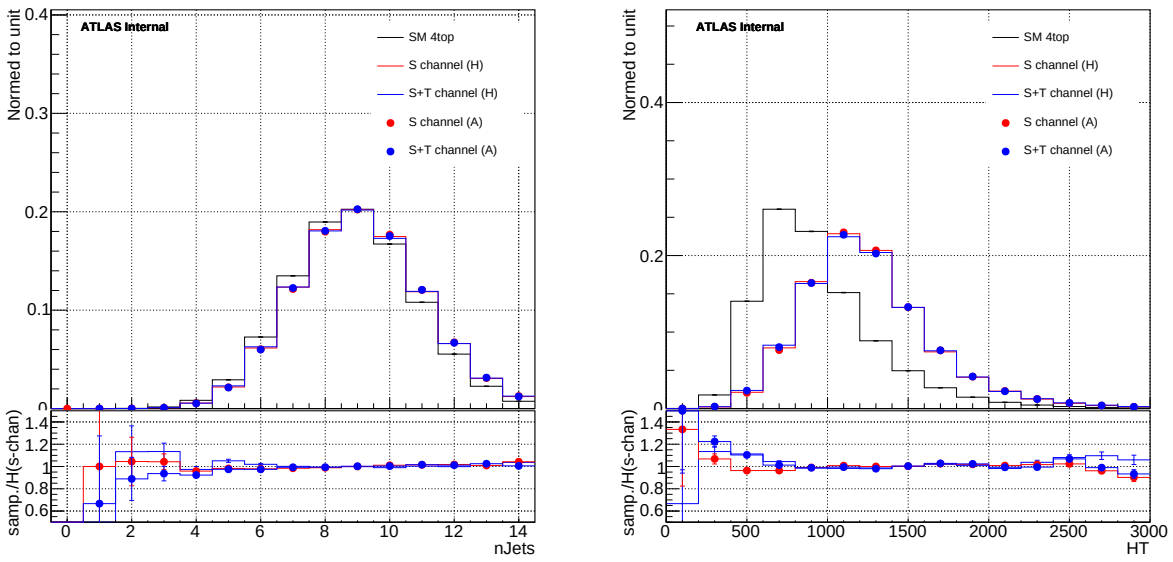

(a) N_{jets} (b) H_T

Figure 8.1: Kinematic comparison of (a) the number of jets and (b) H_T between $t\bar{t}H \to t\bar{t}t\bar{t}$ and $t\bar{t}A \to t\bar{t}t\bar{t}$ productions with $m_{H/A} = 1000$ GeV in both s-channel and s+t-channel at the particle level. The nominal SM $t\bar{t}t\bar{t}$ production, discussed in Section 6.2.1, is included as a reference.

Mass points [GeV]							
400	500	600	700	750	800	900	1000
Widths [GeV]							
5	5	10	20	20	20	20	30

Table 8.1: Heavy Higgs boson mass and width used for the $t\bar{t}H \to t\bar{t}t\bar{t}$ signal generation.

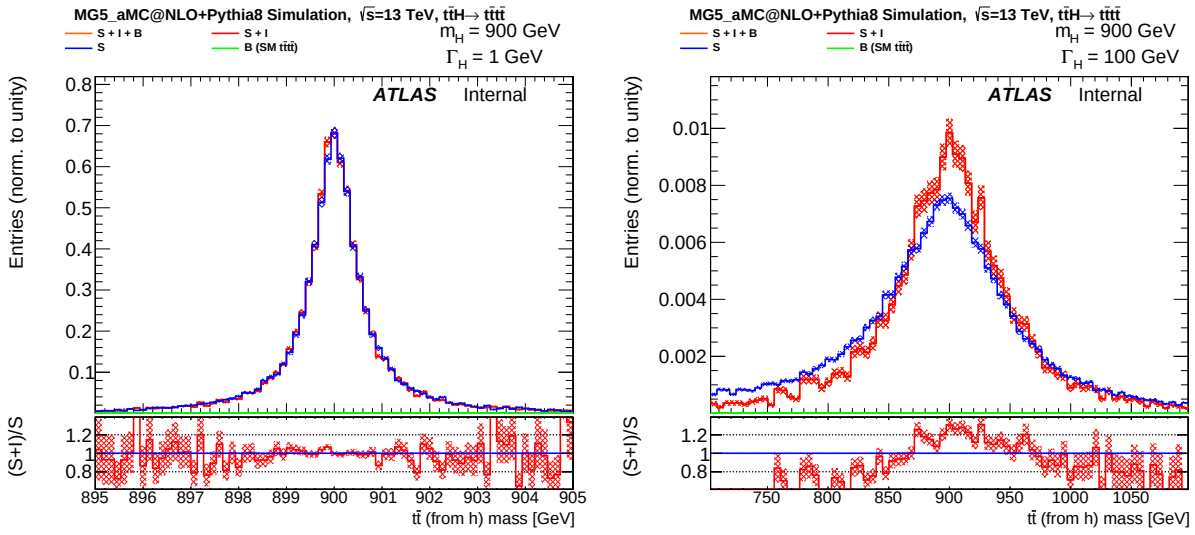

(a) (b)

Figure 8.2: Invariant mass distributions of $t\bar{t}$ from the decays of heavy Higgs boson H/A of (a) $(m_H, \Gamma_H) = (900, 1)$ GeV and (b) $(m_H, \Gamma_H) = (900, 100)$ GeV. Distributions for signal-only (blue), background-only (green), signal+interference (red), and signal+background+interference (orange) assumptions are shown. The signal+background+interference assumption is identical to the signal+interference assumption due to the negligible contribution from the background-only hypothesis. Uncertainty bands refer to the statistical MC uncertainties [293].

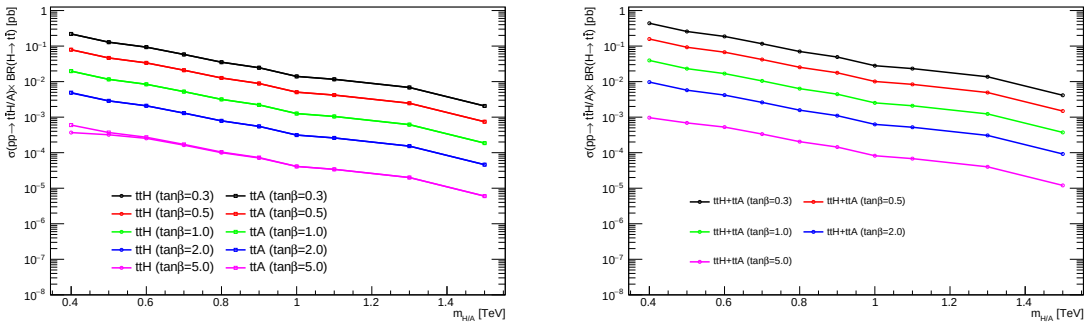

Figure 8.3: The cross section times branching ratio of $t\bar{t}H \to t\bar{t}t\bar{t}$ (left, circle marker), $t\bar{t}A \to t\bar{t}t\bar{t}$ (left, square marker), and $t\bar{t}H + t\bar{t}A \to t\bar{t}t\bar{t}$ (right, circle marker) in type-II 2HDM as a funtion of m_A and $\tan\beta$ at the alignment limit.

8.2 Object and Event Selections

The object selections follow the $t\bar{t}t\bar{t}$ evidence analysis [52] with additional updates on the PFlow jet algorithm and the DL1r b-tagging algorithm, summarized in Section 5.4. The p_T selections of jets and leptons follow the $t\bar{t}t\bar{t}$ evidence analysis with tighter selections than that in the $t\bar{t}t\bar{t}$ observation analysis discussed in Chapter VII. The lepton isolation requirement in this analysis is looser than the PLImproved WPs used in the $t\bar{t}t\bar{t}$ observation analysis. The physics objects considered in this search are electrons, muons, jets, b-jets, and the missing transverse momentum. Table 8.2 summarizes the reconstructed objects and identification criteria used in this search. Section 6.1 describes the trigger selection for this search.

	Electrons	Muons	Jets	b-jets
p_T[GeV]	> 28	> 28	> 25	> 25
$\|\eta\|$	< 1.37 or $1.52 - 2.47$	< 2.5	< 2.5	< 2.5
Identification quality	Tight ECIDS (ee, $e\mu$)	Medium	JVT	DL1r 77%
Isolation	FixedCutTight	FixedCutTightTrackOnly		
Track vertex :				
$-$ $\|d_0/\sigma_{d_0}\|$	< 5	< 3		
$-$ $\|z_0 \sin\theta\|$ [mm]	< 0.5	< 0.5		

Table 8.2: Summary of object identifications and selections. The ECIDS and lepton isolation WPs are introduced in Section 5.3. The JVT and DL1r algorithm are summarized in Section 5.4.

Event selections follow the strategies shown in Section 7.1. Events with SSML and at least one b-tagged jet are preselected. The same m_{ee} cuts are applied to remove the backgrounds from low mass resonances and the Z-bosons. The $t\bar{t}t\bar{t}$ enriched region, called the baseline SR, is defined by events with at least six jets, at least two b-jets, and $H_T > 500\,\text{GeV}$. A BDT discriminant splits the baseline SR into a CR with low BDT scores and a BSM SR with high BDT scores.

8.3 Background Estimation

The background estimation follows the SM $t\bar{t}t\bar{t}$ evidence analysis [52]. Section 6.3 discusses the general strategies for the background estimation used in this search. Section 8.3.1 discusses the charge misidentification background estimation with a data-driven method. Section 8.3.2 describes the template method to estimate the $t\bar{t}W$ QCD and fake/non-prompt lepton background in various CRs. Table 8.3 summarizes the CR definitions used in this search.

Region	Channel	N_{jets}	N_b	Other selection	Fitted variable
CR Conv	SS, ee or $e\mu$	$4 \leq N_{\text{jets}} < 6$	≥ 1	$m_{ee}^{\text{CV}} \in [0, 0.1]$ GeV $200 < H_T < 500$ GeV	m_{ee}^{PV}
CR HF e	eee or $ee\mu$		$= 1$	$100 < H_T < 250$ GeV	Yield
CR HF μ	$e\mu\mu$ or $\mu\mu\mu$		$= 1$	$100 < H_T < 250$ GeV	Yield
CR $t\bar{t}W$	SS, $e\mu$ or $\mu\mu$	≥ 4	≥ 2	$m_{ee}^{\text{CV}} \notin [0, 0.1]$ GeV, $\lvert\eta(e)\rvert < 1.5$ for $N_{b\text{-jets}} = 2$, $H_T < 500$ GeV or $N_{\text{jets}} < 6$; for $N_{b\text{-jets}} \geq 3$, $H_T < 500$ GeV	$\sum p_{\text{T}}^{\ell}$
CR lowBDT	SS+3L	≥ 6	≥ 2	$H_T > 500$ GeV, SM BDT < 0.55	SM BDT
BSM SR	SS+3L	≥ 6	≥ 2	$H_T > 500$ GeV, SM BDT ≥ 0.55	BSM pBDT

Table 8.3: Definitions of the SR and CRs used in the analysis. The N_{jets} and N_b indicate the jet and b-jet multiplicities in the event. The H_T is defined as the scalar sum of the p_T of the leptons and jets. The variable m_{ee}^{CV} (m_{ee}^{PV}) is defined as the invariant mass of the system formed by the track associated with the electron and the closest track at the conversion (primary) vertex, as discussed in Section 5.3.1.4. The η(e) refers to the electron pseudorapidity. The SM BDT and BSM BDT are MVA discriminants to separate signal from backgrounds, described in Section 8.4. The baseline SR is equal to the BSM SR + CR lowBDT [135].

8.3.1 Charge Misidentification

As described in Section 6.3.1, the charge flip rate is determined by a data-driven method with a Poisson likelihood fit from the $Z \to ee$ sample. A 10 GeV window around the Z boson mass is required. Charge flip rates are calculated separately for the SR and

various CRs based on specific electron selections, such as in CR Conv and CR $t\bar{t}W$ (see Table 8.3). For CR Conv, the charge flip rates are parameterized as a function of p_T, $|\eta|$, and m_{ee}^{PV}. For this particular case, the rates are estimated with only two bins in the barrel $|\eta| \in (0, 1.52)$ and endcap $|\eta| \in (1.52, 2.5)$ regions to reduce the statistical uncertainty. For CR $t\bar{t}W$, the charge flip rates are estimated as the nominal setup with additional selection on $m_{ee}^{\mathrm{CV}} \notin [0, 0.1]$ GeV. Figure 8.4 depicts the charge flip rates and their total uncertainties in the SR. Charge flip rates range from 10^{-2} to 10^{-5}, and their uncertainties vary from a few percent to 27% in the SR. The charge flip rates increase with larger values of p_T and $|\eta|$ due to smaller curvature and denser materials, respectively. The low p_T and $|\eta|$ bins have larger uncertainties due to the limited QmisID contribution.

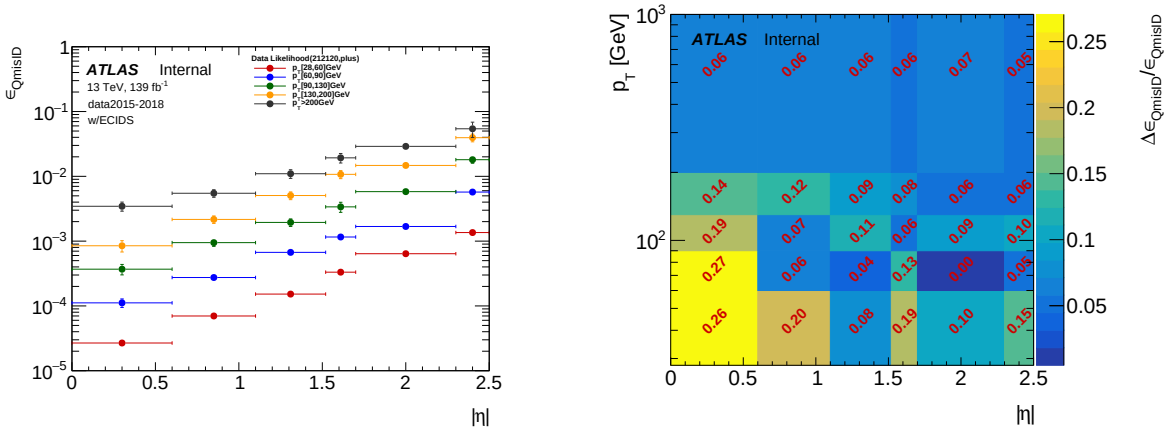

(a) Charge flip rates

(b) Total uncertainties

Figure 8.4: Charge flip rate and total relative uncertainty in the SR as a function of the electron p_T and $|\eta|$.

8.3.2 Fake/non-prompt Lepton and $t\bar{t}W$ Backgrounds

The template method estimates fake/non-prompt lepton backgrounds in this analysis, as described in Section 6.3.2. The fit simultaneously determines the NFs of various background sources with kinematics based on MC simulation. An NF is applied to the $t\bar{t}W$ QCD contribution, including contribution at NLO QCD, and treated as a free pa-

rameter in the fit due to the discrepancy between observed data and the $t\bar{t}W$ predictions in past analyses such as Ref. [51; 148]. The $t\bar{t}W$ EW contribution, containing NLO3 contribution, is fixed at the SM prediction with a 20% uncertainty derived from Ref. [123]. The CRs are defined to estimate the fake/non-prompt lepton background as follows:

- CR Conv : A same-sign di-electron or electron-muon pair is selected, with at least one electron having $m_{ee}^{\text{CV}} \in [0, 0.1]$ GeV, selecting the Mat. Conv. and Low m_{γ^*} candidates as detailed in Section 5.3.1.4. Jet multiplicity is selected as 4 or 5 jets to be orthogonal to SR, with at least one b-jet among the jets. The H_T is required to be within 200 to 500 GeV. The m_{ee}^{PV}distribution is used as the fitted distribution to discriminate between Mat. Conv. and Low m_{γ^*}. The $\text{NF}_{\text{Mat. Conv.}}$ and $\text{NF}_{\text{Low } m_{\gamma^*}}$ are constrained in this region.

- CR HF e (CR HF μ): Trilepton events with eee or $ee\mu$ ($\mu\mu\mu$ or $e\mu\mu$) are required, with exactly one b-jet. The H_T is required to be within 100 to 250 GeV. $\text{NF}_{\text{HF } e}$ ($\text{NF}_{\text{HF } \mu}$) is constrained using counting only.

- CR $t\bar{t}W$: A same-sign di-muon or electron-muon pair is required, with at least four jets and two b-jets. The absolute value of electron pseudo-rapidity is selected to be less than 1.5 to be orthogonal to the CR Conv. The m_{ee}^{CV} is selected outside of $[0, 0.1]$ GeV to be orthogonal to CR Conv. The orthogonality with the SR is ensured by requiring $H_T < 500$ GeV or $N_{\text{jets}} < 6$ in the $N_{b\text{-jets}} = 2$ region and by requiring $H_T < 500$ GeV in the $N_{b\text{-jets}} \geq 3$ region. $\text{NF}_{t\bar{t}W\text{ QCD}}$ is constrained using the sum of lepton p_T ($\sum p_{\text{T}}^{\ell}$), providing good separation power between the $t\bar{t}W$ QCD contribution and other background sources.

- CR lowBDT is constructed from the baseline SR with SM BDT < 0.55. This region is close to the BSM SR and is used to constrain the signal-like background events. This region allows the fits with different signal hypotheses to provide consistent

post-fit background models.

The NFs of various background sources are obtained from the background-only hypothesis, presented in Table 8.4. The NFs are consistent with unities within the uncertainties. The post-fit $t\bar{t}W$ predictions are compatible with the dedicated $t\bar{t}W$ measurements [51; 148]. Figure 8.5 and Figure 8.6 compare the observed data and post-fit predictions in the CRs. Good agreements between data and post-fit predictions are observed. A $t\bar{t}W$ VR is defined with the charge asymmetry characteristic, $N_+ - N_-$ of the total charge of the selected leptons. The $t\bar{t}W$ VR is defined by at least four jets and two b-jets. Figure 8.7 compares the data and post-fit predictions. A residual disagreement at high jet multiplicities is observed, resulting in a 133% (208%) uncertainty assigned to the $t\bar{t}W$ QCD contribution with seven (eight or more) jets. These uncertainties are further constrained and pulled from the central value in the fit, increasing the yields of $t\bar{t}W$ QCD at high jet multiplicities. The final fitted regions are not sensitive to the charge asymmetry. Therefore, the discrepancies in the number of jets and SM BDT of the $t\bar{t}W$ VR cannot be compensated entirely but are within the uncertainties.

Parameter	$\mathrm{NF}_{t\bar{t}W\ \mathrm{QCD}}$	$\mathrm{NF}_{\mathrm{Mat.\ Conv.}}$	$\mathrm{NF}_{\mathrm{Low}\ m_{\gamma^*}}$	$\mathrm{NF}_{\mathrm{HF}\ e}$	$\mathrm{NF}_{\mathrm{HF}\ \mu}$
Value	1.3 ± 0.3	1.5 ± 0.5	0.6 ± 0.5	0.9 ± 0.4	1.0 ± 0.2

Table 8.4: NFs for the different background processes obtained from the background-only fit to all signal and control regions [135]. The fitted distribution in the BSM SR is the BSM BDT with the signal hypothesis of $m_H = 400$ GeV, discussed in Section 8.4.2. The uncertainties include both statistical and systematic uncertainties.

8.4 Multivariate Analysis

This analysis uses two BDT classifiers, trained with the XGBoost algorithm [277] in the baseline SR, to distinguish BSM $t\bar{t}t\bar{t}$ signal from SM backgrounds. A background rejection BDT, namely SM BDT, separates $t\bar{t}t\bar{t}$-like events from other SM processes. A

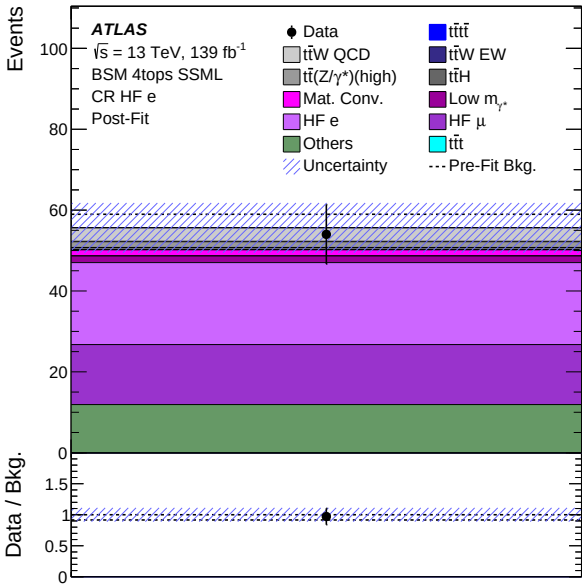

(a) CR HF e

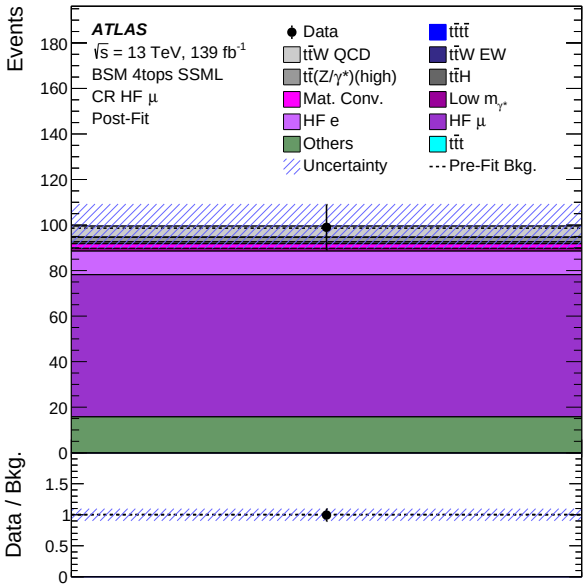

(b) CR HF μ

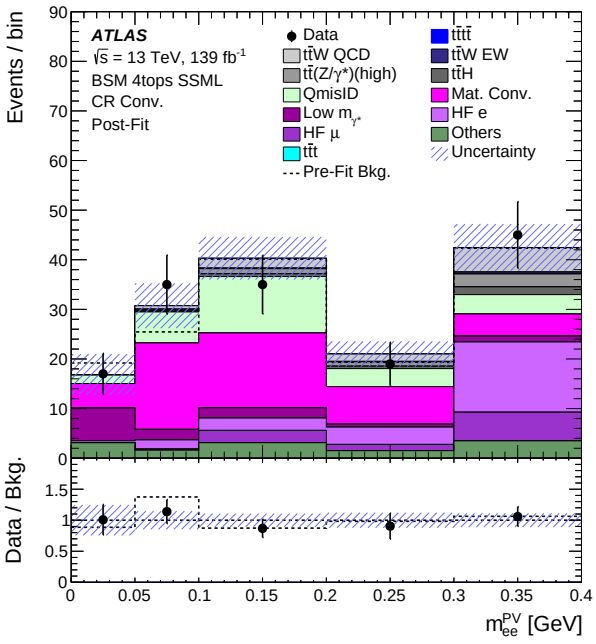

(c) CR Mat. Conv.

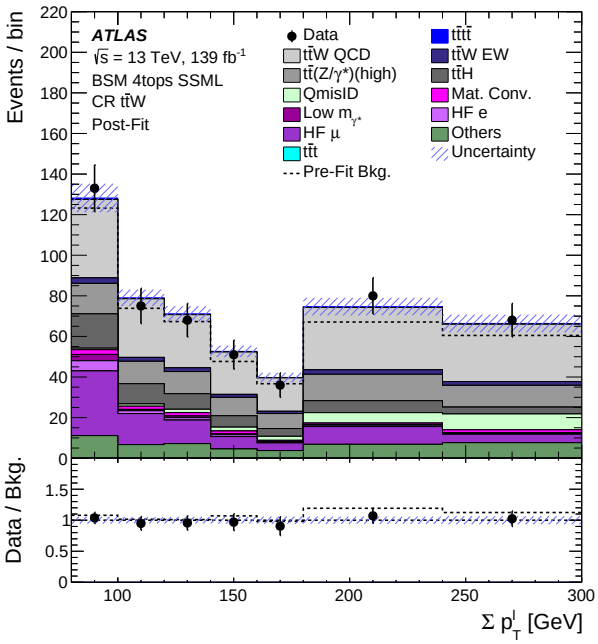

(d) CR Low m_{γ^*}

Figure 8.5: Comparisons between data and predictions in the fake/non-prompt lepton background CRs after the fit to data in the background-only hypothesis [135]. Pre-fit distributions are added as the dashed line in each plot.

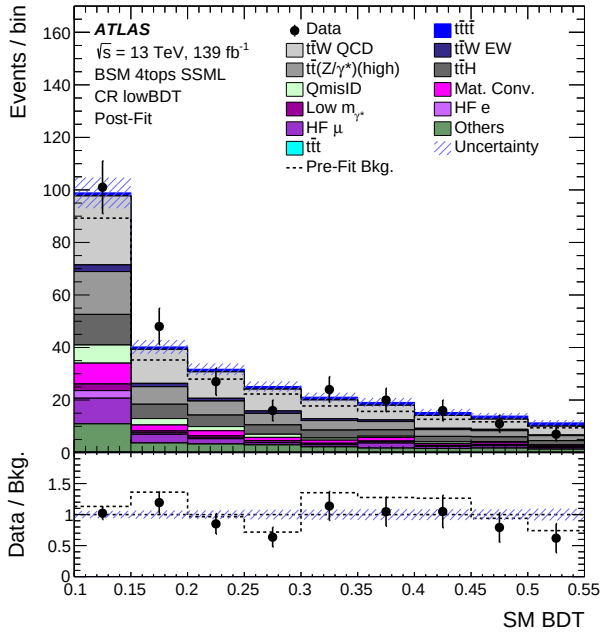

Figure 8.6: Comparisons between data and predictions in the CR lowBDT after the fit to data in the background-only hypothesis [135]. Pre-fit distributions are added as the dashed line in each plot.

separate BSM mass-parameterized Boosted Decision Trees (pBDT) extracts BSM $t\bar{t}t\bar{t}$ from SM $t\bar{t}t\bar{t}$ and other backgrounds.

In the final likelihood fit, the baseline SR of the high SM BDT region is defined as the BSM SR (SM BDT $\geq$ 0.55), and the low SM BDT region is defined as the CR lowBDT (SM BDT $<$ 0.55). The fitting variables used are the SM BDT for the CR lowBDT region and BSM BDT for the BSM SR region. This strategy provides consistent background modeling for fits of BSM signals with different masses.

8.4.1 SM BDT

The SM BDT is trained using MC events to separate the SM $t\bar{t}t\bar{t}$ process from other SM backgrounds. The SM LO $t\bar{t}t\bar{t}$ events are used as the signal in the training. The SM BDT setup shares a strategy similar to that of the $t\bar{t}t\bar{t}$ observation analysis, described in Section 7.3.2. The BDT model utilizes the same high-level input features listed in

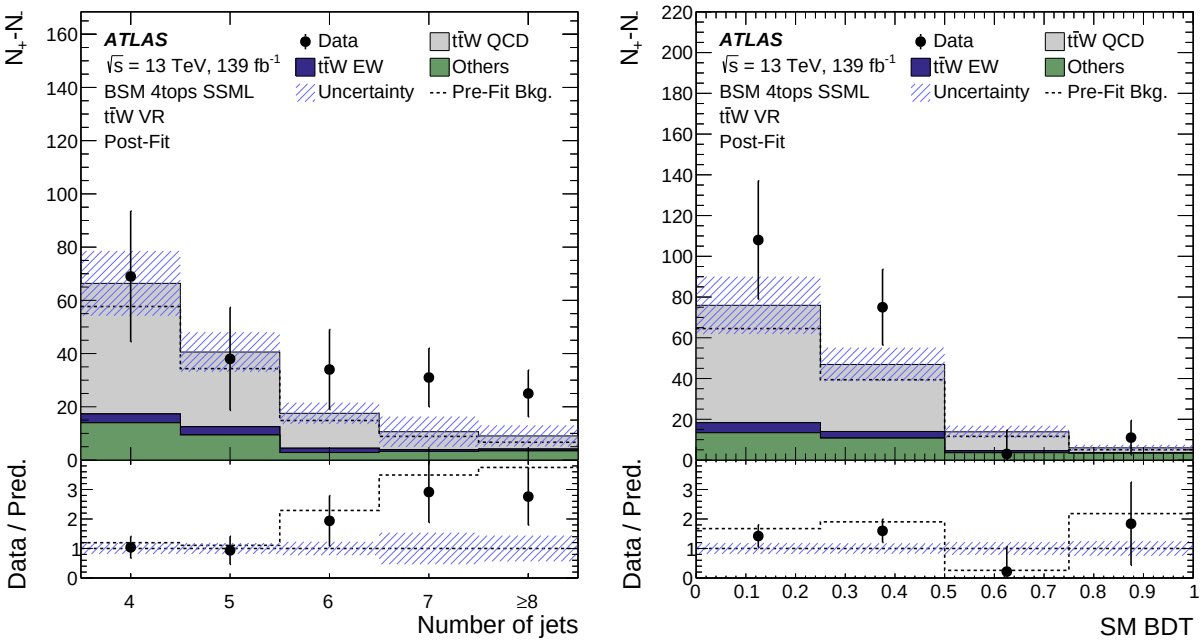

(a) (b)

Figure 8.7: Comparison between the data and the post-fit predictions for the (a) number of jets and (b) SM BDT distribution (see Section 8.4) in the $t\bar{t}W$ VR after the fit to data [135]. The y-axis label $N_+ - N_-$ represents the difference between the number of events with a positive sum and those with a negative sum of the charges of the selected leptons. The ratio of the data to the total post-fit prediction is shown in the lower panel. The shaded band represents the total uncertainty on the post-fit backgrounds.

Table 7.5. Figure 8.8 compares input features between the observed data and the post-fit predictions of the background-only hypothesis. Good modeling of the input features is observed. The MC event weight is applied to each event during the BDT training. Events with negative weights are excluded in the training. In addition, the yields of signal and background are reweighted to be the same in the training to prevent bias towards the majority class. Unlike Section 7.3.2, the SM BDT does not perform the reweighting on the $t\bar{t}W$.

A two-fold strategy is used for the BDT training, following the strategy discussed in Section 7.3.2. Figure 7.11 shows the schematic summary of the strategy. The hyperparameters of the SM BDT are optimized to maximize the AUC of separating SM $t\bar{t}t\bar{t}$ from SM backgrounds. The AUC are 0.864 and 0.866 in the testing and validation dataset, respectively. Figure 8.9 illustrates the SM BDT distributions from the training, testing, and validation, showing good agreements and no overtraining. Figure 8.10 compares the observed data and the predictions in the SM BDT distribution after the fit to data under the background-only hypothesis.

8.4.2 BSM BDT

The BSM BDT is trained to discriminate the BSM $t\bar{t}t\bar{t}$ signal from the SM $t\bar{t}t\bar{t}$ and other backgrounds for events passing the baseline SR selection. A mass parametrization method introduces the truth mass of a heavy Higgs boson as an input label in each event during the training [294]. In training, the BSM $t\bar{t}t\bar{t}$ signals with different masses are merged as an inclusive signal sample carrying their truth mass of each event, while the backgrounds are assigned with a random mass from the set of truth masses. In the BDT model applications, the BSM BDT at each mass point is retrieved by assigning the same truth mass for signal, background, and data samples. Figure 8.11 presents the schematic summary of the BSM BDT mass parameterization procedure.

The BSM BDT utilizes high-level kinematics and SM BDT as input features to maxi-

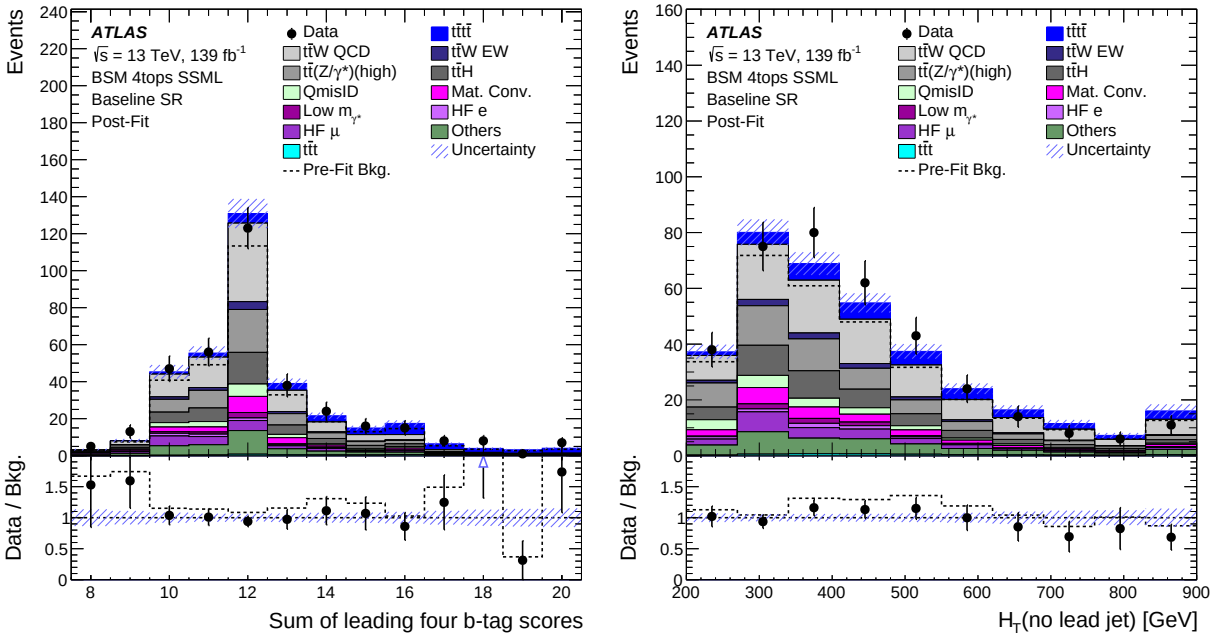

(a) $\sum_{i=0}^{3} w_{\mathrm{PCBT}}$ (b) H_{T}(no lead jet)

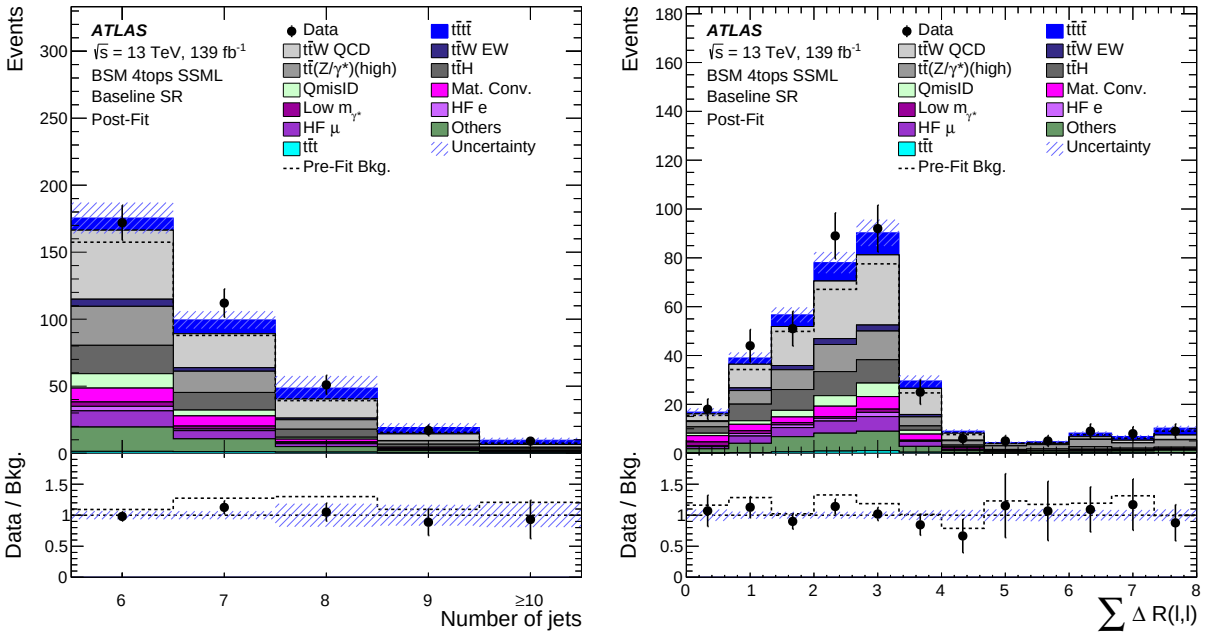

(c) N_{jets} (d) $\sum \Delta R(\ell, \ell)$

Figure 8.8: Comparisons between the data and predictions with input feature distributions in the baseline SR after the fit to data under background-only hypothesis [135]. The uncertainty band includes the total uncertainty from the post-fit computation. The lower panel shows the ratio of the observed data to the post-fit predictions. The ratio of the observed data to the total pre-fit predictions is denoted as the dashed line.

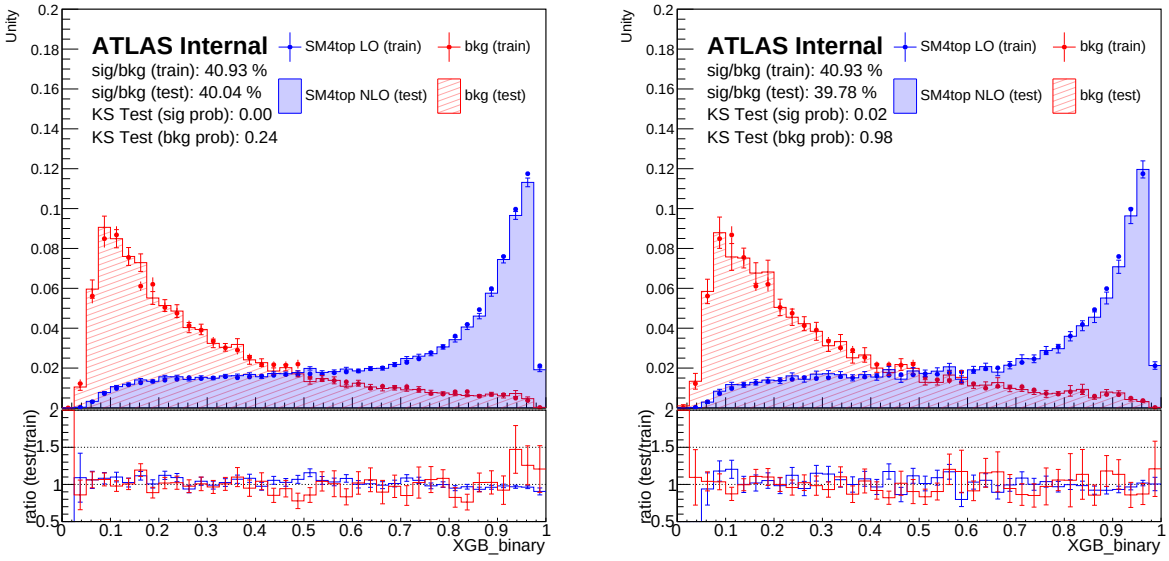

(a) (b)

Figure 8.9: SM BDT distributions of (a) training and testing datasets and (b) training and validation datasets. The training dataset includes the SM $t\bar{t}t\bar{t}$ LO events and other SM backgrounds without negative weight events. The testing and validation data include the SM $t\bar{t}t\bar{t}$ NLO events and other SM backgrounds with all weights included.

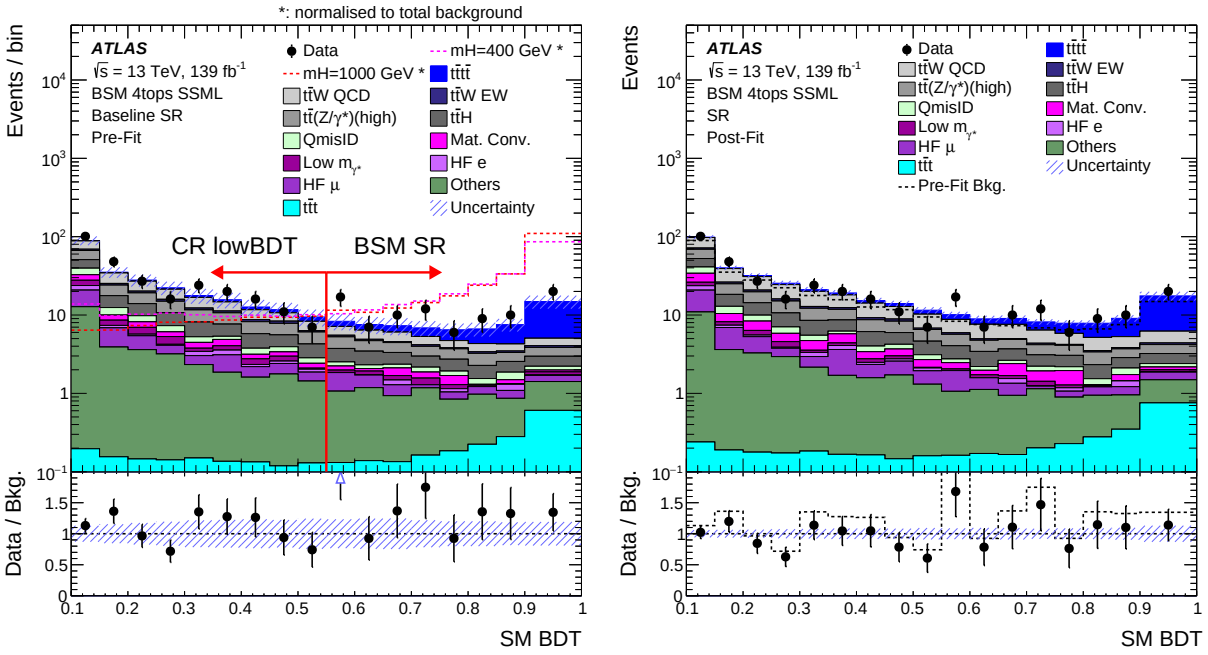

(a) (b)

Figure 8.10: Comparisons between the observed data and predictions in the baseline SR (a) before the fit and (b) after the fit to data under background-only hypothesis [135]. The background-only fit is performed with the BSM SR using the BSM BDT distribution of signal hypothesis with $m_H = 400$ GeV and various CRs. The uncertainty band includes the total uncertainty from (a) the pre-fit priors and (b) the post-fit computation. The lower panel illustrates the ratio of the observed data to (a) the MC simulations and (b) post-fit predictions.

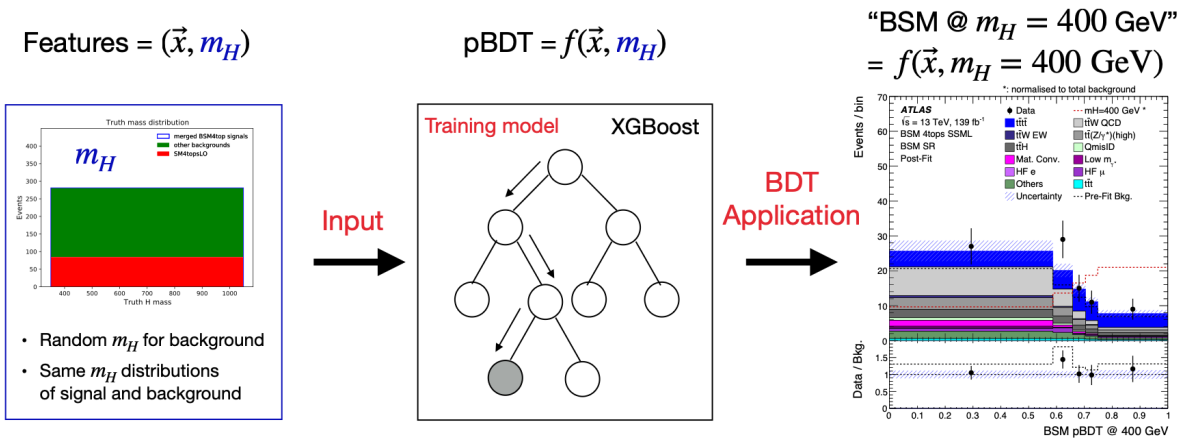

Figure 8.11: Schematic summary of the BSM BDT training and application procedure.

mize the discrimination between BSM $t\bar{t}t\bar{t}$ from SM $t\bar{t}t\bar{t}$ and other backgrounds. Table 8.5 and Figure 8.12 summarize the input features and their modelings after the fit to data under the background-only hypothesis. Good agreements between the data and post-fit predictions are observed. The MC event weight is applied in the BDT training, but events with negative weights are excluded. The BSM BDT is trained in the baseline SR but is used in the BSM SR. Therefore, the SM $t\bar{t}t\bar{t}$ and other backgrounds are reweighted to mimic the fraction of the total background in the BSM SR in the training. This reweighting enhances the relative contribution of the SM $t\bar{t}t\bar{t}$ from 10% to 30% of the total background and provides a better separation between BSM $t\bar{t}t\bar{t}$ and SM $t\bar{t}t\bar{t}$, leading to stronger exclusion sensitivities. Signal and background samples are further reweighted to have a uniform truth mass distribution in the training to factorize the acceptance effect of the signal and background samples. Finally, the yields of signal and background are reweighted to be the same in the training to prevent bias towards the majority class.

A four-fold cross-validation process is performed to increase the training statistics and to prevent overtraining. It splits the samples into four folds and uses three-quarters of events for training and one-quarter for testing and application. The training is performed with the SM $t\bar{t}t\bar{t}$ LO sample to avoid negative weight events, and the optimization is evaluated with the nominal SM $t\bar{t}t\bar{t}$ NLO events. The hyperparameters of the BSM BDT are optimized to maximize the AUC separating BSM $t\bar{t}t\bar{t}$ from backgrounds. The AUC of BSM BDT is examined in both baseline SR (the training region) and BSM SR (the fitting region), as it is crucial to assess the performance in both contexts. Table 8.6 summarizes the AUC across different masses. The results of AUC show that the separation between the low-mass signal and backgrounds is limited due to their similar kinematics. Figure 8.13 illustrates the BSM BDT distributions for the training and testing datasets, showing good agreements and no overtraining. Finally, the binning of BSM BDT distribution is optimized for each signal hypothesis to maximize the separation power and avoid the empty contributions from major backgrounds. Figure 8.14 presents the BSM

BDT distributions after the fits to the data under the background-only hypothesis.

Feature	Definition	Rank
H_T	Scalar sum of all lepton and jet p_T	1
S^{jets}	Geometry of energy-momentum flow of jets (Sphericity) [295]	4
$S_{\text{T}}^{\text{jets}}$	Sphericity in the transverse plane [295]	8
$\Delta R(\ell,\ell)_{\text{min}}$	The minimum angular separation between any lepton pair	7
$\sum \Delta R(\ell,\ell)$	Sum of the angular separation between all lepton pairs	5
E_T^{miss}	Missing transverse energy	6
SM BDT	BDT output probability to discriminate SM $t\bar{t}t\bar{t}$ from backgrounds	3
m_H	Truth mass of heavy Higgs boson	2

Table 8.5: Input features of the BSM BDT. The last column indicates the ranking of the importance of the features evaluated with XGBoost.

Mass [GeV]	Basline SR	BSM SR (Total)	BSM SR (SM $t\bar{t}t\bar{t}$)
400	0.813	0.673	0.573
500	0.818	0.665	0.540
600	0.844	0.688	0.557
700	0.849	0.703	0.593
800	0.870	0.732	0.644
900	0.881	0.763	0.691
1000	0.885	0.786	0.722

Table 8.6: The AUC of BSM BDT in the baseline and BSM SRs. The "BSM SR (Total)" ("BSM SR (SM $t\bar{t}t\bar{t}$)") represents the AUC comparing BSM $t\bar{t}t\bar{t}$ against the total backgrounds (SM $t\bar{t}t\bar{t}$) in the BSM SR.

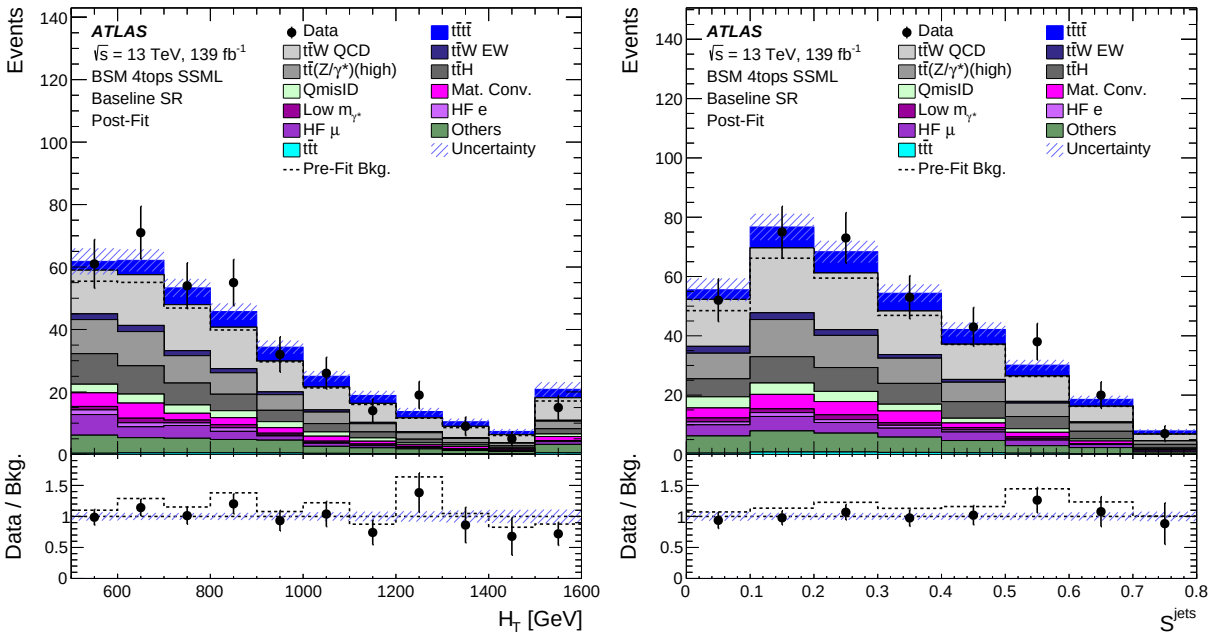

(a) H_T (b) S^{jets}

Figure 8.12: Comparison between data and predictions for (a) H_T and (b) S^{jets} distributions of the baseline SR after the fit to data under background-only hypothesis [135]. The fit is performed with CRs and BSM SR with the BSM BDT using the signal hypothesis of $m_H = 400$ GeV. The uncertainty band includes the total uncertainty on the post-fit computation. The lower panel illustrates the ratio of the observed data to the total post-fit computation. The first and last bins contain the underflow and overflow events, respectively.

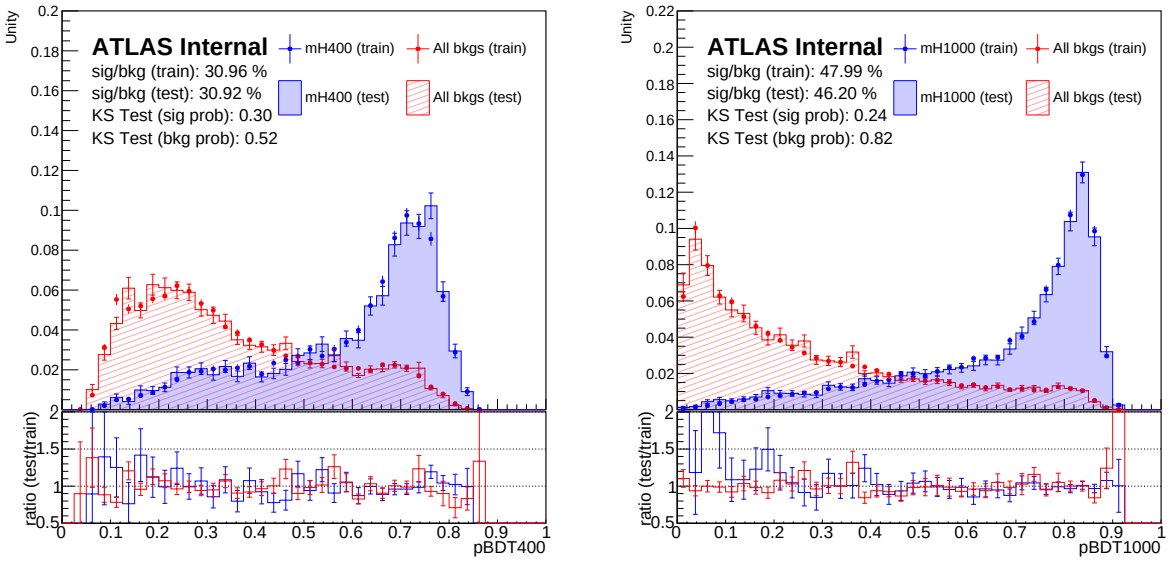

(a) (b)

Figure 8.13: BSM BDT distributions for the training and testing datasets with the signal hypothesis of (a) $m_H = 400$ GeV and (b) $m_H = 1000$ GeV. The background samples contain SM $t\bar{t}t\bar{t}$ LO events and backgrounds without negative weight events in the training dataset. The background samples contain SM $t\bar{t}t\bar{t}$ NLO events and backgrounds with all weights included in the testing dataset.

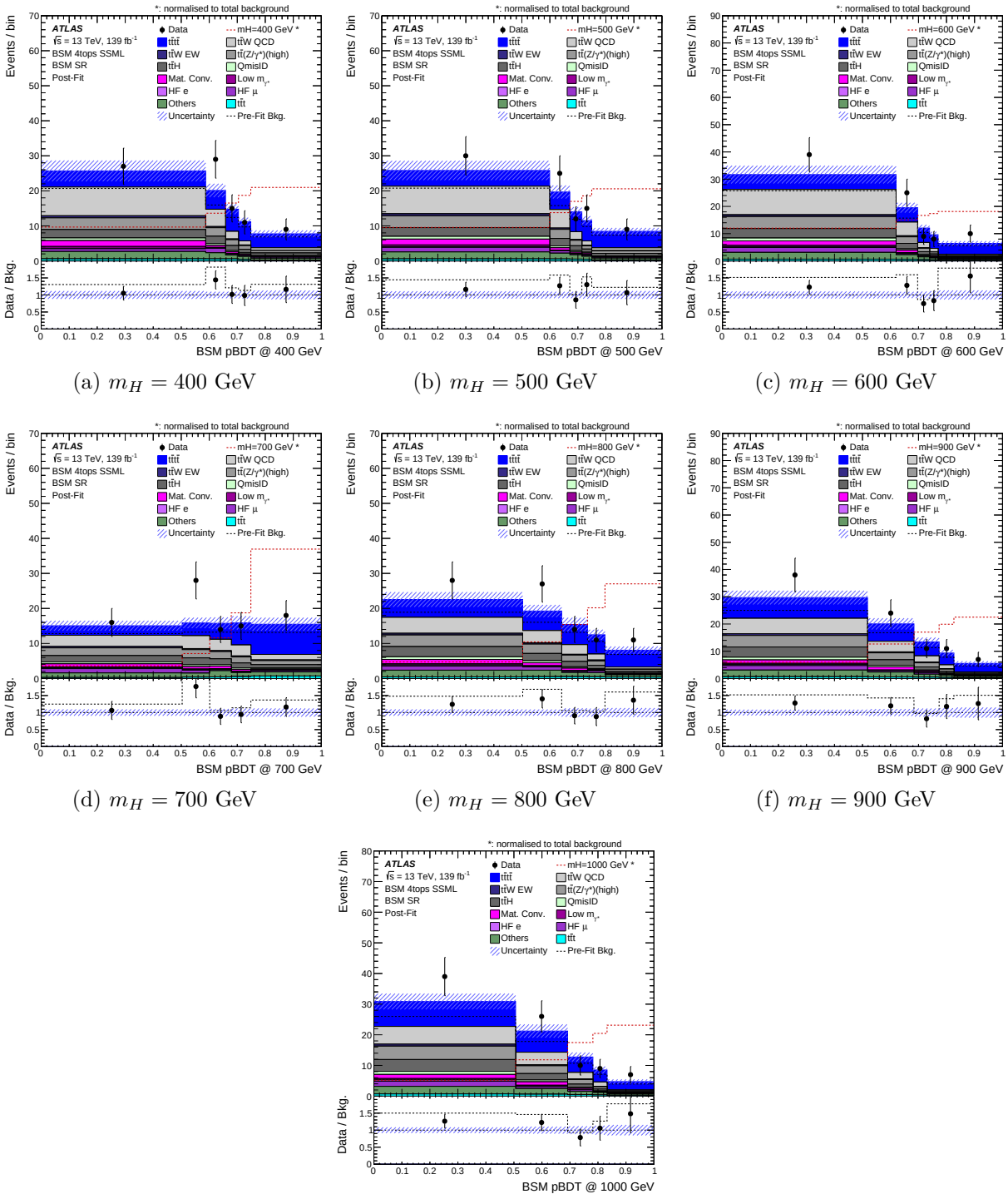

(a) $m_H = 400$ GeV (b) $m_H = 500$ GeV (c) $m_H = 600$ GeV

(d) $m_H = 700$ GeV (e) $m_H = 800$ GeV (f) $m_H = 900$ GeV

(g) $m_H = 1000$ GeV

Figure 8.14: Comparison between data and predictions for BSM BDT distributions of the BSM SR after the fit to data under background-only hypothesis [135]. The fits are performed with CRs and BSM SR with the BSM BDT distribution, assuming different signal hypotheses. The uncertainty band includes the total uncertainty on the post-fit computation. The lower panel illustrates the ratio of the observed data to the total post-fit predictions.

8.5 Systematic Uncertainties

This section presents only theoretical systematic uncertainties for the signal and background modeling, while the experimental systematic uncertainties are discussed in Section 6.4. Table 8.7 and Table 8.8 show an overview of the systematic uncertainties applied in this analysis.

Systematic uncertainty	Components	Typical size [%]
Luminosity	1	1.7
Pile-up reweighing	1	$O(10^{-1}) \sim O(1)$
Physical Objects		
Electron	7	$O(10^{-2}) \sim O(1)$
Muon	13	$O(10^{-2}) \sim O(1)$
Jet energy scale and resolution	39	$O(10^{-2}) \sim O(10)$
Jet vertex tagging	1	$O(10^{-1}) \sim O(1)$
Jet b-tagging	85	$O(10^{-2}) \sim O(1)$
E_T^{miss}	3	$O(10^{-2}) \sim O(10^{-1})$
Total (Experimental)	150	
Electron charge misidentification	1	~ 9
Fake/Non-prompt Lepton Uncertainty		
Material conversions	1	$O(1) \sim 20$
Internal conversions	1	$O(1) \sim 20$
HF non-prompt leptons	2	$O(1) \sim 95$
Other fake leptons	2	30 & 100
Additional heavy flavor jets on $t\bar{t}$	2	$O(1) \sim 30$
Total (Reducible Background)	9	

Table 8.7: Sources of experimental and fake/non-prompt lepton uncertainties considered in the analysis. The uncertainties from "Luminosity" and "Other fake leptons" are taken as normalization only in all regions. Other uncertainties affect the normalization and shape of the fitted distributions and/or the acceptance into the fit regions. The 'Components' column indicates the components of the systematic uncertainties. The decorrelations of experimental systematic uncertainties are summarized in Table 6.4. The 'Typical size' column summarizes ranges of uncertainty sizes in the BSM SR.

8.5.1 Uncertainties on BSM $t\bar{t}t\bar{t}$ Signal Modeling

Two modeling uncertainties for the BSM $t\bar{t}t\bar{t}$ process are considered: scale variations and PDF. The μ_R and μ_F scales are varied simultaneously by factors of 0.5 and 2 with

Systematic uncertainty	Components	Typical size [%]
BSM $t\bar{t}t\bar{t}$ modeling		
Renormalization and factorization scales	1	$O(10^{-1}) \sim 1$
PDF	1	1
SM $t\bar{t}t\bar{t}$ modeling		
Cross section	1	20
Generator choices	1	$O(1) \sim 15$
Parton shower and hadronization model	1	$O(1) \sim 10$
Renormalization and factorization scales	1	$O(1)$
PDF	1	1
Higher-order EW correction	1	$O(1) \sim 10$
$t\bar{t}H$ modeling		
Cross section	1	10
Generator choices	1	$10 \sim 20$
Renormalization and factorization scales	1	$O(1) \sim 20$
PDF	1	1
Additional heavy flavor jets	2	$O(1) \sim 20$
$t\bar{t}W$ QCD modeling		
Generator choices	1	$O(1) \sim 20$
Renormalization and factorization scales	1	~ 20
Additional heavy flavor jets	2	$O(1) \sim 20$
Jets multiplicity modeling	2	$20 \sim 100$
$t\bar{t}W$ EW modeling		
Generator choices	1	~ 30
Renormalization and factorization scales	1	$O(1) \sim 10$
Additional heavy flavor jets	2	$O(1) \sim 30$
$t\bar{t}Z$ modeling		
Cross section	1	12
Generator choices	1	$O(1) \sim 20$
Renormalization and factorization scales	1	$O(1) \sim 30$
PDF	1	1
Additional heavy flavor jets	2	$O(1) \sim 20$
Other background modeling		
Cross section	6	$30 \sim 50$
Additional heavy flavor jets	3	$O(1) \sim 40$
Total (Signal and Irreducible Background)	39	
Total (Overall)	198	

Table 8.8: Sources of theoretical systematic uncertainty considered in the analysis. The uncertainties from "Luminosity", "Cross section", and "PDF" are taken as normalization only for all processes in all regions. Other uncertainties affect the normalization and shape of the fitted distributions and/or the acceptance into the fit regions. The 'Components' column indicates the components of the systematic uncertainties. The 'Typical size' column summarizes ranges of uncertainty sizes in the BSM SR.

respect to the central values to account for the impacts of the missing higher-order QCD correction. An uncertainty of 1% is considered for the PDF.

8.5.2 Uncertainties on Background Modeling

8.5.2.1 Uncertainties on SM $t\bar{t}t\bar{t}$ Background

Several modeling uncertainties are considered for the production of the SM $t\bar{t}t\bar{t}$. The generator uncertainty, covering different ME and PS, is evaluated with the Sherpa 2.2.10 sample. An additional PS uncertainty is evaluated with MadGraph5_aMC@NLO, which is interfaced with Herwig7. The uncertainty of covering missing higher-order QCD corrections is assessed by varying the μ_R and μ_F scales simultaneously by factors of 0.5 and 2 relative to the central values. An uncertainty of 1% is set to account for the PDF choice. The missing EW correction is evaluated by the shape difference between QCD and QCD+EW with Sherpa 2.2.11, propagated to the nominal sample as systematic uncertainty. Additionally, an uncertainty of 20% on the total cross section, calculated from a prediction at NLO in QCD+EW [123], is included.

8.5.2.2 Uncertainties on $t\bar{t}t$ Background

A conservative normalization uncertainty of 100% is included for $t\bar{t}t$ since the NLO prediction is not yet available. In addition, an uncertainty of 50% is applied for $t\bar{t}t$ events with at least four truth b-jets.

8.5.2.3 Uncertainties on $t\bar{t}H$, $t\bar{t}W$ QCD, $t\bar{t}W$ EW and $t\bar{t}Z$ Backgrounds

Theoretical uncertainties for $t\bar{t}H$, $t\bar{t}W$ QCD, $t\bar{t}W$ EW, and $t\bar{t}Z$ processes are assessed similarly from various sources. These include uncertainties about the choice of different generators, scale variations, PDF variations, the total cross section, and additional heavy-flavor jets. Table 8.9 summarizes the generator uncertainties of different

background processes. These uncertainties are evaluated by comparing the nominal and alternative MC predictions, as outlined in Section 6.2.3 and Section 6.2.4. The uncertainties from missing higher-order QCD corrections are assessed by simultaneously altering the μ_R and μ_F scales by factors of 0.5 and 2.0 with respect to their central values. Cross-section uncertainties of 20%, 12%, and 10% are considered for $t\bar{t}W$ EW [144], $t\bar{t}Z$ and $t\bar{t}H$ [117]. A 1% PDF uncertainty is assigned to the $t\bar{t}Z$ and $t\bar{t}H$ processes following Ref. [52]. No cross-section and PDF uncertainties are considered for $t\bar{t}W$ QCD since the normalization of $t\bar{t}W$ QCD is unconstrained in the template method. The $t\bar{t}H$, $t\bar{t}W$ QCD, $t\bar{t}W$ EW, and $t\bar{t}Z$ backgrounds with additional heavy-flavor jets can enter the baseline SR. These events are challenging to model with MC simulations. Therefore, these backgrounds containing three (four or more) truth b-jets are assigned with 50% uncertainties. These uncertainties are evaluated based on the measurement of the $t\bar{t}$+jets production with additional heavy-flavor jets [279] and on the comparison between the data and the prediction of the $t\bar{t}\gamma$ events with three and four b-tagged jets. Finally, data excesses are observed in the high jet multiplicities in the $t\bar{t}W$ VR. An additional uncertainty of 133% (208%) is applied to $t\bar{t}W$ QCD events with seven (eight or more) jets.

Process	Nominal	Alternative	Purpose
$t\bar{t}H$	PowhegBox+Pythia8	MadGraph5_aMC@NLO+ Pythia8	Gen
$t\bar{t}W$ QCD	Sherpa 2.2.10	MadGraph5_aMC@NLO NLO QCD	Gen
$t\bar{t}W$ EW	Sherpa 2.2.10	MadGraph5_aMC@NLO EW	Gen
$t\bar{t}Z$	Sherpa 2.2.1	MadGraph5_aMC@NLO 2.3.3 + Pythia8	Gen

Table 8.9: Summary of alternative samples for generator uncertainties for the $t\bar{t}H$, $t\bar{t}W$ QCD, $t\bar{t}W$ EW, and $t\bar{t}Z$ processes.

8.5.2.4 Uncertainties on Fake and Non-prompt Backgrounds

Uncertainties related to the fake/non-prompt lepton backgrounds are derived from the approaches described in Section 7.4. Uncertainties on HF e and HF μ backgrounds are assessed based on the difference between data and MC simulations with at least one

loose lepton in every fitted region. These uncertainties range from a few percent to 100% across bins in the SR and CRs. For material and internal conversions, the uncertainties are 50% and 100%, respectively, based on the comparison between data and simulation in a VR selecting $Z \to \mu^+\mu^-\gamma(\to e^+e^-)$. An uncertainty of 100% (30%) is applied to events with fake/non-prompt leptons from light jets (other sources) [51; 52; 260]. Additional 30% uncertainties are assigned to $t\bar{t}$ events with three and four or more truth b-jets, respectively, based on the observed discrepancies between the data and MC simulations [279].

8.5.2.5 Uncertainties on Other Backgrounds

An uncertainty of 40% on VV is derived from the studies of WZ+b production. Other uncertainties are evaluated using the same approaches as those described in Section 7.4. An uncertainty of 30% is applied to the sum of the tZq and tWZ processes [239; 280; 281]. A converative uncertainty of 50% is assigned to VH although the precise measurement of $VH(\to b\bar{b})$ provides 20% uncertainty [283]. Uncertainties of 50% are applied to the VVV, $t\bar{t}ZZ$, $t\bar{t}WZ$, $t\bar{t}HH$, $t\bar{t}WH$, and $t\bar{t}WW$ processes [51; 52; 205; 260]. An additional 50% uncertainty is considered for these backgrounds with events containing three (four or more) truth b-jets [279].

8.6 Results

Binned maximum-likelihood fits are performed to the BSM BDT distribution in the BSM SR and various distributions for CRs under the background-only and the signal-plus-background hypotheses. Each fit under the targeted signal hypothesis uses the BSM BDT distribution at its corresponding mass point in the BSM SR. The fit simultaneously determines the BSM signal strength, background NFs, and the systematic uncertainties under the signal-plus-background hypothesis. No significant excess over SM predictions is found. Figure 8.15 presents the observed and expected 95% CL upper limits on $t\bar{t}H/A$ cross sec-

tion times the branching ratio of $H/A \to t\bar{t}$ as a function of the heavy Higgs boson mass ($m_{H/A}$). The observed upper limits on the cross section vary from 14 fb and 6 fb for $m_{H/A}$ between 400 GeV and 1000 GeV. Figure 8.16 presents the event display of the signal candidate event from data collected in 2017. The upper limits on the cross section are interpreted into the exclusion limits on $\tan\beta$ values in the type-II 2HDM model. Figure 8.17 shows the observed and expected 95% CL exclusion regions on $\tan\beta$ values as a function of $m_{H/A}$. Two scenarios are considered: both scalar (H) and pseudo-scalar (A) Higgs bosons with equal mass contribute, or only one scalar (or pseudo-scalar) Higgs boson contributes. The $\tan\beta$ values below 1.6 and 0.6 are excluded in the studied heavy Higgs boson mass range when considering both particles. The $\tan\beta$ values below 1.2 and 0.5 are excluded for the studied range when considering only the scalar Higgs boson. The exclusion of $\tan\beta$ values with only the pseudo-scalar Higgs boson shows similar results as limits when considering only the scalar Higgs boson.

The background modeling is examined through a background-only hypothesis, discussed in Section 8.3.2. Table 8.11 shows the pre-fit and post-fit background yields obtained from the background-only hypothesis. Post-fit yields of various background sources are increased, such as $t\bar{t}t\bar{t}$, $t\bar{t}W$ QCD, $t\bar{t}t$, and other minor backgrounds. The enhancement of the post-fit yields is related to the high NFs and the pulls of NPs, described in Table 8.4 and Table 8.10, respectively. Data and post-fit yields are consistent within around one standard deviation.

Table 8.12 summarizes the impacts of systematic uncertainties on the signal strength. The largest impacts come from the modeling uncertainties of SM $t\bar{t}t\bar{t}$ and $t\bar{t}W$ backgrounds due to their dominant contributions in the BSM SR. Figure 8.18 and Figure 8.19 present the rankings of individual NPs impacting the signal strength under different signal hypotheses. For $m_H = 400$ GeV, the SM $t\bar{t}t\bar{t}$ cross-section uncertainty has the largest impact due to the limited separation between the signal and the SM $t\bar{t}t\bar{t}$. For $m_H = 1000$ GeV, the systematic uncertainty on $t\bar{t}W$ events with ≥ 8 jets has the largest impact due

to the consistent large $t\bar{t}W$ contributions and improved separation between signal and the SM $t\bar{t}t\bar{t}$ with the high-mass signal hypothesis.

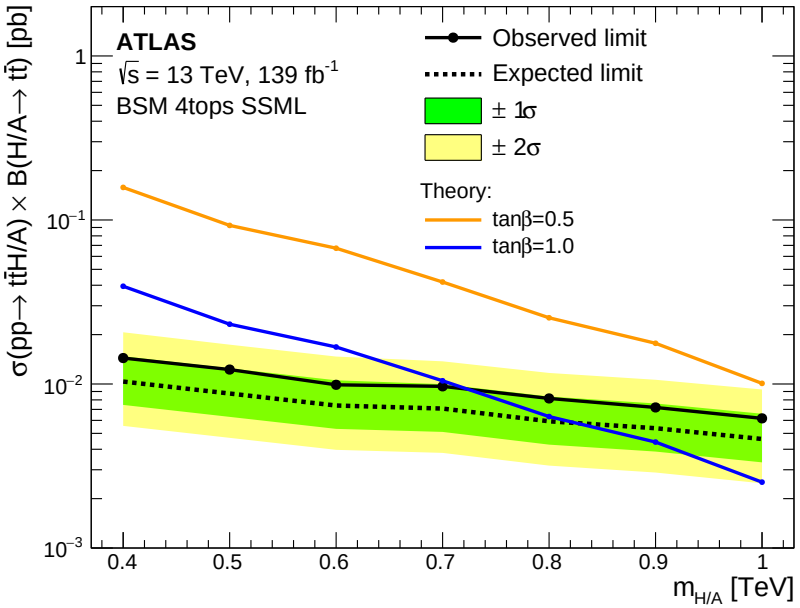

Figure 8.15: Observed (black solid line) and expected (black dashed line) 95% CL upper limits on the $t\bar{t}H/A$ cross section times the branching ratio of $H/A \to t\bar{t}$ in terms of the heavy Higgs boson mass $m_{H/A}$ [135]. The limits are calculated assuming that both scalar and pseudo-scalar bosons contribute to the $t\bar{t}t\bar{t}$ final state with equal mass between these two. The green (yellow) band shows the $\pm 1\sigma$ ($\pm 2\sigma$) variations of the expected limits. The theoretical predictions are derived for $\tan\beta = 0.5$ and $\tan\beta = 1.0$, assuming both heavy Higgs bosons contribute. The regions above the limits are excluded.

Nuisance parameter	400 GeV	1000 GeV
SM $t\bar{t}t\bar{t}$ cross section	$0.44^{+0.94}_{-0.89}$	$0.61^{+0.99}_{-0.93}$
SM $t\bar{t}t\bar{t}$ generator choice	$0.33^{+0.99}_{-0.96}$	$0.32^{+0.97}_{-0.95}$
$t\bar{t}W$ QCD $N_{\text{jets}} = 7$	$0.04^{+0.80}_{-0.67}$	$0.17^{+0.79}_{-0.69}$
$t\bar{t}W$ QCD $N_{\text{jets}} \geq 8$	$0.23^{+0.68}_{-0.42}$	$-0.07^{+0.74}_{-0.42}$
$t\bar{t}t$ cross section	$0.18^{+0.99}_{-0.95}$	$0.21^{+1.01}_{-0.93}$

Table 8.10: The pulls and constraints $(\hat{\theta} \pm \theta_0)/\Delta\theta$ of the important NPs. The $\hat{\theta}$ (θ_0) denotes the best-fit (nominal) value of the NP, while the $\Delta\theta$ is the pre-fit uncertainty. The nominal value for all NPs is 0, with a priori of $\pm 1\sigma$.

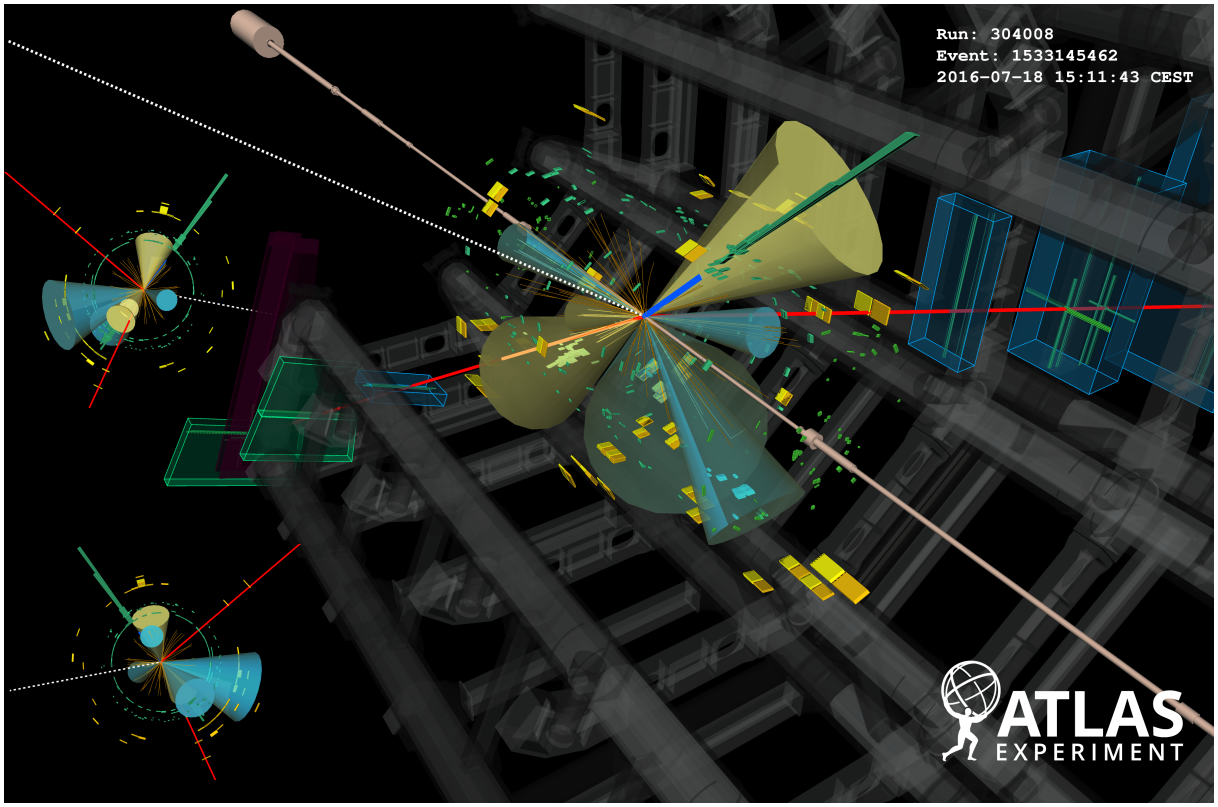

Figure 8.16: Event display of the candidate signal events in the BSM SR. The event consists of an electron-muon pair with the same electric charge and eight jets, four of which are b-tagged. The p_T of the electron and muon are 51 GeV and 31 GeV, respectively. The most energetic jet has a transverse momentum of 219 GeV. The missing transverse energy is 16 GeV. The main visualization shows the track of the reconstructed electron (blue track), the track of the reconstructed muon (red track), four particle jets (the yellow cones), four b-tagged jets (the light green cones), and the missing transverse momentum (white dotted line) [135].

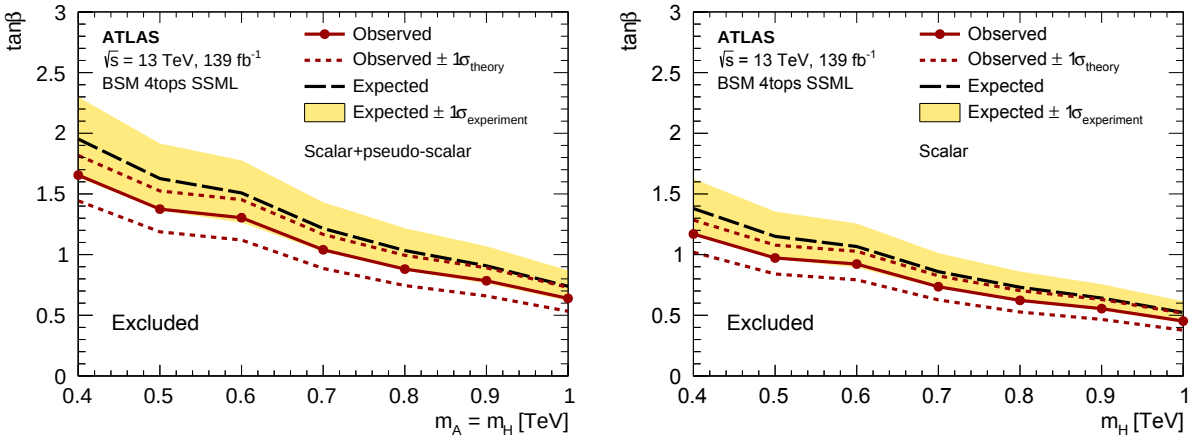

(a) (b)

Figure 8.17: Observed (red solid line) and expected (black dashed line) 95% CL exclusion regions in the $\tan\beta$ versus $m_{H/A}$ plane assuming that (a) both scalar and pseudo-scalar Higgs bosons, with equal mass, contribute to the $t\bar{t}t\bar{t}$ final state or (b) only the scalar Higgs boson contributes to the $t\bar{t}t\bar{t}$ final state [135]. The exclusion limits assuming only pseudo-scalar Higgs boson contribution yield similar exclusion as those in (b). The exclusion limits are interpreted with type-II 2HDM. The region below the red solid line is excluded at 95% CL. The red dashed line (yellow band) shows the $\pm 1\sigma$ variations of observed (expected) exclusion limits.

Process	Pre-fit	Post-fit
$t\bar{t}t\bar{t}$	22.3 ± 5.3	25.8 ± 5.3
$t\bar{t}W$ QCD	9.4 ± 9.6	17.2 ± 6.9
$t\bar{t}W$ EW	1.3 ± 0.5	1.4 ± 0.6
$t\bar{t}WW$	1.8 ± 1.0	1.9 ± 1.0
$t\bar{t}(Z/\gamma^*)$ (high mass)	8.5 ± 2.1	9.2 ± 2.2
$t\bar{t}H$	7.2 ± 1.7	7.8 ± 1.7
QmisID	2.1 ± 0.2	2.1 ± 0.2
Mat. Conv.	1.8 ± 0.6	3.0 ± 1.2
Low m_{γ^*}	1.2 ± 0.6	0.8 ± 0.8
HF e	0.6 ± 0.7	0.6 ± 0.7
HF μ	2.7 ± 1.1	2.9 ± 1.2
LF	1.1 ± 1.2	0.4 ± 1.0
Other fake	1.1 ± 0.7	1.3 ± 0.7
tZ, tWZ	0.9 ± 0.3	0.9 ± 0.3
VV, VH, VVV	0.3 ± 0.1	0.3 ± 0.1
$t\bar{t}t$	1.9 ± 1.9	2.3 ± 2.1
$t\bar{t}WZ$, $t\bar{t}ZZ$, $t\bar{t}WH$, $t\bar{t}HH$	1.3 ± 0.7	1.4 ± 0.8
Total background	65.6 ± 13.4	79.5 ± 6.7
$t\bar{t}H(\to t\bar{t})$, $m_H = 400$ GeV	38.6 ± 2.4	–
$t\bar{t}H(\to t\bar{t})$, $m_H = 1000$ GeV	4.4 ± 0.2	–
Data	91	

Table 8.11: Pre-fit and post-fit yields in the BSM SR obtained before and after the fit to data under the background-only fit [135]. The fit is performed with BSM SR and all CRs. The BSM BDT distribution at $m_H = 400$ GeV is used in the BSM SR. The pre-fit signal yields are estimated in the type-II 2HDM with $\tan\beta = 1$ for $m_H = 400$ GeV and 1000 GeV, assuming only the scalar Higgs boson contributes. The total uncertainty differs from the quadratic sum of the different uncertainties due to the correlations of the NPs.

Uncertainty source	$\Delta\mu$	
Signal modeling		
$t\bar{t}H(\to t\bar{t})$	$+0.01$	-0.00
Background modeling		
$t\bar{t}t\bar{t}$	$+0.17$	-0.17
$t\bar{t}W$	$+0.07$	-0.07
$t\bar{t}t$	$+0.06$	-0.05
Non-prompt leptons	$+0.05$	-0.05
$t\bar{t}Z$	$+0.05$	-0.05
$t\bar{t}H$	$+0.03$	-0.03
Other background	$+0.03$	-0.02
Instrumental		
Jet uncertainties	$+0.12$	-0.09
Jet flavor tagging (b-jets)	$+0.05$	-0.04
Jet flavor tagging (light-flavor jets)	$+0.04$	-0.03
Luminosity	$+0.03$	-0.02
Jet flavor tagging (c-jets)	$+0.02$	-0.02
Other experimental uncertainties	$+0.02$	-0.02
MC statistical uncertainty		
Simulation sample size	$+0.04$	-0.04
Total systematic uncertainty	$+0.31$	-0.28
Statistical		
HF, Mat. Conv., and Low $m_{\gamma*}$ normalization	$+0.05$	-0.04
$t\bar{t}W$ QCD normalization	$+0.05$	-0.04
Total statistical uncertainty	$+0.35$	-0.32
Total uncertainty	$+0.46$	-0.41

Table 8.12: The grouped impact of the uncertainties on the BSM signal strength μ assuming $m_H = 400$ GeV [135]. The impacts are evaluated with the difference in the signal strength derived from a nominal setup and an alternative setup by fixing a set of nuisance parameters in each category to the best value with $\pm 1\sigma$. The total uncertainty differs from the quadratic sum of the components due to correlations among NPs.

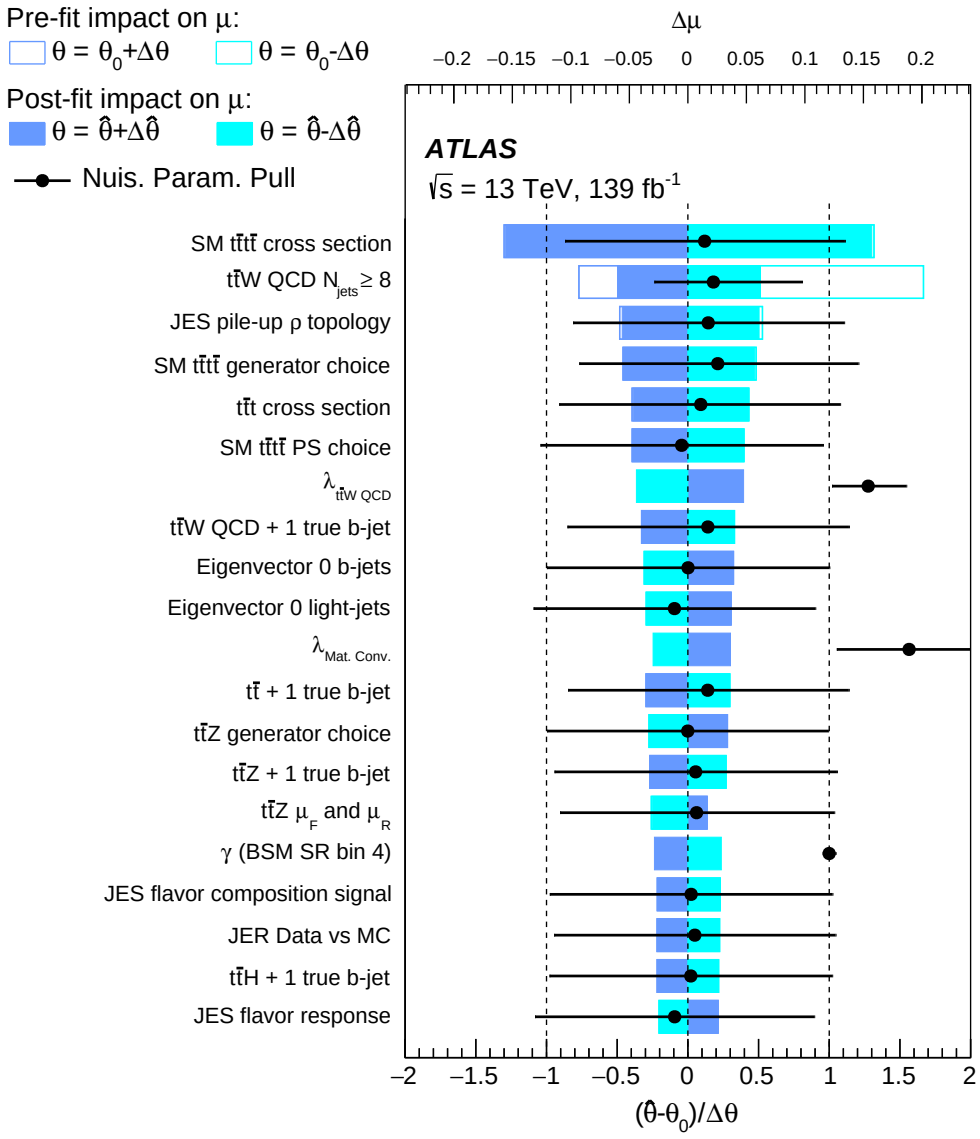

Figure 8.18: Ranking of the impact on BSM signal strength μ from the NPs, assuming the signal hypothesis of $m_H = 400$ GeV [135]. The leading 20 NPs with the largest impacts are shown. The empty (solid) blue rectangles illustrate the pre-fit (post-fit) impacts on the μ, corresponding to the top axis. The pre-fit (post-fit) impacts, $\theta_0 \pm \Delta\theta$ ($\hat{\theta} \pm \Delta\hat{\theta}$), are evaluated with the difference on μ, $\Delta\mu$, derived from a nominal setup and an alternative setup by fixing the NP to the best value with $\pm 1\sigma$. The θ_0 ($\hat{\theta}$) is the nominal (best-fit) value of the NP, and $\Delta\theta$ ($\Delta\hat{\theta}$) is its pre-fit (post-fit) uncertainty. The black points show the pulls and constraints of the NPs relative to their nominal values, θ_0. The nominal value for all NPs is $\theta_0 = 0$ with a priori of $\pm 1\sigma$, excepting the background NFs and the MC statistical uncertainties for which $\theta_0 = 1$ without a priori. These pulls and their relative post-fit errors, $\Delta\hat{\theta}/\Delta\theta$, refer to the bottom axis. The parameters with γ symbol refer to the MC statistical uncertainties, while the ones with λ to the background NFs.

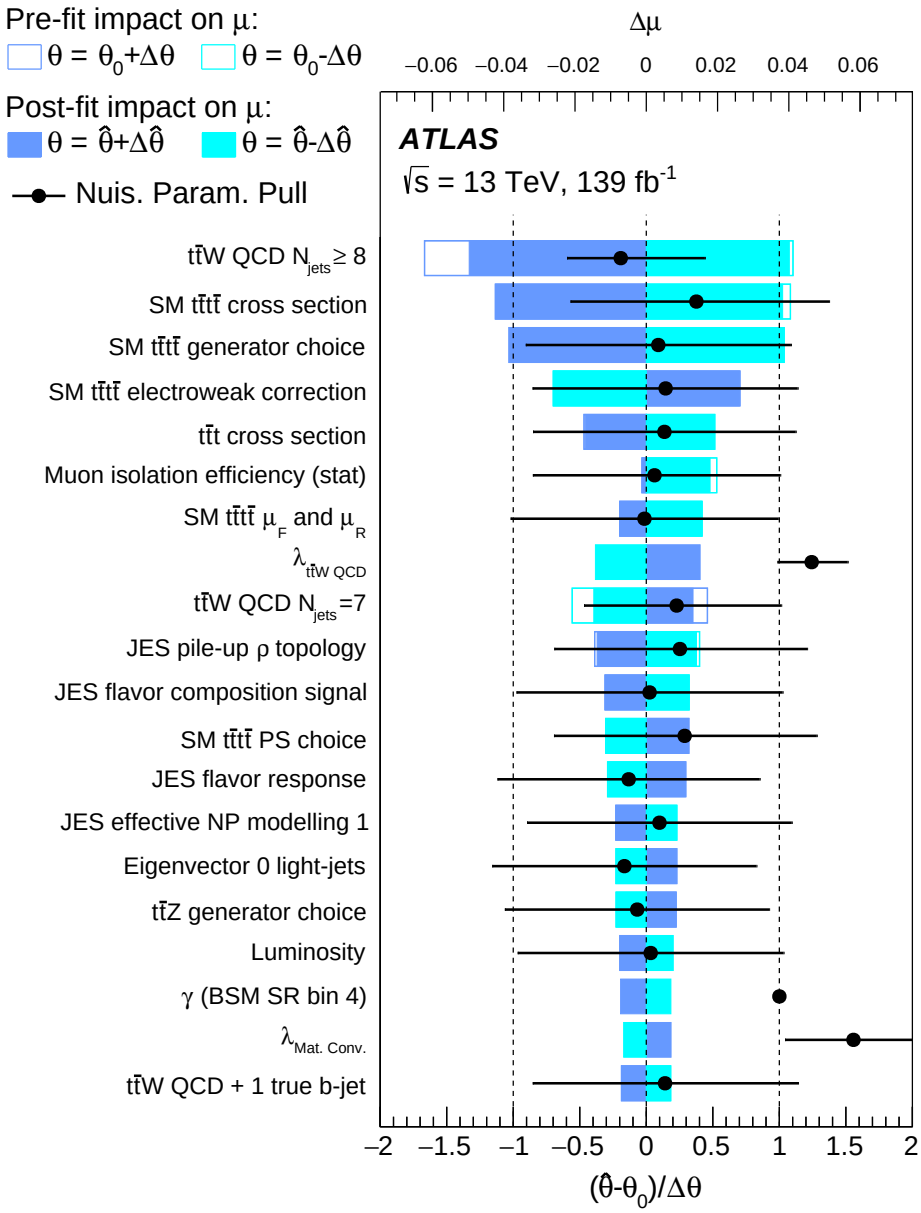

Figure 8.19: Ranking of the impact on BSM signal strength μ from the NPs, assuming the signal hypothesis of $m_H = 1000$ GeV [135]. The leading 20 NPs with the largest impacts are shown. The empty (solid) blue rectangles illustrate the pre-fit (post-fit) impacts on the μ, corresponding to the top axis. The pre-fit (post-fit) impacts, $\theta_0 \pm \Delta\theta$ ($\hat{\theta} \pm \Delta\hat{\theta}$), are evaluated with the difference on μ, $\Delta\mu$, derived from a nominal setup and an alternative setup by fixing the NP to the best value with $\pm 1\sigma$. The θ_0 ($\hat{\theta}$) is the nominal (best-fit) value of the NP, and $\Delta\theta$ ($\Delta\hat{\theta}$) is its pre-fit (post-fit) uncertainty. The black points show the pulls and constraints of the NPs relative to their nominal values, θ_0. The nominal value for all NPs is $\theta_0 = 0$ with a priori of $\pm 1\sigma$, excepting the background NFs and the MC statistical uncertainties for which $\theta_0 = 1$ without a priori. These pulls and their relative post-fit errors, $\Delta\hat{\theta}/\Delta\theta$, refer to the bottom axis. The parameters with γ symbol refer to the MC statistical uncertainties, while the ones with λ to the background NFs.

CHAPTER IX

2HDM+a Combination of Four-Top-Quark Production

The motivation for studying the $t\bar{t}t\bar{t}$ production in the 2HDM+a model was discussed in a published HL-LHC study [296]. The 2HDM+a provides an additional pseudo-scalar Higgs boson (a) as a portal to interact with the DM particles (χ). In addition, the $t\bar{t}t\bar{t}$ production in 2HDM+a is sensitive to the 2HDM parameter space of low $\tan\beta$ values. These characteristics provide unique signatures and an advantage to exclude a specific 2HDM+a parameter space. This chapter reinterprets the BSM $t\bar{t}t\bar{t}$ analysis with $t\bar{t}t\bar{t}$ production predicted in the type-II 2HDM+a. The exclusion limits are further combined with limits from other final states on the 2HDM+a model.

The reinterpretation follows the same analysis strategies from the BSM $t\bar{t}t\bar{t}$ analysis [135], discussed in Chapter VIII. This chapter will focus only on the 2HDM+a $t\bar{t}t\bar{t}$ signal, the strategies apart from the BSM $t\bar{t}t\bar{t}$ analysis, and the results. This chapter is organized as follows. Section 9.1 discusses the $t\bar{t}t\bar{t}$ signal modeling predicted in the 2HDM+a. Section 9.2 presents the optimized MVA strategies to extract the signal from backgrounds with the same BDT discriminants used in Section 8.4. Section 9.3 summarizes the exclusion limits of the $t\bar{t}t\bar{t}$ and other signatures in various scenarios of the 2HDM+a interpretation.

9.1 Signal Modeling

The 2HDM+a $t\bar{t}t\bar{t}$ signal is simulated with MadGraph5_aMC@NLO at LO QCD using 2HDM+a UFO model [81]. The $t\bar{t}t\bar{t}$ ME generation is produced with NNPDF3.0nlo in the 4FS for gg-initiated production and in the 5FS for bb-initiated production. Events are further interfaced with the Pythia8 using the A14 tune and NNPDF2.3lo. A one-lepton filter on all decay products is applied to increase the statistics.

The 2HDM+a $t\bar{t}t\bar{t}$ signal is generated with s- and t-channels including their interference. Figure 3.16 shows example Feynman diagrams of $t\bar{t}(H/A/a) \to t\bar{t}t\bar{t}$ production. The mass ranges cover 200 to 1200 GeV for CP-even (H) and CP-odd (A) Higgs bosons and 100 to 800 GeV for pseudo-scalar mediator (a). The signals are produced with different mixings between CP-even (CP-odd) weak eigenstates with $\sin\alpha$ ($\sin\theta$) to study the exclusion of 2HDM parameter phase space. Table 9.1 summarizes the 2HDM+a parameter settings explored in this analysis.

The relative contributions of the s- and t-channels vary across different parameter setups. With CP-even and CP-odd Higgs masses above the $m_{t\bar{t}}$ threshold, the s-channel with $H/A \to t\bar{t}$ is the dominant channel. The s-channel with $a \to t\bar{t}$ is generally subdominant from a few percent to 20% of the total contribution. The t-channel contribution is generally at a few percent level in different parameter setups except in two cases: the $m_{H/A}$ below $m_{t\bar{t}}$ threshold or large $\tan\beta$ ($\tan\beta \gtrsim 3$). When $m_{H/A}$ is below the $m_{t\bar{t}}$ threshold, the t-channel becomes the dominant channel with 80% to almost 100% of the total contribution for different values of m_a, and the rest of the contribution is from the s-channel via $a \to t\bar{t}$. The ratio of branching ratios between $a \to \chi\chi$ and $a \to t\bar{t}$ varies with the $\tan\beta$ and $\sin\theta$ values [81] as

$$\frac{\mathrm{BR}(a \to \chi\chi)}{\mathrm{BR}(a \to t\bar{t})} \simeq 0.7 y_\chi^2 \tan^2\beta / \tan^2\theta, \tag{9.1}$$

and the ratio of branching ratios between $A \to \chi\chi$ and $A \to t\bar{t}$ is

$$\frac{\mathrm{BR}(A \to \chi\chi)}{\mathrm{BR}(A \to t\bar{t})} \simeq 0.9 y_\chi^2 \tan^2\beta \tan^2\theta, \tag{9.2}$$

where y_χ is the Yukawa coupling of the pseudo-scalar mediator to the DM χ particles. With a larger $\tan\beta$, the $A/a \to t\bar{t}$ contributions decrease, increasing the contributions of $H \to t\bar{t}$ and t-channel. With a large $\sin\theta$, the contribution of $a \to t\bar{t}$ increases, decreasing the $A \to t\bar{t}$ contributions.

Scenario		Fixed parameter values					Varied parameters
		$\sin\theta$	m_A[GeV]	m_a[GeV]	m_χ[GeV]	$\tan\beta$	
1	a	0.35	–	–	10	1.0	(m_a, m_A)
	b	0.70	–	–	10	1.0	
2	a	0.35	–	250	10	–	$(m_A, \tan\beta)$
	b	0.70	–	250	10	–	
3	a	0.35	600	–	10	–	$(m_a, \tan\beta)$
	b	0.70	600	–	10	–	
4	a	–	600	200	10	1.0	$\sin\theta$
	b	–	1000	350	10	1.0	
5		0.35	1000	400	–	1.0	m_χ
6		0.35	1200	–	–	1.0	$(m_a,\ m_\chi)$

Table 9.1: Summary of the 2HDM+a parameters in the scenarios explored in this analysis [297]. The $t\bar{t}t\bar{t}$ signature is included in all scenarios except the (m_a, m_χ) interpretation.

9.2 Analysis Strategies

The analysis strategies follow those of the BSM $t\bar{t}t\bar{t}$ analysis, described in Chapter VIII, including object selections, background estimation, BDT methods, systematic uncertainties, and statistical interpretation. The differences are from the 2HDM+a $t\bar{t}t\bar{t}$ signal modeling and the usage of the BSM BDT.

The 2HDM+a $t\bar{t}t\bar{t}$ signals include additional s-channel contributions through the pseudo-scalar ($a \to t\bar{t}$) and the t-channel contribution, compared to 2HDM $t\bar{t}t\bar{t}$ s-channel

signal in BSM $t\bar{t}t\bar{t}$ analysis. In addition, different parameter choices can change the kinematics of the 2HDM+a $t\bar{t}t\bar{t}$ signal. Nonetheless, the kinematics of 2HDM+a $t\bar{t}t\bar{t}$ and 2HDM $t\bar{t}t\bar{t}$ production do not differ significantly due to the dominant s-channel $H/A \to t\bar{t}$ contribution. Moreover, the kinematics of t-channel contributions are similar to that of $H/A \to t\bar{t}$ production with a low H/A mass. Therefore, the SM BDT and BSM BDT, described in Section 8.4, are used to extract the 2HDM+a $t\bar{t}t\bar{t}$ signal from backgrounds. Decent performances of separation are obtained for the 2HDM+a $t\bar{t}t\bar{t}$ signal despite the BSM BDT being trained with the m_H parameterization of the 2HDM $t\bar{t}t\bar{t}$ signal.

As the same strategy in Section 8.4.1, the SM BDT is used to extract the $t\bar{t}t\bar{t}$ events from the backgrounds. Figure 9.1 presents the good separation between the 2HDM+a $t\bar{t}t\bar{t}$ signals and the backgrounds. With the SM BDT, the 2HDM+a $t\bar{t}t\bar{t}$ signal is extracted in the BSM SR, with SM BDT ≥ 0.55, regardless of the parameter setups. Figure 9.2 presents the BSM BDT distributions in the BSM SR for the 2HDM+a signals of different parameter setups. Fig. 9.2a shows that the 2HDM+a $t\bar{t}t\bar{t}$ signals with $\sin\theta = 0.35$ are independent of the m_a choice due to the small contributions of $a \to t\bar{t}$. However, the relative contribution of $a \to t\bar{t}$ becomes important with $\sin\theta = 0.7$. In this case, the kinematics is softer for $m_a < m_A$. Fig. 9.2b shows that the kinematics stay similar for different $\tan\beta$ values. With a larger $\tan\beta$ value, the $H \to t\bar{t}$ and t-channel contributions increase, and the other contributions decrease. In this case, the $H/A \to t\bar{t}$ relative contributions dominate and keep the kinematics similar. Fig. 9.2c shows that the separation power of the BSM BDT remains when applied to a signal mass of m_A higher than the trained mass range. In conclusion, the kinematic of 2HDM+a $t\bar{t}t\bar{t}$ signal cannot be singly parameterized with m_A, as the 2HDM $t\bar{t}t\bar{t}$ signal in the BSM $t\bar{t}t\bar{t}$ analysis, and is dependent on a combination of effects from the $\sin\theta$, $\tan\beta$, m_a, and m_A choices. Despite the kinematics varying with the parameters, it can still be well captured by the BSM BDT under different mass hypotheses. When a low-mass s-channel production or a t-channel contribution is dominant, a low-mass BSM BDT can well separate the 2HDM+a signal

from the background. On the other hand, when a high-mass s-channel production is dominant, the BSM BDT with a high-mass hypothesis can provide a good separation between the signal and the background. Therefore, the mass choice for BSM BDT is optimized to achieve the strongest sensitivity based on the separation power $\langle S^2 \rangle$ [180] defined as

$$\langle S^2 \rangle = \frac{1}{2} \int \frac{(\hat{y}_S(y) - \hat{y}_B(y))^2}{\hat{y}_S(y) + \hat{y}_B(y)} dy \tag{9.3}$$

where y is the classifier, and $\hat{y}_S(y)$ and $\hat{y}_B(y)$ are the signal and background probability density function of y. This metric quantifies the ability of the classifier to separate the signal from the background. The separation powers of BSM BDTs are studied for each signal hypothesis with a set of 2HDM+a parameters. The BSM BDT with the highest separation power is utilized as the final discriminant.

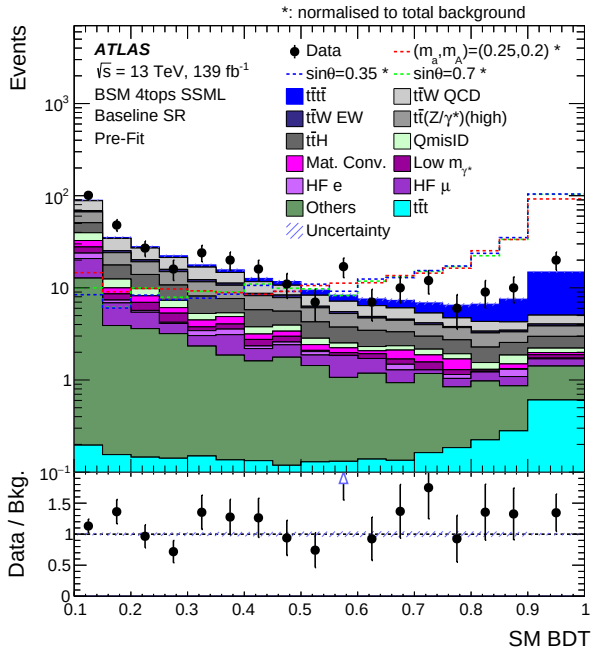

Figure 9.1: SM BDT distributions of backgrounds and 2HDM+a $t\bar{t}t\bar{t}$ signals under different hypotheses: (a) $(m_a, m_A) = (250, 200)$ GeV with $\sin\theta = 0.35$ (red dashed line), (b) $(m_a, m_A) = (800, 1200)$ GeV with $\sin\theta = 0.35$ (blue dashed line), and (c) $(m_a, m_A) = (800, 1200)$ GeV with $\sin\theta = 0.7$ (green dashed line).

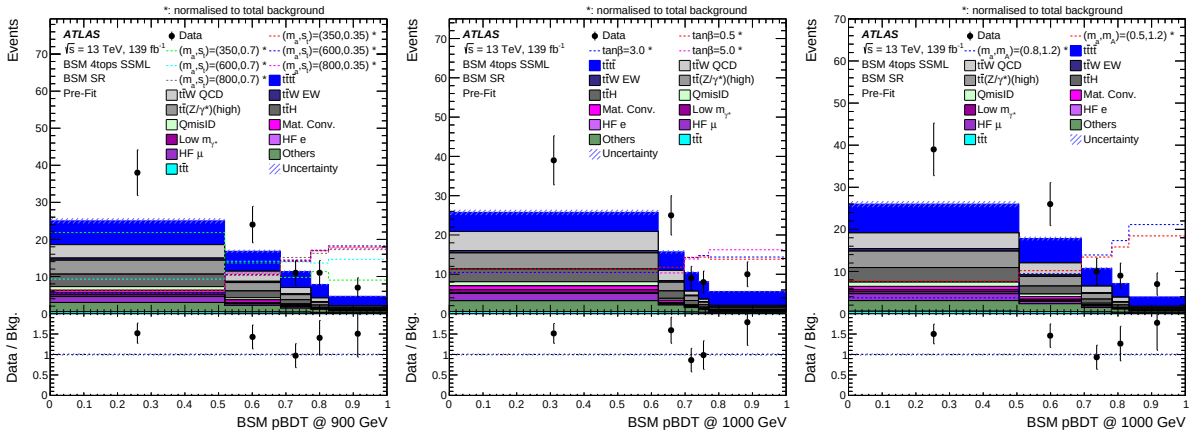

(a) (b) (c)

Figure 9.2: BSM BDT distributions of backgrounds and 2HDM+a $t\bar{t}t\bar{t}$ signals under different hypotheses: (a) various m_a and $\sin\theta$ with $m_A = 900$ GeV using BSM BDT at 900 GeV, (b) various $\tan\beta$ with $(m_a, m_A) = (800, 600)$ GeV using BSM BDT at 1000 GeV, and (c) various m_a with $m_A = 1200$ GeV using BSM BDT at 1000 GeV.

9.3 Results

This section summarizes the exclusion limits and contours in different parameter planes: m_a-m_A plane, m_A-$\tan\beta$ plane, m_a-$\tan\beta$ plane, variations of $\sin\theta$, and variations of m_χ. This section will focus only on the interpretation results of the $t\bar{t}t\bar{t}$ signature.

9.3.1 m_a-m_A Plane

The exclusion contours at 95% CL in the (m_a, m_A) plane with $\sin\theta = 0.35$ and $\sin\theta = 0.7$, assuming $\tan\beta = 1$, are summarized in Figure 9.3. For $\sin\theta = 0.35$, the $H/A \to t\bar{t}$ contribution dominates when the $m_{H/A}$ is above the $m_{t\bar{t}}$ threshold, while t-channel dominates when $m_{H/A}$ is below the $m_{t\bar{t}}$ threshold. Therefore, the sensitivity is driven from resonant $H/A \to t\bar{t}$ and largely independent of m_a. In addition, the smaller cross section with t-channel production results in weaker sensitivities and a lower bound of the exclusion limits around 400 GeV. For $\sin\theta = 0.7$, the relative $a \to t\bar{t}$ contribution increases, while the relative $H/A \to t\bar{t}$ contribution decreases. This results in a smaller cross section in the regime where $a \to t\bar{t}$ production becomes kinematically inaccessible

($m_a < 2m_{t\bar{t}}$) or when $m_a > m_A$. Therefore, a narrower exclusion contour is observed with $\sin\theta = 0.7$ than those with $\sin\theta = 0.35$.

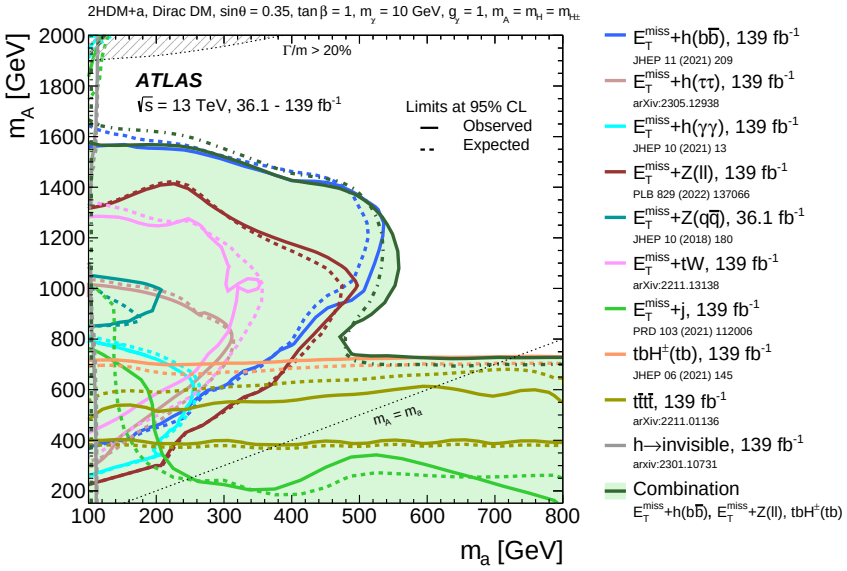

(a)

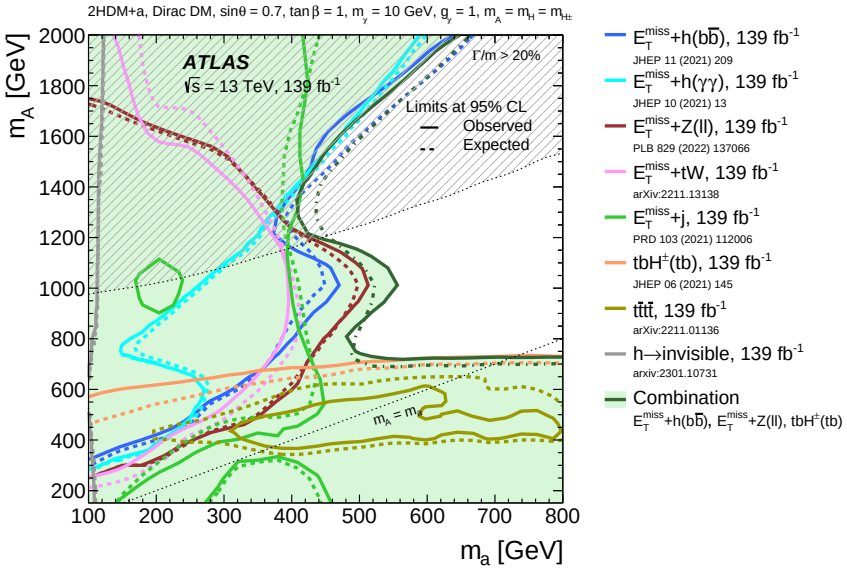

(b)

Figure 9.3: Observed (solid line and filled area) and expected (dashed line) exclusion contours at 95% CL in the (m_a, m_A) plane assuming (a) $\sin\theta = 0.35$ and (b) $\sin\theta = 0.7$ [297]. The exclusion on the $t\bar{t}t\bar{t}$ signature is shown as yellow lines.

9.3.2 m_A-$\tan\beta$ Plane

The exclusion contours at 95% CL in the $(m_A, \tan\beta)$ plane with $\sin\theta = 0.35$ and $\sin\theta = 0.7$, assuming $m_a = 250$ GeV, are summarized in Figure 9.4. The $m_a = 250$ GeV assumption disallows the $a \to t\bar{t}$ decay, resulting in the cross sections of signals independent of the $a \to t\bar{t}$ contribution and only dependent on the $H/A \to t\bar{t}$ production and t-channel production with a few percent to 20% contributions. Therefore, the cross sections decrease as a function of $1/\tan^2\beta$ for $A \to t\bar{t}$ and of $1/\sin^2\beta$ for $H \to t\bar{t}$, following Table 2.3. The smaller cross sections lead to weaker sensitivities at the high m_A or $\tan\beta$ values. The exclusion contours of $t\bar{t}t\bar{t}$ dominate the low m_A and $\tan\beta$ parameters.

9.3.3 m_a-$\tan\beta$ Plane

The exclusion contours at 95% CL in the $(m_a, \tan\beta)$ plane with $\sin\theta = 0.35$ and $\sin\theta = 0.7$, assuming $m_A = 600$ GeV, are summarized in Figure 9.5. Similar to Section 9.3.2, signal productions dominate with the $H/A \to t\bar{t}$ contributions, leading to a negligible dependence on the m_a. In addition, the low $\tan\beta$ values increase the cross sections of the $t\bar{t}t\bar{t}$ production. These result in the exclusion contour being generally independent of the m_a and sensitive in the low $\tan\beta$ values regime.

9.3.4 Variation of $\sin\theta$

The exclusion limits at 95% CL for different $\sin\theta$ values in two scenarios of $(m_a, m_A) = (200, 600)$ GeV and $(m_a, m_A) = (350, 1000)$ GeV, assuming $\tan\beta = 0.5$, are summarized in Figure 9.6. For the scenario of $(m_a, m_A) = (200, 600)$ GeV, the $a \to t\bar{t}$ decay is kinematically disallowed, resulting in dominant $H/A \to t\bar{t}$ contributions. In addition, the branching ratio of $\mathrm{BR}(A \to t\bar{t})$ depends on $1/\tan^2\theta$. Therefore, a larger $\sin\theta$ value results in a smaller production cross section, leading to weaker sensitivities in the high $\sin\theta$ regime. For the scenario of $(m_a, m_A) = (350, 1000)$ GeV, the $a \to t\bar{t}$ decay is kinematically

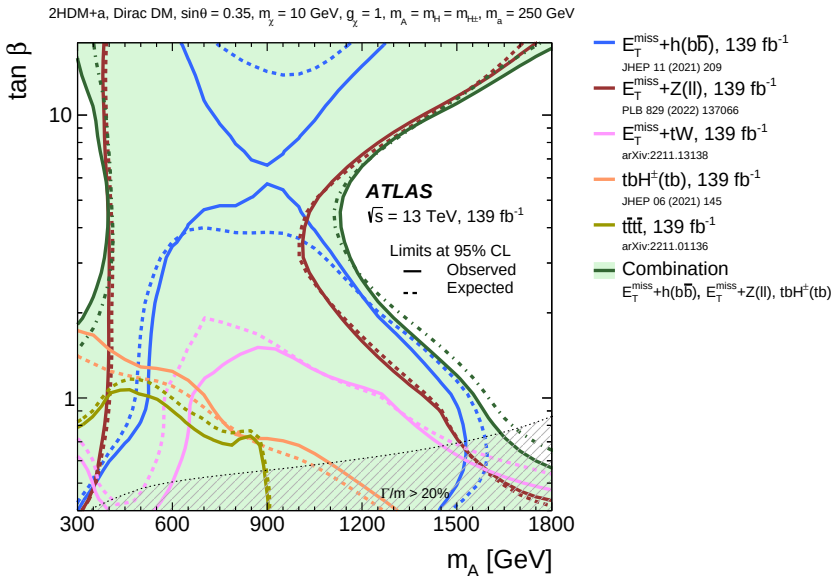

(a)

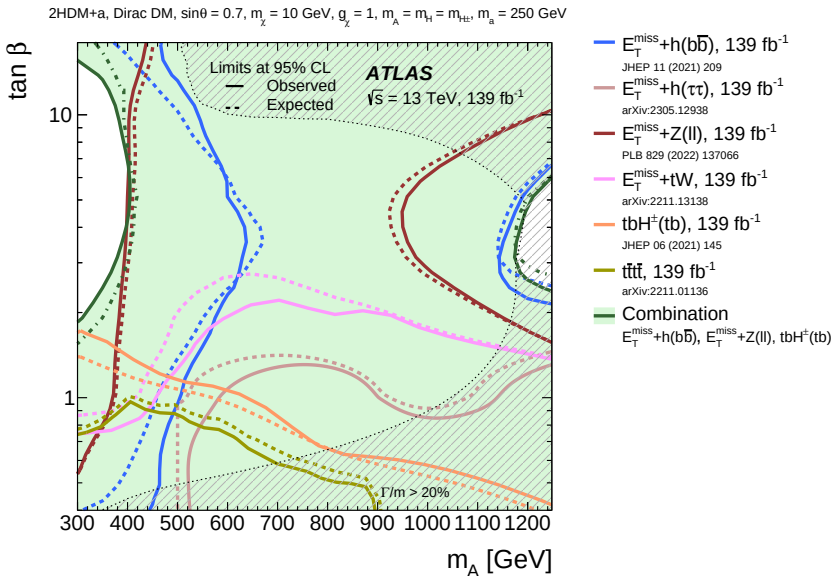

(b)

Figure 9.4: Observed (solid line and filled area) and expected (dashed line) exclusion contours at 95% CL in the $(m_A, \tan\beta)$ plane assuming (a) $\sin\theta = 0.35$ and (b) $\sin\theta = 0.7$ [297]. The exclusion on the $t\bar{t}t\bar{t}$ signature is shown as yellow lines.

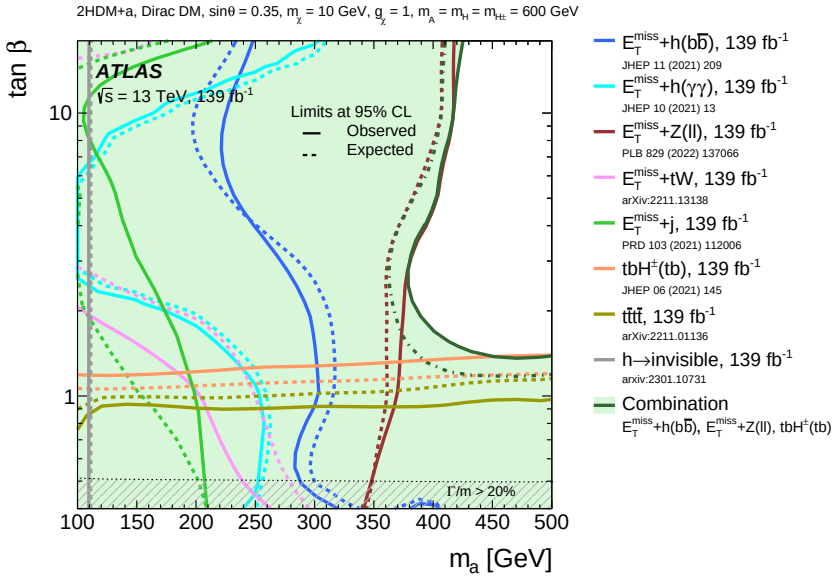

(a)

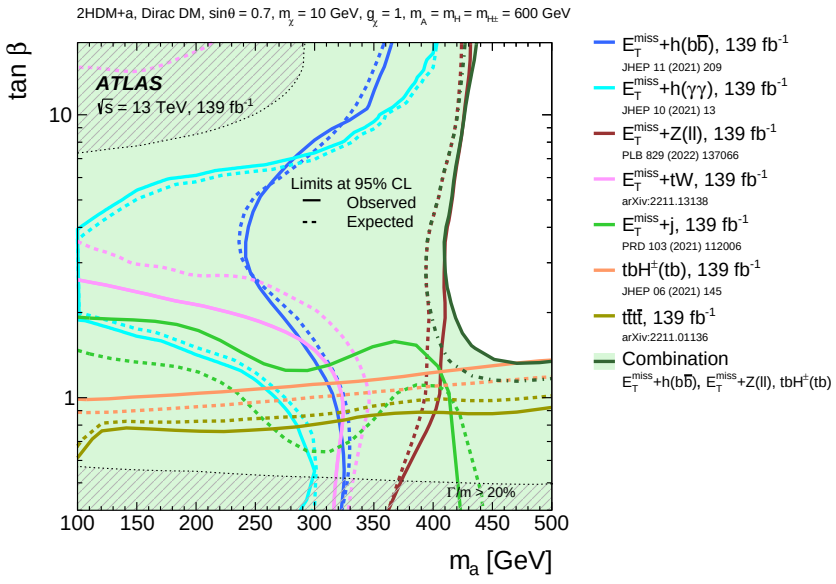

(b)

Figure 9.5: Observed (solid line and filled area) and expected (dashed line) exclusion contours at 95% CL in the $(m_a, \tan\beta)$ plane assuming (a) $\sin\theta = 0.35$ and (b) $\sin\theta = 0.7$ [297]. The exclusion on the $t\bar{t}t\bar{t}$ signature is shown as yellow lines.

allowed. The increase of $\sin\theta$ enhances the mixing between A and a, opening up additional $a \to t\bar{t}$ contributions for $\sin\theta > 0.5$ and resulting in larger cross sections. This leads to a stronger exclusion limit in the high $\sin\theta$ regime.

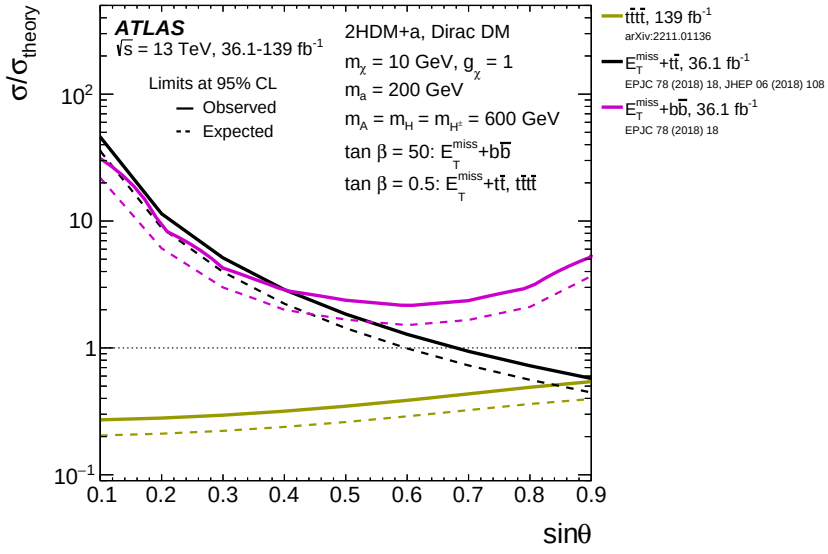

(a)

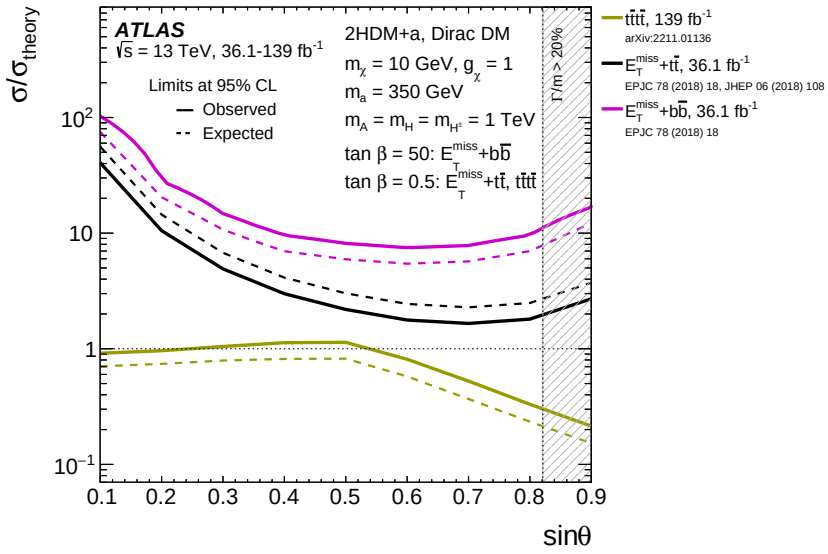

(b)

Figure 9.6: Observed (solid lines) and expected (dashed lines) limits at 95% CL for the 2HDM+a as a function of $\sin\theta$ assuming $\tan\beta = 0.5$ for the $t\bar{t}t\bar{t}$ signature with (a) $(m_a, m_A) = (200, 600)$ GeV and (b) $(m_a, m_A) = (350, 1000)$ GeV [297]. The exclusion on the $t\bar{t}t\bar{t}$ signature is shown as yellow lines. The regime below $\sigma/\sigma_{\text{theory}} = 1$ is excluded at 95% CL.

9.3.5 Variation of m_χ

The exclusion limits at 95% CL as a function of m_χ, assuming $(m_a, m_A) = (400, 1000)$ GeV and $(\tan\beta, \sin\theta) = (1, 0.35)$, are summarized in Figure 9.7. The sensitivities of $t\bar{t}t\bar{t}$ remain generally independent of m_χ since the DM is not included in the $t\bar{t}t\bar{t}$ production.

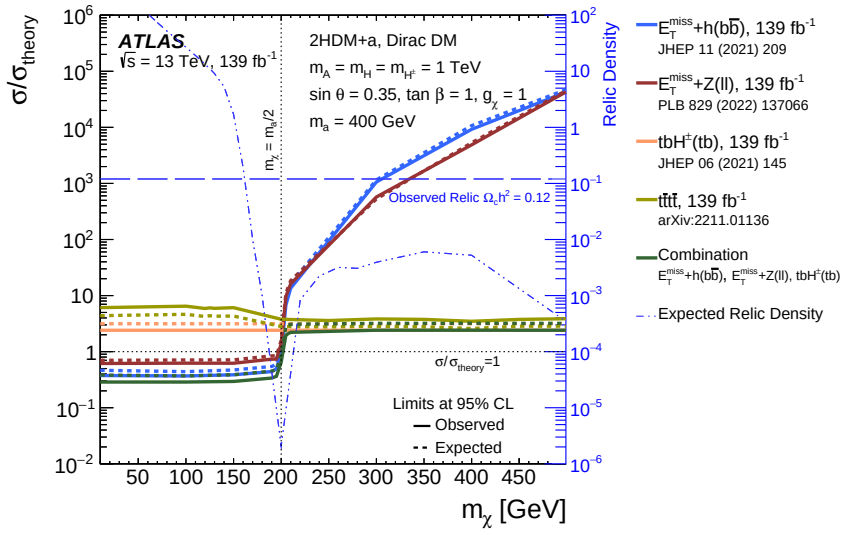

Figure 9.7: Observed (solid lines) and expected (dashed lines) exclusion limits at 95% CL as a function of m_χ with the parameters of $(m_a, m_A) = (400, 1000)$ GeV, $\tan\beta = 1$ and $\sin\theta = 0.35$ [297]. The exclusion on the $t\bar{t}t\bar{t}$ signature is shown as yellow lines. The regime below $\sigma/\sigma_{\text{theory}} = 1$ is excluded at 95% CL.

CHAPTER X

Summary and Outlook

This dissertation summarizes intensive studies on the $t\bar{t}t\bar{t}$ production in the SSML final states: the observation of SM $t\bar{t}t\bar{t}$ production, a search for BSM $t\bar{t}t\bar{t}$ production predicted in the type-II 2HDM and 2HDM+a models.

The SM $t\bar{t}t\bar{t}$ production is first observed using 140 fb^{-1} of pp collision data collected with the ATLAS detector, with an observed significance of 6.1 standard deviations against the background-only hypothesis. The measured cross section of $t\bar{t}t\bar{t}$ production is $22.5\,^{+6.6}_{-5.5}$ fb, in agreement with the SM prediction of 12.0 ± 2.4 ($13.4^{+1.0}_{-1.8}$) fb [123; 124] at 1.8 (1.7) standard deviations. The new $t\bar{t}W$ estimation is performed to improve the modeling, showing consistent results as the dedicated $t\bar{t}W$ measurment [148]. A simultaneous fit determining the $t\bar{t}t\bar{t}$ and $t\bar{t}t$ normalizations shows a large anti-correlation of -93%. The best-fit values of $t\bar{t}t\bar{t}$ and $t\bar{t}t$ cross sections vary with different fit scenarios. Fits with the cut-based method and with the BDT prefer a large $t\bar{t}t\bar{t}$ cross section and a $t\bar{t}t$ cross section of zero, while the nominal fit with the GNN prefers a $t\bar{t}t\bar{t}$ cross section of zero and a large $t\bar{t}t$ cross section. Results with different fit scenarios all deviate from the SM prediction at around 2 standard deviations. Improvements in the separation between $t\bar{t}t\bar{t}$ and $t\bar{t}t$ processes and the $t\bar{t}t$ modeling are required. Besides, the data excess of $t\bar{t}t\bar{t}$ and $t\bar{t}t$ might indicate potential BSM effects. Studies on the Higgs-top Yuakwa coupling, Higgs CP properties, EFT interpretations are performed in this analysis, showing consistent

results with SM predictions.

A search for BSM $t\bar{t}t\bar{t}$ production, $t\bar{t}H/A \to t\bar{t}t\bar{t}$, is performed with 139 fb^{-1} of pp collision data collected with the ATLAS detector. This analysis shows no significant excess over SM predictions. The observed and expected 95% CL upper limits on $t\bar{t}H/A$ cross section times the branching ratio of $H/A \to t\bar{t}$ as a function of the heavy Higgs boson mass ($m_{H/A}$) vary from 14 fb and 6 fb for $m_{H/A}$ between 400 GeV and 1000 GeV. The observed and expected 95% CL exclusion regions on $\tan\beta$ values as a function of $m_{H/A}$ can exclude the $\tan\beta$ values below 1.6 and 0.6 (1.2 and 0.5) for the studied mass range when considering both particles (only the scalar Higgs boson) contribute.

The 2HDM+a combination analysis reinterprets the BSM $t\bar{t}t\bar{t}$ analysis in the 2HDM+a model, $t\bar{t}(H/A/a) \to t\bar{t}t\bar{t}$. This analysis derives multiple exclusion limits and contours in different parameter spaces: m_a-m_A plane, m_A-$\tan\beta$ plane, m_a-$\tan\beta$ plane, variations of $\sin\theta$, and variations of m_χ.

These analyses show a slight data excess in the $t\bar{t}t\bar{t}$ and $t\bar{t}t$ enriched phase spaces. Several possible BSM effects are studied to explore the excess, but only mild deviations are found. As the LHC program continues, more data will be collected in the Run 3 operation. The increased statistics will allow us to better understand these data excesses and explore other exciting rare processes in the SSML final state.

BIBLIOGRAPHY

BIBLIOGRAPHY

[1] S. Tomonaga, *On a relativistically invariant formulation of the quantum theory of wave fields*, Prog. Theor. Phys. **1** (1946) 27.

[2] R. P. Feynman, *Space-Time Approach to Quantum Electrodynamics*, Phys. Rev. **76** (1949) 769.

[3] R. P. Feynman, *The Theory of Positrons*, Phys. Rev. **76** (1949) 749.

[4] R. P. Feynman, *Mathematical Formulation of the Quantum Theory of Electromagnetic Interaction*, Phys. Rev. **80** (1950) 440.

[5] Julian Schwinger, *On Quantum-Electrodynamics and the Magnetic Moment of the Electron*, Phys. Rev. **73** (1948) 416.

[6] Julian Schwinger, *Quantum Electrodynamics. I. A Covariant Formulation*, Phys. Rev. **74** (1948) 1439.

[7] F. A. Scott, *Energy Spectrum of the Beta-Rays of Radium E*, Phys. Rev. **48** (1935) 391.

[8] Wolfgang Pauli, *Pauli letter collection: letter to Lise Meitner*, URL: `https://cds.cern.ch/record/83282`.

[9] E. Fermi, *An attempt of a theory of beta radiation. 1.*, Z. Phys. **88** (1934) 161.

[10] Chen-Ning Yang and Robert L. Mills, *Conservation of Isotopic Spin and Isotopic Gauge Invariance*, Phys. Rev. **96** (1954) 191.

[11] R. L. Mills and Chen-Ning Yang, *Treatment of Overlapping Divergences in the Photon Selfenergy Function*, Prog. Theor. Phys. Suppl. **37** (1966) 507.

[12] Steven Weinberg, *A Model of Leptons*, Phys. Rev. Lett. **19** (1967) 1264.

[13] Sheldon L. Glashow, *Partial-symmetries of weak interactions*, Nucl. Phys. **22** (1961) 579.

[14] Abdus Salam, *Weak and Electromagnetic Interactions*, Conf. Proc. C **680519** (1968) 367.

[15] Peter W. Higgs, *Broken Symmetries and the Masses of Gauge Bosons*, Phys. Rev. Lett. **13** (1964) 508.

[16] F. Englert and R. Brout, *Broken Symmetry and the Mass of Gauge Vector Mesons*, Phys. Rev. Lett. **13** (1964) 321.

[17] Peter W. Higgs, *Broken symmetries, massless particles and gauge fields*, Phys. Lett. **12** (1964) 132.

[18] UA1 Collaboration, *Experimental Observation of Isolated Large Transverse Energy Electrons with Associated Missing Energy at* $\sqrt{s} = 540$ *GeV*, Phys. Lett. B **122** (1983) 103.

[19] UA2 Collaboration, *Observation of Single Isolated Electrons of High Transverse Momentum in Events with Missing Transverse Energy at the CERN* $\bar{p}p$ *Collider*, Phys. Lett. B **122** (1983) 476.

[20] UA2 Collaboration, *Evidence for* $Z^0 \to e^+e^-$ *at the CERN* $\bar{p}p$ *Collider*, Phys. Lett. B **129** (1983) 130.

[21] D0 Collaboration, *Observation of the Top Quark*, Phys. Rev. Lett. **74** (1995) 2632, arXiv: 9503003 [hep-ex].

[22] CDF Collaboration, *Observation of Top Quark Production in* $\bar{p}p$ *Collisions with the Collider Detector at Fermilab*, Phys. Rev. Lett. **74** (1995) 2626.

[23] ATLAS Collaboration, *Observation of a new particle in the search for the Standard Model Higgs boson with the ATLAS detector at the LHC*, Phys. Lett. B **716** (2012) 1, arXiv: 1207.7214 [hep-ex].

[24] CMS Collaboration, *Observation of a New Boson at a Mass of 125 GeV with the CMS Experiment at the LHC*, Phys. Lett. B **716** (2012) 30, arXiv: 1207.7235 [hep-ex].

[25] Super-Kamiokande Collaboration, *Evidence for Oscillation of Atmospheric Neutrinos*, Phys. Rev. Lett. **81** (1998) 1562.

[26] SNO Collaboration, *Measurement of the Rate of* $\nu_e + d \to p + p + e^-$ *Interactions Produced by* ^8B *Solar Neutrinos at the Sudbury Neutrino Observatory*, Phys. Rev. Lett. **87** (2001) 071301.

[27] SNO Collaboration, *Direct Evidence for Neutrino Flavor Transformation from Neutral-Current Interactions in the Sudbury Neutrino Observatory*, Phys. Rev. Lett. **89** (2002) 011301.

[28] Riccardo Barbieri and G.F. Giudice, *Upper bounds on supersymmetric particle masses*, Nucl. Phys. B **306** (1988) 63.

[29] B. de Carlos and J.A. Casas, *One-loop analysis of the electroweak breaking in supersymmetric models and the fine-tuning problem*, Phys. Lett. B **309** (1993) 320, arXiv: 9303291 [hep-ph].

[30] Peter Minkowski, $\mu \to e\gamma$ *at a rate of one out of* 10^9 *muon decays?*, Phys. Lett. B **67** (1977) 421.

[31] Tsutomu Yanagida, *Horizontal gauge symmetry and masses of neutrinos*, Conf. Proc. C **7902131** (1979) 95.

[32] S. L. Glashow, *The Future of Elementary Particle Physics*, NATO Sci. Ser. B **61** (1980) 687.

[33] Murray Gell-Mann, Pierre Ramond, and Richard Slansky, *Complex Spinors and Unified Theories*, Conf. Proc. C **790927** (1979) 315, arXiv: 1306.4669 [hep-th].

[34] Rabindra N. Mohapatra and Goran Senjanović, *Neutrino Mass and Spontaneous Parity Nonconservation*, Phys. Rev. Lett. **44** (1980) 912.

[35] Y.A. Golfand and E.P. Likhtman, *Extension of the Algebra of Poincare Group Generators and Violation of P Invariance*, JETP Lett. **13** (1971) 323.

[36] D.V. Volkov and V.P. Akulov, *Is the neutrino a goldstone particle?*, Phys. Lett. B **46** (1973) 109.

[37] J. Wess and B. Zumino, *Supergauge transformations in four dimensions*, Nucl. Phys. B **70** (1974) 39.

[38] J. Wess and B. Zumino, *Supergauge invariant extension of quantum electrodynamics*, Nucl. Phys. B **78** (1974) 1.

[39] S. Ferrara and B. Zumino, *Supergauge invariant Yang-Mills theories*, Nucl. Phys. B **79** (1974) 413.

[40] Abdus Salam and J. Strathdee, *Super-symmetry and non-Abelian gauges*, Phys. Lett. B **51** (1974) 353.

[41] F Del Aguila and Mark J Bowick, *The possibility of new fermions with* $\Delta I = 0$ *mass*, Nucl. Phys. B **224** (1983) 107.

[42] David B Kaplan, Howard Georgi, and Savas Dimopoulos, *Composite Higgs scalars*, Phys. Lett. B **136** (1984) 187.

[43] Kaustubh Agashe, Roberto Contino, and Alex Pomarol, *The minimal composite Higgs model*, Nucl. Phys. B **719** (2005) 165, arXiv: 0412089 [hep-ph].

[44] Roberto Contino, Leandro Da Rold, and Alex Pomarol, *Light custodians in natural composite Higgs models*, Phys. Rev. D **75** (2007) 055014, arXiv: 0612048 [hep-ph].

[45] N. Arkani-Hamed, A.G. Cohen, E. Katz, and A.E. Nelson, *The Littlest Higgs*, JHEP **07** (2002) 034, arXiv: 0206021 [hep-ph].

[46] Yutaka Hosotani, Shusaku Noda, and Kazunori Takenaga, *Dynamical gauge-Higgs unification in the electroweak theory*, Phys. Lett. B **607** (2005) 276, arXiv: 0410193 [hep-ph].

[47] Ignatios Antoniadis, Karim Benakli, and Mariano Quirós, *Finite Higgs mass without supersymmetry*, New J. Phys. **3** (2001) 20, arXiv: 0108005 [hep-th].

[48] Thomas Appelquist, Hsin-Chia Cheng, and Bogdan A Dobrescu, *Bounds on universal extra dimensions*, Phys. Rev. D **64** (2001) 035002, arXiv: 0012100 [hep-ph].

[49] F Del Aguila, Ll Ametller, Gordon L Kane, and Jorge Vidal, *Vector-like fermion and standard Higgs production at hadron colliders*, Nucl. Phys. B **334** (1990) 1.

[50] J.A. Aguilar-Saavedra, *Identifying top partners at LHC*, JHEP **11** (2009) 030, arXiv: 0907.3155 [hep-ph].

[51] ATLAS Collaboration, *Analysis of $t\bar{t}H$ and $t\bar{t}W$ production in multilepton final states with the ATLAS detector*, ATLAS-CONF-2019-045, 2019, URL: https://cds.cern.ch/record/2693930.

[52] ATLAS Collaboration, *Evidence for $t\bar{t}t\bar{t}$ production in the multilepton final state in proton–proton collisions at $\sqrt{s} = 13\,TeV$ with the ATLAS detector*, Eur. Phys. J. C **80** (2020) 1085, arXiv: 2007.14858 [hep-ex].

[53] David Galbraith and Carsten Burgard, *UX: Standard Model of the Standard Model*, URL: https://davidgalbraith.org/portfolio/ux-standard-model-of-the-standard-model/, accessed: 2024-01-31.

[54] M.H. Poincaré, *Sur la dynamique de l'électron*, Rend. Circ. Matem. Palermo **21** (1906) 129–175.

[55] Emmy Noether, *Invariant Variation Problems*, Gott. Nachr. **1918** (1918) 235, arXiv: 0503066 [physics].

[56] C. S. Wu, E. Ambler, R. W. Hayward, D. D. Hoppes, and R. P. Hudson, *Experimental Test of Parity Conservation in β Decay*, Phys. Rev. **105** (1957) 1413.

[57] M. Gell-Mann, *The interpretation of the new particles as displaced charge multiplets*, Nuovo Cim. **4** (1956) 848.

[58] Antonio Pich, *The Standard Model of Electroweak Interactions*, arXiv: 0705.4264 [hep-ph].

[59] Patrick Meade and Lisa Randall, *Black holes and quantum gravity at the LHC*, JHEP **2008** (2008) 003.

[60] Xavier Calmet, Wei Gong, and Stephen D.H. Hsu, *Colorful quantum black holes at the LHC*, Phys. Lett. B **668** (2008) 20.

[61] Martin Schmaltz and David Tucker-Smith, *Little Higgs Theories*, Ann. Rev. Nucl. Part. Sci. **55** (2005) 229, arXiv: 0502182 [hep-ph].

[62] Edvige Corbelli and Paolo Salucci, *The Extended Rotation Curve and the Dark Matter Halo of M33*, MNRAS **311** (2000) 441, arXiv: 9909252 [astro-ph].

[63] V. C. Rubin, N. Thonnard, and W. K. Ford, Jr., *Rotational properties of 21 SC galaxies with a large range of luminosities and radii, from NGC 4605 (R=4kpc) to UGC 2885 (R=122kpc)*, Astrophys. J. **238** (1980) 471.

[64] K. G. Begeman, A. H. Broeils, and R. H. Sanders, *Extended rotation curves of spiral galaxies: Dark haloes and modified dynamics*, MNRAS **249** (1991) 523.

[65] WMAP Collaboration, *Nine-Year Wilkinson Microwave Anisotropy Probe (WMAP) Observations: Cosmological Parameter Results*, Astrophys. J. Suppl. **208** (2013) 19, arXiv: 1212.5226 [astro-ph].

[66] Planck Collaboration, *Planck 2018 results. I. Overview and the cosmological legacy of Planck*, Astron. Astrophys. **641** (2020) A1, arXiv: 1807.06205 [astro-ph].

[67] Virginia Trimble, *Existence and Nature of Dark Matter in the Universe*, Ann. Rev. Astron. Astrophys. **25** (1987) 425.

[68] G. Bertone, D. Hooper, and J. Silk, *Particle dark matter: evidence, candidates and constraints*, Phys. Rept. **405** (2005) 279–390.

[69] Jonathan L. Feng, *Dark Matter Candidates from Particle Physics and Methods of Detection*, Ann. Rev. Astron. Astrophys. **48** (2010) 495–545.

[70] Howard M Georgi, D B Kaplan, and Lisa Randall, *Manifesting the invisible axion at low energies*, Phys. Lett. B **169** (1986) 73.

[71] Kiwoon Choi, Kyungsik Kang, and Jihn E. Kim, *Effects of η' in Low-energy Axion Physics*, Phys. Lett. B **181** (1986) 145.

[72] John Preskill, Mark B. Wise, and Frank Wilczek, *Cosmology of the Invisible Axion*, Phys. Lett. B **120** (1983) 127.

[73] L. F. Abbott and P. Sikivie, *A Cosmological Bound on the Invisible Axion*, Phys. Lett. B **120** (1983) 133.

[74] Michael Dine and Willy Fischler, *The Not So Harmless Axion*, Phys. Lett. B **120** (1983) 137.

[75] Gary Steigman and Michael S. Turner, *Cosmological Constraints on the Properties of Weakly Interacting Massive Particles*, Nucl. Phys. B **253** (1985) 375.

[76] A. D. Sakharov, *Violation of CP Invariance, C asymmetry, and baryon asymmetry of the universe*, Soviet Physics Uspekhi **5** (1967) 32.

[77] G. C. Branco, P. M. Ferreira, L. Lavoura, M. N. Rebelo, Marc Sher, and Joao P. Silva, *Theory and phenomenology of two-Higgs-doublet models*, Phys. Rept. **516** (2012) 1, arXiv: 1106.0034 [hep-ph].

[78] R. D. Peccei and Helen R. Quinn, CP *Conservation in the Presence of Pseudoparticles*, Phys. Rev. Lett. **38** (1977) 1440.

[79] Mark Trodden, *Electroweak Baryogenesis: A Brief Review*, arXiv: 9805252 [hep-ph].

[80] ATLAS Collaboration, *Interpretations of the ATLAS measurements of Higgs boson production and decay rates and differential cross-sections in pp collisions at* $\sqrt{s} = 13$ *TeV*, arXiv: 2402.05742 [hep-ex].

[81] Martin Bauer, Ulrich Haisch, and Felix Kahlhoefer, *Simplified dark matter models with two Higgs doublets: I. Pseudoscalar mediators*, JHEP **05** (2017) 138, arXiv: 1701.07427 [hep-ph].

[82] Sally Dawson, Samuel Homiller, and Samuel D. Lane, *Putting standard model EFT fits to work*, Phys. Rev. D **102** (2020) 055012, arXiv: 2007.01296 [hep-ph].

[83] W. Buchmüller and D. Wyler, *Effective lagrangian analysis of new interactions and flavour conservation*, Nucl. Phys. B **268** (1986) 621.

[84] Céline Degrande, Nicolas Greiner, Wolfgang Kilian, Olivier Mattelaer, Harrison Mebane, Tim Stelzer, Scott Willenbrock, and Cen Zhang, *Effective field theory: A modern approach to anomalous couplings*, Annals Phys. **335** (2013) 21–32.

[85] B. Grzadkowski, M. Iskrzynski, M. Misiak, and J. Rosiek, *Dimension-Six Terms in the Standard Model Lagrangian*, JHEP **10** (2010) 085, arXiv: 1008.4884 [hep-ph].

[86] K. Hagiwara, S. Ishihara, R. Szalapski, and D. Zeppenfeld, *Low energy effects of new interactions in the electroweak boson sector*, Phys. Rev. D **48** (1993) 2182.

[87] Gian Francesco Giudice, Christophe Grojean, Alex Pomarol, and Riccardo Rattazzi, *The strongly-interacting light Higgs*, JHEP **2007** (2007) 045–045.

[88] Celine Degrande, Jean-Marc Gerard, Christophe Grojean, Fabio Maltoni, and Geraldine Servant, *Non-resonant new physics in top pair production at hadron colliders*, JHEP **03** (2011) 125, arXiv: 1010.6304 [hep-ph].

[89] Cen Zhang, *Constraining qqtt operators from four-top production: a case for enhanced EFT sensitivity*, Chin. Phys. C **42** (2018) 023104, arXiv: 1708.05928 [hep-ph].

[90] Giovanni Banelli, Ennio Salvioni, Javi Serra, Tobias Theil, and Andreas Weiler, *The present and future of four top operators*, JHEP **02** (2021) 043, arXiv: 2010.05915 [hep-ph].

[91] Rafael Aoude, Hesham El Faham, Fabio Maltoni, and Eleni Vryonidou, *Complete SMEFT predictions for four top quark production at hadron colliders*, JHEP **10** (2022) 163, arXiv: 2208.04962 [hep-ph].

[92] Christoph Englert, Gian F. Giudice, Admir Greljo, and Matthew Mccullough, *The $\hat{H}$-parameter: an oblique Higgs view*, JHEP **09** (2019) 041, arXiv: 1903.07725 [hep-ph].

[93] Lyndon Evans and Philip Bryant, *LHC Machine*, JINST **3** (2008) S08001.

[94] ATLAS Collaboration, *The ATLAS Experiment at the CERN Large Hadron Collider*, JINST **3** (2008) S08003.

[95] CMS Collaboration, *The CMS Experiment at the CERN LHC*, JINST **3** (2008) S08004.

[96] ALICE Collaboration, *The ALICE experiment at the CERN LHC*, JINST **3** (2008) S08002.

[97] LHCb Collaboration, *The LHCb Detector at the LHC*, JINST **3** (2008) S08005.

[98] I. Zurbano Fernandez et al., *High-Luminosity Large Hadron Collider (HL-LHC): Technical design report*, CERN-2020-010, 2020, URL: https://cds.cern.ch/record/2749422.

[99] Ewa Lopienska, *The CERN accelerator complex, layout in 2022*, URL: https://cds.cern.ch/record/2800984, accessed: 2024-03-08.

[100] Cinzia De Melis, *The CERN accelerator complex*, URL: https://cds.cern.ch/record/2119882, accessed: 2024-03-08.

[101] Werner Herr and B Muratori, *Concept of luminosity*, CERN-2006-002, 2006, URL: https://cds.cern.ch/record/941318.

[102] Lyndon Evans, *The Large Hadron Collider (LHC)*, New J. Phys. **9** (2007) 335.

[103] ATLAS Collaboration, *Luminosity determination in pp collisions at $\sqrt{s} = 13$ TeV using the ATLAS detector at the LHC*, Eur. Phys. J. C **83** (2023) 982, arXiv: 2212.09379 [hep-ex].

[104] ATLAS Collaboration, *Luminosity determination in pp collisions at $\sqrt{s} = 13$ TeV using the ATLAS detector at the LHC*, ATLAS-CONF-2019-021, 2019, URL: https://cds.cern.ch/record/2677054.

[105] J M Campbell, J W Huston, and W J Stirling, *Hard interactions of quarks and gluons: a primer for LHC physics*, Rept. Prog. Phys. **70** (2006) 89–193.

[106] Z. Kunszt, *Recent Developments in Perturbative QCD*, In: Heimo Latal and Heinrich Mitter, editors, *Physics for a New Generation*, Springer Berlin Heidelberg, 1990, URL: https://doi.org/10.1007/978-3-642-75567-5_6.

[107] NNPDF Collaboration, *Parton distributions from high-precision collider data*, Eur. Phys. J. C **77** (2017) 663.

[108] J. Pumplin et al., *New Generation of Parton Distributions with Uncertainties from Global QCD Analysis*, JHEP **07** (2002) 012, arXiv: 0201195 [hep-ph].

[109] A. D. Martin, W. J. Stirling, R. S. Thorne, and G. Watt, *Parton distributions for the LHC*, Eur. Phys. J. C **63** (2009) 189, arXiv: 0901.0002 [hep-ph].

[110] NNPDF Collaboration, *Parton distributions for the LHC Run II*, JHEP **04** (2015) 040, arXiv: 1410.8849 [hep-ph].

[111] ATLAS Collaboration, *Standard Model Summary Plots October 2023*, ATL-PHYS-PUB-2023-039, 2023, URL: https://cds.cern.ch/record/2882448.

[112] ATLAS Collaboration, *Combined measurement of the Higgs boson mass from the $H \to \gamma\gamma$ and $H \to ZZ^* \to 4\ell$ decay channels with the ATLAS detector using $\sqrt{s}$ = 7, 8 and 13 TeV pp collision data*, Phys. Rev. Lett. **131** (2023) 251802, arXiv: 2308.04775 [hep-ex].

[113] ATLAS Collaboration, *Evidence of off-shell Higgs boson production from ZZ leptonic decay channels and constraints on its total width with the ATLAS detector*, Phys. Lett. B **846** (2023) 138223, arXiv: 2304.01532 [hep-ex].

[114] ATLAS Collaboration, *Study of the spin and parity of the Higgs boson in diboson decays with the ATLAS detector*, Eur. Phys. J. C **75** (2015) 476, arXiv: 1506.05669 [hep-ex].

[115] CMS Collaboration, *Constraints on the spin-parity and anomalous HVV couplings of the Higgs boson in proton collisions at 7 and 8 TeV*, Phys. Rev. D **92** (2015) 012004, arXiv: 1411.3441 [hep-ex].

[116] ATLAS Collaboration, *A detailed map of Higgs boson interactions by the ATLAS experiment ten years after the discovery*, Nature **607** (2022) 52, arXiv: 2207.00092 [hep-ex].

[117] LHC Higgs Cross Section Working Group Collaboration, *Handbook of LHC Higgs Cross Sections: 4. Deciphering the Nature of the Higgs Sector*, arXiv: 1610.07922 [hep-ph].

[118] Stefano Catani, Simone Devoto, Massimiliano Grazzini, Stefan Kallweit, Javier Mazzitelli, and Chiara Savoini, *Higgs Boson Production in Association with a Top-Antitop Quark Pair in Next-to-Next-to-Leading Order QCD*, Phys. Rev. Lett. **130** (2023) 111902.

[119] CMS Collaboration, *Measurement of the Higgs boson production rate in association with top quarks in final states with electrons, muons, and hadronically decaying tau leptons at $\sqrt{s} = 13$ TeV*, Eur. Phys. J. C **81** (2021) 378, arXiv: 2011.03652 [hep-ex].

[120] S. Alekhin, A. Djouadi, and S. Moch, *The top quark and Higgs boson masses and the stability of the electroweak vacuum*, Phys. Lett. B **716** (2012) 214, arXiv: 1207.0980 [hep-ph].

[121] Fedor Bezrukov and Mikhail Shaposhnikov, *Why should we care about the top quark Yukawa coupling?*, J. Exp. Theor. Phys. **120** (2015) 335, arXiv: 1411.1923 [hep-ph].

[122] ATLAS Collaboration, *Top Quarks + X Summary Plots November 2023*, ATL-PHYS-PUB-2023-035, 2023, URL: https://cds.cern.ch/record/2882247.

[123] Rikkert Frederix, Davide Pagani, and Marco Zaro, *Large NLO corrections in $t\bar{t}W^{\pm}$ and $t\bar{t}t\bar{t}$ hadroproduction from supposedly subleading EW contributions*, JHEP **02** (2018) 031, arXiv: 1711.02116 [hep-ph].

[124] Melissa van Beekveld, Anna Kulesza, and Laura Moreno Valero, *Threshold Resummation for the Production of Four Top Quarks at the LHC*, Phys. Rev. Lett. **131** (2023) 211901, arXiv: 2212.03259 [hep-ph].

[125] ATLAS Collaboration, *Observation of four-top-quark production in the multilepton final state with the ATLAS detector*, Eur. Phys. J. C **83** (2023) 496, arXiv: 2303.15061 [hep-ex].

[126] Qing-Hong Cao, Shao-Long Chen, and Yandong Liu, *Probing Higgs width and top quark Yukawa coupling from $t\bar{t}H$ and $t\bar{t}t\bar{t}$ productions*, Phys. Rev. D **95** (2017) 053004, arXiv: 1602.01934 [hep-ph].

[127] Qing-Hong Cao, Shao-Long Chen, Yandong Liu, Rui Zhang, and Ya Zhang, *Limiting top quark-Higgs boson interaction and Higgs-boson width from multitop productions*, Phys. Rev. D **99** (2019) 113003, arXiv: 1901.04567 [hep-ph].

[128] Hans Peter Nilles, *Supersymmetry, supergravity and particle physics*, Phys. Rept. **110** (1984) 1.

[129] Glennys R. Farrar and Pierre Fayet, *Phenomenology of the production, decay, and detection of new hadronic states associated with supersymmetry*, Phys. Lett. B **76** (1978) 575.

[130] Tilman Plehn and Tim M. P. Tait, *Seeking sgluons*, J. Phys. G **36** (2009) 075001, arXiv: 0810.3919 [hep-ph].

[131] Samuel Calvet, Benjamin Fuks, Philippe Gris, and Loic Valéry, *Searching for sgluons in multitop events at a center-of-mass energy of 8 TeV*, JHEP **04** (2013) 043, arXiv: 1212.3360 [hep-ph].

[132] Gabriele Ferretti and Denis Karateev, *Fermionic UV completions of Composite Higgs models*, JHEP **03** (2014) 077, arXiv: 1312.5330 [hep-ph].

[133] Luca Vecchi, *A dangerous irrelevant UV-completion of the composite Higgs*, JHEP **02** (2017) 094, arXiv: 1506.00623 [hep-ph].

[134] Kaustubh Agashe, Antonio Delgado, Michael J. May, and Raman Sundrum, *RS1, custodial isospin and precision tests*, JHEP **08** (2003) 050, arXiv: 0308036 [hep-ph].

[135] ATLAS Collaboration, *Search for $t\bar{t}H/A \to t\bar{t}t\bar{t}$ production in the multilepton final state in proton–proton collisions at $\sqrt{s} = 13$ TeV with the ATLAS detector*, JHEP **07** (2023) 203, arXiv: 2211.01136 [hep-ex].

[136] Luca Buonocore, Simone Devoto, Massimiliano Grazzini, Stefan Kallweit, Javier Mazzitelli, Luca Rottoli, and Chiara Savoini, *Precise Predictions for the Associated Production of a W Boson with a Top-Antitop Quark Pair at the LHC*, Phys. Rev. Lett. **131** (2023) 231901.

[137] Rikkert Frederix and Ioannis Tsinikos, *On improving NLO merging for* $\mathrm{t\bar{t}W}$ *production*, JHEP **11** (2021) 029, arXiv: 2108.07826 [hep-ph].

[138] Anna Kulesza, Leszek Motyka, Daniel Schwartländer, Tomasz Stebel, and Vincent Theeuwes, *Associated production of a top quark pair with a heavy electroweak gauge boson at NLO+NNLL accuracy*, Eur. Phys. J. C **79** (2019) 249, arXiv: 1812.08622 [hep-ph].

[139] Alessandro Broggio, Andrea Ferroglia, Rikkert Frederix, Davide Pagani, Benjamin D. Pecjak, and Ioannis Tsinikos, *Top-quark pair hadroproduction in association with a heavy boson at NLO+NNLL including EW corrections*, JHEP **08** (2019) 039, arXiv: 1907.04343 [hep-ph].

[140] Anna Kulesza, Leszek Motyka, Daniel Schwartländer, Tomasz Stebel, and Vincent Theeuwes, *Associated top quark pair production with a heavy boson: differential cross sections at NLO+NNLL accuracy*, Eur. Phys. J. C **80** (2020) 428, arXiv: 2001.03031 [hep-ph].

[141] Giuseppe Bevilacqua, Huan-Yu Bi, Heribertus Bayu Hartanto, Manfred Kraus, and Malgorzata Worek, *The simplest of them all: $t\bar{t}W^{\pm}$ at NLO accuracy in QCD*, JHEP **08** (2020) 043, arXiv: 2005.09427 [hep-ph].

[142] Ansgar Denner and Giovanni Pelliccioli, *NLO QCD corrections to off-shell $\bar{t}tW^{\pm}$ production at the LHC*, JHEP **11** (2020) 069, arXiv: 2007.12089 [hep-ph].

[143] Giuseppe Bevilacqua, Huan-Yu Bi, Heribertus Bayu Hartanto, Manfred Kraus, Jasmina Nasufi, and Malgorzata Worek, *NLO QCD corrections to off-shell $t\bar{t}W^{\pm}$ production at the LHC: correlations and asymmetries*, Eur. Phys. J. C **81** (2021) 675, arXiv: 2012.01363 [hep-ph].

[144] F. Febres Cordero, M. Kraus, and L. Reina, *Top-quark pair production in association with a $W^{\pm}$ gauge boson in the POWHEG-BOX*, Phys. Rev. D **103** (2021) 094014, arXiv: 2101.11808 [hep-ph].

[145] Ansgar Denner and Giovanni Pelliccioli, *Combined NLO EW and QCD corrections to off-shell $t\bar{t}W$ production at the LHC*, Eur. Phys. J. C **81** (2021) 354, arXiv: 2102.03246 [hep-ph].

[146] G. Bevilacqua, H. Y. Bi, F. Febres Cordero, H. B. Hartanto, M. Kraus, J. Nasufi, L. Reina, and M. Worek, *Modeling uncertainties of $t\bar{t}W^{\pm}$ multilepton signatures*, Phys. Rev. D **105** (2022) 014018, arXiv: 2109.15181 [hep-ph].

[147] Lars Ferencz et al., *Study of ttbb and ttW background modelling for ttH analyses*, arXiv: 2301.11670 [hep-ex].

[148] ATLAS Collaboration, *Measurement of the total and differential cross-sections of $t\bar{t}W$ production in pp collisions at $\sqrt{s} = 13$ TeV with the ATLAS detector*, arXiv: 2401.05299 [hep-ex].

[149] CMS Collaboration, *Measurement of the cross section of top quark-antiquark pair production in association with a W boson in proton-proton collisions at $\sqrt{s} = 13$ TeV*, JHEP **07** (2023) 219, arXiv: 2208.06485 [hep-ex].

[150] S. Frixione, V. Hirschi, D. Pagani, H. S. Shao, and M. Zaro, *Electroweak and QCD corrections to top-pair hadroproduction in association with heavy bosons*, JHEP **06** (2015) 184, arXiv: 1504.03446 [hep-ph].

[151] ATLAS Collaboration, *Inclusive and differential cross-section measurements of $t\bar{t}Z$ production in pp collisions at $\sqrt{s} = 13$ TeV with the ATLAS detector, including EFT and spin-correlation interpretations*, arXiv: 2312.04450 [hep-ex].

[152] CMS Collaboration, *Measurement of top quark pair production in association with a Z boson in proton-proton collisions at $\sqrt{s} = 13$ TeV*, JHEP **03** (2020) 056, arXiv: 1907.11270 [hep-ex].

[153] ATLAS Collaboration, *ATLAS Insertable B-Layer Technical Design Report*, URL: https://cds.cern.ch/record/1291633.

[154] ATLAS Collaboration, *IBL Efficiency and Single Point Resolution in Collision Events*, ATL-INDET-PUB-2016-001, 2016, URL: https://cds.cern.ch/record/2203893.

[155] ATLAS Collaboration, *ATLAS Liquid Argon Calorimeter: Technical Design Report*, URL: https://cds.cern.ch/record/331061.

[156] ATLAS Collaboration, *ATLAS Tile Calorimeter: Technical Design Report*, URL: https://cds.cern.ch/record/331062.

[157] Christian Wolfgang Fabjan and F Gianotti, *Calorimetry for Particle Physics*, Rev. Mod. Phys. **75** (2003) 1243.

[158] ATLAS Collaboration, *ATLAS Detector and Physics Performance: Technical Design Report, Volume 1*, URL: https://cds.cern.ch/record/391176.

[159] ATLAS Collaboration, *Performance of the muon spectrometer alignment in 2017 and 2018 data*, ATL-MUON-PUB-2021-002, 2021, URL: https://cds.cern.ch/record/2753329.

[160] A Salvucci, *Measurement of muon momentum resolution of the ATLAS detector*, ATL-PHYS-PROC-2012-013, 2012, URL: https://cds.cern.ch/record/1417538.

[161] Ana Maria Rodriguez Vera and Joao Antunes Pequenao, *ATLAS Detector Magnet System*, URL: https://cds.cern.ch/record/2770604.

[162] ATLAS Collaboration, *Operation of the ATLAS trigger system in Run 2*, JINST **15** (2020) P10004, arXiv: 2007.12539 [hep-ex].

[163] ATLAS Collaboration, *Athena*, URL: https://doi.org/10.5281/zenodo.4772550.

[164] Joao Pequenao and Paul Schaffner, *How ATLAS detects particles: diagram of particle paths in the detector*, URL: https://cds.cern.ch/record/1505342.

[165] T Cornelissen, M Elsing, S Fleischmann, W Liebig, E Moyse, and A Salzburger, *Concepts, Design and Implementation of the ATLAS New Tracking (NEWT)*, ATL-SOFT-PUB-2007-007, ATL-COM-SOFT-2007-002, 2007, URL: https://cds.cern.ch/record/1020106.

[166] P F Åkesson, T Atkinson, M J Costa, M Elsing, S Fleischmann, A N Gaponenko, W Liebig, E Moyse, A Salzburger, and M Siebel, *ATLAS Tracking Event Data Model*, ATL-SOFT-PUB-2006-004, ATL-COM-SOFT-2006-005, CERN-ATL-COM-SOFT-2006-005, 2006, URL: https://cds.cern.ch/record/973401.

[167] T G Cornelissen, N Van Eldik, M Elsing, W Liebig, E Moyse, N Piacquadio, K Prokofiev, A Salzburger, and A Wildauer, *Updates of the ATLAS Tracking Event Data Model (Release 13)*, ATL-SOFT-PUB-2007-003, ATL-COM-SOFT-2007-008, 2007, URL: https://cds.cern.ch/record/1038095.

[168] A Salzburger, S Todorova, and M Wolter, *The ATLAS Tracking Geometry Description*, ATL-SOFT-PUB-2007-004, ATL-COM-SOFT-2007-009, 2007, URL: https://cds.cern.ch/record/1038098.

[169] Andreas Salzburger, *Optimisation of the ATLAS Track Reconstruction Software for Run-2*, J. Phys. Conf. Ser. **664** (2015) 072042.

[170] R. Fruhwirth, *Application of Kalman filtering to track and vertex fitting*, Nucl. Instrum. Meth. A **262** (1987) 444.

[171] D Wicke, *A New Algorithm for Solving Tracking Ambiguities*, DELPHI-98-163-PROG-236-TRACK-92, 1998, URL: https://cds.cern.ch/record/2625731.

[172] ATLAS Collaboration, *Muon reconstruction performance of the ATLAS detector in proton–proton collision data at* $\sqrt{s} = 13$ *TeV*, Eur. Phys. J. C **76** (2016) 292, arXiv: 1603.05598 [hep-ex].

[173] ATLAS Collaboration, *Reconstruction of primary vertices at the ATLAS experiment in Run 1 proton–proton collisions at the LHC*, Eur. Phys. J. C **77** (2017) 332, arXiv: 1611.10235 [hep-ex].

[174] ATLAS Collaboration, *The ATLAS Experiment at the CERN Large Hadron Collider: A Description of the Detector Configuration for Run 3*, arXiv: 2305.16623.

[175] G Piacquadio, K Prokofiev, and A Wildauer, *Primary vertex reconstruction in the ATLAS experiment at LHC*, J. Phys. Conf. Ser. **119** (2008) 032033.

[176] Wolfgang Waltenberger, Rudolf Frühwirth, and Pascal Vanlaer, *Adaptive vertex fitting*, J. Phys. G **34** (2007) N343.

[177] ATLAS Collaboration, *Electron reconstruction and identification in the ATLAS experiment using the 2015 and 2016 LHC proton–proton collision data at* $\sqrt{s} = 13$ *TeV*, Eur. Phys. J. C **79** (2019) 639, arXiv: 1902.04655 [hep-ex].

[178] ATLAS Collaboration, *Electron and photon performance measurements with the ATLAS detector using the 2015–2017 LHC proton–proton collision data*, JINST **14** (2019) P12006, arXiv: 1908.00005 [hep-ex].

[179] ATLAS Collaboration, *Topological cell clustering in the ATLAS calorimeters and its performance in LHC Run 1*, Eur. Phys. J. C **77** (2017) 490, arXiv: 1603.02934 [hep-ex].

[180] TMVA Collaboration, *TMVA - Toolkit for Multivariate Data Analysis*, arXiv: 0703039 [physics].

[181] ATLAS Collaboration, *Measurement of the photon identification efficiencies with the ATLAS detector using LHC Run-1 data*, Eur. Phys. J. C **76** (2016) .

[182] ATLAS Collaboration Collaboration, *Evidence for the associated production of the Higgs boson and a top quark pair with the ATLAS detector*, Phys. Rev. D **97** (2018) 072003.

[183] ttHML Analysis Team, *Search for the Associated Production of a Higgs Boson and a Top Quark Pair in multilepton final states in 80fb-1 pp Collisions at 13 TeV with the ATLAS Detector*, Technical Report, 2019, URL: https://cds.cern.ch/record/2314122.

[184] ATLAS Collaboration, *Muon reconstruction and identification efficiency in ATLAS using the full Run 2 pp collision data set at* $\sqrt{s} = 13$ *TeV*, Eur. Phys. J. C **81** (2021) 578, arXiv: 2012.00578 [hep-ex].

[185] ATLAS Collaboration, *Electron and photon efficiencies in LHC Run 2 with the ATLAS experiment*, arXiv: 2308.13362 [hep-ex].

[186] Fudong He, Rustem Ospanov, Jianbei Liu, Hao Xu, and Hanlin Xu, *Tagging non-prompt electrons and muons using lifetime and isolation information*, ATL-COM-PHYS-2022-042, 2022, URL: https://cds.cern.ch/record/2800472.

[187] ATLAS Collaboration, *Jet reconstruction and performance using particle flow with the ATLAS Detector*, Eur. Phys. J. C **77** (2017) 466, arXiv: 1703.10485 [hep-ex].

[188] Matteo Cacciari, Gavin P. Salam, and Gregory Soyez, *The anti-k_t jet clustering algorithm*, JHEP **04** (2008) 063, arXiv: 0802.1189 [hep-ph].

[189] ATLAS Collaboration, *Jet energy scale measurements and their systematic uncertainties in proton–proton collisions at* $\sqrt{s} = 13$ *TeV with the ATLAS detector*, Phys. Rev. D **96** (2017) 072002, arXiv: 1703.09665 [hep-ex].

[190] ATLAS Collaboration, *Jet energy scale and resolution measured in proton–proton collisions at* $\sqrt{s} = 13$ *TeV with the ATLAS detector*, Eur. Phys. J. C **81** (2020) 689, arXiv: 2007.02645 [hep-ex].

[191] ATLAS Collaboration, *Performance of pile-up mitigation techniques for jets in pp collisions at* $\sqrt{s} = 8$ *TeV using the ATLAS detector*, Eur. Phys. J. C **76** (2016) 581, arXiv: 1510.03823 [hep-ex].

[192] ATLAS Collaboration, *ATLAS flavour-tagging algorithms for the LHC Run 2 pp collision dataset*, arXiv: 2211.16345 [hep-ex].

[193] ATLAS Collaboration, *Optimisation and performance studies of the ATLAS b-tagging algorithms for the 2017-18 LHC run*, ATL-PHYS-PUB-2017-013, 2017, URL: https://cds.cern.ch/record/2273281.

[194] ATLAS Collaboration, *Identification of Jets Containing b-Hadrons with Recurrent Neural Networks at the ATLAS Experiment*, ATL-PHYS-PUB-2017-003, 2017, URL: https://cds.cern.ch/record/2255226.

[195] ATLAS Collaboration, *Secondary vertex finding for jet flavour identification with the ATLAS detector*, ATL-PHYS-PUB-2017-011, 2017, URL: https://cds.cern.ch/record/2270366.

[196] ATLAS Collaboration, *Topological b-hadron decay reconstruction and identification of b-jets with the JetFitter package in the ATLAS experiment at the LHC*, ATL-PHYS-PUB-2018-025, 2018, URL: https://cds.cern.ch/record/2645405.

[197] ATLAS Collaboration, *Measurement of VH, $H \to b\bar{b}$ production as a function of the vector-boson transverse momentum in 13 TeV pp collisions with the ATLAS detector*, JHEP **05** (2019) 141, arXiv: 1903.04618 [hep-ex].

[198] ATLAS Collaboration, *Measurement of Higgs boson decay into b-quarks in associated production with a top-quark pair in pp collisions at $\sqrt{s} = 13$ TeV with the ATLAS detector*, JHEP **06** (2022) 097, arXiv: 2111.06712 [hep-ex].

[199] ATLAS Collaboration, *Performance of b-jet identification in the ATLAS experiment*, JINST **11** (2016) P04008, arXiv: 1512.01094 [hep-ex].

[200] ATLAS Collaboration, *ATLAS b-jet identification performance and efficiency measurement with $t\bar{t}$ events in pp collisions at $\sqrt{s} = 13$ TeV*, Eur. Phys. J. C **79** (2019) 970, arXiv: 1907.05120 [hep-ex].

[201] ATLAS Collaboration, *Monte Carlo to Monte Carlo scale factors for flavour tagging efficiency calibration*, ATL-PHYS-PUB-2020-009, 2020, URL: https://cds.cern.ch/record/2718610.

[202] ATLAS Collaboration, *Flavour-tagging efficiency corrections for the 2019 ATLAS PFlow jet and VR track jets b-taggers with the full LHC Run II dataset*, URL: https://atlas.web.cern.ch/Atlas/GROUPS/PHYSICS/PLOTS/FTAG-2021-001/, accessed: 2024-02-11.

[203] ATLAS Collaboration, *E_T^{miss} performance in the ATLAS detector using 2015-2016 LHC p-p collisions*, ATLAS-CONF-2018-023, 2018, URL: https://cds.cern.ch/record/2625233.

[204] Particle Data Group Collaboration, *Review of Particle Physics*, PTEP **2022** (2022) 083C01.

[205] J. Alwall, R. Frederix, S. Frixione, V. Hirschi, F. Maltoni, O. Mattelaer, H. S. Shao, T. Stelzer, P. Torrielli, and M. Zaro, *The automated computation of tree-level and next-to-leading order differential cross sections, and their matching to parton shower simulations*, JHEP **07** (2014) 079, arXiv: 1405.0301 [hep-ph].

[206] Paolo Nason, *A new method for combining NLO QCD with shower Monte Carlo algorithms*, JHEP **11** (2004) 040, arXiv: 0409146 [hep-ph].

[207] Stefano Frixione, Paolo Nason, and Carlo Oleari, *Matching NLO QCD computations with parton shower simulations: the POWHEG method*, JHEP **11** (2007) 070, arXiv: 0709.2092 [hep-ph].

[208] Simone Alioli, Paolo Nason, Carlo Oleari, and Emanuele Re, *A general framework for implementing NLO calculations in shower Monte Carlo programs: the POWHEG BOX*, JHEP **06** (2010) 043, arXiv: 1002.2581 [hep-ph].

[209] G. Corcella et al., *HERWIG 6: an event generator for hadron emission reactions with interfering gluons (including supersymmetric processes)*, JHEP **01** (2001) 010, arXiv: 0011363 [hep-ph].

[210] M. Bähr et al., *Herwig++ physics and manual*, Eur. Phys. J. C **58** (2008) 639, arXiv: 0803.0883 [hep-ph].

[211] Johannes Bellm et al., *Herwig 7.0/Herwig++ 3.0 release note*, Eur. Phys. J. C **76** (2016) 196, arXiv: 1512.01178 [hep-ph].

[212] Torbjorn Sjöstrand, Stephen Mrenna, and Peter Z. Skands, *PYTHIA 6.4 physics and manual*, JHEP **05** (2006) 026, arXiv: 0603175 [hep-ph].

[213] Torbjörn Sjöstrand, Stefan Ask, Jesper R. Christiansen, Richard Corke, Nishita Desai, Philip Ilten, Stephen Mrenna, Stefan Prestel, Christine O. Rasmussen, and Peter Z. Skands, *An introduction to PYTHIA 8.2*, Comput. Phys. Commun. **191** (2015) 159, arXiv: 1410.3012 [hep-ph].

[214] T. Gleisberg, Stefan. Hoeche, F. Krauss, M. Schonherr, S. Schumann, F. Siegert, and J. Winter, *Event generation with SHERPA 1.1*, JHEP **02** (2009) 007, arXiv: 0811.4622 [hep-ph].

[215] Enrico Bothmann et al., *Event generation with Sherpa 2.2*, SciPost Phys. **7** (2019) 034, arXiv: 1905.09127 [hep-ph].

[216] ATLAS Collaboration. *ATLAS Pythia 8 tunes to 7 TeV data*, . ATL-PHYS-PUB-2014-021, 2014, URL: https://cds.cern.ch/record/1966419.

[217] S. Agostinelli et al., *GEANT4 – a simulation toolkit*, Nucl. Instrum. Meth. A **506** (2003) 250.

[218] John Allison et al., *Geant4 developments and applications*, IEEE Trans. Nucl. Sci. **53** (2006) 270.

[219] ATLAS Collaboration, *The ATLAS Simulation Infrastructure*, Eur. Phys. J. C **70** (2010) 823, arXiv: 1005.4568 [physics].

[220] Fabio Cascioli, Philipp Maierhöfer, and Stefano Pozzorini, *Scattering Amplitudes with Open Loops*, Phys. Rev. Lett. **108** (2012) 111601, arXiv: 1111.5206 [hep-ph].

[221] Tanju Gleisberg and Stefan Höche, *Comix, a new matrix element generator*, JHEP **12** (2008) 039, arXiv: 0808.3674 [hep-ph].

[222] Steffen Schumann and Frank Krauss, *A parton shower algorithm based on Catani–Seymour dipole factorisation*, JHEP **03** (2008) 038, arXiv: 0709.1027 [hep-ph].

[223] Stefan Höche, Frank Krauss, Marek Schönherr, and Frank Siegert, *QCD matrix elements + parton showers. The NLO case*, JHEP **04** (2013) 027, arXiv: 1207.5030 [hep-ph].

[224] Rikkert Frederix and Stefano Frixione, *Merging meets matching in MC@NLO*, JHEP **12** (2012) 061, arXiv: 1209.6215 [hep-ph].

[225] M. Beneke, P. Falgari, S. Klein, and C. Schwinn, *Hadronic top-quark pair production with NNLL threshold resummation*, Nucl. Phys. B **855** (2012) 695, arXiv: 1109.1536 [hep-ph].

[226] Matteo Cacciari, Michal Czakon, Michelangelo Mangano, Alexander Mitov, and Paolo Nason, *Top-pair production at hadron colliders with next-to-next-to-leading logarithmic soft-gluon resummation*, Phys. Lett. B **710** (2012) 612, arXiv: 1111.5869 [hep-ph].

[227] Peter Bärnreuther, Michal Czakon, and Alexander Mitov, *Percent Level Precision Physics at the Tevatron: First Genuine NNLO QCD Corrections to $q\bar{q} \to t\bar{t} + X$*, Phys. Rev. Lett. **109** (2012) 132001, arXiv: 1204.5201 [hep-ph].

[228] Michal Czakon and Alexander Mitov, *NNLO corrections to top-pair production at hadron colliders: the all-fermionic scattering channels*, JHEP **12** (2012) 054, arXiv: 1207.0236 [hep-ph].

[229] Michal Czakon and Alexander Mitov, *NNLO corrections to top pair production at hadron colliders: the quark-gluon reaction*, JHEP **01** (2013) 080, arXiv: 1210.6832 [hep-ph].

[230] Michał Czakon, Paul Fiedler, and Alexander Mitov, *Total Top-Quark Pair-Production Cross Section at Hadron Colliders Through $O(\alpha_S^4)$*, Phys. Rev. Lett. **110** (2013) 252004, arXiv: 1303.6254 [hep-ph].

[231] Michal Czakon and Alexander Mitov, *Top++: A Program for the Calculation of the Top-Pair Cross-Section at Hadron Colliders*, Comput. Phys. Commun. **185** (2014) 2930, arXiv: 1112.5675 [hep-ph].

[232] Michiel Botje et al., *The PDF4LHC Working Group Interim Recommendations*, arXiv: 1101.0538 [hep-ph].

[233] A. D. Martin, W. J. Stirling, R. S. Thorne, and G. Watt, *Uncertainties on alpha(S) in global PDF analyses and implications for predicted hadronic cross sections*, Eur. Phys. J. C **64** (2009) 653, arXiv: 0905.3531 [hep-ph].

[234] Hung-Liang Lai, Marco Guzzi, Joey Huston, Zhao Li, Pavel M. Nadolsky, Jon Pumplin, and C. P. Yuan, *New parton distributions for collider physics*, Phys. Rev. D **82** (2010) 074024, arXiv: 1007.2241 [hep-ph].

[235] Jun Gao, Marco Guzzi, Joey Huston, Hung-Liang Lai, Zhao Li, Pavel Nadolsky, Jon Pumplin, Daniel Stump, and C. P. Yuan, *CT10 next-to-next-to-leading order global analysis of QCD*, Phys. Rev. D **89** (2014) 033009, arXiv: 1302.6246 [hep-ph].

[236] Richard D. Ball et al., *Parton distributions with LHC data*, Nucl. Phys. B **867** (2013) 244, arXiv: 1207.1303 [hep-ph].

[237] Nikolaos Kidonakis, *Two-loop soft anomalous dimensions for single top quark associated production with a W^- or H^-*, Phys. Rev. D **82** (2010) 054018, arXiv: 1005.4451 [hep-ph].

[238] Nikolaos Kidonakis, *Top Quark Production*, arXiv: 1311.0283 [hep-ph].

[239] ATLAS Collaboration, *Modelling Wt and tWZ production at NLO for ATLAS analyses*, arXiv: 1612.00440 [hep-ph].

[240] Charalampos Anastasiou, Lance Dixon, Kirill Melnikov, and Frank Petriello, *High-precision QCD at hadron colliders: Electroweak gauge boson rapidity distributions at next-to-next-to leading order*, Phys. Rev. D **69** (2004) 094008, arXiv: 0312266 [hep-ph].

[241] ATLAS Collaboration, *Measurements of top-quark pair to Z-boson cross-section ratios at $\sqrt{s} = 13, 8, 7$ TeV with the ATLAS detector*, JHEP **02** (2017) 117, arXiv: 1612.03636 [hep-ex].

[242] ATLAS Collaboration. *Multi-boson simulation for* 13 *TeV ATLAS analyses*, . ATL-PHYS-PUB-2016-002, 2016, URL: `https://cds.cern.ch/record/2119986`.

[243] Celine Degrande, Claude Duhr, Benjamin Fuks, David Grellscheid, Olivier Mattelaer, and Thomas Reiter, *UFO - The Universal FeynRules Output*, Comput. Phys. Commun. **183** (2012) 1201, arXiv: 1108.2040 [hep-ph].

[244] Adam Alloul, Neil D. Christensen, Céline Degrande, Claude Duhr, and Benjamin Fuks, *FeynRules 2.0 - A complete toolbox for tree-level phenomenology*, Comput. Phys. Commun. **185** (2014) 2250, arXiv: 1310.1921 [hep-ph].

[245] P. Artoisenet et al., *A framework for Higgs characterisation*, JHEP **11** (2013) 043, arXiv: 1306.6464 [hep-ph].

[246] Céline Degrande, Gauthier Durieux, Fabio Maltoni, Ken Mimasu, Eleni Vryonidou, and Cen Zhang, *Automated one-loop computations in the SMEFT*, Phys. Rev. D **103** (2021) 096024, arXiv: 2008.11743 [hep-ph].

[247] Valentin Hirschi and Olivier Mattelaer, *Automated event generation for loop-induced processes*, JHEP **10** (2015) 146, arXiv: 1507.00020 [hep-ph].

[248] Stefan Höche, Frank Krauss, Marek Schönherr, and Frank Siegert, *A critical appraisal of NLO+PS matching methods*, JHEP **09** (2012) 049, arXiv: 1111.1220 [hep-ph].

[249] S. Catani, F. Krauss, B. R. Webber, and R. Kuhn, *QCD Matrix Elements + Parton Showers*, JHEP **11** (2001) 063, arXiv: 0109231 [hep-ph].

[250] Stefan Höche, Frank Krauss, Steffen Schumann, and Frank Siegert, *QCD matrix elements and truncated showers*, JHEP **05** (2009) 053, arXiv: 0903.1219 [hep-ph].

[251] Ansgar Denner, Stefan Dittmaier, and Lars Hofer, *COLLIER: A fortran-based complex one-loop library in extended regularizations*, Comput. Phys. Commun. **212** (2017) 220, arXiv: 1604.06792 [hep-ph].

[252] Federico Buccioni, Jean-Nicolas Lang, Jonas M. Lindert, Philipp Maierhöfer, Stefano Pozzorini, Hantian Zhang, and Max F. Zoller, *OpenLoops 2*, Eur. Phys. J. C **79** (2019) 866, arXiv: 1907.13071 [hep-ph].

[253] Stefan Kallweit, Jonas M. Lindert, Philipp Maierhöfer, Stefano Pozzorini, and Marek Schönherr, *NLO QCD+EW predictions for V + jets including off-shell vector-boson decays and multijet merging*, JHEP **04** (2016) 021, arXiv: 1511.08692 [hep-ph].

[254] Christian Gütschow, Jonas M. Lindert, and Marek Schönherr, *Multi-jet merged top-pair production including electroweak corrections*, Eur. Phys. J. C **78** (2018) 317, arXiv: 1803.00950 [hep-ph].

[255] Heribertus B. Hartanto, Barbara Jager, Laura Reina, and Doreen Wackeroth, *Higgs boson production in association with top quarks in the POWHEG BOX*, Phys. Rev. D **91** (2015) 094003, arXiv: 1501.04498 [hep-ph].

[256] ATLAS Collaboration. *Simulation of top-quark production for the ATLAS experiment at* $\sqrt{s}$ = 13 *TeV*, . ATL-PHYS-PUB-2016-004, 2016, URL: https://cds.cern.ch/record/2120417.

[257] Emanuele Re, *Single-top Wt-channel production matched with parton showers using the POWHEG method*, Eur. Phys. J. C **71** (2011) 1547, arXiv: 1009.2450 [hep-ph].

[258] ATLAS Collaboration. *Studies on top-quark Monte Carlo modelling for Top2016*, . ATL-PHYS-PUB-2016-020, 2016, URL: https://cds.cern.ch/record/2216168.

[259] Stefano Frixione, Eric Laenen, Patrick Motylinski, Chris White, and Bryan R. Webber, *Single-top hadroproduction in association with a W boson*, JHEP **07** (2008) 029, arXiv: 0805.3067 [hep-ph].

[260] ATLAS Collaboration, *Search for new phenomena in events with same-charge leptons and b-jets in pp collisions at* $\sqrt{s} = 13$ *TeV with the ATLAS detector*, JHEP **12** (2018) 039, arXiv: 1807.11883 [hep-ex].

[261] ATLAS Collaboration, *Search for R-parity-violating supersymmetry in a final state containing leptons and many jets with the ATLAS experiment using* $\sqrt{s} = 13TeV$ *proton–proton collision data*, Eur. Phys. J. C **81** (2021) 1023, arXiv: 2106.09609 [hep-ex].

[262] G. Avoni et al., *The new LUCID-2 detector for luminosity measurement and monitoring in ATLAS*, JINST **13** (2018) P07017.

[263] ATLAS Collaboration, *Jet energy measurement with the ATLAS detector in proton–proton collisions at* $\sqrt{s} = 7$ *TeV*, Eur. Phys. J. C **73** (2013) 2304, arXiv: 1112.6426 [hep-ex].

[264] ATLAS Collaboration, *Jet energy resolution in proton–proton collisions at* $\sqrt{s} = 7$ *TeV recorded in 2010 with the ATLAS detector*, Eur. Phys. J. C **73** (2013) 2306, arXiv: 1210.6210 [hep-ex].

[265] ATLAS Collaboration. *Tagging and suppression of pileup jets*, . ATL-PHYS-PUB-2014-001, 2014, URL: `https://cds.cern.ch/record/1643929`.

[266] ATLAS Collaboration, *Jet energy measurement and its systematic uncertainty in proton–proton collisions at* $\sqrt{s} = 7$ *TeV with the ATLAS detector*, Eur. Phys. J. C **75** (2015) 17, arXiv: 1406.0076 [hep-ex].

[267] ATLAS Collaboration, *Determination of jet calibration and energy resolution in proton–proton collisions at* $\sqrt{s} = 8$ *TeV using the ATLAS detector*, Eur. Phys. J. C **80** (2020) 1104, arXiv: 1910.04482 [hep-ex].

[268] ATLAS Collaboration, *Measurements of b-jet tagging efficiency with the ATLAS detector using* $t\bar{t}$ *events at* $\sqrt{s} = 13$ *TeV*, JHEP **08** (2018) 089, arXiv: 1805.01845 [hep-ex].

[269] ATLAS Collaboration, *Performance of missing transverse momentum reconstruction with the ATLAS detector using proton–proton collisions at* $\sqrt{s} = 13$ *TeV*, Eur. Phys. J. C **78** (2018) 903, arXiv: 1802.08168 [hep-ex].

[270] ATLAS Collaboration, *Combined search for the Standard Model Higgs boson in pp collisions at* $\sqrt{s} = 7$ *TeV with the ATLAS detector*, Phys. Rev. D **86** (2012) 032003, arXiv: 1207.0319 [hep-ex].

[271] Glen Cowan, Kyle Cranmer, Eilam Gross, and Ofer Vitells, *Asymptotic formulae for likelihood-based tests of new physics*, Eur. Phys. J. C **71** (2011) 1554, arXiv: 1007.1727 [physics].

[272] S. S. Wilks, *The Large-Sample Distribution of the Likelihood Ratio for Testing Composite Hypotheses*, Annals Math. Statist. **9** (1938) 60.

[273] Alexander L. Read, *Presentation of search results: the CL_S technique*, J. Phys. G **28** (2002) 2693.

[274] Erik Gerwick, Tilman Plehn, Steffen Schumann, and Peter Schichtel, *Scaling patterns for QCD jets*, JHEP **10** (2012) 162, arXiv: 1208.3676 [hep-ph].

[275] Peter W. Battaglia et al., *Relational inductive biases, deep learning, and graph networks*, arXiv: 1806.01261 [cs.LG].

[276] Martín Abadi et al., *TensorFlow: Large-Scale Machine Learning on Heterogeneous Distributed Systems*, arXiv: 1603.04467 [cs.DC].

[277] Tianqi Chen and Carlos Guestrin, *XGBoost: A Scalable Tree Boosting System*, ACM, Aug 2016, URL: http://dx.doi.org/10.1145/2939672.2939785.

[278] Jon Butterworth et al., *PDF4LHC recommendations for LHC Run II*, J. Phys. G **43** (2016) 023001, arXiv: 1510.03865 [hep-ph].

[279] *Measurements of inclusive and differential fiducial cross-sections of $t\bar{t}$ production with additional heavy-flavour jets in proton-proton collisions at $\sqrt{s} = 13$ TeV with the ATLAS detector*, JHEP **04** (2019) 046, arXiv: 1811.12113 [hep-ex].

[280] ATLAS Collaboration, *Measurement of the production cross-section of a single top quark in association with a Z boson in proton-proton collisions at 13 TeV with the ATLAS detector*, Phys. Lett. B **780** (2018) 557.

[281] Hesham El Faham, *tWZ production at NLO in QCD in the SMEFT*, arXiv: 2112.13282 [hep-ph].

[282] ATLAS Collaboration, *Measurement of $W^{\pm}Z$ production cross sections and gauge boson polarisation in pp collisions at $\sqrt{s} = 13$ TeV with the ATLAS detector*, Eur. Phys. J. C **79** (2019) 535, arXiv: 1902.05759 [hep-ex].

[283] ATLAS Collaboration, *Measurements of WH and ZH production in the $H \to b\bar{b}$ decay channel in pp collisions at 13 TeV with the ATLAS detector*, Eur. Phys. J. C **81** (2021) 178, arXiv: 2007.02873 [hep-ex].

[284] ATLAS Collaboration, *Measurement of the $t\bar{t}Z$ and $t\bar{t}W$ cross sections in proton–proton collisions at $\sqrt{s} = 13$ TeV with the ATLAS detector*, Phys. Rev. D **99** (2019) 072009, arXiv: 1901.03584 [hep-ex].

[285] Steve Baker and Robert D. Cousins, *Clarification of the Use of Chi Square and Likelihood Functions in Fits to Histograms*, Nucl. Instrum. Meth. **221** (1984) 437.

[286] Robert D. Cousins, *Generalization of Chisquare Goodness-of Fit Test for Binned Data Using Saturated Models, with Application to Histograms*, URL: https://www.physics.ucla.edu/~cousins/stats/cousins_saturated.pdf, accessed: 2024-03-09.

[287] Qing-Hong Cao, Shao-Long Chen, Yandong Liu, and Xiao-Ping Wang, *What can we learn from triple top-quark production?*, Phys. Rev. D **100** (2019) 055035, arXiv: 1901.04643 [hep-ph].

[288] Hamzeh Khanpour, *Probing top quark FCNC couplings in the triple-top signal at the high energy LHC and future circular collider*, Nucl. Phys. B **958** (2020) 115141, arXiv: 1909.03998 [hep-ph].

[289] ATLAS Collaboration, *CP Properties of Higgs Boson Interactions with Top Quarks in the $t\bar{t}H$ and tH Processes Using $H \to \gamma\gamma$ with the ATLAS Detector*, Phys. Rev. Lett. **125** (2020) 061802, arXiv: 2004.04545 [hep-ex].

[290] CMS Collaboration, *Search for production of four top quarks in final states with same-sign or multiple leptons in proton-proton collisions at $\sqrt{s} = 13$ TeV*, Eur. Phys. J. C **80** (2020) 75, arXiv: 1908.06463 [hep-ex].

[291] ATLAS Collaboration, *Combined measurements of Higgs boson production and decay using up to 80 fb^{-1} of proton–proton collision data at $\sqrt{s} = 13$ TeV collected with the ATLAS experiment*, Phys. Rev. D **101** (2020) 012002, arXiv: 1909.02845 [hep-ex].

[292] D. J. Lange, *The EvtGen particle decay simulation package*, Nucl. Instrum. Meth. A **462** (2001) 152.

[293] ATLAS Collaboration, *Search for heavy Higgs bosons in $t\bar{t}$ final states with additional heavy-flavour jets in pp collisions at $\sqrt{s} = 13$ TeV with the ATLAS detector*, ATL-COM-PHYS-2017-352, Apr 2017, URL: https://cds.cern.ch/record/2258130.

[294] Pierre Baldi, Kyle Cranmer, Taylor Faucett, Peter Sadowski, and Daniel Whiteson, *Parameterized neural networks for high-energy physics*, Eur. Phys. J. C **76** (2016) 235, arXiv: 1601.07913 [hep-ex].

[295] James D. Bjorken and Stanley J. Brodsky, *Statistical Model for Electron-Positron Annihilation into Hadrons*, Phys. Rev. D **1** (1970) 1416.

[296] ATLAS Collaboration. *ATLAS sensitivity to Two-Higgs-Doublet models with an additional pseudoscalar exploiting four top quark signatures with 3ab^{-1} of $\sqrt{s} =$ 14 TeV proton–proton collisions*, . ATL-PHYS-PUB-2018-027, 2018, URL: https://cds.cern.ch/record/2645845.

[297] ATLAS Collaboration, *Combination and summary of ATLAS dark matter searches interpreted in a 2HDM with a pseudo-scalar mediator using 139 fb^{-1} of $\sqrt{s} = 13$ TeV pp collision data*, arXiv: 2306.00641 [hep-ex].